



FACULTAD DE
INGENIERÍA
UDELAR



UNIVERSIDAD
DE LA REPUBLICA
URUGUAY

Light propagation in multilayered nanostructures

Characterization and modelling of morphological effects on the
optical properties of stratified media

Juan P. Martínez Alvarez

Postgraduate program in Engineering-Physics
Facultad de Ingeniería
Universidad de la República

Montevideo – Uruguay
May of 2024



FACULTAD DE
INGENIERÍA
UDELAR



AGENCIA NACIONAL
DE INVESTIGACIÓN
E INNOVACIÓN



UNIVERSIDAD
DE LA REPUBLICA
URUGUAY

Light propagation in multilayered nanostructures

Characterization and modelling of morphological effects on the
optical properties of stratified media

Juan P. Martínez Alvarez

Master's Thesis submitted to the Postgraduate Program in Engineering-Physics, Facultad de Ingeniería of the Universidad de la República, as part of the necessary requirements for obtaining the title of Master in Engineering-Physics.

Directors:

Dr. Prof. Paulo Valente

Dr. Prof. Carlos Javier Pereyra

Academic director:

Dr. Prof. Carlos Javier Pereyra

Montevideo – Uruguay

May of 2024

Martínez Alvarez, Juan P.

Light propagation in multilayered nanostructures / Juan P. Martínez Alvarez. - Montevideo: Universidad de la República, Facultad de Ingeniería, 2024.

XXXIII, 203 p.: il.; 29, 7cm.

Directors:

Paulo Valente

Carlos Javier Pereyra

Academic director:

Carlos Javier Pereyra

Tesis de Maestría – Universidad de la República,
Program in Engineering-Physics, 2024.

Bibliography: p. 131 – 164.

1. Nanotecnología, 2. Optica, 3. Fotónica,
4. Morfología, 5. Modelado. I. Valente, Paulo,
Pereyra, Carlos Javier, . II. Universidad de la República,
Postgraduate Program in Engineering-Physics. III. Title

MEMBERS OF THE THESIS DEFENSE COURT

Dr. Prof. Erna Frins

Dr. Prof. Sofia Favre

Dr. Prof. Mauricio Rodríguez

Montevideo – Uruguay

May of 2024

To my mom, Gabriela, my sister
Lucia and to Laura

Acknowledgements

I wish to convey my gratitude to professors Javier Pereyra and Paulo Valente, who gave me the opportunity to initiate my journey in research. Their knowledge and guidance were invaluable in driving, motivating, and enhancing the discussions throughout the last couple of years. I extend the gratitude to the rest of the Group of Solid-State Physics, particularly to Prof. Ricardo Marotti and Prof. Enrique Dalchiele, their contributions were fundamental in my development as a researcher.

I am indebted to the Catalan Institute of Nanoscience and Nanotechnology (ICN2), especially Prof. Clivia Sotomayor-Torres, Prof. Javier Rodriguez-Viejo and Dr. Peng Xiao, for giving me the opportunity to do a research stay in their group, which resulted in one of the best experiences of my career. Their support, encouragement, and the skills they taught me not only made me feel welcomed and motivated, but I am sure will be instrumental in my future career.

My friends and family made it possible to reach this point and for that, I am forever grateful. There are no words to describe the importance of the support and care that my mother and sister have given me. Thank you, you both mean the world to me. Lastly, to Laura, I could not have done it without you, thank you for sharing the journey.

RESUMEN

Los materiales nanoestructurados, aquellos con al menos una dimensión física del orden de los 100 nm o menos, han impulsado avances tecnológicos significativos en las últimas décadas. Su capacidad para manipular las interacciones entre la luz y la materia a esta escala, permitiendo un control por debajo de la longitud de onda, ha impulsado a la fotónica como uno de los principales campos de investigación en los últimos tiempos. Aunque los materiales ópticos nanoestructurados naturales son abundantes, no fue hasta el reciente desarrollo de técnicas de síntesis que permitieron el control nanométrico de materiales sintéticos. Entre estos materiales, las nanoestructuras multicapa, con espesor confinado a la nanoescala, han surgido como un elemento clave en tecnologías fundamentales como los dispositivos fotovoltaicos para la generación de energía renovable.

La comprensión de las propiedades ópticas de los materiales nanoestructurados demanda un enfoque multifacético debido a su complejidad y la diversidad de fenómenos. Estos materiales suelen tener propiedades interesantes de transmitancia y reflectancia, efectos de dispersión notable y propiedades dependientes de la polarización debido a su morfología única. Este estudio explora materiales con naturalezas muy diferentes mediante métodos ópticos, mostrando la variedad de materiales ópticos y las técnicas utilizadas para estudiarlos. Los materiales más simples estudiados fueron películas de dióxido de Silicio crecidas sobre Silicio cristalino mediante medidas de reflectancia. Luego, se estudiaron las estructuras complejas en las alas de la mariposa translúcida *Episcada hymenaea* y la polilla común *Saturniidae Heliconisa pagenstecheri*, ambas autóctonas del Uruguay, empleando medidas en el rango UV-vis, en las que se observaron efectos de conversión de polarización particularmente llamativos. Por último, se aplicaron técnicas ópticas al estudio de nanoestructuras unidimensionales (1D), se examinaron nanovarillas de ZnO sensibilizadas con SnS, para conocer sus propiedades de transmitancia, reflectancia, absorción y polarización. Se observaron efectos interesantes relacionados con la morfología de las nanoestructuras—en particular la formación de nanotubos—abriendo el camino para futuros trabajos en semiconductores nanoestructurados.

Para interpretar los resultados de manera efectiva, se implementó una herramienta matemática capaz de manejar nanoestructuras multicapa, el método de matriz de transferencia, que proporciona información sobre algunos fenómenos específicos observados en las muestras. La aplicación de esta herramienta subyace todo el trabajo, que en última

instancia muestra el potencial y las limitaciones de la técnica.

Palabras claves:

Nanotecnología, Óptica, Fotónica, Morfología, Modelado.

ABSTRACT

Nanostructured materials, those with at least one physical dimension of the order of 100 nm or less, have driven significant technological advancements in the last decades. Their ability to manipulate light-matter interactions at this scale, enabling control below the wavelength, has propelled photonics into one of the leading research fields. While natural nanostructured optical materials abound, it was not until the recent development of synthesis techniques that allowed custom fabrication. Among the nanoscale materials, multilayered nanostructures, with thickness confined to the nanoscale, have emerged as a key element in fundamental technologies such as photovoltaic devices for clean energy generation.

Understanding the optical properties of nanostructured materials demands a multifaceted approach due to their complexity and diverse phenomena. These materials usually have interesting transmittance and reflectance properties, remarkable scattering effects and polarization dependent effects due to their unique morphology. This study explores materials with very different natures by optical methods, showcasing the variety of optical materials and the techniques used to study them. The simplest materials studied were Silicon dioxide films grown over crystalline Silicon by reflectance measurements. Then, the complex structures in the wings of the *Episcada hymenaea* translucent butterfly and the *Saturniidae Heliconisa pagenstecheri* common moth were studied employing measurements in the UV-vis range, with particularly striking polarization conversion effects observed. Lastly, optical techniques were applied to the study of unidimensional (1D) nanostructures, ZnO nanorods sensitized with SnS, were examined for their transmittance, reflectance, absorption, and polarization properties. Interesting effects related to the morphology of the nanostructures—and the formation of nanotubes—were observed, paving the way for future work on nanostructured semiconductors.

To interpret the results effectively, a mathematical tool capable of handling multilayered nanostructures, the transfer matrix method, was implemented, providing insights into specific phenomena observed in the samples. The application of this tool underscores the whole work, which ultimately showcases the potential, and the limitations, of the technique.

Keywords:

Nanotechnology, Optics, Photonics, Morphology, Modeling.

List of Figures

2.1	Direct and indirect optical transitions. Note that in the indirect transition the process is mediated by a phonon with energy $\hbar\omega_{ph}$, the electron can either absorb or emit a phonon, depending on the photon energy.	8
2.2	Diagram of the Urbach tail phenomenon. Absorption in real materials does not follow the sharp trend expected for ideal crystals. There is an onset of absorption at energies below the bandgap, which widens the absorption edge, creating a tail. This tail, called the Urbach tail, can be modelled by an exponential function.	9
2.3	Schematic of the interaction of light with a sample	12
2.4	Diagram used in the derivation of the Fresnel coefficients	14
2.5	Calculated a) reflectance and b) transmittance spectra for an air-glass interface at a wavelength of 544 nm. Notice that the angular position of the minimum of R_p is indicated by a vertical grey dashed line labeled Brewster angle, discussed in subsection 2.3.2	16
2.6	Schematic of the situations analysed to obtain the Stokes relations. In a) a wave incident from medium 1 is reflected and transmitted, and thus, due to time-reversal invariance, the situation b) must also be possible. In c) we consider each of the fields approaching the boundary in b) individually, each of which is transmitted and reflected. The resulting fields must be equivalent to those of situation b) and this determines the Stokes relations.	17
2.7	Normalized autocorrelation function displaying the coherence time as the width of the curve and the corresponding spectral density with the linewidth $\Delta\nu$. Reproduced from [35]	22
2.8	Schematic of the model used to calculate the transmittance of a thin film. An incoming beam is multiply reflected and transmitted between the two interfaces of the freestanding film. The transmission and reflection is calculated as the infinite sum of all the transmitted and reflected beams, respectively.	25

2.9	Schematic of the situations analysed to obtain the matrices required to implement the transfer matrix method. In a) the propagation of the fields around the boundary between two layers and in b) the propagation inside the layer i	29
2.10	Basic scheme for including incoherent layers to the transfer matrix method. We divide the stack in sections delimited by the incoherent layers. Calculate the transfer matrix for the coherent substack and from its elements obtain an intensity matrix. Then multiply those intensity matrices with the intensity propagation matrices from the incoherent layers.	32
3.1	Schematic of the setup used for transmittance measurements at normal incidence employing the UPB-150-ART integrating sphere	42
3.2	Measurements repeated for each sample in order to correct for the transmittance of the sphere. Their usage appears in equation 3.1. Notice that I_1 and I_3 are collected with the sample in the entrance Port, while I_2 and I_4 collect the lamp signal directly.	43
3.3	Setup used for total and polarized transmittance measurements. The a) top block indicates the configuration used for detecting total and diffuse transmittance. The sample was placed at the entrance orifice of the integrating sphere. b) The bottom block indicates the configuration for polarization dependent measurements, detailed in section 3.2.1. P and A are the polarizer and analyzer, respectively. The polarization sensitive measurement does not use an integrating sphere.	44
3.4	The configurations of the 5 measurements done to obtain the reflectance corrected by the effects of the integrating sphere. The reference used was a Lambertian white surface	45
3.5	Reflection probe used for reflectance at normal incidence. Taken from Thorlabs [53]	48
3.6	Experimental setup for reflectance measurement. The rotating sample holder is mounted on a goniometer, the tray holding the Wollaston prism and two silicon detectors is allowed to rotate around the sample by means of an articulated arm. The signal is modulated with a chopper, which allows the detection through lock-in amplifiers.	49
3.7	a) Schematic representation of the procedure used to align the Wollaston prism. The optics used to condition the incoming beam is omitted for clarity. b) Normalized I_s/I_p curves for the glass substrate taken with a 785 nm wavelength laser	50

3.8	Configurations used to calibrate the position of the QWP in order to measure the S3 Stokes parameter. Notice that for each orientation of the HWP there are a set of observables at the detectors, I_x and I_y . FA and SA are the fast and slow axis of the waveplates, respectively.	52
4.1	Schematic of the heating program used in the growth of Silicon dioxide films. The temperature was varied, with the plateau lasting for 4 hours. The temperature increase and decrease were both at a rate of 120 °C/h. . .	56
4.2	a) Image of the as grown samples under white light. Note the interference colors [27, 28] arising from the different thicknesses. For reference a clean silicon wafer is shown. b) Reference table relating the thickness with the color, taken from the UIUC [75]. For clarity, arrows on the right indicate the observed colors in the fabricated samples.	57
4.3	SEM micrographs of the SiO_2 films grown by 4 hours of thermal oxidation in ambient air at temperatures of a) 900°C, b) 950°C, c) 1050°C and d) 1150°C. The inset in the figures present a lower magnification image to demonstrate the general quality of the cleaved films. In the images some of the sampled thicknesses are shown. Notice that in d) there is surface charge accumulation.	58
4.4	a) Schematic of the model employed to fit the thickness of the silicon dioxide films. Air and Si are semi infinite media that bound a SiO_2 film of thickness d . The two interfaces are linked to two interface matrices, while the propagation inside the layer is modeled by a propagation matrix. b) Calculated reflectance spectra obtained from the application of TMM to the model presented in a). Notice the spectral color reference on the top left, which shows an approximate correspondence of the color of light (as perceived by human eyes) for that wavelength range.	60
4.5	Measured and calculated reflectance spectra of the SiO_2 films grown by 4 hours of thermal oxidation in ambient air at temperatures of a) 900°C, b) 950°C, c) 1050°C and d) 1150°C. The thickness resulting from the fit (d) is shown in the figures. Grey solid line is the measured spectra and red dashed line is the calculated spectra.	61

5.1	SEM micrographs of the wing of the <i>Episcada hymenaea</i> translucent butterfly. a) General structure of the wing (scale bar $200\mu m$), we see the edge composed of scales and the inner region, both have long bristles. b) Image along the edge of the wing, where there appears to be two layers on the wing membrane, a bottom bulk and a top corrugated region (scale $500nm$). c) Image at the edge of the wing, and example of 3 sections sampled for the thickness, the scale bar represents $500 nm$, the bottom inset is an optical image of the studied wing, sample 1. d) Highest magnification (scale $200nm$) close to the sample surface, we see the general shape of the wing surface, which displays an irregular structure formed by lobes.	66
5.2	SEM micrographs of the wing of a <i>Saturniidae Heliconisa pagenstecheri</i> common moth specimen. a) Transparent region away from scale and inset a close up of that region, where we see there is no nanostructure, the scale bars represent $100 \mu m$ and $1 \mu m$, respectively. b) Image of a single scale on the wing (scale bar $50 \mu m$, in the inset an optical image of the studied wing).	67
5.3	UV-vis absorbance spectrum of the butterfly (<i>Episcada hymenaea</i>) and the moth (<i>Saturniidae Heliconisa pagenstecheri</i>). Arrows indicate the position of the maximum. In the insert the logarithm of the absorbances in the range $400 nm$ to $800 nm$ are displayed, alongside the absorbance of pure chitin calculated from the κ values reported by Azofeifa et.al and assuming a sample thickness of $1\mu m$. The reported absorption band of chitin at $\lambda =280 nm$ is indicated, alongside the position of the $1/e$ decay of the peaks, to aid in width visualization.	68
5.4	Total transmittance spectra at different angles of incidence for the a) <i>Episcada hymenaea</i> translucent butterfly and the b) <i>Saturniidae Heliconisa pagenstecheri</i> common moth.	69
5.5	Total reflectance spectra of specimen 1 of <i>Episcada hymenaea</i> translucent butterfly and of <i>Saturniidae Heliconisa pagenstecheri</i> moth. The angle of incidence is $\phi_i = 8^\circ$	70

5.6	a-d) Experimental reflectance (black solid line) and transmittance (blue spheres) with the calculated spectra (dashed red and blue lines, respectively) using the obtained effective refractive index (\hat{n}) of the wing membrane for a smooth layer of thickness a) 450 nm and d) 810 nm. Models including a top roughness layer of 10 nm thickness composed of a membrane air mixture with air fraction equal 0.6 on top of a layer of membrane of thickness b) 450 nm and e) 810 nm). A schematic of the model described is shown in c). f) The obtained effective refractive indices obtained through Nichelatti's procedure for both thicknesses, where it is clear that the difference in the real part (n) is negligible.	72
5.7	a)Real and b) imaginary parts of the calculated effective refractive index for the wing material following Nichelatti's procedure, for three different samples and two regions in sample 2. In all cases the thickness that better matched the spectra (better coincidence with the period of the reflectance spectra) was used.	74
5.8	Measured angle dependant total transmittance spectra for sample 1 with the simulated results using the calculated refractive index assuming a layer of thickness 810 nm and an incoherent 10nm layer to account for roughness.	76
5.9	a) Transmittance spectra of a single layer of chitin-chitosan with $f_{chitosan} = 0.7$ and experimental results, both for 0 and 40 degrees incident angle. b) Calculated spectra with the linear mixing model compared to experimental data, a schematic of the model is shown in c)	78
5.10	a) Schematic of the Gaussian profile approach for chitin-chitosan-air mixing. b) Statistic of the measured standard deviation (σ_m) of the lobes in the wing surface and c) Results of the model after averaging over 1000 profiles. For comparison with the linear model see the light gray dashed and dotted lines.	80
5.11	Schematic of the reflection process for the cases of a surface with a) low scattering and b) high scattering. The thickness of the arrows represents the amount of light. The width of the arrows represent the intensity of light. Solid and dashed arrows correspond to specular and diffuse components, respectively. In the high scattering case, b), a large fraction of the reflected light is deviated from the main beam and is not incident upon the detector	82

5.12	a) Diffuse reflectance at $\phi_i = 8^\circ$, b) diffuse transmittance at $\phi_i = 0^\circ$ c) Reflectance haze, obtained from measurements performed at an angle of incidence of $\phi_i = 8^\circ$ and d) Transmittance haze at normal incidence ($\phi_i = 0^\circ$). Notice the vertical grey dashed lines, which indicate the wavelengths that will be used in the angle resolved transmittance measurements.	83
5.13	Measured intensity for monochromatic transmittance through the moth sample around the main beam position for different angles of incidence. In a) the incident wavelength is $\lambda = 405$ nm and all the data sets were fitted with Lorentzian curves in order to estimate the FWHM. In b) the incident wavelength is $\lambda = 632$ nm and some data were fitted with a Gaussian curve, the fitting curve used are indicated next to the legend. The insert shows a schematic of the experimental setup.	84
5.14	Direct transmittance spectra for both configurations and different angles of incidence. The full lines correspond to the configuration 11 (T_{11}) and the dashed lines to T_{22} . Note that both polarizations mimic each other, a behaviour that is not expected from the Fresnel coefficients, that assume isotropic homogeneous surfaces.	86
5.15	Modeled transmittance of each polarization using the TMM for a) Gaussian gradient index and b) the effective refractive index (ERI) previously calculated from reflection and transmission spectra. Solid lines correspond to s-polarized light and dashed lines to p-polarized. Black and grey lines are for $\phi_i = 0^\circ$, while red and blue are for $\phi_i = 30^\circ$ and $\phi_i = 60^\circ$, respectively.	87
5.16	Direct and crossed transmittance spectra as a function of the angle of incidence (ϕ_i) probed with a laser of wavelength a) 405 nm and b) 632.2 nm	88
5.17	a) Polarized transmittance as a function of the angle of incidence at a) 405 nm and b) 632.2 nm. Shown are the experimental data for the total polarized transmittance ($T_i = T_{ii} + T_{ij}$), with T_1 in black squares and T_2 is red triangles. The results from the isotropic model (iso) are shown with dashed and dot dashed lines, while the spectra calculated with the anisotropic (anis) model are shown with dotted curves.. In c) a schematic of the model used for anisotropic calculations.	89
5.18	Estimation of the haze as a function of the angle of incidence. For reference, the value obtained with the integrating sphere ($\phi_i = 0^\circ$) for low wavelengths is shown (horizontal dashed line)	90
5.19	Transmittance spectra for the a) T_{12} and b) T_{21} configurations with varying angles of incidence. As a visual aid, the arrows indicate the position of the extrema used in the thickness calculation.	92

6.1	SEM images of samples prepared with a ZnO precursor concentration of a),c) and e) 4 mM and b),d),f) 12 mM, with 0 (a and b), 10 (c, d) and 15 (e, f) SILAR cycles. The insets show images of the samples at 45°	101
6.2	Total and diffuse reflectance (TR and DR) of the 4mM (a and c, respectively) and 12mM (b and d) sets. Notice that the maximum of each spectra is indicated next to the corresponding curve.	105
6.3	Total and diffuse transmittance (TT and DT, respectively) of the 4mM (a and c, respectively) and 12mM (b and d) sets. Notice that in the diffuse transmittance spectra, the positions of the maxima of each curve are indicated.	107
6.4	Reflectance and transmittance transmittance (RH and TH) of the 4mM (a and c, respectively) and 12mM (b and d) sets. The arrow remarks the tendencies with the number of SILAR cycles. The length (L), diameter (D) and coverage factor (C	108
6.5	Absorbance spectra and fitted absorbance contributions for a) 4mM 10 cycles, b) 12mM 10 cycles, c) 4mM 15 cycles and d) 12mM 15 cycles. . . .	110
6.6	Simulated von Mises stress as a function of diameter for NRs (closed symbols) and NTs (open symbols), for two different thicknesses of the shell (t_{SnS}), 14 nm (circles) and 28 nm (squares). The length and the ratio of inner hole to total diameter are kept at 700 nm and 0.6, respectively. The two outermost datasets show an exponential decay fit intended to aid the viewer in identifying the general tendency. In dotted vertical lines the average diameter for the sensitized 12mM samples is displayed.	113
6.7	Simulated von Mises stress for a) 12mM 10 cycle nanorod and b) 12mM 15 cycle nanotube. The parameters are taken from the SEM measurements of the samples, which appear in table 6.1.	114
6.8	Experimental and fitted total transmittance spectra for the a) 4 mM and b) 12 mM sets. The fitted curves are represented with grey lines, solid, dash-and short dot corresponding to 0, 10 and 15 cycles, respectively. The corresponding reflectance spectra and the obtained from the model with the fitted parameters appear in c) and d) for the 4 mM and 12 mM sets, respectively.	116
6.9	Degree of polarization as a function of the angle of incidence in transmittance for the a) 4 mM and b) 12 mM sets and in reflectance for the c) 4 mM and d) 12 mM sets. All plots have a dashed line that indicates the measured degree of polarization for a glass slide 1.25 mm thick.	120

6.10	Schematics used to discuss the angular dependence of the degree of polarization. in a) the angle of incidence is close to the preferential growth direction, and the light rays can go straight through caps, while at b) oblique incidence there are more interactions with the nanorods, enhancing multiple scattering.	122
6.11	Average degree of Polarization (P) and Haze as at $\lambda = 785nm$ in the cases of a) transmittance, where the inset shows a close up of the degree of polarization, and b) reflectance. Dashed gray line indicates the linear fit for the polarization of the samples. The samples that show nanotubes (NTs) are indicated.	123
A.1	Train of optical elements used to analyze the state of polarization. First a retarder plate that introduces a phase difference between its fast and slow axes of γ , the fast axis (FA) of which makes an angle of ϕ with the horizontal \hat{x} axis of the lab. After the retarder we have a linear polarizer with a transmission axis making an angle of θ with the \hat{x} axis of the lab . .	168
B.1	a) Schematic representation of a Wollaston prism, which separates orthogonal polarization components by employing the birefringence on two calcite crystals. The images are taken from [319] and [27]. b) Spectral dependence of the deviation angle, obtained from [319]	175
B.2	On the left we can see a schematic of the radiation reflected by a perfect Lambertian surface. On the right, the reflectance spectra of barium sulfate. The images were obtained from [320]	176
B.3	On the left we can see a schematic of one model of integrating sphere used. On the right, the distribution of the different ports and baffled located around the equatorial plane. Images obtained from [320]	177
B.4	Jones matrices for the different optical elements used in this work. Extracted from [28].	178
D.1	SEM micrographs of the wing of the <i>Episcada hymenaea</i> translucent butterfly. a) General structure of the wing (scale bar $200\mu m$), we see the edge composed of scales and the inner region, both have long bristles. b) Image of the bristles (scale bar $20\mu m$, c) close up of a single bristle, where the general structure can be seen (scale bar $1\mu m$) and d) highest magnification of the structure, where the reticular structure is apparent (scale bar $0.5\mu m$)	184

D.2	Extinction coefficient (k) as a function of frequency (f) as a black solid curve. The red dashed line shows the fitting with a Lorentz oscillator, which is in excellent agreement with experiment ($R^2 > 0.99$). The blue dotted line shows the calculated index of refraction (n) using the Kramers-Kronig relations truncated to the shown frequency range. In dark blue dash dotted line the index of refraction reported by Azofeifa and others [125] is shown for comparison.	185
D.3	Schematic of the width at a given height for a Gaussian distribution	187
D.4	Resulting Gaussian profile used in gradient index calculations, obtained by averaging the results for 1000 samples of the standard deviation form a uniform distribution. For comparison the linear profile is shown in the red dashed line	188
E.1	SEM images of samples prepared with a ZnO precursor concentration of a),c) and e) 4 mM and b),d),f) 12 mM, with 0 (a and b), 10 (c, d) and 15 (e, f) SILAR cycles. The scale bars represent 500 nm.	190
E.2	a) SEM image of the 12 mM 10 cycle sample, where the white circles indicate some of the structures called “clusters” and the white dash box shows the region shown in b). In the closeup b), some of the structures called nanocrystals are shown,. The scale bars represent 500 nm.	191
E.3	Threshold area selection in the program ImageJ with intensity boundaries of 35 to 255 applied to the 12 mM, 15 cycle sample. In a) the original image, and b) the selected nanostructures in red. The scale bars represent 500 nm.	192
E.4	EDX results for the 4 mM set with a) 10 SILAR cycles and b) 15 SILAR cycles. The images show the analyzed area, and in the top right of the EDX results the weight percentage of each element is shown. The K indicates that the excited electrons relaxed to the K shell, the one closest to the nucleus. Scale bars represent 1 μm	193
E.5	EDX results for the 12 mM set with a) 10 SILAR cycles on the basal plane and b) on the side wall. In c) the results for the 15 cycles sample. The images show the analyzed area, and in the top right of the EDX results the weight percentage of each element is shown. The K indicates that the excited electrons relaxed to the K shell, the one closest to the nucleus [323, 324]. Scale bars in a) and b) represent 1 μm and that of c) 2 μm	194
F.1	Schematic of the model of concentric hollow cylinders used to model a nanotube	195

F.2	width=0.4	197
F.3	Histogram of sampled hole ratio (fraction of hole diameter to external diameter) from SEM images for a) 4mM and b) 12 mM nanotubes	199
F.4	Percentage temperature increase of a nanorod relative to a nanotube in the profile of the shell with varying a) thickness and b) external diameter. The hole ratio is 0.6. In a) the external diameter is kept fixed at 300 nm and in b) the shell thickness is 28 nm. The power generated is $2.5 \times e^{13}W/m^3$. Notice that in b) the average diameter of the 15 cycles (which showed NTs) 4 mM and 12 mM samples are indicated with grey dashed lines	199
F.5	Simulated temperature profiles for nanotube and nanorod in COMSOL . .	200
G.1	Schematic of the directions defining the stress tensor	201

List of Tables

- 4.1 Thickness results obtained for thermally oxidized for 4 hours at varying temperatures with different methods. The estimate from the interference color, the predictions of the Deal-Grove model, the measurements using SEM microscopy and the optically found thickness through fitting of the reflectance spectra are shown. The uncertainty in the SEM measurement is given by the standard deviation of the measurements of different regions of the film while in the case of reflectance results from the 95 59
- 5.1 Best fit parameters for the complex refractive index, where $n = A\lambda + B$ and $k = A_0e^{-\frac{\lambda}{q}} + y_0$ with λ the wavelength of light in nm 75
- 5.2 Calculated thickness values obtained for the *Episcada hymenaea* butterfly wing using various refractive indices. The presented values include measurements for each individual configuration, as well as an average that incorporates all extrema observed in both configurations. The reported values represent the average of results from different extrema, the standard deviation was used as the uncertainty. 93
- 6.1 Values of morphological features for each sample taken from the SEM images. The average and the standard deviation of different measurements within each sample were employed as the nominal value and uncertainty, respectively. The apparent length (L_{app}) is taken from the images at 45° (see inset of figure 6.1). The coverage factor is calculated using the color threshold with boundaries of 35 and 255. Con stands for concentration. 103
- 6.2 Parameters obtained from the Tauc plot method 112
- 6.3 Volume fractions of air (f_{air}) and SnS (f_{SnS}) obtained from fitting of the experimental transmittance spectra. 117
- D.1 Best fit parameters for the extinction coefficient (k) using a Lorentzian curve. 186

Contents

Acknowledgements	XI
List of Figures	XVII
List of Tables	XXVII
1 Introduction	1
1.1 Motivation and background	1
1.1.1 Specific objectives of this work	2
1.2 The structure of this thesis	3
2 Theoretical Fundamentals	5
2.1 The absorption of light	5
2.1.1 The absorption coefficient α	5
2.1.2 Expression for the absorption coefficient	6
2.1.3 The Urbach Tail parameter	8
2.1.4 Quantum dots and size effects	9
2.2 Optical parameters	10
2.2.1 The dielectric function ϵ and the refractive index	10
2.2.2 Useful definitions for the study of light interaction with a sample .	11
2.3 Planar interfaces and the Fresnel coefficients	13
2.3.1 The Stokes relations	16
2.3.2 Brewster's angle	17
2.4 Interference of waves	18
2.4.1 Interference color	19
2.4.2 Formal treatment of interference: Coherence theory	20
2.5 The general problem of light propagation	23
2.5.1 The freestanding film	24
2.5.2 Working with a stack of films: the transfer matrix method (TMM) .	28
2.6 Effective Medium Approximation	34

2.6.1	Wiener's bounds: Boundaries of the effective refractive index	35
2.7	Stokes parameters: representation of polarized light	36
2.7.1	The theory of partial polarization	38
3	Experimental Setups	41
3.1	Total transmittance and reflectance measurements	41
3.1.1	Transmittance measurements	41
3.1.2	Variable angle of incidence transmittance	43
3.1.3	Reflectance measurements	44
3.2	Specular measurements	46
3.2.1	Spectral polarized transmittance measurements	46
3.2.2	Reflectance at normal incidence	47
3.2.3	Variable angle of incidence reflectance, transmittance and Stokes Parameters	48
3.2.4	Stokes Parameters	51
3.2.5	UV-vis absorbance	52
4	Thickness determination of Silicon Dioxide films	55
4.1	SiO_2 thin film growth by thermal oxidation	56
4.2	SEM thickness characterization	57
4.3	Thickness determination by reflectance characterization	59
4.4	Conclusion and perspectives	61
5	Optical Properties of the traslucent butterfly and the common moth	63
5.1	Morphological characterization	65
5.2	UV-vis absorbance	67
5.3	Integrating Sphere measurements	69
5.3.1	Total transmittance	69
5.3.2	Total reflectance	70
5.3.3	Effective refractive index of the <i>Episcada hymenaea</i> translucent but- terfly	71
5.4	Scattering Properties	81
5.5	Behaviour of the butterfly wings under polarized light	85
5.5.1	Spectral direct transmittance	85
5.5.2	Variable angle transmittance under laser illumination	87
5.5.3	Crossed Polarized transmittance	91
5.6	Conclusion and future perspectives	93

6 ZnO nanorods sensitized with SnS	97
6.1 Sample fabrication	100
6.1.1 Deposition of ZnO nanorods	100
6.1.2 SnS nanoparticle deposition	100
6.2 Morphological characterization by SEM microscopy	100
6.3 Transmittance and Reflectance spectra	104
6.3.1 Reflectance spectra	105
6.3.2 Transmittance spectra	106
6.3.3 Haze	108
6.3.4 Absorption Edges	109
6.4 Application of the TMM	115
6.5 Polarized light analysis	118
6.6 Conclusions and future perspectives	124
7 Conclusion and future perspectives	127
7.1 List of publications	128
7.1.1 In peer reviewed Journals	128
7.1.2 Congress presentations	128
References	131
Appendices	165
Appendix A Proof of the Stokes parameters measurement configuration . . .	167
A.1 The S_2 Stokes parameter	169
A.2 The S_3 Stokes parameter	170
Appendix B On the specialized equipment used in this work	173
B.1 Lock-in amplifier	173
B.2 The Wollaston Prism	175
B.3 The integrating sphere	176
B.4 Waveplates and linear polarizers	177
B.5 Collimators	178
Appendix C The Deal-Grove model	181
Appendix D Further elements of the <i>Episcada hymenaea</i> traslucent butterfly wings	183
D.1 SEM characterization of the bristles	183
D.2 Gradient index model considerations	184
D.2.1 The extinction coefficient of chitin, k	184
D.2.2 The width of the Gaussian curve, $w(h)$	186

D.2.3	Air fraction profile obtain with the Gaussian model	187
Appendix E	Additional elements of the ZnO-SnS NT/NRs analysis	189
E.1	Additional SEM images	189
E.2	Clusters and Nanocrystals	190
E.3	Cover factor and threshold selection	192
E.4	Energy-dispersive X-ray spectroscopy (EDX)	193
Appendix F	Heat transfer in the nanorods and nanotubes	195
F.1	Nanotube	195
F.2	Nanorod	197
F.3	Application to the measured samples	198
F.4	Numerical modelling employing COMSOL	200
Appendix G	von Mises stress	201

Chapter 1

Introduction

1.1. Motivation and background

The study of light-matter interactions at the nanoscale has paved the way for groundbreaking advancements in modern technology. Among these, multilayered nanostructures or stratified media, have emerged as a cornerstone in the development of high-efficiency photovoltaic devices, antireflection coatings, and complex layered materials such as heterostructures composed of Transition Metal Dichalcogenides (TMDs).

There is growing interest in these nanostructures due to their ability to manipulate light at scales smaller than the wavelength, with the potential to develop materials with tailored optical properties. This ability is important in addressing the need for more efficient energy conversion systems and photonic materials.

In the field of optics the multilayered approach is a well known scheme to produce anti reflection coatings which enhance the transmission of light. This principle is crucial in applications like eyeglasses and camera lenses, solar panels and optical instruments. In recent times photonic crystals represent a cutting-edge application of layered structures in optics. By arranging materials with different refractive indices in a periodic structure, it's possible to create photonic band gaps that control the propagation of light within the crystal. This ability to manipulate light at the nanoscale has implications for developing new optical devices, including highly efficient lasers, LEDs, and sensors.

Crucially, multilayered structures play a pivotal role in the efficiency and effectiveness of solar cells, particularly regarding multijunction solar cells. These advanced solar cells utilize several layers of semiconductor materials, each tailored to absorb a different segment of the solar spectrum. This stratification allows them to overcome the limitations of traditional single-junction cells, which are constrained by the material's bandgap and can only absorb a narrow range of light frequencies efficiently. By stacking multiple semiconductor layers with varying bandgaps, multijunction cells significantly increase the

range of absorbed sunlight, from the ultraviolet through to the infrared. This capability enables these cells to convert a larger portion of solar energy into electricity, dramatically improving the photoconversion efficiency. Such multilayered structures are crucial for applications requiring high power-to-weight ratios, such as satellites and space vehicles, and are also being explored for terrestrial use to maximize the efficiency of solar power generation.

One of the main research lines of The Group of Solid State Physics (GFES), where this thesis work was developed, is the study of nanomaterials for photovoltaic applications. Recent works have explored the interesting properties of novel semiconductor materials, such as thin films, quantum dots, perovskites and 1D nanostructures. The integration of these materials into working devices necessitates the understanding of multilayered structures. Indeed, even in the case of single-junction solar cells, a front and back electrode are necessary for charge extraction. Furthermore, it is of great interest to the progress of the technology to integrate a combination of the novel materials under study into a single device, with the possibility of achieving higher efficiencies.

In this context, it was of interest to develop analysis tools to study multilayered structures, particularly from a computational perspective, in order to complement the probing capabilities of the group. The approach selected was the transfer matrix method, because of its relative theoretical simplicity, its versatility, and computational efficiency. As will be seen in this work, the technique can be augmented and used to study nanomaterials other than films, such as porous media, rough layers and sensitized semiconductors.

To gauge its suitability to work in tandem with the characterization tools and in the workflow of the group, it is necessary to position the technique in the broader context of the study of light propagation in nanostructured materials. To achieve this goal, a multifaceted characterization of different materials is required, with the transfer matrix method applied to explain some of the observed properties.

1.1.1. Specific objectives of this work

The first objective is to develop and computationally implement the transfer matrix method and its augmentations presented in the literature. The method should allow for simulations with varying parameters and, conversely, the fitting of parameters from experimental data. The second is to confirm the correct functioning of the tool by applying it to samples with simple characteristics that are well aligned with the hypotheses of the method. Thirdly, we want to explore more complex nanostructures, that require extensions of the model. This will allow us to showcase the possibilities of the technique and, perhaps more importantly, its limitations. Lastly, it is important to observe the application of the model in the context of the broad characterization of the materials. To

do this we will study 3 sets of samples of extremely different natures. We will begin with SiO_2 films, which are well within the hypothesis of the core models, and then will work on samples that progressively deviate from them, starting with insect wings and finishing with ZnO nanorods, which show very large scale inhomogeneities.

1.2. The structure of this thesis

This thesis begins with chapter 2, where the fundamental theoretical concepts employed in the rest of the work are presented. Due to the multifaceted nature of this work the chapter presents a variety of concepts. It begins with the definition of important physical parameters, like the refractive index or the absorption coefficient, and develops a brief theoretical introduction on their characteristics, relationships and expressions. Then it introduces key concepts of optics, in preparation of the description of the transfer matrix method (TMM). This concepts are then built up progressively: from a single interface, passing through a single layer, until we arrive at the transfer matrix method, which is suitable to model hundreds of stacked layers. Then, some of the ways to enhance the capabilities of the TMM are described. Lastly, an introduction to polarization is provided. Note that some specific elements used in single chapters are reserved for the appendices, which are indicated in the relevant sections of the main work.

Following that chapter, a description of the experimental setups used is presented in chapter 3. This is followed by the study of the most basic set of samples, silicon dioxide films grown over silicon, in chapter 4. As will be seen, these films are smooth and homogenous and are ideal to test the suitability of the TMM. The model is used to fit reflectance spectra and find the film thickness, with results in excellent agreement with those from other methods.

In chapter 5 we study the first set of complex samples: the wings of the *Episcada hymenaea* translucent butterfly and the *Saturniidae Heliconisa pagenstecheri* common moth. This work, which required an interdisciplinary approach, was done in collaboration with the groups of Entomology and Analytical Biochemistry of the Faculty of Sciences (FCIEN). These complex samples showcase the full capabilities of the TMM, and stretch it to its limits. Many interesting optical phenomena arise, in particular an apparent polarization conversion effect, which limits the success of the model. Nevertheless, the TMM successfully reproduces most of the spectral characteristics, highlighting its potential to treat, at least partially, complex biological samples.

Finally, in chapter 6 we study the optical properties of ZnO nanorods sensitized with SnS which were fabricated by collaborators in the Universidad de Valparaíso. This samples showcase interesting properties, particularly the formation of nanotubes. As will be

shown, the TMM completely breaks down for these samples, highlighting the limitations of the model.

The thesis closes with chapter 7, where a brief evaluation of the full thesis is presented, alongside future perspectives and the publications and conference presentations derived from this thesis work.

Chapter 2

Theoretical Fundamentals

In this chapter we will establish the meaning of the absorption coefficient, its expression in terms of the properties of a bulk semiconductor, the deviations from the perfect absorbance spectra and modifications to the bulk material properties due to size effects when the dimensions are reduced to the nanoscale. Then we will introduce the parameters that characterize the interaction of light with a sample, and the way they can be obtained in terms of the material parameters. We then introduce the Fresnel coefficients, which model light propagation at an interface in section 2.3.

In section 2.4 we will discuss the necessary conditions for the interference of waves. With that we will be ready to treat light propagation in real materials. We begin with the simplest case of a freestanding film (2.5.1) and then follow it by developing tools to model stratified samples—a stack of films (section 2.5.2). Later, a way to model material composites is presented. In the end we will discuss the polarization nature of light and how to characterize it in terms of the Stokes parameters.

2.1. The absorption of light

2.1.1. The absorption coefficient α

The electric field \vec{E} of a monochromatic wave of angular frequency ω propagating along the z axis with propagation velocity v can be expressed as shown in equation 2.1, where k is the wavevector, defined as $k = \frac{2\pi}{\lambda}$, λ being the wavelength of the wave. In the equation the fact that $f\lambda = v$, with f the frequency of the wave, was used.

$$E(z, t) = E_0 e^{-i(kz - \omega t)} = E_0 e^{-i\omega(z/v - t)} \quad (2.1)$$

The velocity of propagation of the wave (v) is related to the velocity of propagation of light in vacuum (c) through the index of refraction (n): $n = \frac{c}{v}$. The wavevector inside

a non absorbing material can be expressed in terms of the wavelength in free space (λ) as follows, noting that the frequency of light in linear materials is constant:

$$k = \frac{2\pi}{(\lambda/n)} = \frac{n\omega}{c} \quad (2.2)$$

This can be generalized to the case of an absorbing medium by making the index of refraction a complex number, denoted by \hat{n} , with $\hat{n} = n - ik$. The complex number \hat{n} is called the refractive index, its real part (n) the index of refraction, and the imaginary part (k) the extinction coefficient. Using the refractive index, the propagating wave inside a material can be expressed as shown in equation 2.3.

$$E(z, t) = E_0 e^{-i\omega(z/v-t)} = E_0 e^{-i\omega(z\hat{n}/c-t)} = E_0 e^{-i\omega(z(n-ik)/c-t)} = E_0 e^{-i\omega(zn/c-t)} e^{-\frac{k\omega}{c}z} \quad (2.3)$$

Notice that 2.3 implies that the amplitude of a wave experiences an exponential decay with propagation inside a material. To study this dependency it is useful to define the absorption coefficient $\alpha(\omega)$, which is defined as the fraction of the power absorbed per unit length of the medium. In the following the frequency dependence will be dropped in favour of clarity. If the intensity at position z is $I(z)$ then the decrease in intensity after traversing an infinitesimal slice of thickness dz is given by:

$$dI = -\alpha dz \times I(z) \quad (2.4)$$

This equation can be integrated to obtain Beer's law [1], equation 2.5.

$$I(z) = I_0 e^{-\alpha z} \quad (2.5)$$

Considering that the intensity is proportional to the square of the amplitude, comparing between equations 2.3 and 2.5 results in the relationship between absorption coefficient and extinction coefficient shown in equation 2.6.

$$\alpha = \frac{2k\omega}{c} \quad (2.6)$$

2.1.2. Expression for the absorption coefficient

In semiconductor materials the valence band is the last energy band filled and the conduction band is the first empty energy band. These bands are separated by an energy gap with unavailable states, called the bandgap. The absorption properties of a material are mainly determined by the energy levels close to the bandgap.

Each individual photon transports an energy $\hbar\omega$. The amount of energy lost by a light beam—an ensemble of photons—will be directly proportional to the probability of an electron absorbing that energy. If an electron in the valence band absorbs that energy, it will transition to the conduction band, provided that the energy absorbed is larger than the bandgap. Therefore, the probability that the transition occurs will be directly proportional to the square of the matrix element of the optical transition.

If one considers that the conduction and valence bands are parabolic, and that the semiconductor has a bandgap energy E_g it is possible to show that the absorption coefficient is proportional to the excess photon energy relative to the bandgap [2, 3]:

$$(\alpha \cdot \hbar\omega) \propto B(\hbar\omega - E_g)^\gamma \quad \text{if } \hbar\omega > E_g \quad (2.7)$$

If the photon energy is less than the energy of the bandgap, there is no absorption. In equation 2.7 B is a constant and γ is a factor that depends of the nature of the electronic transition. If the transition is direct, meaning that the maximum of the valence band occurs at the same wavevector (\vec{k}) than the minimum of the conduction band (see figure 2.1) then $\gamma = 1/2$. In indirect transitions the maximum of the valence band occurs at a different \vec{k} than the minimum of the conduction band, which implies that the transition must be mediated by a phonon to conserve total momentum. A diagram of an indirect transition is shown in the right of figure 2.1, notice that in the transition the electron can either absorb or emit a phonon (i.e. phonon energy can be either positive or negative in the figure). For indirect transitions $\gamma = 2$

This relationship between the absorption coefficient and the bandgap energy allows us to obtain E_g by plotting $(\alpha \cdot \hbar\omega)^{1/\gamma}$ as a function of photon energy. γ is determined by inspection of the resulting curve, which should be linear. We fit the linear region of the curve, to find E_g , which is the x-intercept of the line of best fit. This is known as the Tauc plot method [4, 5]. When there are multiple absorption edges each contribution is isolated by first fitting edges at low energy and then subtracting their contributions for subsequent fittings. In real samples, particularly nanostructured materials, the “zero” absorption line may be shifted due to effects like light scattering and absorption from sub-bandgap states or amorphous phases. To address this the absorption spectra is corrected for a “background absorption” (α_{back}), which gives the correct “zero” line. This absorption coefficient is obtained from the transparency region, at energies lower than any other bandgap. The resulting experimental absorbance spectra (α_{exp}) is then given by $\alpha_{exp} = \alpha_{back} + \sum_i^N \alpha_i$, where α_i is the contribution due to the absorption of the i-th constituent [6].

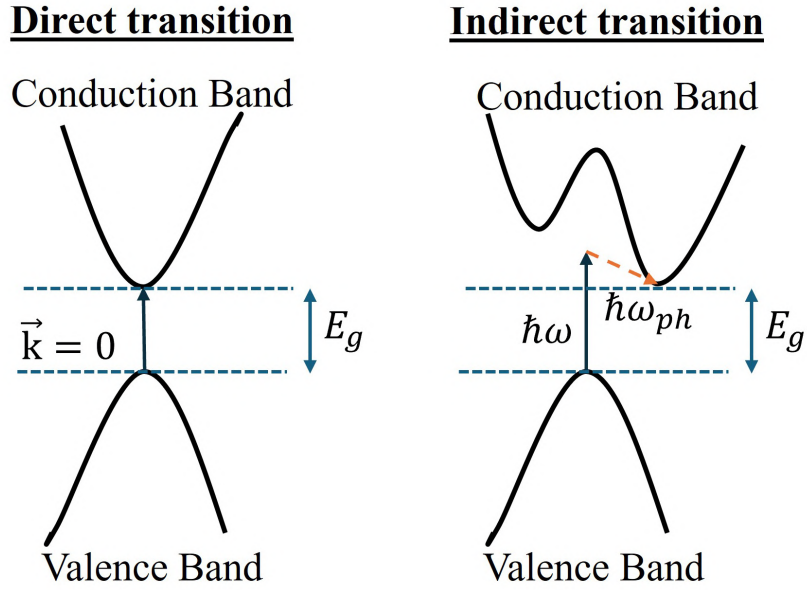


Figure 2.1: *Direct and indirect optical transitions. Note that in the indirect transition the process is mediated by a phonon with energy $\hbar\omega_{ph}$, the electron can either absorb or emit a phonon, depending on the photon energy.*

2.1.3. The Urbach Tail parameter

The relationship presented in equation 2.7 implies that no absorption should be possible at energies below E_g and a sharp increase should arise at the onset of absorption when the photon energy reaches E_g . This behaviour can be seen in figure 2.2. However, in real materials there is usually a gradual increase in absorption, called the Urbach tail, which can be represented by an exponential function [7]:

$$\alpha(E) = \alpha_0 e^{\frac{E-E_g}{E_U}} \quad (2.8)$$

The parameter E_U is called the Urbach tail parameter and is an empirical measure of the widening of the absorption edge. The onset of absorption at energies below the bandgap energy are caused by transitions from midgap states. These states are induced by microfields in materials, which arise due to excitonic interactions with non uniform electric fields [8]. The existence of the Urbach tail is often attributed to disorder [5, 9]. Specifically, the microfields stem from four primary sources: structural disorder (grain boundaries, defects and mechanical stress), impurity scattering of the carrier from donors or acceptors, and phonons [10–13].

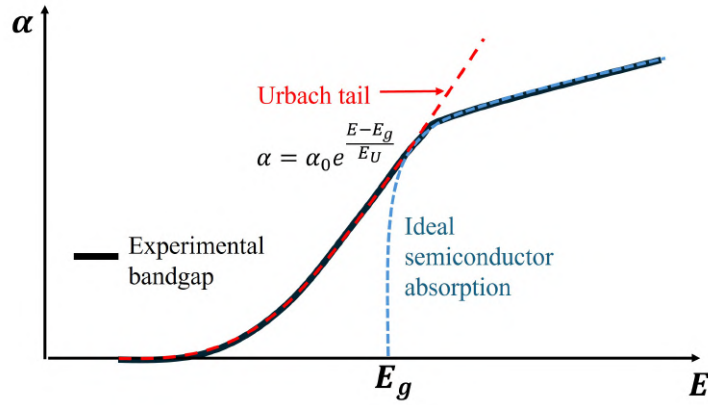


Figure 2.2: Diagram of the Urbach tail phenomenon. Absorption in real materials does not follow the sharp trend expected for ideal crystals. There is an onset of absorption at energies below the bandgap, which widens the absorption edge, creating a tail. This tail, called the Urbach tail, can be modelled by an exponential function.

The Urbach energy shows a dependence with temperature which can be attributed to phonon interactions and the resulting changes in the material's structural disorder [14, 15]. As temperature increases, the lattice vibrations become more intense and the number of high energy phonons increases, leading to an increase in absorption from interband states. Mathematically, the temperature dependence of the E_U parameter can be described by the following equation [16, 17]:

$$E_U(T) = E_U(0) + \frac{2E_U(0)}{\exp\left(\frac{\theta_E}{T}\right) - 1} \quad (2.9)$$

Where $E_U(0)$ is a temperature-independent parameter, referred to as the static component of the Urbach energy. It is material specific and depends on the intrinsic disorder of the material. The second term, called the dynamic component, describes how vibrations influence the electrical properties. T is the absolute temperature and θ_E is the Einstein phonon temperature (the temperature with half-filled active phonon states) [18].

2.1.4. Quantum dots and size effects

When materials have dimensions of the order of the de Broglie wavelength of the electrons they exhibit quantum behaviour, intermediate between the bulk material and the individual atoms. Their properties are strongly dependent on size, particularly the bandgap energy E_g , which, from an application standpoint, introduces a control parameter for bandgap engineering.

Quantum dots (QDs) are spherical nanocrystals in which the electron-hole pairs are essentially confined in all three spacial dimensions by a spherical infinite well. In this configuration the bandgap energy increases over that of the bulk material due to confinement,

a phenomenon known as quantum confinement. The increase in energy can be calculated by solving the Schrödinger equation with the boundary conditions of the infinite spherical well. From this it is possible to obtain the Brus equation [19–21]:

$$E_{QD} = E_{Bulk} + \frac{\hbar^2}{2\mu} \left(\frac{\pi}{R}\right)^2 - 1.786 \frac{e^2}{\epsilon R} \quad (2.10)$$

The first term in the equation is the bandgap energy of the bulk material (E_{bulk}) and the second term is the blueshift in the bandgap due to quantum confinement, which depends on the reduced electron-hole (exciton) effective mass, μ . The third term is a correction due to the Coulomb interaction of the electron-hole pair. Equation 2.10 allows for the calculation of the bandgap given the radius R of the quantum dot, or vice versa. Nonspherical nanoparticles of arbitrary shapes are usually treated with the same equation.

2.2. Optical parameters

2.2.1. The dielectric function ϵ and the refractive index

From the constitutive relations of electromagnetic theory we have that the electric displacement field \vec{D} can be expressed in terms of the electric field \vec{E} and the polarization field \vec{P} as shown in equation 2.11 [1, 22].

$$\vec{D}(\vec{r}, t) = \epsilon_0 \vec{E}(\vec{r}, t) + \vec{P}(\vec{r}, t) \quad (2.11)$$

Introducing the linear dielectric susceptibility χ the polarization field can be expressed as $\vec{P} = \epsilon_0 \chi \vec{E}$. Using this definition in equation 2.11 we obtain the following:

$$\vec{D}(\vec{r}, t) = \epsilon_0 \vec{E}(\vec{r}, t) + \vec{P}(\vec{r}, t) = \epsilon_0 [1 + \chi(\omega)] \vec{E} = \epsilon_0 \epsilon(\omega) \vec{E} \quad (2.12)$$

Where we have defined the dielectric function $\epsilon(\omega)$:

$$\epsilon(\omega) \equiv 1 + \chi(\omega) \quad (2.13)$$

The dielectric function is related to the refractive index by $\hat{n} = \sqrt{\epsilon}$ and therefore is a complex number of the form $\epsilon = \epsilon_1 + i\epsilon_2$. The frequency dependence of the refractive index is called dispersion. The real and imaginary part of the dielectric function can be expressed in terms of the refractive index as follows:

$$\begin{aligned} \epsilon_1 &= n^2 - k^2 \\ \epsilon_2 &= 2nk \end{aligned} \quad (2.14)$$

And conversely, the index of refraction and extinction coefficient in terms of the dielectric function:

$$\begin{aligned} n &= \frac{1}{\sqrt{2}}[\epsilon_1 + (\epsilon_1^2 + \epsilon_2^2)^{1/2}]^{1/2} \\ k &= \frac{1}{\sqrt{2}}[-\epsilon_1 + (\epsilon_1^2 + \epsilon_2^2)^{1/2}]^{1/2} \end{aligned} \quad (2.15)$$

2.2.1.1. The Kramers-Kronig relations

The index of refraction (n) and the extinction coefficient (k) are not independent, they are intrinsically linked through their spectral dependence. Using the principle of causality—an effect can not precede its cause—and complex number analysis [1], it is possible to derive the relationship between them. These are known as the Kramers-Kronig relations and are given by equations 2.16 and 2.17.

$$n(\omega) - 1 = \frac{2}{\pi} \mathcal{P} \int_0^\infty \frac{\omega' k(\omega')}{\omega'^2 - \omega^2} d\omega', \quad (2.16)$$

$$k(\omega) = -\frac{2\omega}{\pi} \mathcal{P} \int_0^\infty \frac{n(\omega') - 1}{\omega'^2 - \omega^2} d\omega', \quad (2.17)$$

ω represents the angular frequency of light and \mathcal{P} denotes the Cauchy principal value of the integral. In practical terms, the Kramers-Kronig relations imply that knowledge of a material absorption spectrum ($k(\omega)$) across a broad frequency range enables the calculation of its index of refraction dispersion relation ($n(\omega)$), and vice versa. This principle is invaluable in the examination of the material optical properties, allowing for the comprehensive characterization of the response to electromagnetic waves through either absorption or dispersion measurements. Furthermore, these relations underscore the impossibility of a material exhibiting dispersive behavior without absorption, or absorption without dispersion.

2.2.2. Useful definitions for the study of light interaction with a sample

Figure 2.3 shows a sample irradiated with light at an angle of incidence ϕ_i with an intensity I_E . After interaction with the sample, the light may [22]:

1. be transmitted through the sample in a well defined direction, also called specular direction. The fraction of intensity transmitted relative to the incident intensity is called the **transmittance T**.

2. be reflected in a well defined (specular direction). The **specular reflectance (R)** is defined as the ratio of reflected intensity to incident intensity
3. be diffusely scattered at the surface or the volume, which gives rise to the optical **Scatter (S)**.
4. be absorbed by the sample surface or the volume, the fraction of which is quantified in terms of the **absorptance (A)**.

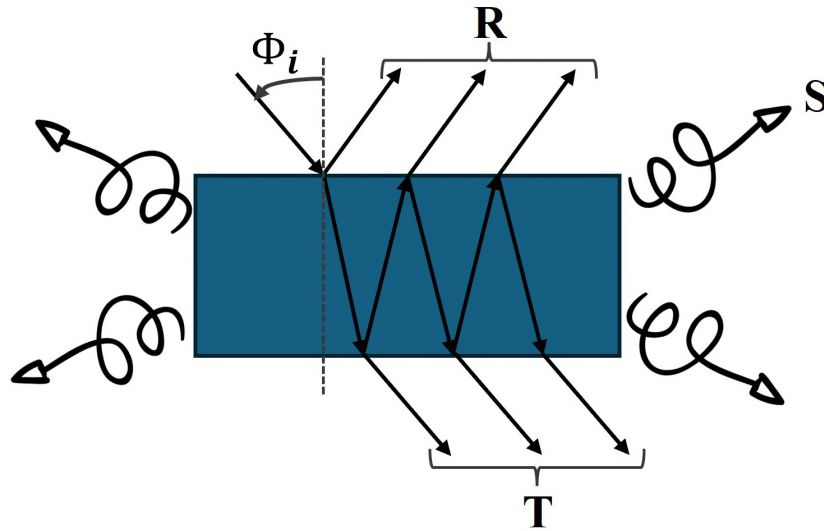


Figure 2.3: Schematic off the interaction of light with a sample

The previous definitions can be written as a fraction of intensities as shown in equation 2.18, where I_T , I_R , I_S and I_A are the transmitted, reflected, scattered and absorbed intensities, respectively.

$$\begin{aligned}
 T &\equiv \frac{I_T}{I_E} \\
 R &\equiv \frac{I_R}{I_E} \\
 S &\equiv \frac{I_S}{I_E} \\
 A &\equiv \frac{I_A}{I_E}
 \end{aligned}
 \tag{2.18}$$

Due to conservation of energy, the total energy after the interaction has to be equal to the incident energy: $I_T + I_R + I_S + I_A = I_E$. This relationship can be expressed as:

$$T + R + S + A = 1
 \tag{2.19}$$

The scattered light may be scattered in the hemisphere containing the incident ray (backscattered) or the opposite one (forward scattered). It is sometimes useful, particularly experimentally, to consider both components separately. The backscattered diffuse light is called the diffuse reflectance (DR) and similarly, the forward scattered light is called the diffuse transmittance (DT). Then the sum is equal to the optical scatter: $S = DR + DT$.

Notice that in each hemisphere there may be light that is specular (E) and diffuse (D), the addition of them is the total reflectance (TR) and total transmittance (TT):

$$\begin{aligned} TT &= ET + DT \\ TR &= ER + DR \end{aligned} \tag{2.20}$$

When separating diffuse of specular components, the specular transmittance and reflectance are called ET and ER, respectively, for clarity. It is useful to know the fraction of light in each hemisphere that is diffuse. This is quantified by the haze in both transmittance (HT) and reflectance (HR), which are defined as the ratio between the diffuse component and the total component [23–25]:

$$\begin{aligned} HT &\equiv \frac{DT}{TT} \\ HR &\equiv \frac{DR}{TR} \end{aligned} \tag{2.21}$$

Experimentally it is often difficult to measure the absorbed intensity directly and obtain the absorptance. It is useful to define the absorbance (A_b), which can be directly obtained with a spectrometer:

$$A_b \equiv -\ln(T) = -\ln(1 - A - S - R) \tag{2.22}$$

Clearly any non-vanishing reflectance, scatter or absorption may give rise to a finite absorbance, and therefore it may not be connected with a physical absorption process. However, the concept is useful because, in the absence of resonant scattering [26], the reflectance and scattering are smooth functions and therefore any sharp features in the transmittance spectra correspond to sharp features in absorption. This proves particularly useful in elucidating the position of the absorption edges.

2.3. Planar interfaces and the Fresnel coefficients

Consider the situation depicted in figure 2.4, where an electromagnetic wave is incident from medium 1, with refractive index \hat{n}_1 to a planar interface separating medium 1 from medium 2 (\hat{n}_2) at an angle ϕ . The effect of the boundary is to reflect part of the beam

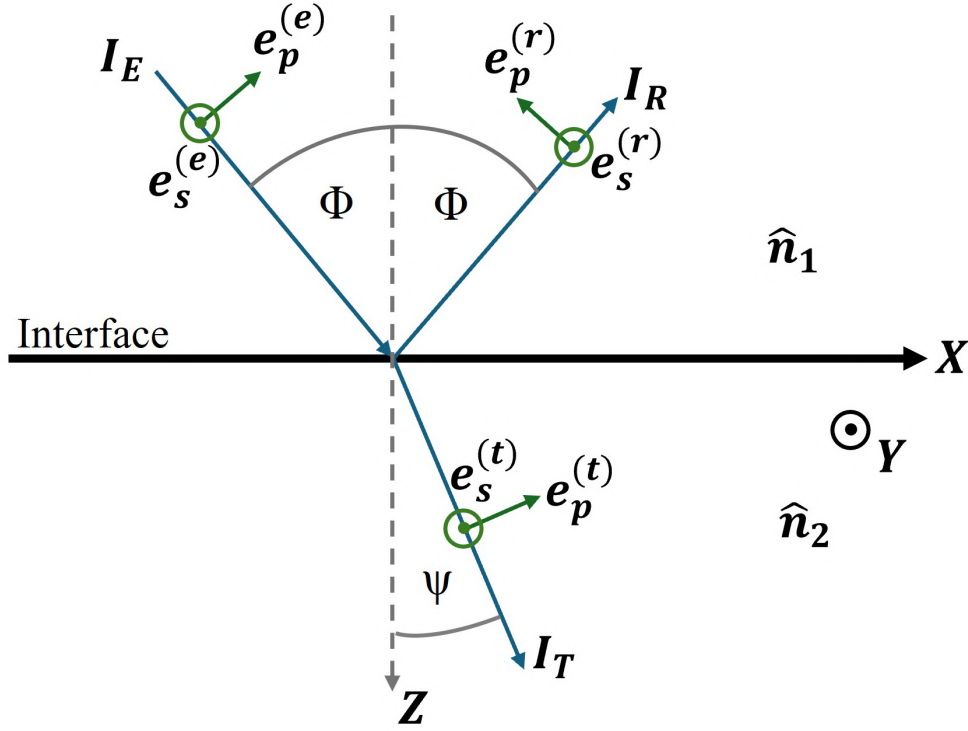


Figure 2.4: Diagram used in the derivation of the Fresnel coefficients

and transmit another at an angle ψ consistent with Snell's law [22, 27].

The electric field may be resolved into two orthogonal components, called the polarization directions [22, 28]. We can define the polarization basis as shown in the figure, where one component is parallel to the plane of incidence (plane of the page) and is called the p-polarized component, and the other is polarized perpendicular to the plane of incidence, it is s-polarized (from *senkrecht*, perpendicular in German). The s component is always along the \hat{y} direction. Note that in many references the p-polarized component is instead called transverse magnetic (TM) and the s-polarized is called transverse electric (TE), due to the fact that the electric field is associated to an orthogonal magnetic field, consistent with Poynting vector $\vec{S} = \vec{E} \times \vec{H}$, where \vec{S} is along the direction of propagation.

We wish to describe the effects of the interface as ratios of electric fields. This leads to the definition of the transmission and reflection coefficients for each of the polarizations:

$$\begin{aligned}
 r_p &= \frac{E_p^{(r)}}{E_p^{(e)}}, & r_s &= \frac{E_s^{(r)}}{E_s^{(e)}} \\
 t_p &= \frac{E_p^{(t)}}{E_p^{(e)}}, & t_s &= \frac{E_s^{(t)}}{E_s^{(e)}}
 \end{aligned}
 \tag{2.23}$$

Treating each polarization independently, and applying the continuity of the electric and magnetic field (\vec{H}) at the boundary (in the \hat{x} and \hat{y} directions) it is possible to obtain

an expression for the reflection and transmission coefficients in terms of the parameters at the boundary. For a detailed deduction the reader is referred to classic treatises like those of Hecht [27], Stenzel [22] or Born and Wolf [29]. The reflection and transmission coefficients for isotropic nonmagnetic materials appear in equations 2.24 through 2.27. These are usually called the Fresnel coefficients (also Fresnel equations), in honour of Augustin-Jean Fresnel, who first derived them.

$$r_p = \frac{\hat{n}_2 \cos \phi - \hat{n}_1 \cos \psi}{\hat{n}_2 \cos \phi + \hat{n}_1 \cos \psi} \quad (2.24)$$

$$t_p = \frac{2\hat{n}_1 \cos \phi}{\hat{n}_2 \cos \phi + \hat{n}_1 \cos \psi} \quad (2.25)$$

$$r_s = \frac{\hat{n}_1 \cos \phi - \hat{n}_2 \cos \psi}{\hat{n}_1 \cos \phi + \hat{n}_2 \cos \psi} \quad (2.26)$$

$$t_s = \frac{2\hat{n}_1 \cos \phi}{\hat{n}_1 \cos \phi + \hat{n}_2 \cos \psi} \quad (2.27)$$

Experimentally it is complicated measuring directly EM wave amplitudes and phases, and often intensities are measured instead, which motivated the definitions presented in section 2.2.2. The reflectance and transmittance of an interface for each polarization may be calculated from the corresponding reflection coefficient using the fact that intensity is proportional to the square of the modulus of the electric field (the amplitude squared), the dielectric function and the z-component of the velocity of light. Therefore the reflectance and transmittance can be expressed as shown in equations 2.28 and 2.29, respectively. The factor that multiplies $|t|^2$ arises from the change of medium that the wave experiences.

$$R = |r|^2 \quad (2.28)$$

$$T = 1 - R = \frac{\text{Re}(\hat{n}_2 \cos \psi)}{\text{Re}(\hat{n}_1 \cos \phi)} |t|^2 \quad (2.29)$$

Notice that there is transmittance and a reflectance for each polarization direction, for example, the reflectance for p-polarized light given by $R_p = |r_p|^2$. When dealing with unpolarized light, the total reflectance or transmittance is simply the average of the two polarized values, because unpolarized light is a superposition of both polarizations with equal intensity (see section 2.7.1).

In order to get an intuitive understanding of the angular dependencies observe the results for an air-glass interface presented in figures 2.5a and 2.5b for reflectance and transmittance, respectively. We see that the total reflectance (R) increases as the angle of

incidence increases from normal incidence ($\phi = 0^\circ$) to grazing incidence ($\phi = 90^\circ$). The s-polarized reflectance (R_s) increases monotonically, contrary to the p-polarized component (R_p), which decreases until it reaches a minimum with 0 reflectance and then it increases. Notice that the position where R_p is a minimum is labeled as Brewster angle, which is discussed in subsection 2.3.2. At this angle of incidence all of the reflected light is polarized in the s direction.

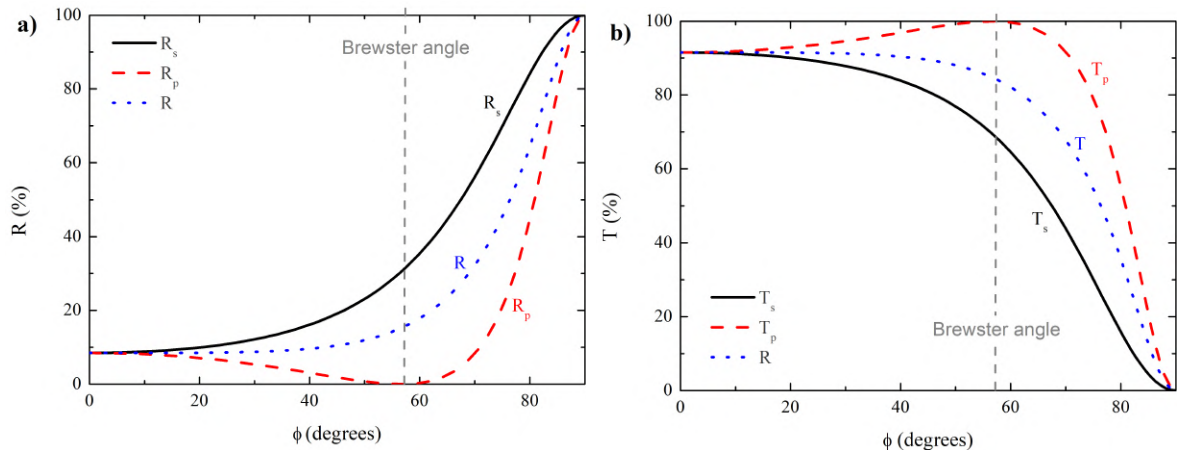


Figure 2.5: Calculated a) reflectance and b) transmittance spectra for an air-glass interface at a wavelength of 544 nm. Notice that the angular position of the minimum of R_p is indicated by a vertical grey dashed line labeled Brewster angle, discussed in subsection 2.3.2

The transmittance displays the complementary behaviour, as expected. T_s decreases monotonically whereas T_p has a maximum with 100% transmittance at the Brewster angle. The total transmittance (T) decreases monotonically. Even though these curves are for a specific material, it is important to note that the observations are a general trend of the Fresnel coefficients observed in most interfaces when there is no absorption nor scattering. In general terms, the reflectance increases when approaching grazing incidence, with the consequent reduction in transmitted light. The polarizations also follow the trend shown, where the s component changes monotonically while the p component has a maximum (minimum) and then decreases (increases).

2.3.1. The Stokes relations

If there is no absorption, the behaviour of a wave must be reversible. Given a situation like that shown in figure 2.6a then what is shown in figure 2.6b must also be physically possible. In general, if one situation is possible, another where all directions are reversed must also be possible. This principle is called *time-reversal invariance* [27].

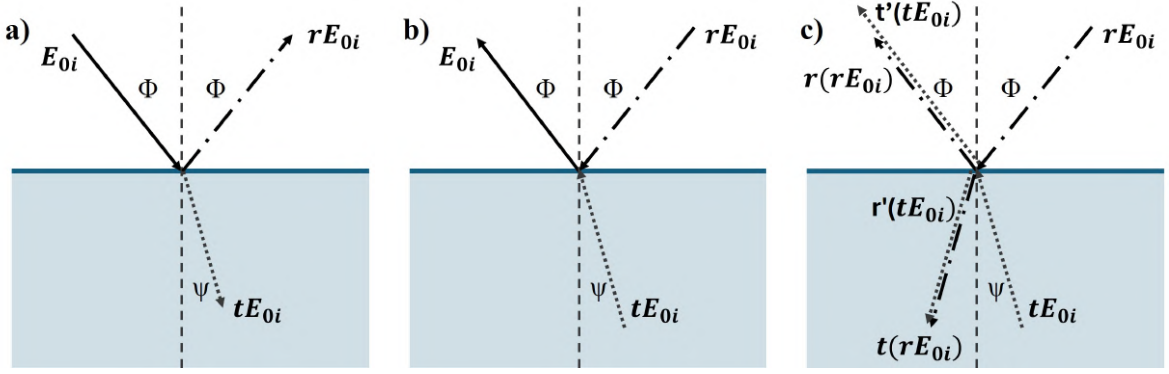


Figure 2.6: Schematic of the situations analysed to obtain the Stokes relations. In a) a wave incident from medium 1 is reflected and transmitted, and thus, due to time-reversal invariance, the situation b) must also be possible. In c) we consider each of the fields approaching the boundary in b) individually, each of which is transmitted and reflected. The resulting fields must be equivalent to those of situation b) and this determines the Stokes relations.

Notice that in figure 2.6b there are two incident fields. We can consider the reflection and transmission of each field individually in terms of the corresponding coefficients, without assuming any particular form, just the ratio of outgoing to incident field. We will denote with t (t') and r (r') the transmission and reflection coefficient from the top (bottom) side, respectively. This scenario is represented in figure 2.6c. Notice that the incoming field rE_{0i} is reflected and transmitted, and the same is true for the other incoming field tE_{0i} .

The situation in 2.6c must be equivalent to that shown in figure 2.6b. Therefore, we have that:

$$\begin{aligned} E_{0i} &= r(rE_{0i}) + t'(tE_{0i}) \Rightarrow 1 = r^2 + t't \\ 0 &= t(rE_{0i}) + r'(tE_{0i}) \Rightarrow r = -r' \end{aligned} \quad (2.30)$$

The relations can shown in equation 2.30 are known as the Stokes relations. These can be combined by noting that $r^2 = -rr'$:

$$t't - rr' = 1 \quad (2.31)$$

It is important to consider that the Stokes relations only apply to perfectly planar (well defined coefficients) and non absorbing (time reversal) interfaces.

2.3.2. Brewster's angle

There is a special angle of incidence, called Brewster's angle (ϕ_B) or principal angle in which the reflectivity of p-polarized light becomes 0 if the samples are non absorbing

(\hat{n} is real). A sample illuminated at this angle will reflect light perfectly polarized in the s direction. This can be proven as follows. Consider $r_p = 0$, then $\cos^2\psi = (\frac{n_2\cos(\phi)}{n_1})^2$. Furthermore, the refraction angle is related to the other parameters through Snell's law: $\sin^2\psi = (\frac{n_1\sin(\phi)}{n_2})^2$. Adding these two equations we obtain:

$$\sin^2\psi + \cos^2\psi = 1 = \sin^2\phi + \cos^2\phi = \frac{n_2^2}{n_1^2}\cos^2\phi + \frac{n_1^2}{n_2^2}\sin^2\phi \quad (2.32)$$

Grouping the sine and cosine and eliminating it is possible to obtain Brewster's angle in terms of the refractive indices, where we have introduced the subscript B for clarity:

$$\tan\phi_B = \frac{n_2}{n_1} \Rightarrow \phi_B = \tan^{-1}\left(\frac{n_2}{n_1}\right) \quad (2.33)$$

In non smooth or absorbing interfaces, there is no condition such that $r_p = 0$, and it only approaches a minima. This is sometimes called the pseudo-Brewster angle [30, 31], particularly when working with highly absorbing samples. In polished dielectrics like a glass plate, the reflectance at Brewster's angle can be orders of magnitude lower than that at other angles, with the behaviour very much like that predicted for ideal surfaces.

2.4. Interference of waves

Consider two waves propagating along the z-axis, each with its own phase, as shown in equation 2.34. We neglect the effects of polarization and treat the scalar problem, which is equivalent to limiting the analysis to waves with the same polarization direction. The phase α includes both spatial and temporal components, such that $\alpha(z, \delta) = -(kz + \delta)$.

$$\begin{aligned} E_1 &= E_{01}\sin(\omega t + \alpha_1) \\ E_2 &= E_{02}\sin(\omega t + \alpha_2) \end{aligned} \quad (2.34)$$

The resultant perturbation at a given point (E) in space is given by the addition of the two waves which can be expressed as shown in equation 2.35 after making use of the sine trigonometric identity to expand $\sin(\omega t + \alpha)$.

$$E = (E_{01}\cos\alpha_1 + E_{02}\cos\alpha_2)\sin(\omega t) + (E_{01}\sin\alpha_1 + E_{02}\sin\alpha_2)\cos(\omega t) \quad (2.35)$$

The squared amplitude of the resultant field, E_0 can be expressed as:

$$E_0^2 = E_{01}^2 + E_{02}^2 + 2E_{01}E_{02}\cos(\alpha_2 - \alpha_1) \quad (2.36)$$

Thus, the resultant intensity is not simply the addition of the individual intensities

[28, 32], but there is an interference term that depends on the phase difference. This can be generalized to the interaction of N waves of the same frequency:

$$E_0^2 = \sum_{i=1}^N E_{0i}^2 + 2 \sum_{j>i}^N \sum_{i=1}^N E_{0i} E_{0j} \cos(\alpha_i - \alpha_j) \quad (2.37)$$

Since flux density is proportional to the time average of E_0^2 , taken over a long interval of time compared to the frequency of light, the interference term will make contributions of the form $\langle \cos[\alpha_i(t) - \alpha_j(t)] \rangle$. Now, remembering that $\alpha = -(kz + \delta)$, we can express the term in the cosine as:

$$\alpha_i(t) - \alpha_j(t) = k(z_j - z_i) + (\delta_j - \delta_i) \quad (2.38)$$

Therefore, we can distinguish between 3 cases, depending on the relationship between the δ :

1. Coherent light: If $\delta_j - \delta_i$ is constant, then the contribution of the interference term will be maintained and there will be interference oscillations in experimental spectra. In this case it is said that the light is propagating coherently.
2. Incoherent light: If $\delta_j - \delta_i$ varies randomly, then the cosine will average to zero due to the rapid variations in phase and the equal probability for the positive and negative cosine values. In this case, no interference oscillations will be present and the superposition is just the independent addition of the intensities, and it is said that light travels incoherently.
3. Partially coherent light: In between the extreme cases of coherent and incoherent propagation, there exists partially coherent light. In this case the phase differences are correlated, but not completely. The interference oscillations will be attenuated.

It can be proven that completely coherent light is not physically possible because it would require a completely monochromatic wave. Similarly, complete incoherence cannot exist in free space either [32]. While the extreme cases are idealizations, they are simpler to compute mathematically and are used to model experimental spectra. As will be seen in the results, the simplification is usually in good agreement with real spectra.

2.4.1. Interference color

Interference color is a phenomenon where colors are produced through the constructive and destructive interference of light waves. This occurs when light is reflected from or transmitted through thin films, layers, or structures with thicknesses comparable to

the wavelength of visible light. The superposition of the reflected light waves from the multiple interfaces of these thin films causes some wavelengths of light to be enhanced (constructive interference) and others to be diminished or cancelled out (destructive interference), resulting in the appearance of vivid colors [27, 28].

A classic example of interference color can be seen in soap bubbles and oil slicks on water. These thin films vary in thickness across their surfaces, leading to a spectrum of colors when illuminated by white light. The variation in color across the film is due to changes in film thickness, which alter the path length difference between light waves reflected from the top and bottom surfaces of the film, thus affecting which wavelengths undergo constructive or destructive interference.

Structural coloration, of which interference color is one example, is a fascinating phenomenon in which color is produced by microscopically structured surfaces rather than by pigments [33, 34]. Unlike pigment-based coloration, where color comes from the selective absorption and reflection of certain wavelengths of light by chemical compounds, structural color arises from the interaction of light with nanostructured materials. This interaction can involve diffraction, scattering, interference, and reflection, leading to vibrant colors that can change based on the angle of view or the angle of illumination.

2.4.2. Formal treatment of interference: Coherence theory

In order to understand the mechanisms that cause a loss of coherence due to interaction of the light wave with a sample, it is useful to formalize the concept of coherence. In particular, we are interested in gaining insights on the meaning of correlation between the phases of the propagating waves.

Any optical wave can be described by a wavefunction $u(\vec{r}, t) = \text{Re}\{U(\vec{r}, t)\}$. For random light $U(\vec{r}, t)$ is a random function characterized by a number of statistical averages, some of which we introduce in this section. As the intensity varies, the average intensity is employed, which is computed by taking an ensemble average over many realization of the function [35]:

$$I(\vec{r}, t) = \langle |U(\vec{r}, t)|^2 \rangle \quad (2.39)$$

If the average intensity is time independent the optical wave is statistically stationary, and we will concern ourselves with this case. In this cases taking the statistical average is equivalent to time averaging over a long duration, which is what is done in a spectrometer.

Now consider the fluctuations of stationary light at a fixed point in space (we drop the \vec{r} dependence). The fluctuations in $U(t)$ are characterized by a certain time scale representing the “memory” that the wave has of itself, so points separated by more than

this time are completely independent. The function is relatively smooth and well defined within its memory time, but appears “erratic” when examined over longer time scales. A quantitative measurement of this “memory” is established by defining the autocorrelation function, which describes the degree of relation between two points that fluctuate separated a certain time.

The autocorrelation function (G) of a stationary complex random function $U(t)$ is defined as shown in equation 2.40, where the superscript $\{*\}$ denotes the complex conjugate.

$$G(\tau) = \langle U^*(t)U(t + \tau) \rangle = \lim_{T \rightarrow \infty} \frac{1}{2T} \int_{-T}^T U^*(t)U(t + \tau) dt \quad (2.40)$$

To gain an intuitive understanding consider the simple case where $\langle U(t) \rangle = 0$, meaning that the phase of the wave is equally likely to be in the range of 0 to 2π . Now, $U^*(t)U(t + \tau)$ is the angle of the phasors between the waves. If the waves are uncorrelated, the difference is equally likely to be anywhere from 0 to 2π and therefore the time average will yield $G(\tau) = 0$. Instead, if the functions are correlated, the product phasor will have a preferential direction and the autocorrelation function will not vanish. Notice that if the time delay is 0, the autocorrelation function just gives the intensity of the function at time t : $G(0) = \langle U^*(t)U(t) \rangle = I$

The temporal coherence function has information on both correlation and intensity. It is useful to normalize the wave in order to obtain a measure of coherence (correlation) insensitive to intensity. This is the normalized autocorrelation function (g) or degree of temporal coherence, the value of which cannot exceed unity:

$$g(\tau) = \frac{G(\tau)}{G(0)} = \frac{\langle U^*(t)U(t + \tau) \rangle}{\langle U^*(t)U(t) \rangle} \quad (2.41)$$

If $|g(\tau)|$ decreases monotonically as a function of time delay, then there is a critical value for which the waves are said to be uncorrelated, usually at 1/e decay (figure 2.7). This quantity, τ_c is called the coherence time. Waves separated a time interval larger than τ_c are said to be weakly correlated. The exact value of the coherence time depends on the profile of $g(\tau)$.

From the velocity of the wave we can also obtain the coherence length (l_c) as shown in equation 2.42. If the dimension scales of an optical system (or a sample) are much larger than the coherence length, then the light is effectively incoherent.

$$l_c = v\tau_c \quad (2.42)$$

Light sources are polychromatic, with the light spectral density $S(\nu)$ (intensity per unit area per unit frequency) often confined to a band around the central frequency ν_0 .

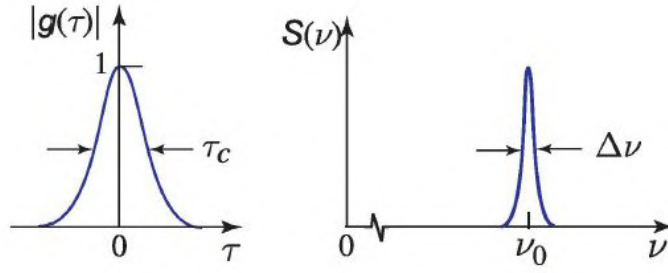


Figure 2.7: Normalized autocorrelation function displaying the coherence time as the width of the curve and the corresponding spectral density with the linewidth $\Delta\nu$. Reproduced from [35]

Note that in this section ν , which in the rest of this work is used for the wavenumber, is used for the frequency to match the notation of the main reference [35]. The spectral density and the autocorrelation function form a Fourier transform pair [35]. The width of the spectra is called the spectral width or linewidth, denoted by $\Delta\nu$ (see figure 2.7) and it can be shown that the line width is equal to the inverse of the coherence time:

$$\Delta\nu = \frac{1}{\tau_c} \quad (2.43)$$

This explains why very narrow bandwidth sources like lasers possess very large coherence times while broadband sources, like halogen lamps, have shorter coherence times. As we will see, coherence is a requisite for interference. The broadband nature of white light explains why it is difficult to see interference phenomena under natural illumination and why lasers are usually employed in interferometric experiments [27].

Now we will consider the interference of two waves, U_1 and U_2 , in the framework of coherence theory. The waves are characterized by their individual autocorrelation functions and the degree in which their fluctuations are correlated, defined by the cross-correlation function. At a given point and time the intensities are $I_1 = \langle |U_1|^2 \rangle$ and $I_2 = \langle |U_2|^2 \rangle$. The crossed correlation function (G_{12}) and normalized crossed correlation function (g_{12}) are defined similarly to the autocorrelation function, as shown in equation 2.44.

$$\begin{aligned} G_{12} &= \langle U_1^* U_2 \rangle \\ g_{12} &= \frac{\langle U_1^* U_2 \rangle}{\sqrt{I_1 I_2}} \end{aligned} \quad (2.44)$$

When two waves are superposed, the average intensity of their sum is given by:

$$\begin{aligned}
I = \langle |U_1 + U_2|^2 \rangle &= \langle |U_1|^2 \rangle + \langle |U_2|^2 \rangle + \langle U_1^* U_2 \rangle + \langle U_1 U_2^* \rangle = I_1 + I_2 + G_{12} + G_{12}^* \\
&= I_1 + I_2 + 2\text{Re}\{G_{12}\} = I_1 + I_2 + 2\sqrt{I_1 I_2} \text{Re}\{g_{12}\}
\end{aligned}
\tag{2.45}$$

Finally, we can express the intensity as shown in equation 2.46, where δ is the argument of g_{12} . The last term represents the optical interference. Notice that for completely correlated waves $|g_{12}| = 1$ and we recover equation 2.37. Similarly, for two completely uncorrelated waves $|g_{12}| = 0$ and there is no interference.

$$I = I_1 + I_2 + 2\sqrt{I_1 I_2} |g_{12}| \cos\delta \tag{2.46}$$

Coherence theory allows us to gain insights into which processes decrease the degree of coherence of a light wave. Loss of coherence is a consequence of random processes that reduce the correlation between light rays of the beam. It is important to clarify that if a process is well defined, even though it may be complicated, it does not reduce the degree of coherence. For example, Mie scattering from a perfectly homogeneous particle is well defined and does not in principle alter the degree of coherence. The processes that tend to vary the correlation between light waves are:

1. Random path length differences: this may be a consequence of propagation in turbulent or time varying media.
2. Scattering from rough surfaces: Scattering objects can introduce phase delays to specific parts of a wavefront, which can not be predicted in the presence of multiple scatterers. This destroys the original phase relationships.
3. Multiple scattering: the wave undergoes numerous phase shifts with each interaction. These accumulated, random phase changes completely disrupt the original phase relationship, leading to a significant loss of coherence.

2.5. The general problem of light propagation

In the previous sections we have presented the optical constants and defined the parameters that characterize the interaction of light with a sample. As was shown in section 2.3 it is possible to express the effects of a boundary on the propagation of an EM wave in terms of the material parameters. However, no real material possesses only one boundary due to their finite thickness. The first treatment applicable to a real sample is that of a uniform layer embedded in two semi infinite media, a situation often called the free-standing film. This configuration involves reflections and transmissions between the two

boundaries of the layer, has a simple treatment and can give close form solutions to most parameters. This configuration is presented in section 2.5.1.

The next degree of complexity involves samples composed of multiple stacked layers, often called stratified media. In this case the simple treatment used to solve for the freestanding film is cumbersome, and more efficient computational tools are required. In this work we employ the transfer matrix method, discussed in section 2.5.2

2.5.1. The freestanding film

Consider the situation depicted in figure 2.8, where a single unsupported film of complex refractive index \hat{n}_s is embedded in air, and light is incident with an angle ϕ_i measured from the normal to the film. Light incident on the first boundary will be partially reflected, while the rest will be transmitted. This transmitted portion propagates through the sample, acquiring a phase δ . When it reaches the second surface, part of it is transmitted and the other is reflected back to the sample. There are an infinite number of reflections and transmissions, and the superposition of the outgoing fields composes the total reflected and transmitted fields. We can write each field in the sample using the Fresnel coefficients [27], where t_{as} and r_{as} represent the transmission and reflection coefficients of light when it approaches the interface from air. Similarly, t_{sa} and r_{sa} correspond to the case of the incident wave coming from the sample.

The phase gain δ is given by equation 2.47, where Snell's law [22] was used to express it in terms of the incident angle and $\nu = \frac{1}{\lambda}$ is the wavenumber. Given that δ is a complex number if \hat{n}_s has a non zero extinction coefficient, its imaginary part introduces a decay in the wave that accounts for the absorption, as explained in section 2.1.1.

$$\delta = 2\pi\nu d \sqrt{\hat{n}_s^2 - \sin^2\phi_i} \quad (2.47)$$

By keeping track of each field, we can write the transmission (t) and reflection (r) as infinite sums, as shown in equations 2.48 and 2.49 respectively [36]. As the modulus of the term in the summation is strictly less than unity in real passive materials (no gain), the summation, which has the form of a geometric series, converges. In this way, the total transmitted and reflected fields are given by equations 2.50 and 2.51.

$$t = t_{as}e^{i\delta}t_{sa}[1 + r_{sa}^2e^{2i\delta} + (r_{sa}^2e^{2i\delta})^2 + \dots] = t_{as}e^{i\delta}t_{sa} \sum_{j=0}^{\infty} (r_{sa}^2e^{2i\delta})^j \quad (2.48)$$

$$r = r_{as} + t_{as}r_{sa}t_{sa}e^{2i\delta}[1 + r_{sa}^2e^{2i\delta} + (r_{sa}^2e^{2i\delta})^2 + \dots] = r_{as} + t_{as}r_{sa}t_{sa}e^{2i\delta} \sum_{j=0}^{\infty} (r_{sa}^2e^{2i\delta})^j \quad (2.49)$$

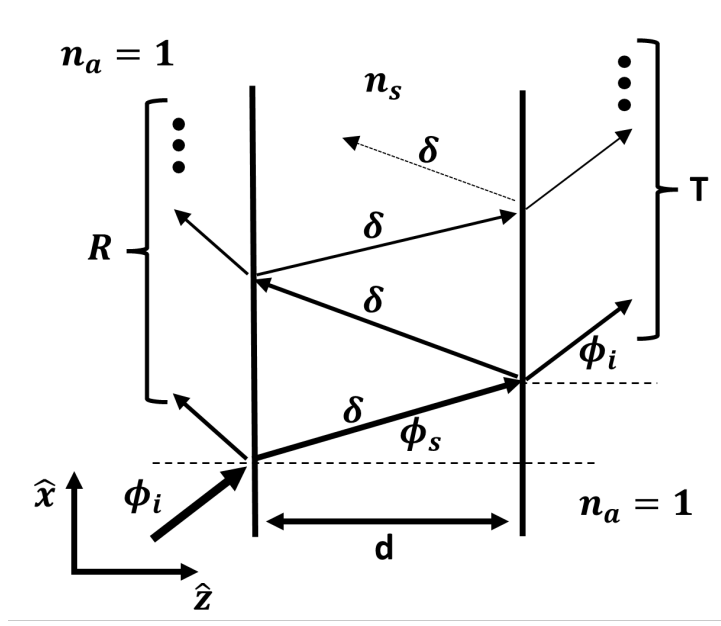


Figure 2.8: Schematic of the model used to calculate the transmittance of a thin film. An incoming beam is multiply reflected and transmitted between the two interfaces of the freestanding film. The transmission and reflection is calculated as the infinite sum of all the transmitted and reflected beams, respectively.

$$t = \frac{t_{as}t_{sa}e^{i\delta}}{1 - r_{sa}^2e^{2i\delta}} \quad (2.50)$$

$$r = r_{as} + \frac{t_{as}r_{sa}t_{sa}e^{2i\delta}}{1 - r_{sa}^2e^{2i\delta}} \quad (2.51)$$

Experimentally, we measure intensities and not fields. The transmittance (T) and Reflectance (R) are defined as shown in equations 2.29 and 2.28. In the case of an isotropic homogeneous medium embedded in air $\hat{n}_{out} = \hat{n}_{in}$ and $\phi_{out} = \phi_{in}$, therefore the transmittance is simply $T = |t|^2$ [36].

2.5.1.1. Special Case: Vanishing damping

When there is no damping, the extinction coefficient k is equal to 0, and thus the refractive index is purely real. This in turn implies that the Fresnel coefficients and the phase factor δ are also purely real [22]. In this particular case, for a freestanding film embedded in air, the transmittance (T) and reflectance (R) can be expressed as shown in equations 2.52 and 2.53.

$$T = \frac{t_{as}^2 t_{sa}^2}{1 + r_{as}^2 r_{sa}^2 + 2r_{as} r_{sa} \cos(2\delta)} \quad (2.52)$$

$$R = \frac{r_{as}^2 + r_{sa}^2 + 2r_{as}r_{sa}\cos(2\delta)}{1 + r_{as}^2r_{sa}^2 + 2r_{as}r_{sa}\cos(2\delta)} \quad (2.53)$$

These equations display an interference term proportional to 2δ , which is proportional to the wavenumber (equation 2.47). Therefore, we expect that the transmittance and reflectance spectra exhibit an oscillatory behaviour. This is particularly useful in cases where the dispersion of the refractive index is negligible in the studied range (i.e. n is approximately constant) because the extrema of the spectra correspond simply to the extremum values of the cosines that occur when $2\delta = j\pi$, where $j = 0, 1, 2, \dots$ is the extremal order. In this way the thickness can be calculated as $d = \frac{j}{4\nu_j\sqrt{n_s^2 - \sin^2\phi_i}}$, where ν_j is the wavenumber corresponding to the extrema of order j . However, this equation requires knowledge of the correspondence between the experimental extrema and the extremal order j , which often proves impractical. By considering two consecutive extrema we can dispense with this information, as can be seen in equation 2.54. This equation can be used as a simple tool to obtain the thickness of a sample provided that the absorption and the dispersion are minimal, both of which are usual when measuring far from an absorption edge, and when the sample is homogeneous and isotropic.

$$d = \frac{1}{4(\nu_{j+1} - \nu_j)\sqrt{n_s^2 - \sin^2\phi_i}} \quad (2.54)$$

2.5.1.2. Obtaining the complex refractive index from measured spectra

Nichelatti [37] presented a method to solve analytically the problem of obtaining the complex refractive index of a material from reflectance and transmittance measurements performed at normal incidence, assuming incoherent light propagation. The transmittance (T_F) and reflectance (R_F) of a single interface (i.e. the square of the corresponding Fresnel coefficients for the interface) at normal incidence can be expressed as shown in equation 2.55. Notice that the negative sign convention ($\hat{n}_s = n - ik$) was used. This applies to both the sample-air and the air-sample interfaces.

$$\begin{aligned} T_F &= \frac{4n}{|n - ik + 1|^2} \\ R_F &= \left| \frac{n - ik - 1}{n - ik + 1} \right|^2 \end{aligned} \quad (2.55)$$

If we consider the same situation previously analysed (figure 2.8) but in the case of incoherent propagation, where we perform the summation over intensities, we can arrive at the expressions presented in equations 2.56 and 2.57 for the total transmittance (T) and reflectance (R) of the freestanding film, where $\alpha(\lambda) = \frac{4\pi k(\lambda)}{\lambda}$ is the absorption coefficient [22].

$$T = \frac{T_F^2 e^{-\alpha d}}{1 - R_F^2 e^{-2\alpha d}} \quad (2.56)$$

$$R = R_F + \frac{R_F T_F^2 e^{-2\alpha d}}{1 - R_F^2 e^{-2\alpha d}} \quad (2.57)$$

If we consider $\frac{R-R_F}{T}$ and take the natural logarithm we arrive at equation 2.58, which we can use to eliminate αd from equation 2.56 and use $T_F = 1 - R_F$ to obtain a quadratic equation on R_F with coefficients determined by the measured spectra, T and R. The solution to this equation is given in 2.59. The other solution is discarded on physical grounds because it would imply $R_F > R$, which is clearly not possible if one considers the summation of non negative terms that lead to the expression for R.

$$\alpha d = \ln\left(\frac{R_F T}{R - R_F}\right) \quad (2.58)$$

$$R_F = \{2 + T^2 - (1 - R)^2 - ([2 + T^2 - (1 - R)^2]^2 - 4R(2 - R))^{1/2}\} [2(2 - R)]^{-1} \quad (2.59)$$

Substituting the expression in 2.59 for R_F in equation 2.58 and using the fact that $k(\lambda) = \frac{\alpha \lambda}{4\pi}$ we arrive to the analytical expression for the extinction coefficient presented in equation 2.60, where the dependence on the reflectance (R) and transmittance (T) spectra was explicitly introduced.

$$k(R, T) = \frac{\lambda}{4\pi d} \ln \left[\frac{R_F(R, T) T}{R - R_F(R, T)} \right] \quad (2.60)$$

In order to obtain an expression for the index of refraction n, Nichelatti expresses the refractive index in polar form: $\hat{n}_s = \rho e^{i\phi}$. Using this in the definitions of the boundary coefficients presented in equation 2.55 we can arrive at the expressions in equation 2.61.

$$\begin{aligned} |\rho e^{i\phi} + 1|^2 &= \rho^2 + 2\rho \cos\phi + 1 = \frac{4n}{T_F} \\ |\rho e^{i\phi} - 1|^2 &= \rho^2 - 2\rho \cos\phi + 1 = \frac{4nR_F}{T_F} \end{aligned} \quad (2.61)$$

Adding the two expressions and using $T_F = 1 - R_F$ we can get expression 2.62 for ρ .

$$\rho^2 = 2n \frac{1 + R_F}{1 - R_F} - 1 \quad (2.62)$$

Finally, using the fact that $\rho^2 = n^2 + k^2$, and substituting ρ^2 , we find a quadratic equation in n.

$$n^2 - 2n \frac{(1 + R_F)}{1 - R_F} + (1 + k^2) = 0 \quad (2.63)$$

Both solutions of the equation are in principle valid, and the selection has to be made on physical grounds. For example, by comparing with similar materials. The final expression for the index of refraction (n_{\pm}) is given in equation 2.64.

$$n_{\pm} = \frac{1 + R_F}{1 - R_F} \pm \left[\frac{4R_F}{(1 - R_F)^2} - k^2 \right]^{1/2} \quad (2.64)$$

By employing successively equations 2.59, 2.60 and 2.64 it is possible to obtain both the real and complex parts of the refractive index from total transmittance and reflectance measurements, assuming incoherent light propagation.

2.5.2. Working with a stack of films: the transfer matrix method (TMM)

Stratified media—which have constant properties within each plane perpendicular to a fixed direction [29]—are of considerable importance in optics. For example, multilayers, a stack of thin plane parallel films, can be employed as anti-reflection films, beam splitters, filters, and polarizers.

Unlike the propagation through a single planar, homogeneous and isotropic thin film between two isotropic media treated in section 2.5.1, the case of several stacked films is more complicated, because of the need to keep track of more terms in the sum. To calculate propagation in a stack of several layers, Abeles [29] pioneered an approach that used matrix algebra to simplify computations. By using the linearity of Maxwell’s equations he could couple the waves in both sides of an interface by matrix multiplication. In this way, it suffices to define matrices for each interface and for the propagation inside the layers. The total transfer matrix, from which the transmission and reflection coefficients of the stack can be extracted, is calculated by multiplying those matrices. Later, other authors modified this method to express the matrices in terms of the Fresnel coefficients. In general, matrix multiplication is a simple process for computers, making this approach very efficient and capable of modelling large systems. In this work we implemented the transfer matrix approach with the Fresnel coefficients formulation in Matlab.

The basic procedure is as follows: we define a matrix for each interface and another for the displacement within each layer, then, due to the linearity of the operations we multiply them successively to form the scattering matrix for the whole stack from which we finally obtain the reflection and transmission coefficients.

2.5.2.1. The Interface Matrix, $I_{i,i+1}$

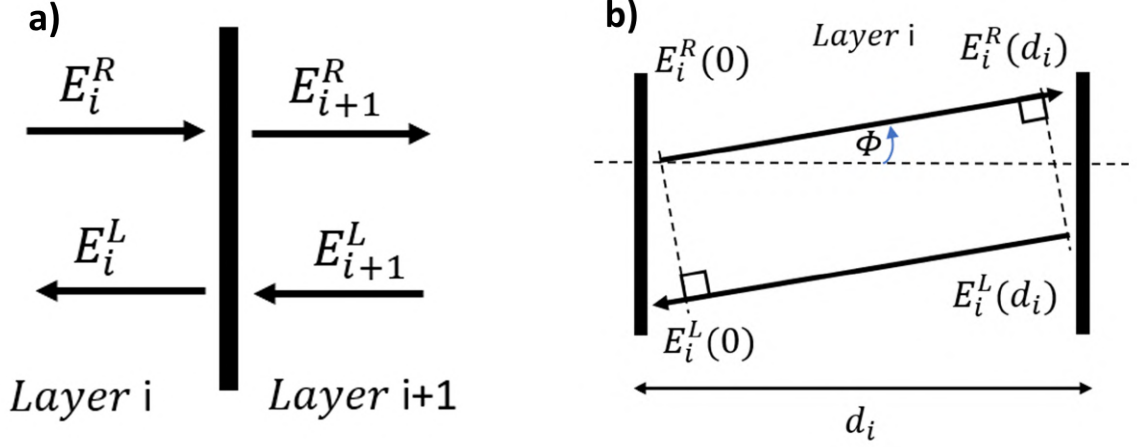


Figure 2.9: Schematic of the situations analysed to obtain the matrices required to implement the transfer matrix method. In a) the propagation of the fields around the boundary between two layers and in b) the propagation inside the layer i .

For the interface matrix we follow the procedure introduced by Azzam and Bashara [38], who define it in terms of the Fresnel coefficients for the interface. We start by looking at a boundary between two media with right (superscript R) and left (superscript L) going electric fields in each side, as show in figure 2.9a. Notice that nothing is assumed about the angle of incidence, which will be contained in the Fresnel coefficients. Matching the incoming and outgoing electric fields, we obtain the following equations using the Fresnel coefficients, which account for the angle of incidence and transmission:

$$E_i^R t_{i,i+1} + E_{i+1}^L r_{i+1,i} = E_{i+1}^R \quad (2.65)$$

$$E_i^R r_{i,i+1} + E_{i+1}^L t_{i+1,i} = E_i^L \quad (2.66)$$

The aim is to express the fields in the i -th layer in terms of the fields in the $i+1$ layer. We readily obtain E_i^R from equation 2.65 and plug it into equation 2.66 to obtain:

$$E_i^L = E_{i+1}^R \left(\frac{r_{i,i+1}}{t_{i,i+1}} \right) + E_{i+1}^L \left(t_{i+1,i} - r_{i,i+1} \frac{r_{i+1,i}}{t_{i,i+1}} \right) \quad (2.67)$$

By using the known properties of the Fresnel coefficients presented in section 2.3.1 [27, 38]:

$$r_{i,i+1} = -r_{i+1,i}$$

$$t_{i,i+1}t_{i+1,i} - r_{i,i+1}r_{i+1,i} = 1$$

We find that the factor multiplying E_{i+1}^L in equation 2.67 is equal to $\frac{1}{t_{i,i+1}}$. Therefore, the equations can be expressed in the following way:

$$\begin{aligned} E_i^R &= \frac{1}{t_{i,i+1}}(E_{i+1}^R - E_{i+1}^L r_{i+1,i}) \\ E_i^L &= \frac{1}{t_{i,i+1}}(E_{i+1}^R r_{i,i+1} + E_{i+1}^L) \end{aligned} \quad (2.68)$$

Finally, we can write the set of equations in matrix form:

$$\boxed{\begin{bmatrix} E_i^R \\ E_i^L \end{bmatrix} = \frac{1}{t_{i,i+1}} \begin{bmatrix} 1 & r_{i,i+1} \\ r_{i,i+1} & 1 \end{bmatrix} \begin{bmatrix} E_{i+1}^R \\ E_{i+1}^L \end{bmatrix} = \mathbf{I}_{i,i+1} \begin{bmatrix} E_{i+1}^R \\ E_{i+1}^L \end{bmatrix}} \quad (2.69)$$

Where $\mathbf{I}_{i,i+1}$ is called the interface matrix for the interface between the i and $i+1$ layer. In some references this matrix is called the dynamic matrix, $\mathbf{D}_{i,i+1}$.

2.5.2.2. The Layer Matrix, L_i

We want to find the matrix that relates the electric fields in the leftmost part of the layer to those on the right immediately before the boundary for a particular layer of width d_i . The situation is depicted in figure 2.9b, where the superscript indicated right (R) and left (L) travelling waves. It is clear that the only effect of the propagation in a homogeneous, isotropic layer is the addition of a phase. For the right travelling wave we can write the field at d_i as shown in equation 2.70, where E_{i0}^R is the initial amplitude of the right travelling wave at the leftmost boundary.

$$E_i^R(d_i) = E_{i0}^R e^{i(\vec{k} \cdot \vec{r}_{d_i} - \omega t)} = e^{i\beta} E_i^R(0) \quad (2.70)$$

With $\beta = \frac{2\pi \hat{n} d_i \cos(\phi)}{\lambda}$, where \hat{n} is the complex refractive index, λ is the wavelength of light (in vacuum) and ϕ is the angle between the stratification direction and the direction of propagation of the electric field inside the layer. We proceed in the same manner for the left travelling wave and arrive to the following relationship [39, 40]:

$$\boxed{\begin{bmatrix} E_i^R(0) \\ E_i^L(0) \end{bmatrix} = \begin{bmatrix} e^{-i\beta} & 0 \\ 0 & e^{i\beta} \end{bmatrix} \begin{bmatrix} E_i^R(d_i) \\ E_i^L(d_i) \end{bmatrix} = \mathbf{L}_i \begin{bmatrix} E_i^R(d_i) \\ E_i^L(d_i) \end{bmatrix}} \quad (2.71)$$

$$\beta = \frac{2\pi \hat{n} d_i \cos(\phi)}{\lambda}$$

The matrix \mathbf{L}_i is called the layer matrix for the i -th layer. In some references it is termed the propagation matrix \mathbf{P}_i .

2.5.2.3. System Transfer Matrix, \mathbf{S}

By virtue of the linearity of the Maxwell equations, we can “follow” the electric fields through each successive layer and compute the result of the propagation through the whole stack. For a stack of N layers:

$$\begin{bmatrix} E_0^R \\ E_0^L \end{bmatrix} = I_{0,1}L_1I_{1,2}L_2 \cdots I_{N-2,N-1}L_{N-1}I_{N-1,N}L_NI_{N,0} \begin{bmatrix} E_{out}^R \\ E_{out}^L \end{bmatrix} = \mathbf{S} \begin{bmatrix} E_{out}^R \\ E_{out}^L \end{bmatrix} \quad (2.72)$$

Where \mathbf{S} is the system transfer matrix—also called scattering matrix—of the whole stack, which contains the entirety of the information about the propagation of the fields inside the ensemble. From the elements of \mathbf{S} we can compute the reflection and transmission coefficients for the stack. First, we assume that the sample is not illuminated from the backside, so we can set $E_{out}^L = 0$:

$$\begin{bmatrix} E_0^R \\ E_0^L \end{bmatrix} = \begin{bmatrix} S_{11} & S_{12} \\ S_{21} & S_{22} \end{bmatrix} \begin{bmatrix} E_{out}^R \\ 0 \end{bmatrix} \quad (2.73)$$

Considering that the reflection and transmission coefficients are defined as the ratio of outgoing fields to the incoming field, from equation 2.73 we find that:

$$\boxed{\begin{aligned} \frac{E_{out}^R}{E_0^R} &= \mathbf{t} = \frac{1}{S_{11}} \\ \frac{E_0^L}{E_0^R} &= \mathbf{r} = \frac{S_{21}}{S_{11}} \end{aligned}} \quad (2.74)$$

While these coefficients relate electric fields, the transmittance and reflectance relate intensities. They are easily calculated in the usual fashion [27]

$$\begin{aligned} \mathbf{T} &= Re\left(\frac{\hat{n}_{out}\cos(\phi_{out})}{\hat{n}_{in}\cos(\phi_{in})}\right)|\mathbf{t}|^2 \\ \mathbf{R} &= |\mathbf{r}|^2 \end{aligned} \quad (2.75)$$

2.5.2.4. Incoherence

The assumption of coherent light propagation leads to oscillations in the calculated spectra due to interference effects. In practice, this effects may not be visible due to coherence-destroying effects like nonparallel surfaces, roughness, limited resolution of the instrumentation or due to the bandwidth of the light source [28, 41], see section 2.4.2 for details.

In the cases where there is no interference it suffices to add the intensities instead of

the electric fields. This can be done straightforwardly by taking the square amplitude of the Fresnel coefficients and the phase elements in each of the \mathbf{I} and \mathbf{L} matrices. It is important to note that this is not equivalent to taking the norm squared of the elements of the system transfer matrix \mathbf{S} , as this only takes the intensity *after* the interference was allowed to happen. If all layers are incoherent, it suffices to take the matrices for each layer, take the modulus squared of its elements and apply the TMM, which results in an intensity scattering matrix.

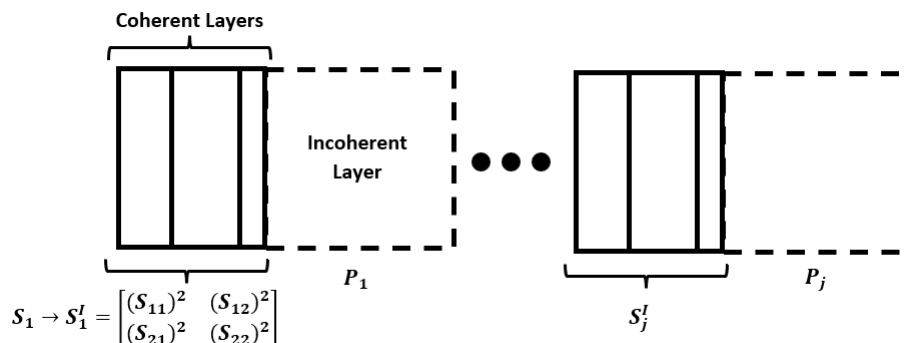


Figure 2.10: Basic scheme for including incoherent layers to the transfer matrix method. We divide the stack in sections delimited by the incoherent layers. Calculate the transfer matrix for the coherent substack and from its elements obtain an intensity matrix. Then multiply those intensity matrices with the intensity propagation matrices from the incoherent layers.

The problem is: how do we deal with multilayer stacks where only some layers produce loss of coherence? We certainly want to allow interference in some layers, while adding just intensities in others. We followed the ideas presented in the literature [39, 41], of which the basic scheme is depicted in figure 2.10. There are packets of coherent layers bounded by incoherent layers. In the coherent packets, we can apply the regular TMM as previously described. Then, we obtain scattering matrices for each packet, which we connect through the incoherent layers by incoherent layer matrices. The only caveat is that incoherence can be caused by scattering, which invalidates the Stokes relations. Therefore, when connecting matrices through incoherent boundaries, the transfer matrix of the coherent stack has to be modified.

In the calculation of the intensity matrix for the coherent packets the initial and final interfaces are accounted for—the incoming and outgoing media of each packet are the surroundings or the incoherent layers. This effectively reduces the coherent packets to interfaces bounding the incoherent layers. Thus, the effect of the incoherent layers is just the addition of a phase which can be written, in matrix form as:

$$\boxed{\begin{aligned} \begin{bmatrix} E_i^R(0) \\ E_i^L(0) \end{bmatrix} &= \begin{bmatrix} |e^{-i\beta}|^2 & 0 \\ 0 & |e^{i\beta}|^2 \end{bmatrix} \begin{bmatrix} E_i^R(d_i) \\ E_i^L(d_i) \end{bmatrix} = \mathbf{D}_i \begin{bmatrix} E_i^R(d_i) \\ E_i^L(d_i) \end{bmatrix} \\ \beta &= \frac{2\pi\hat{n}d_i\cos(\phi)}{\lambda} \end{aligned}} \quad (2.76)$$

To compute the intensity matrix for the coherent packet we can not use directly the \mathbf{I} matrix as previously calculated. In cases where the interfaces are non ideal (such as those that cause loss of coherence, i.e the boundary with incoherent layers) it is generally the case that $t_{i,i+1}t_{i+1,i} - r_{i,i+1}r_{i+1,i} \neq 1$ [41]. We thus begin with the more general transfer matrix:

$$\mathbf{I}_{j,k} = \frac{1}{t_{j,k}} \begin{bmatrix} 1 & -r_{k,j} \\ r_{j,k} & (t_{j,k}t_{k,j} - r_{j,k}r_{k,j}) \end{bmatrix} \quad (2.77)$$

When the coefficients are replaced with their square amplitudes we have:

$$\boxed{\mathbf{T}_{j,k} = \frac{1}{|t_{j,k}|^2} \begin{bmatrix} 1 & -|r_{k,j}|^2 \\ |r_{j,k}|^2 & (|t_{j,k}t_{k,j}|^2 - |r_{j,k}r_{k,j}|^2) \end{bmatrix}} \quad (2.78)$$

This is the intensity transfer matrix for the coherent layer packet going from the j to k layers when the Stokes relations are not valid. Now, it is evident we need the equivalent Fresnel coefficients in both directions for the group, which we have not previously calculated. Fortunately, these can be recovered as we did in equation 2.74. Following the notation used in section 2.5.2.1 we find that they are contained in the elements of the scattering matrix for the coherent stack \mathbf{S} [39, 41]:

$$\begin{aligned} r_{j,k} &= \left. \frac{E_j^-}{E_j^+} \right|_{E_k^- = 0} = \frac{S_{21}}{S_{11}} \\ t_{j,k} &= \left. \frac{E_k^+}{E_j^+} \right|_{E_k^- = 0} = \frac{1}{S_{11}} \\ r_{k,j} &= \left. \frac{E_k^+}{E_k^-} \right|_{E_j^+ = 0} = \frac{-S_{1,2}}{S_{11}} \\ t_{k,j} &= \left. \frac{E_j^-}{E_k^-} \right|_{E_j^+ = 0} = \frac{Det(S)}{S_{11}} \end{aligned} \quad (2.79)$$

To compute the transfer matrix for the entire multilayer, called \mathbf{S}^{incoh} we thus proceed as follows:

1. Divide the stack in packets of coherent layers bounded by incoherent layers.
2. Calculate the transfer matrix for the coherent substack by means of the

classical method as presented in sections 2.5.2.1 through 2.5.2.3.

3. From the scattering matrix for each packet of coherent layers obtain the Fresnel coefficients using equation 2.79.
4. Construct the intensity transfer matrix ($T_{j,k}$) for each packet using equation 2.78.
5. For the incoherent layers calculate the propagation matrices by means of equation 2.76
6. Multiply each matrix successively, as shown in equation 2.80.

$$\begin{bmatrix} I_0^R \\ I_0^L \end{bmatrix} = \dots T_{j,k} D_k \dots T_{q,l} D_l \dots \begin{bmatrix} I_{out}^R \\ I_{out}^L \end{bmatrix} = \mathbf{S}^{incoh} \begin{bmatrix} E_{out}^R \\ E_{out}^L \end{bmatrix} \quad (2.80)$$

The transmission and reflection coefficients are directly obtained from the elements of the system incoherent matrix S^{incoh} , considering we are already dealing with intensities:

$$\begin{aligned} R^{incoh} &= \frac{S_{21}^{incoh}}{S_{11}^{incoh}} \\ T^{incoh} &= Re\left(\frac{n_{out} \cos(\phi_{out})}{n_{in} \cos(\phi_{in})}\right) \frac{1}{S_{11}^{incoh}} \end{aligned} \quad (2.81)$$

2.6. Effective Medium Approximation

In many cases one or several layers of the stack are a mixture of two or more materials. When the inhomogeneities are on a scale considerably smaller than the wavelength of probing light, the mixture can reasonably be treated as an effective medium. In this theory it is assumed that the optical constants of the mixture are the product of a superposition of the optical constants of the constituents [22]. If the different materials are regarded as polarized objects embedded in a host medium, subjected to an homogeneous electric field it is possible to obtain a general equation that relates the effective dielectric function of the composite material to that of the host and the constituents [22, 42]:

$$\frac{\epsilon_{eff} - \epsilon_h}{\epsilon_h + (\epsilon_{eff} - \epsilon_h)L} = \sum_j f_j \frac{\epsilon_j - \epsilon_h}{\epsilon_h + (\epsilon_j - \epsilon_h)L} \quad (2.82)$$

Where ϵ_{eff} , ϵ_h and ϵ_j are the dielectric constants of the effective medium, the host, and the j-th component, respectively. L is a factor that depends on the morphology of the inclusions and $f_j \equiv \frac{V_j}{V}$, is the volume fraction [22].

From this general case there are several schemes to obtain the dielectric constant of the

effective medium, depending on what component is considered to be the host. In this work we follow the Bruggeman approach, also called Effective Medium Approximation (EMA), where the effective medium itself acts as the host ($\epsilon_h = \epsilon_{eff}$) [22]. The EMA tends to lead to better results when there is no preponderance of a particular component and is employed in the specialized literature when dealing with samples similar to the ones used in this work [22, 43]. In this approach we have that equation 2.82 becomes:

$$0 = \sum_j f_j \frac{\epsilon_j - \epsilon_{eff}}{\epsilon_{eff} + (\epsilon_j - \epsilon_{eff})L} \quad (2.83)$$

It is evident from equation 2.83 that this method supports as many constituents in the mixture as desired. However, the degree of the polynomial in ϵ_{eff} that one needs to solve is the same as the number of components in the mixture. Thus, obtaining the solution becomes cumbersome when there are more than two materials. For these cases, we follow the approach presented by Nazarov et al. [43] in which the effective properties of the composite are calculated by the recursive application of the EMA approach for two constituents.

Another complication of this method is that the selection of the physically significant root of the second degree polynomial is not trivial. As a side note, this further adds to the complication of using more than two constituents. To select the appropriate solution, we implement the method developed by Roussel and others [44] in which the application of successive transformations results in only one root. It is important to note that this method is only applicable to two types of inclusions: homogeneous mixture of spheres and spherical inclusions embedded in a matrix. However, some results show that there is not a strong dependence on the shape [4], and therefore this cases are considered a good enough approximation.

2.6.1. Wiener's bounds: Boundaries of the effective refractive index

We wish to know what is the range possible for the effective refractive index when mixing J components in the context of the effective medium approximation. The approximation is essentially a sophisticated way to ponder each material, so the expectation is that the maximum and minimum possible results in this context are simply the refractive indices of the constituents with higher and lowest indices, respectively, independent of the mixing method. This can formally be derived from what is known as Wiener bounds [45].

Wiener proved that for a mixture of J components with real and positive refractive indices, the bound of an effective medium in the context of effective medium theory is

given by equation 2.84 [46], where the nomenclature of the previous section is employed.

$$\left(\sum_{j=1}^J \frac{f_j}{\epsilon_j}\right)^{-1} < \epsilon_{eff} < \sum_{j=1}^J f_j \epsilon_j \quad (2.84)$$

This result corresponds to the possible boundaries for different mixing methods and inclusion morphologies (i.e. different L parameter) with a given fraction of constituents f_j . Now we wish to derive the limits of these bounds when the fraction of constituents is allowed to vary. We will focus on the derivation of the lower bound, the higher bound is analogous.

We have that the Wiener lower bound (ϵ_w^{lb}) can be expressed as in the left side of equation 2.85. Now, we wish to minimize this fraction by varying the fraction of constituents, f_k . First note that the numerator is a constant, so the lowest possible value is achieved when the denominator is a maximum. As the denominator is a simple weighted average of terms of the form $\prod_{j \neq k} \epsilon_j$, the maximum is achieved when all of the weight is given to the largest term. As all terms in the product are real and positive, the largest term is the one that does not include the smallest of them: ϵ_q . In our expression this means that the largest denominator is obtained when $k = q$ and $f_q = 1$. Simplifying the resulting expression we find that that Wiener's lower bound is in turn bounded by ϵ_q .

$$\epsilon_w^{lb} = \left(\sum_{j=1}^J \frac{f_j}{\epsilon_j}\right)^{-1} = \frac{\prod_{j=1}^J \epsilon_j}{\sum_{k=1}^J f_k \prod_{j \neq k} \epsilon_j} \geq \epsilon_q \quad \text{where} \quad \min\{\epsilon_1, \epsilon_2, \dots, \epsilon_J\} = \epsilon_q \quad (2.85)$$

The hypotheses used in Wiener's work (positive and real refractive index of the constituents) are a reasonable approximation in the experiments presented in this work, where the effective refractive indices are calculated far from the absorption edges of non-metallic, non-magnetic media [1]. In a later work Milton [47] derived a generalization of the bounds in effective medium theory for arbitrary dielectric functions of the constituents, and the lowest and largest possible values of the effective dielectric function are still set by the constituents when mixing two media, which is the case in this work.

2.7. Stokes parameters: representation of polarized light

Any state of polarized light can be completely described by the Stokes parameters [48, 49]. While other representations directly using the polarization ellipse [29, 49] are very useful, these parameters have a very practical advantage: they describe polarization using

a directly measurable observable—irradiance [27].

This set of parameters is usually described using a hypothetical set of four filters which, under natural illumination, transmit half of the incident light [27, 49]. The choice is not unique, but the idea is that the four parameters are the total irradiance (S_0), and the tendencies towards horizontally linearly polarized (LP) light compared to vertically polarized light (S_1), linearly polarized light at 45° versus light at 135° (S_2) and right handed circularly polarized light (RHCP) compared to left handed circular (LHCP) is accounted with S_3 . Note that in many references the parameters are named, in order: I, M, C, S (see Shurcliff book for example [49]). These can also be related to the parameters of the polarization ellipse or the ellipsometric parameters [48, 50] but for our purposes, the complex amplitude representation will prove most useful. The parameters can be expressed in terms of the components of the electric field in the x-y plane (E_x and E_y) as follows, where the superscript $\{*\}$ denotes the complex conjugate [48]:

$$\begin{aligned}
S_0 = I &= |E_x|^2 + |E_y|^2 = E_x E_x^* + E_y E_y^* \\
S_1 &= I_{0^\circ} - I_{90^\circ} = E_x E_x^* - E_y E_y^* \\
S_2 &= I_{45^\circ} - I_{135^\circ} = E_x E_y^* + E_y E_x^* \\
S_3 &= I_{RHCP} - I_{LHCP} = i(E_x E_y^* - E_y E_x^*)
\end{aligned} \tag{2.86}$$

There are several intensity measuring schemes to access these parameters. In the case of the experimental setup used in this work, which includes a Wollaston prism, the S_1 parameter is directly accessed in one measurement from the intensity at both detectors, S_2 can be obtained by placing a half wave plate (HWP) at a specific angle relative to the lab basis and S_3 by using a quarter wave plate (QWP) at -45° relative to the \hat{x} axis of the lab. For a proof of the validity of this measuring method see Appendix A.

Finally, the degree of polarization (P) is used to quantify how polarized is the light beam and is defined as shown in equation 2.87 [27]. If it is equal to unity then the beam is perfectly polarized, whereas the case of $P = 0$ represents completely unpolarized light. Values between 0 and 1 are the more realistic case of partially polarized light. Perfectly polarized is a state where there is a definite relationship of phase of the polarization components whereas unpolarized light can be thought of as a superposition of all possible polarization directions, with the phases of the polarization components varying rapidly in time. Partial polarization is an intermediate state, where there is some relationship between the polarization states.

$$P = \frac{I_{polarized}}{I_{total}} = \frac{\sqrt{S_1^2 + S_2^2 + S_3^2}}{S_0} \tag{2.87}$$

2.7.1. The theory of partial polarization

The qualitative description of partially polarized light should be reminiscent of the discussions presented in section 2.4.2 when formalizing the treatment of partial coherence. Indeed, in the theory of polarization the components of polarization are characterized by correlations and cross-correlations similar to the ones presented in that section.

Consider that an EM wave travelling in the z direction has two polarization components $E_x(t)$ and $E_y(t)$, which are generally random. The wave is fully characterized by the correlation and cross correlation functions, as before (see section 2.4.2 for details):

$$\begin{aligned}
 G_{xx}(\tau) &= \langle E_x^*(t)E_x(t+\tau) \rangle \\
 G_{yy}(\tau) &= \langle E_y^*(t)E_y(t+\tau) \rangle \\
 G_{xy}(\tau) &= \langle E_x^*(t)E_y(t+\tau) \rangle \\
 g_{xy}(\tau) &= \frac{G_{xy}(\tau)}{\sqrt{G_{xx}(0)G_{yy}(0)}}
 \end{aligned}
 \tag{2.88}$$

For quasi monochromatic light the τ dependency is exponential and so the polarization properties are described by the values at $\tau = 0$. It is then useful to define the coherence matrix \mathbf{G} [35]:

$$\mathbf{G} = \begin{bmatrix} G_{xx} & G_{xy} \\ G_{yx} & G_{yy} \end{bmatrix}
 \tag{2.89}$$

The Stokes parameters can be expressed in terms of the elements of the coherency matrix:

$$\begin{aligned}
 S_0 &= I = \langle |E_x|^2 \rangle + \langle |E_y|^2 \rangle = G_{xx} + G_{yy} \\
 S_1 &= E_x E_x^* - E_y E_y^* = \langle |E_x|^2 \rangle - \langle |E_y|^2 \rangle = G_{xx} - G_{yy} \\
 S_2 &= E_x E_y^* + E_y E_x^* = 2\text{Re}\{\langle E_x^* E_y \rangle\} = 2\text{Re}\{G_{xy}\} \\
 S_3 &= i(E_x E_y^* - E_y E_x^*) = 2\text{Im}\{\langle E_x^* E_y \rangle\} = 2\text{Im}\{G_{xy}\}
 \end{aligned}
 \tag{2.90}$$

Unpolarized light of (average) intensity \bar{I} has the two components with the same intensity and they are totally uncorrelated. In this case the coherency matrix becomes:

$$\mathbf{G}_{\text{incoh}} = \frac{1}{2}\bar{I} \begin{bmatrix} 1 & 0 \\ 0 & 1 \end{bmatrix}
 \tag{2.91}$$

This matrix is invariant to rotations of the coordinate system, the two components always have (on average) equal intensities and are uncorrelated. This implied that the electric field vector is equally likely to be in any direction of the x-y plane. This is why, for example, wave plates do not have any effect on unpolarized light, because they introduce

phase delays between components that have totally random phases.

If the cross correlation coefficient has unit magnitude (i.e. $|g_{xy}| = 1$) then the light is said to be perfectly polarized (or just polarized). Partially polarized light lies between the two limits. The degree of polarization in the context of statistical optics is defined as shown in equation 2.92 where Tr is the trace and \det is the determinant of the matrix.

$$P = \sqrt{1 - \frac{4\det\mathbf{G}}{(\text{Tr}\mathbf{G})^2}} = \sqrt{1 - 4 \left[\frac{I_x I_y}{(I_x + I_y)^2} \right] (1 - |g_{xy}|^2)} \quad (2.92)$$

This definition of the degree of polarization is invariant to rotations of the coordinate system, since determinant and trace are invariant to unitary transformations, which is useful because changes in the coordinate system should not affect the degree of polarization. Moreover, it shows explicitly the dependence with the cross correlation function. Notice that the degree of polarization is unity if the polarization components are totally correlated ($|g_{xy}| = 1$) and it is a minimum if they are completely uncorrelated ($|g_{xy}| = 0$). In particular it is 0 if, besides being uncorrelated, the intensities are the same ($I_x = I_y$), as expected from the description of unpolarized light. This definition is equivalent to the one presented in equation 2.87.

From this treatment, it is clear that the degree of polarization is deeply connected to the coherence properties of light. Polarization is maintained in deterministic processes which preserve the coherence of the polarization components [35]. True depolarization occurs when the processes introduce randomness, leading to a reduction in the cross-correlation values. In general there are two possible mechanisms:

- **Multiple Scattering:** Involves light interacting with particles or irregularities, leading to random changes in polarization due to the unpredictable nature of the scattering events.
- **Random Polarization Fluctuations:** Stem from thermal, mechanical, or quantum noise in the system, which introduces randomness in the phase and amplitude of the electromagnetic field's components, thereby affecting the cross-correlation functions and reducing coherence.

It is important to clarify here that the framework developed in section 2.4.2 is a scalar treatment, neglecting polarization directions. The interference of waves in that section assumed that the polarization directions in the interacting waves were equal. In general the interference is proportional to the scalar product of each field, and therefore beams of orthogonal polarizations do not interfere. Although both cases are treated with coherence theory, it is important to differentiate between the coherence of two different beams, which

may or may not interfere depending on their polarization directions, and the coherence of the polarization components of a *single beam*.

Chapter 3

Experimental Setups

In the first section of this chapter I will explain the general use of the integrating spheres to measure total and diffuse reflectance and transmittance, and to obtain the haze. In that section the experimental setups and the corrections employed are shown. In the next sections the measurement of specular (i.e. without integrating spheres) reflectance and transmittance is described. The last sections also introduces the measurement of the polarization components of light and the characterization by UV-vis absorbance.

3.1. Total transmittance and reflectance measurements

In this section we will explain the setups used to measure the spectral dependence of the total transmission and reflection. The main tool used in these measurements are the integrating spheres. These allow the capture of diffuse light and, in some cases the differentiation between diffuse and specular components. We will detail the experimental configuration and the way the measurements are corrected to account for the effects of the integrating spheres. Finally, we will describe how to make spectral measurements sensitive to polarization. A description of all the specialized equipment used in this work is reserved for Appendix [B](#).

3.1.1. Transmittance measurements

Transmittance measurements at normal incidence were performed with a 150 mm diameter integrating sphere model UPB-150-ART from Gigahertz-Optik. Figure [3.1](#) shows a schematic representation of the setup employed. We used a halogen lamp by Ocean Optics, model HL-2000, the output of which was guided to the sample placed in the input of the integrating sphere by means of a $1000\mu\text{m}$ diameter optical fiber. The output of the

sphere was read by a computer after passing through a spectrometer Ocean Optics S2000 coupled to the outlet of the integrating sphere by a 600 μm optical fiber.

This sphere can be fitted with an accessory, called light trap, located opposite to the entrance port that, by a combination of a specific cone-like geometry and an opaque coating, blocks the reflection of light directly transmitted by the sample (i.e. the specular ray). By using this light trap, it is possible to differentiate between the specular and diffuse components of light.

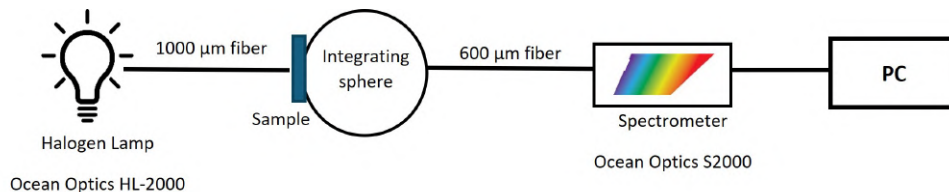


Figure 3.1: Schematic of the setup used for transmittance measurements at normal incidence employing the UPB-150-ART integrating sphere

In order to obtain values of the direct and diffuse transmittances for the sample corrected for the effects of the experimental setup, 4 spectral measurements (I_i) are performed for each sample, the configuration of each can be seen in figure 3.2. The total (T_T) and diffuse (T_D) transmittances are calculated as shown in equation 3.1[25, 51, 52], where the intensities (I_i) follow the notation presented in figure 3.2. I_1 represents the total light transmitted by the sample, incorporating both direct and diffuse components. On the other hand, I_3 specifically quantifies the diffuse component of the transmitted light, isolating the effect of scattering within the sample. The other spectra are collected without a sample and serve to characterize the incoming beam and the effects of the sphere on it. The incident light intensity, corrected for potential losses at the sphere's entrance port, is denoted by I_2 . This correction is crucial for accurate baseline measurement. Lastly, I_4 serves as a corrective measurement for the scattering effects introduced by the sphere itself, ensuring that the final data accurately reflects the sample's properties rather than artifacts of the measurement apparatus.

$$T_T = \frac{I_1}{I_2} \quad (3.1)$$

$$T_D = \frac{I_3 - T_T I_4}{I_2}$$

The haze (H) is defined as the ratio of diffuse light to total light (equation 3.2, where the subscript T indicates that it is for transmittance)[23–25].

$$H_T = \frac{T_D}{T_T} \quad (3.2)$$

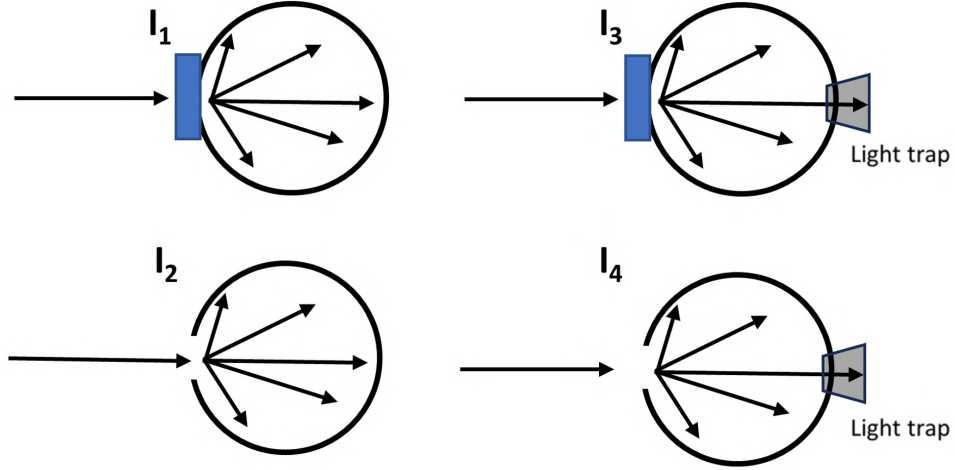


Figure 3.2: Measurements repeated for each sample in order to correct for the transmittance of the sphere. Their usage appears in equation 3.1. Notice that I_1 and I_3 are collected with the sample in the entrance Port, while I_2 and I_4 collect the lamp signal directly.

3.1.2. Variable angle of incidence transmittance

Measuring the transmittance of a sample for different angles of incidence is a useful technique. Firstly, it gives the behaviour for samples under natural illumination, where light is expected to impinge with a relatively uniform distribution of angles of incidence. Secondly, having extra data can be useful in order to obtain or check parameters through fitting procedures, as adjusting several curves with the same set of parameters can improve the uniqueness of the solution[42]. The previously discussed setup, while powerful in the sense that it allows to differentiate between specular and diffuse components of light, does not allow to vary the angle of incidence (ϕ_i). In order to measure the angular dependence of transmitted light a different setup, displayed in figure 3.3 (top block of the figure), was employed. The samples are placed at the entrance of a FOIS-1 integrating sphere (Ocean Optics) and illuminated using an optical fiber 1000 μm in diameter, coupled to a halogen lamp (HL-2000 from Ocean Optics). To hold the samples in place, we clamped them with a black matte mask with an aperture smaller than the sphere's entrance port. This aperture ensured that all the light passed through a small region of the sample, which increases the homogeneity of the studied area. The output from the sphere was collected using a 200 μm optical fiber and detected by a spectrometer model S2000 from Ocean Optics. The sphere was mounted on a goniometer, allowing measurements at different angles of incidence. Unlike the previous device, this sphere can not be equipped with a light trap, and thus is only able to determine the total transmittance. Thus, for each angle of incidence, two measurements were performed, one with the sample (I_1) and a reference signal (I_2) without the sample.

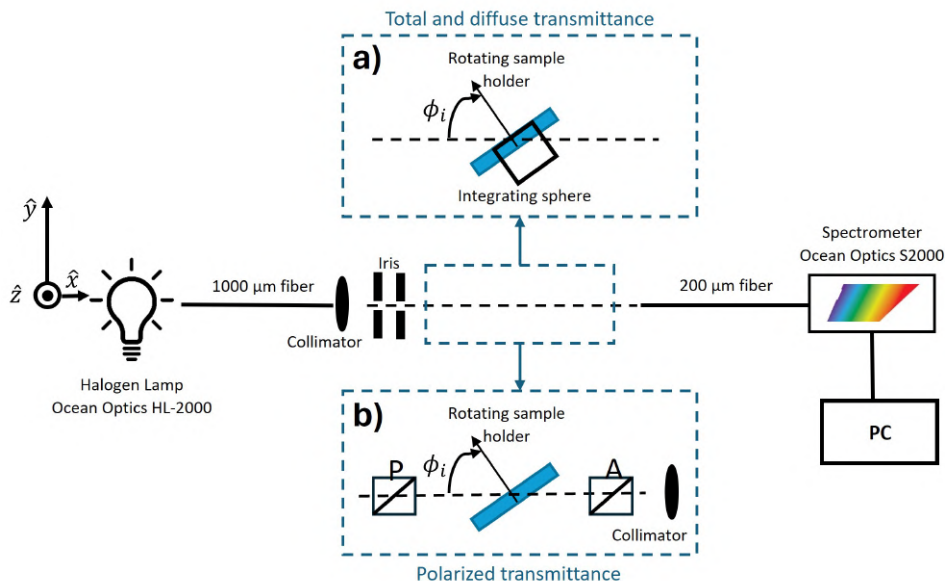


Figure 3.3: Setup used for total and polarized transmittance measurements. The a) top block indicates the configuration used for detecting total and diffuse transmittance. The sample was placed at the entrance orifice of the integrating sphere. b) The bottom block indicates the configuration for polarization dependent measurements, detailed in section 3.2.1. P and A are the polarizer and analyzer, respectively. The polarization sensitive measurement does not use an integrating sphere.

In this setup, direct coupling of the fiber to the sphere’s entrance port is not feasible; instead, the fiber must be positioned approximately 5 cm away to accommodate sphere rotation. To effectively channel light into the entrance port, the system utilizes a collimator along with two irises. The collimator serves to restrict the spreading of the beam, while the irises help in defining the beam’s direction of propagation, aiding in precise alignment towards the entrance port. The second iris is crucial for adjusting the spot size on the sample surface, which is maintained at about 2 mm in diameter. This spot size is intentionally kept smaller than the orifice of the mask, guaranteeing optimal illumination of the sample and enhancing the accuracy of the measurements.

3.1.3. Reflectance measurements

In the samples studied in this work using the integrating spheres, the transmittance generally is greater than the reflectance. In order to obtain a better signal to noise ratio in the reflected spectra, a smaller integrating sphere, ISP-REF by Ocean Insight, was used. This sphere has an integrated lamp and the angle of incidence is 8 degrees. It is also equipped with a light trap, which can be either activated or deactivated in order to determine both the diffuse and total reflected components, respectively. In this case, to correct for the effects of the integrating sphere, five measurements were made for each sample.

For reference a Lambertian white surface—of the same material as the sphere interior—was used. The additional measurement when compared to transmittance obviously arises from the fact that in reflectance, the effects of the device can not account for the incident irradiance. In this case, the total light reflected from the reference is considered the light incident on the sample. It is debatable whether a sixth measurement, a reference without including the specular reflectance, should be employed for the normalization of the diffuse reflectance. In this work it was found that for highly reflective samples this resulted in reflectances slightly higher than unity. The five configurations are represented schematically in figure 3.4. The subscript I and E refer to inclusion or exclusion of the specular reflectance from the sample (total and diffuse reflectance, respectively), and follows the notation used in the device. I_I^{sph} accounts for the total reflectance of the integrating sphere itself. Conversely, I_E^{sph} is used to adjust for any scattering effects introduced by the sphere itself, ensuring accurate measurement of the diffuse component. I_{ref} is the total incident light as measured by the sphere, where a Lambertian white surface was used.

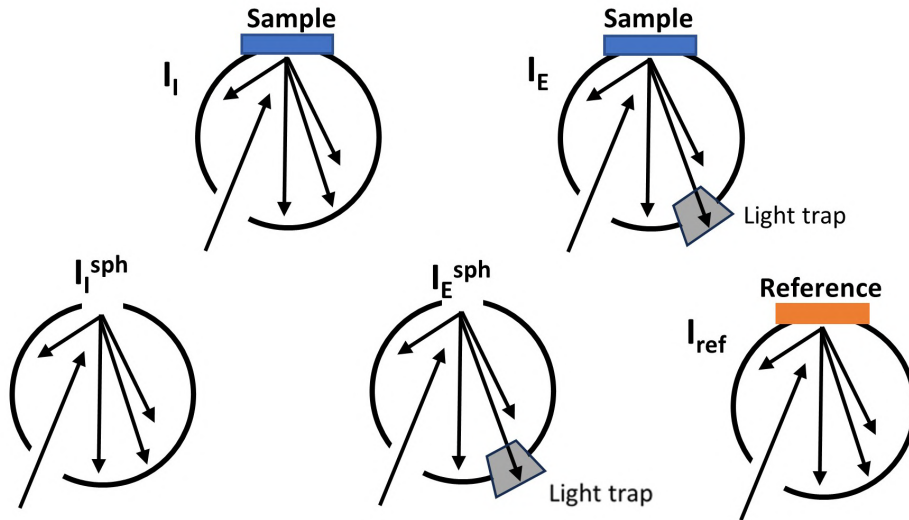


Figure 3.4: The configurations of the 5 measurements done to obtain the reflectance corrected by the effects of the integrating sphere. The reference used was a Lambertian white surface

The total (R_T) and diffuse (R_D) reflectances are calculated as shown in equation 3.3. The haze is defined in the same way as in transmittance (equation 3.2): $H_R = \frac{R_D}{R_T}$.

$$\begin{aligned}
 R_T &= \frac{I_I - I_I^{sph}}{I_{ref} - I_I^{sph}} \\
 R_D &= \frac{I_E - I_E^{sph}}{I_{ref} - I_E^{sph}}
 \end{aligned}
 \tag{3.3}$$

3.2. Specular measurements

Integrating spheres, as described in the previous section, are useful devices for spectral characterization. However, they have some limitations. In reflectance they do not allow for different angles of incidence, since the sample has to be placed at the fixed entrance port. Further, the spheres rely on the effect of multiple reflections and thus the detector can not be placed directly on the beam, which means that reflectance at normal incidence can not be measured. This last point is particularly important, because the case of normal incidence is the simplest to understand and many interesting properties can be extracted from it, as was shown in section 2.5.1. Lastly, they can not account for polarization sensitive effects because the multiple reflections inside the sphere alter the polarization state of light and the detectors are not polarization sensitive.

This section describes the experimental setups employed in order to obtain information on the polarized transmittance, the reflectance with variable angle of incidence and information on the polarization state of a beam by measuring the Stokes parameters. We use specular detection, where the signal is directly incident on an optical fiber or on Silicon detectors.

3.2.1. Spectral polarized transmittance measurements

The setup described in the previous section allows for convenient characterization of the angular dependence of reflected and transmitted monochromatic light. However, it can not be fitted with a white light source because, even dispensing with the half and quarter wave plates, the Wollaston prism deviation is wavelength dependant, meaning that no detector position guarantees the collection of all the light.

To obtain information on the spectral transmittance, a setup very similar to that described in section 3.1.2 was used, see figure 3.3. Instead of employing an integrating sphere (top block, a), the transmitted light was collected with a collimator attached to the same optical fiber (bottom block, b), suitably aligned. As the alignment process is difficult and introduces imprecision due to the large dependence of the coupling to the optical fiber with the angle of incidence of light on the collimator, this setup was only used to measure transmittance, which only requires an initial alignment.

By not using the integrating sphere it is possible to obtain information on the influence of the sample in the polarization state of light. To do this, we place the goniometer between a polarizer-analyzer pair, in the positions P and A indicated in figure 3.3, respectively. The positions of the polarizer (incident beam side) that match the p-s basis of the sample were the ones obtained in the calibration presented in section 3.2.4. The positions of the analyzer that matched this polarization directions were obtained simply by finding

the angle at which the detected intensity was maximized (parallel polarizers) and minimized (orthogonal polarizers). This leaves 4 possible polarizer-analyzer configurations, denoted as T_{ij} , ($i, j = 1, 2$, corresponding to p and s polarized, respectively). The first index refers to the position of the polarizer, while the second index corresponds to the position of the analyzer. Therefore, the configurations T_{11} and T_{22} represent the case of parallel polarizer-analyzer, also called direct polarization measurement. Similarly, T_{12} and T_{21} correspond to orthogonal polarizers, also called crossed polarization measurement.

To obtain the transmittance it is necessary to normalize the intensity to a reference signal. In the parallel configuration this is straightforward, incident intensity is just the measurement performed without a sample (lamp signal). This already accounts for possible losses in the polarizers. In the case of crossed polarization measurements however, it is not as direct, because the crossed signal is very small (would be 0 with ideal polarizers), and, if the sample has an effect on crossed polarization, the intensity increases with the presence of the sample. This in turn would lead to a transmittance higher than unity, which is not possible. To normalize the crossed spectra, the direct measurement of the lamp signal was employed, in the configuration that matched the first index of the crossed polarization signal. For example, T_{12} was normalized with T_{11} . As in the other setups, to calibrate normal incidence ($\phi_i = 0^\circ$), a glass plate was placed on the sample holder, and its position was adjusted until the reflection aligned with the incoming beam.

3.2.2. Reflectance at normal incidence

To measure reflectance at normal incidence we used a simple setup, consisting of a sample holder and a reflection probe model RP20 supplied by Thorlabs. This is a bifurcated optical fiber with a 200 μm diameter core. One leg couples to a spectrometer (S2000 Ocean Optics) and the other to the lamp (HL-2000 Ocean Optics). The other side of the fiber, which has both the incident and reflected light fibers, illuminates the sample and also detects the reflection. An image of the fiber is presented in figure 3.5. The fiber was placed at around 2 mm from the sample surface. To determine the light intensity incident on the sample, a glass plate with a known refractive index ($n = 1.52$) and thickness of 1.25 mm was utilized. The reflected spectra from the samples were divided by the reflection from the glass surface, and the resulting ratio was multiplied by the theoretical incoherent reflectance spectra of a 1.25 mm-thick glass plate. The direction of normal incidence was determined in two steps using the glass plate. First, a rough alignment was obtained by looking at the reflected light and positioning the reflected light spot on the fiber surface. Then, a more precise position is obtained by maximizing the signal detected by the spectrometer.

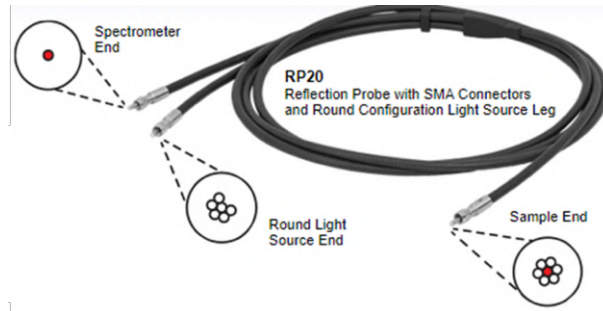


Figure 3.5: Reflection probe used for reflectance at normal incidence. Taken from Thorlabs [53]

3.2.3. Variable angle of incidence reflectance, transmittance and Stokes Parameters

In order to measure the reflectance with different angles of incidence we built a setup that is schematically represented in figure 3.6. The alignment of the beam produced by a laser diode was controlled by two irises, while the one closest to the sample also determined the spot size, around 2 mm in diameter at the sample surface. The sample was mounted on an in house designed and fabricated sample holder, which was placed on a goniometer. This element has a precision screw that controls the exact position of the sample surface, in order to align it with the rotation axis of the goniometer. This in turns matches the angular position of the sample surface (i.e the change in incident angle) with the one spanned by the goniometer.

The detection arm consisted of a tray which is allowed to rotate around the shaft of the goniometer (sample axis) by means of an articulated arm. On top of the tray we mounted two silicon detectors and a Wollaston prism which separates the orthogonal components of polarization, allowing for their simultaneous detection using the two silicon detectors, previously calibrated to have the same gain factor. Two different lasers were used in the experiments, with wavelength of 405 nm and 785 nm.

A linear polarizer was placed on the incident path to control the direction of polarization, which was positioned such that the same intensity was recorded by each detector, which means the incident light is a superposition of two linearly polarized fields that are the same intensity in the basis of the Wollaston prism. Because the laser source produces a linearly polarizer beam, with a direction not necessarily aligned with the polarizer, a half wave plate (HWP), which rotates the direction of linear polarization, was placed before the entrance polarizer in order to increase the intensity by aligning the oscillation direction with the transmission axis of the linear polarizer. The positions of the linear polarizer that matched the basis of the Wollaston prism was determined by placing the tray opposite to the incoming beam, without a sample, and rotating the polarizer until

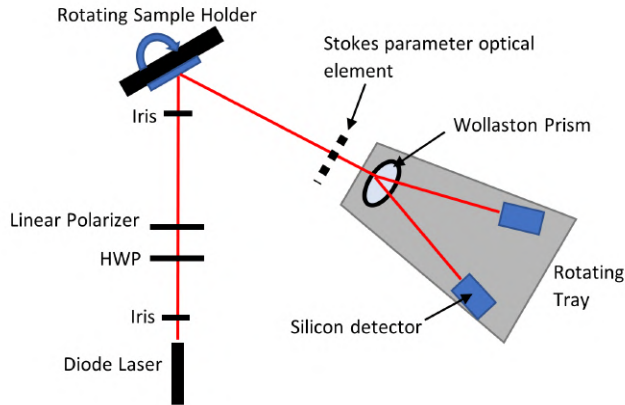


Figure 3.6: *Experimental setup for reflectance measurement. The rotating sample holder is mounted on a goniometer, the tray holding the Wollaston prism and two silicon detectors is allowed to rotate around the sample by means of an articulated arm. The signal is modulated with a chopper, which allows the detection through lock-in amplifiers.*

the two positions that minimized the signal on one of each of the detectors was found. In each position the transmission axis is parallel to the direction corresponding to the detector with high intensity.

In order to obtain the intensity of both the s (TE) and p (TM) polarizations *directly* from the measurements of the detectors, it is necessary that the eigenbasis of the sample’s plane and of the polarizing prism are parallel. In other words, the principal axes of the Wollaston prism must coincide with the direction parallel and perpendicular to the plane of incidence. To achieve this, we first make a rough alignment using the indicator in the prism that marks the direction of the axes. Then the quality of this alignment is checked and adjusted by using the properties of Brewster’s angle [27, 29]. When p-polarized light is incident on a plane parallel surface with negligible absorption, there is an angle of incidence θ_B (Brewster’s angle) such that there is no reflected light. By rotating the “pair” of entrance polarizer and Wollaston prism around the rough adjustment (both elements must still be aligned, as explained previously), we could obtain a position where one of the reflected polarizations from a glass plate ($n=1.52$, thickness of 1.25 mm) approached zero at a certain angle. To visualize this position, we compute the ratio $\frac{I_s}{I_p}$, displayed in figure 3.7b as a function of the angle of incidence. Clearly, it should diverge at $\theta = \theta_B$ ($I_p = 0$). This procedure is represented in the schematic in figure 3.7a. When the axis of the prism is aligned with that of the sample we have that $\frac{I_s}{I_p} = \frac{I'_y}{I'_x} \rightarrow \infty$. This in practice does not happen because of small scattering effects [54], residual polarization in the s-direction, absorption and the fact that a real material has two boundaries. As a consequence, we find a finite peak (figure 3.7b), and to obtain the correct alignment we look to maximize the contrast between this peak and the values at other angles. We see that from 3 independent measurements at the optimized position, the position of Brewster’s angle is

the same within experimental uncertainty (the uncertainty of the goniometer is $\pm 0.5^\circ$, and the spot has finite size). The values outside the uncertainty range of the peak are negligible, consistent with Brewster's condition. Further, the obtained value for θ_B of 56.6° is in good agreement with the theoretical values expected from the studied glass plate [27].

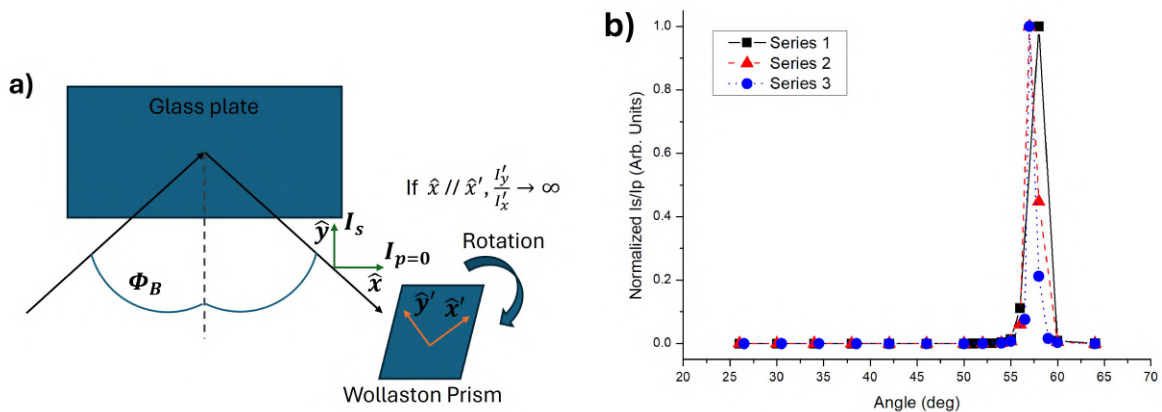


Figure 3.7: a) Schematic representation of the procedure used to align the Wollaston prism. The optics used to condition the incoming beam is omitted for clarity. b) Normalized I_s/I_p curves for the glass substrate taken with a 785 nm wavelength laser

Normal incidence (incident angle $\phi_i = 0^\circ$) was calibrated by placing the glass plate in a position such that all of the reflected light was backscattered into the incoming beam. This alignment was repeated each time a new sample was placed on the sample holder. The laser was modulated with a mechanical chopper, at a frequency of around 570 Hz, so that the detection could be performed with two lock-in amplifiers, one for each Si detector.

It is important to note certain chromatic precautions. While the linear polarizers have high efficiency in a wide range of frequencies, the HWP and QWP are designed to introduce the required phase shift only at a specific wavelength. Further, the wavelength alters the deviation of the two polarizations introduced by the Wollaston prism. Therefore, when a laser diode of different wavelength is used, it is necessary to reposition the Si detectors on the tray and to change to the corresponding QWP and HWP for the working wavelength.

This setup can be used to characterize the monochromatic reflectance and transmittance as a function of angle of incidence, as well as to obtain an estimate of the angular distribution of light by fixing the angle of incidence and varying the angle of the detection arm. For this measurement the Wollaston prism is removed, as the prism works on specular light only. The reflection angles are limited to between 25 and 70 degrees because of the limitations imposed by the dimensions of the setup.

By varying the positions of the entrance polarizer it is possible to measure both the direct and crossed polarized transmittance and reflectance, with the analyzer directions given by the positions of the Wollaston prism. The parallel and crossed polarizer orientations that define $T_{i,j}$ are obtained as in section 3.2.1.

3.2.4. Stokes Parameters

The same setup described in the previous section can be used to obtain the Stokes parameters of a sample. The parameters are normalized with respect to S_0 , which is also measured with this setup. Therefore, it is enough to measure voltages on the detectors without the need to convert to intensity of light through the sensitivity, provided that both detectors are properly calibrated. If the incoming radiance (S_0) was measured by an external power detector, as is done in other setups, the results should be adjusted for the possible differences in gain in the power meter and the silicon detectors.

As described in section 2.7 the parameter S_0 and S_1 are the addition and difference between horizontal and vertical polarization intensities, which are measured directly using the Wollaston prism.

In order to obtain S_2 we place a HWP before the prism, see figure 3.6. This element rotates the plane of polarization of linearly polarized (LP) light. From the definition of the Stokes parameters we know that if the direction of polarization of light is at 45° then $S_2 = 1$. If we want to obtain the parameters as the intensity difference between the detector corresponding to the horizontal direction (I_x) and to the vertical direction (I_y) then the effect of the HWP must be such that it rotates the incident light at 45° towards the horizontal (\hat{x}) direction. Where \hat{x} and \hat{y} are the horizontal and vertical directions relative to the lab coordinate system and match the direction of p and s polarized light, respectively. To calibrate the position of the HWP we use precisely this idea. First, without a sample, and the detection arm collecting the incoming light, we place the linear polarizer in such a way that the intensity is the same in each detector, meaning that the direction of polarization is at 45° . Then we place the HWP, and rotate it until the intensity in the \hat{y} direction is minimum. This position is the one that must be used to find the S_2 parameter. In this configuration $S_2 = I_x - I_y$.

To measure the S_3 parameter we use a QWP instead. This transforms perfectly circularly polarized light into linearly polarized light at 45° of the QWP's basis. Now, following the same idea used in the S_2 measurement, we want the optical element to transform right circularly polarized light into horizontally polarized light in the basis of the lab (\hat{x} direction). This is achieved by placing the fast axis of the QWP at -45° relative to the \hat{x} direction. Now, as our setup is not precise regarding the angular position of the elements, we want to implement a robust procedure that allows us to obtain the

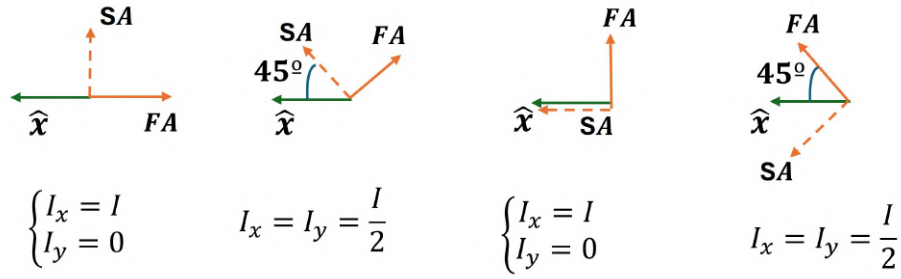


Figure 3.8: Configurations used to calibrate the position of the QWP in order to measure the S_3 Stokes parameter. Notice that for each orientation of the HWP there are a set of observables at the detectors, I_x and I_y . FA and SA are the fast and slow axis of the waveplates, respectively.

correct position of the QWP. As we only have one QWP it is not possible to generate circularly polarized light—which requires a linear polarized and a QWP—and then rotate a second QWP until we find the angular position in which the correct reading for the known polarization state is found. We need to find the correct position working only with linearly polarized light. To do this, we note that for perfectly circularly polarized light the amplitude, and thus the intensity in both the \hat{x} and \hat{y} directions is the same. By using the first polarizer to define the plane of polarization of the incoming beam at 0° of the \hat{x} direction, we can then place and rotate counter clockwise the QWP starting from the fast axis (FA) indicator aligned to the horizontal and record the position when the intensity in the \hat{y} detector is null and when it is equal at both detectors. Then looking at the fast axis indicator on the QWP we can tell which position out of the two that do not affect the beam ($I_x = I$) is aligned to the horizontal axis (the indicator is close to the horizontal plane). We know that of the two positions that resulted in equal intensities at the detectors (circular polarization) the one that is at -45° is the one that made a larger angle with respect to the position aligned with the horizontal direction. The measurements and their corresponding observables are shown in figure 3.8.

The particular cases of polarizations used to better illustrate the calibration procedure of the optical elements are demonstrated to yield the correct Stokes parameters for an arbitrary beam in Appendix A.

3.2.5. UV-vis absorbance

The absorption spectra of a sample contains two key pieces of information: 1) by identifying low absorption regions, we can choose which wavelengths to probe the sample with in order to have high signal to noise ratio and simplify analysis by not having absorption effects and 2) absorption peaks can be associated to specific compounds, which can give an idea of the sample's chemical composition. We would like to determine the

absorptance, defined, as expected, as the ratio between absorbed and incident intensities, $A = \frac{I_A}{I_E}$ [22]. The knowledge of the absorbed intensity is difficult to obtain, and thus the concept of *absorbance* is employed. The absorbance is defined as shown in equation 3.4 [22], where energy conservation is used, $T + R + S + A = 1$, T and R being the specular transmittance and reflectance respectively, and S is the scattered intensity. The main advantage is that it can be directly measured with a spectrometer.

$$A_b = -\ln T = -\ln(1 - R - S - A) \quad (3.4)$$

As is clear from the expression, any non negligible reflectance or scattering give rise to an “absorption”, and therefore may not allow for a quantitative analysis of the absorption. However, it is still useful, because, as reflectance and scattering are usually smooth functions (unless there is resonant scattering [55–58]), sharp features on the spectra can be correlated to absorption bands. Further, other measurements can be performed on the sample to quantify reflectance and scattering and, if the absorbance peaks coincide with the absorption band of one of the expected constituents, it is reasonably safe to ascribe the spectral feature to it.

To acquire the spectra we used a 150W Xe lamp (Newport 96000) as the light source, and coupled the transmitted signal directly through a $200\mu m$ optical fiber to a spectrometer model Flame-S-UV-VIS from Ocean Optics. While in our study the samples exhibited important scattering effects, the scattering is a smooth function of wavelength, and thus directly transmitted light is enough to observe the position of the absorption bands.

Chapter 4

Thickness determination of Silicon Dioxide films

Silicon dioxide is ubiquitous in the semiconductor industry. Thin layers of SiO_2 are the most common material used as gate dielectrics in ultra large scale integration (ULSI) microelectronics [59–62], making it the heart of the modern transistor [63, 64]. It also finds applications as a mask for silicon etching[65], device isolation, impurity gettering and junction passivation, among others [66]. They are usually grown over silicon wafers by simple thermal oxidation of silicon, which results in almost defect-free films [65, 67]. While the oxidation rate is faster in the presence of water, dry oxygen results in denser films with better interface properties [65] making it the preferred method for growing thin films for microelectronic applications.

The massive technological and economic interest led to enormous characterization efforts, resulting in an extensive mapping of the properties of SiO_2 and Si in different regimes [68–70]. Coupled with the possibility to grow smooth, low defect films by readily available thermal oxidation, they are prime candidates to test the adequacy and capabilities of the implemented transfer matrix model (TMM) and the reflectance setup.

The chapter begins with a description of the fabrication procedure, followed by an estimation of the resulting thicknesses by inspection and by the most common theoretical model for film growth—the Deal-Grove model. Then, the thickness is determined from SEM images of the cross section. Finally, the results for the fitted thickness using the TMM are presented, which show remarkable agreement with the expected values, demonstrating the adequacy of the implemented model.

4.1. SiO_2 thin film growth by thermal oxidation

Silicon dioxide films were grown over (100) silicon wafers by thermal oxidation as part of this thesis. They were subjected to ambient air, with a relative humidity between 23% and 35% and temperature in the 8°C to 14°C range. All samples were grown with an oxidation (plateau) time of 4 hours, while the temperature (T_{set}) were: 900°C, 950°C, 1050°C and 1150°C. These values were chosen because, from the predictions of the Deal Grove model [71], were enough to generate discernible and measurable thickness differences (reflectance struggles with films less than 30 nm thick [72]). To avoid potential damage due to thermal shock [73] the samples were heated (cooled) from (to) room temperature at a rate of 120°C/hour. A schematic of the temperature program is shown in figure 4.1. Before introducing the wafers in the furnace, they were cleaned for 5 minutes with acetone followed by 10 minutes in deionized water, both processes aided by a ultrasonic bath. The substrates were then dried in ambient conditions. The 900°C and 950°C samples were grown on a Thermo Scientific furnace, model Lindberg Blue E, while the 1050°C and 1150°C were grown in a furnace model HFA 40 from Hornos Atec.

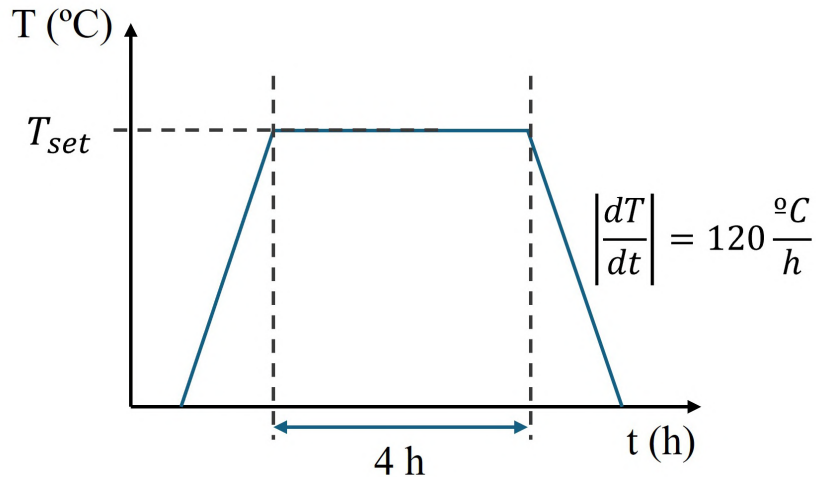


Figure 4.1: Schematic of the heating program used in the growth of Silicon dioxide films. The temperature was varied, with the plateau lasting for 4 hours. The temperature increase and decrease were both at a rate of 120 °C/h.

The as grown samples are pictured in figure 4.2a. Note the emergence of different colors produced by thin film interference [32], which immediately indicate that the samples are of different thicknesses. This effect is well documented, and reference tables that relate color and thickness are readily available, which is a tool for an initial thickness estimation. From the table presented in figure 4.2b we can see that the estimated thicknesses are 50, 120, 320 and 460 nm for temperatures 900°C through 1150°C (note the arrows indicating the values and compare with the image). The results are summarized in table 4.1.

In order to obtain another estimate of the thickness, we compute the expected thickness using the Deal-Grove model [72, 74]. This model assumes Fickian diffusion of the reactants, and is the most widespread model for silicon dioxide growth over silicon for films thicker than 28 nm [60, 67] (some authors report deviations for films less than 50 nm thick [66]). The calculated values are displayed in table 4.1.

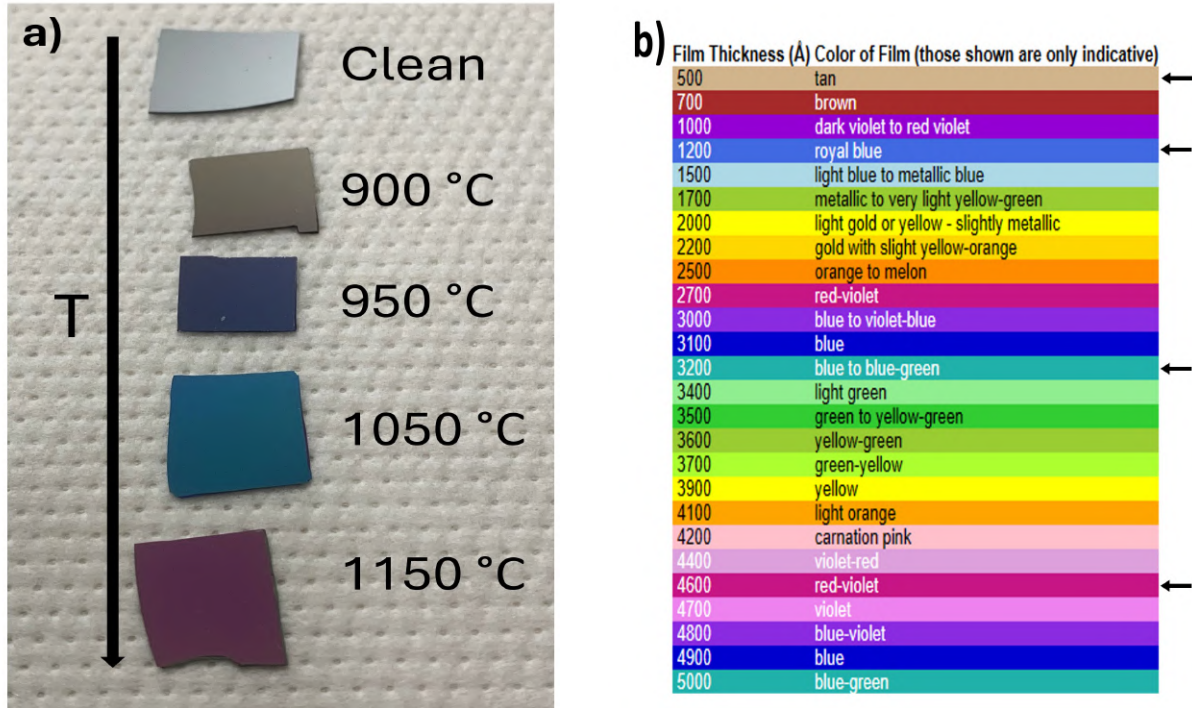


Figure 4.2: a) Image of the as grown samples under white light. Note the interference colors [27, 28] arising from the different thicknesses. For reference a clean silicon wafer is shown. b) Reference table relating the thickness with the color, taken from the UIUC [75]. For clarity, arrows on the right indicate the observed colors in the fabricated samples.

4.2. SEM thickness characterization

The samples were cleaved and the cross sections were imaged using a Field Emission Scanning Electron Microscope (FE-SEM) model Magellan 400L set at the ICN2 in Barcelona, Spain. In order to reduce charge buildup in the surface of the insulating SiO₂, a 2 nm thick layer of Au was spin coated on the samples. The images appear in figure 4.3.

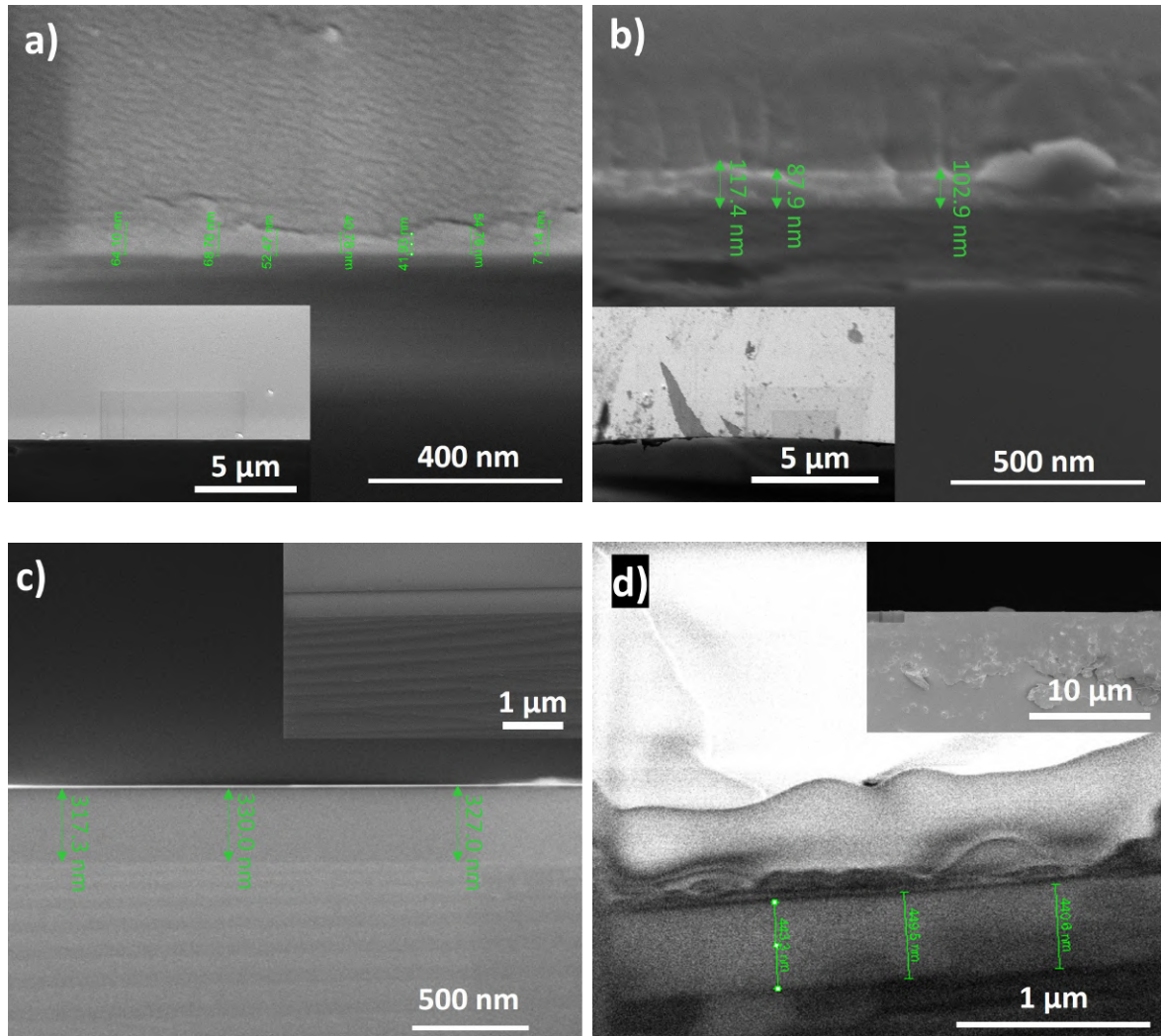


Figure 4.3: SEM micrographs of the SiO_2 films grown by 4 hours of thermal oxidation in ambient air at temperatures of a) 900°C , b) 950°C , c) 1050°C and d) 1150°C . The inset in the figures present a lower magnification image to demonstrate the general quality of the cleaved films. In the images some of the sampled thicknesses are shown. Notice that in d) there is surface charge accumulation.

Multiple regions of the cross section of each film were sampled, and the thickness (d) was determined by averaging the measured values, with the standard deviation serving as the uncertainty. The results, presented in table 4.1, closely align with the expected color characteristics of the samples. However, it's important to note that uncertainties are substantial due to two factors. First, the sample cross sections lack smoothness, possibly caused by the cleaving process, growth conditions, or oxidation during the 3-month period between fabrication and image capture. Second, incomplete Au deposition led to charge buildup in the samples, as evident in figure 4.3d.

Temperature (°C)	Interference (nm)	Deal-Grove (nm)	SEM $\times 10^1$ (nm)	Optical (nm)
900	50	36	6.7 ± 0.8	68.5 ± 0.4
950	120	70	10 ± 1	103.6 ± 0.4
1050	320	179	33 ± 1	329.4 ± 0.7
1150	460	318	46 ± 1	446.0 ± 0.8

Table 4.1: Thickness results obtained for thermally oxidized for 4 hours at varying temperatures with different methods. The estimate from the interference color, the predictions of the Deal-Grove model, the measurements using SEM microscopy and the optically found thickness through fitting of the reflectance spectra are shown. The uncertainty in the SEM measurement is given by the standard deviation of the measurements of different regions of the film while in the case of reflectance results from the 95% confidence interval of the fitting.

4.3. Thickness determination by reflectance characterization

Reflectance data at normal incidence for each sample was collected using the setup detailed in section 3.2.2. To apply the TMM method and determine thickness, the system was modelled as a silicon dioxide film within two infinite media (a freestanding film)—air and silicon. A schematic of the model used is shown in figure 4.4a. The air- SiO_2 and the SiO_2 - Si interfaces are associated with their respective interface matrices, $I_{0,1}$ and $I_{1,2}$, respectively. The propagation inside the layer of thickness (d) is modeled by a layer matrix L_1 . The calculations were performed employing the refractive indices of SiO_2 thin film and crystalline Si from Gao et al. [76] and Schinke et al. [77], respectively.

Calculated spectra for selected thicknesses (d) is shown in figure 4.4b. Notice how the amplitude and period of the oscillations change with thickness. In order to understand the interference colors observed in the samples and presented in figure 4.2b, it is useful to observe the color reference in the top left. For example, the reflectance of the 50 nm thick sample is mostly flat with a slight increase near the red region, which results in a redish-white or tan color. In contrast, the 500 nm film has a very clear maxima between blue and green, while the other maxima occur near the infrared (IR) and UV, resulting in a blue-green color.

To obtain the thickness of the fabricated samples, the reflectance spectra was fitted with the least square method, with the parameter d as the free (or fitting) parameter. Figure 4.5 displays the measured and calculated spectra with nearly perfect fitting, deviating by less than 2% in all cases.

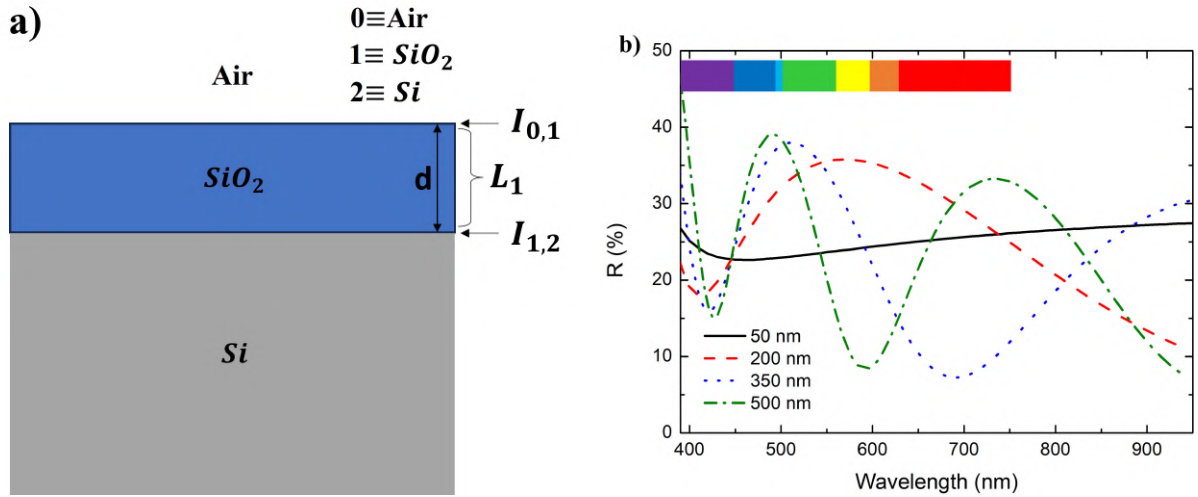


Figure 4.4: a) Schematic of the model employed to fit the thickness of the silicon dioxide films. Air and Si are semi infinite media that bound a SiO₂ film of thickness d . The two interfaces are linked to two interface matrices, while the propagation inside the layer is modeled by a propagation matrix. b) Calculated reflectance spectra obtained from the application of TMM to the model presented in a). Notice the spectral color reference on the top left, which shows an approximate correspondence of the color of light (as perceived by human eyes) for that wavelength range.

Table 4.1 presents the obtained thicknesses (optical method). Remarkably, there is strong concordance among thickness values obtained from interference color, SEM micrographs, and reflectance measurements. The 95% confidence interval of the fit was used as the uncertainty. Even though this value is extremely low, it is important to consider that it does not include the uncertainty in the wavelength, given by the resolution of the spectrometer, and, more importantly, in the measured reflectance. Therefore, the real uncertainty in the determined thickness of the developed experimental technique is not determined in this work.

It's notable that, in all instances, the thickness calculated from the Deal-Grove model is smaller compared to other methods. This discrepancy is anticipated for two reasons. Firstly, the model accounts only for the temperature plateau, while our silicon wafers experienced high temperatures during both cooling and heating phases, as shown in figure 4.1. Secondly, Deal-Grove calculations assume completely dry air, whereas our study's samples were grown in ambient air, with a relative humidity of 23-35%, leading to increased growth rates [60, 65, 74].

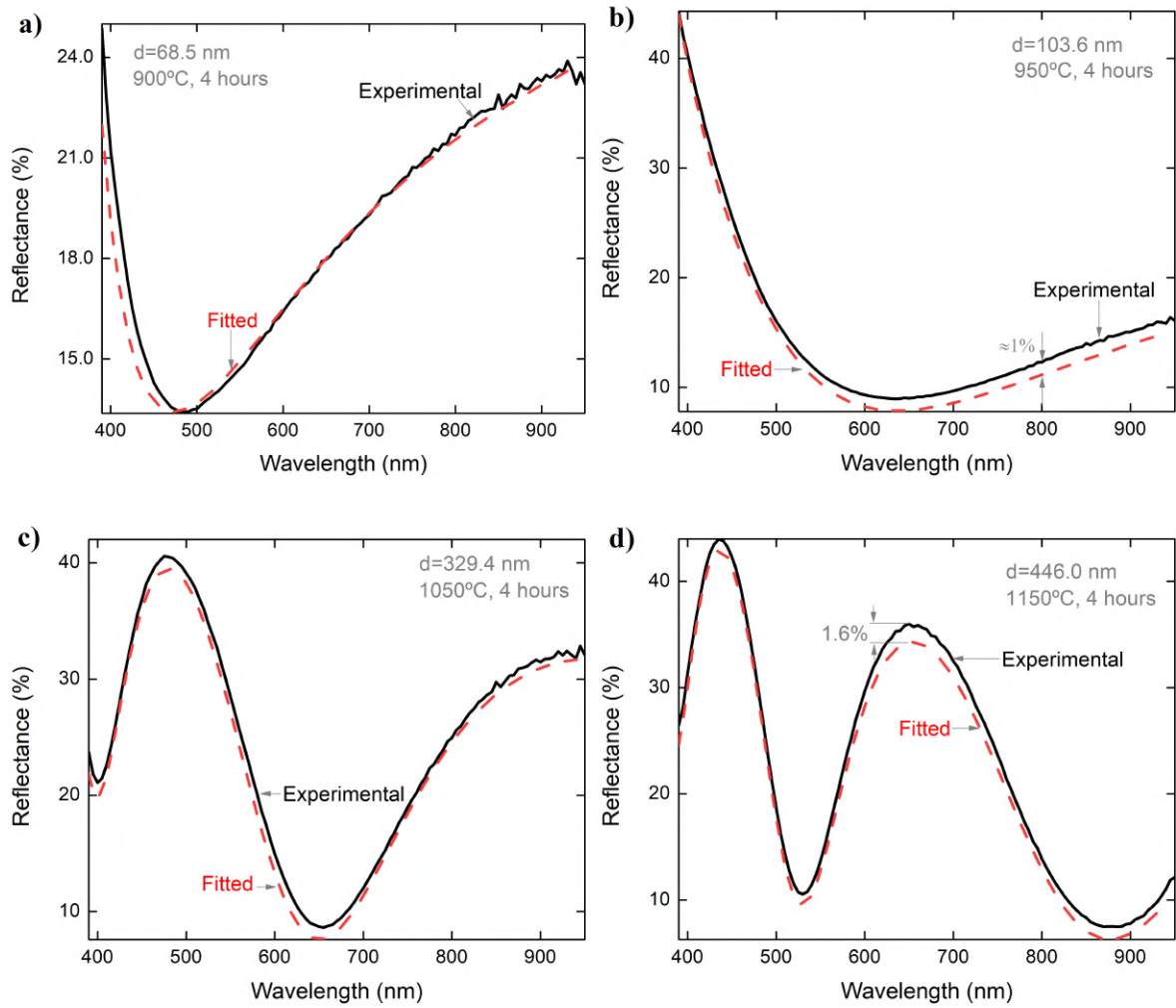


Figure 4.5: Measured and calculated reflectance spectra of the SiO_2 films grown by 4 hours of thermal oxidation in ambient air at temperatures of a) 900°C , b) 950°C , c) 1050°C and d) 1150°C . The thickness resulting from the fit (d) is shown in the figures. Grey solid line is the measured spectra and red dashed line is the calculated spectra.

4.4. Conclusion and perspectives

We effectively showcased the precision of our experimental arrangement and the applied model by fitting reflectance at normal incidence measurements, yielding thickness values closely matching those obtained through alternative methods. Consequently from this work, the Optical Properties of Materials lab within the Solid State Physics Group has gained enhanced capabilities for sample characterization, thanks to the incorporation of a reflectance setup and a computational model apt for parameter fitting.

In order to better gauge the accuracy of the method employed, it would be necessary to obtain the thickness with another, more precise method. While SEM images offer a

reasonable estimate, surface charging and cleaving-induced irregularities introduce errors. The intermixing region between the silicon dioxide film and silicon wafer, with reported thickness variations (0.5 to 3 nm) [63] adds further complexity to the discernment of the oxide layer. A better approach involves utilizing an AFM or profilometer after introducing a “step” in the samples, achieved through silicon dioxide etching in hydrogen fluoride (HF) [78] or covering a section of the wafer during thermal oxidation to prevent oxide growth.

The results demonstrate the methodology’s capability to confidently determine material parameters, paving the way for its application in probing complex systems, particularly multilayers.

Chapter 5

Optical Properties of the traslucent butterfly and the common moth

In the last 40 years several biological samples were found to possess remarkable properties, superior in many regards to man-made materials. In particular since the 1990s, with the growing focus in nanotechnology, the physical basis of properties such as high tensile strength [79], hydrophobicity [80, 81] and reduced drag [82] present in biological tissue were better understood. In general, the properties arise from a complex interplay between morphology and physical and chemical composition [81, 83]. One of the earliest examples were the lotus leaves, where an array of complex hierarchical nanostructures with sub micrometer roughness leads to hydrophobicity resulting in self-cleaning properties [80, 81].

The attractiveness of many of these properties for industrial and scientific processes has lead to the growth of the field of biomimetics, concerned with taking inspiration or adapting structures found in nature [82] to develop novel materials. In particular, structural color—coloration arising from structures with features comparable to the wavelength of light [33, 34]—has emerged as a topic of growing interest. Having fascinated scientist over the centuries, this type of effects, which are responsible for the beautiful iridescent colors in, for example, pearls, peacock feathers and fish [33, 84], now present a promising avenue for reducing the use of contaminating dyes [85, 86], while having a higher resilience to discoloration induced by chemical change [87, 88].

The *Morpho* genus of butterflies, comprising 29 species that inhabit Central and South America [89–91], is perhaps the most emblematic example to date of structural color. The striking blue color of the scales of most species has been extensively studied and a lot of work has gone into reproducing the nanostructures [92, 93]. This has fostered an interest in the study of other butterfly species. Several works have revealed remarkable properties, like polarization conversion effects [94–97] or omnidirectional reflectance [98,

99], as a consequence of intricate structures. Some of these have been shown to be photonic in nature [100–102], while others achieve the effects through random shapes or scatterer distributions [98, 103]. Recent developments have harnessed the structural properties for various technological applications. Butterfly wings have been employed as vapor detectors [104], thermal sensors [105] and platforms for Surface Enhanced Raman Spectroscopy (SERS) [106].

Butterfly wings are primarily formed by a membrane composed of thin layers of a hardened protein called chitin [107]. In some species the presence of chitosan [108, 109]—derived from chitin by the removal of an acetyl group—has been reported. The ratio of chitosan to chitin is called the deacetylation factor [110]. The membrane is supported by a structure of veins that visually divide the wing in different regions [98, 107, 111]. The wings are usually covered in scales, which serve functions such as coloration [107, 112] and improving aerodynamic performance during flight [113]. These scales are formed by cuticle, a plastic biological product, composed of chitin embedded in a matrix of proteins, secreted by a single cell [114–116]. Scales tend to be flat, elongated structures arranged in a way that resembles shingles on a roof [114] and they are usually responsible for the iridescent colors observed in many butterfly species [117]. However, transparent specimens have developed elongated, high aspect ratio structures called piliform scales or bristles [118]. For clarity, in this work we will call the former simply scales and the latter bristles. Other structures like sensilla (a sensory organ) may be present, usually in the veins [107], and the structure may be covered in wax or other materials [119].

In this work we studied the optical properties of the wings of the *Episcada hymenaea* translucent butterfly species, autochthonous to south America [120, 121]. This species is particularly intriguing due to its similarity with the *Greta oto*, which exhibits remarkably low reflectance over a wide range of incident angles. Notably, both species are one of the few examples of transparency-based camouflage found in terrestrial environments [98, 122]. This mechanism is extremely difficult to achieve on land due to the large discrepancy in refractive index between biological tissue ($n \approx 1.5$) and air [123, 124], which results in high reflectances. In order to perform a comparative analysis, the properties of the *Saturniidae Heliconisa pagenstecheri*—common moth, which also has relatively transparent wings—were also studied. The structures on the wings of both species are very different, which we expect manifests in the optical properties. As this is a multidisciplinary topic, the work was done in collaboration with the groups of Entomology and the Area of Analytical Biochemistry from the Faculty of Science of the Universidad de la República. Note that the *Episcada hymenaea* and the *Saturniidae Heliconisa pagenstecheri* are interchangeably called in the text by their scientific names or butterfly and moth, respectively.

This chapter starts with the morphological characterization of the samples by means of SEM microscopy. Then it is followed by their optical characterization, where total and diffuse reflectance and transmittance are reported. From the measurements at normal incidence the effective refractive index of the wing of *Episcada hymenaea* is calculated. The scattering properties are discussed and a qualitative description is possible by means of angle resolved transmittance. Finally, an interesting polarization conversion effect is observed in the butterfly's wings, which is effectively exploited to measure the thickness of the sample by optical techniques only, in very good agreement with the thickness obtained from SEM images. Finally, a general evaluation and future perspectives are presented.

5.1. Morphological characterization

The SEM images of one specimen of the *Episcada hymenaea* wing taken by our collaborators with a JEOL JSM/5900 LV SEM are shown in figure 5.1. An optical image of the studied wing is shown in the inset of 5.1c and the general structure can be seen in figure 5.1a. The transparent inner region appears as a solid block whereas the edge, that looks brownish under natural light, is covered with scales. Both regions have long bristles, but their density and length are larger along the edge.

A close up of the bristles are shown in appendix D, where we see they are around 5 μm thick and formed by a reticular structure. The separation between these is around 60 μm and that region appears devoid of any additional structure.

In figures 5.1c and 5.1d we can see the structure in the transparent region between the bristles. The surface is rough, with lobes of around 100 nm in height, below of which we find a compact region. From figure 5.1b we see that the top rough region is around 100nm thick while the interior has a thickness of 350 to 360 nm.

The thickness of the sample was determined more precisely from the side image (5.1c) by sampling at 22 locations to account for thickness variations. Three of these are shown in the main part of figure 5.1c. To compute the thickness and the uncertainty we used the mean and standard deviation, respectively. The resulting thickness was determined to be $\bar{d} = 446 \pm 45$ nm.

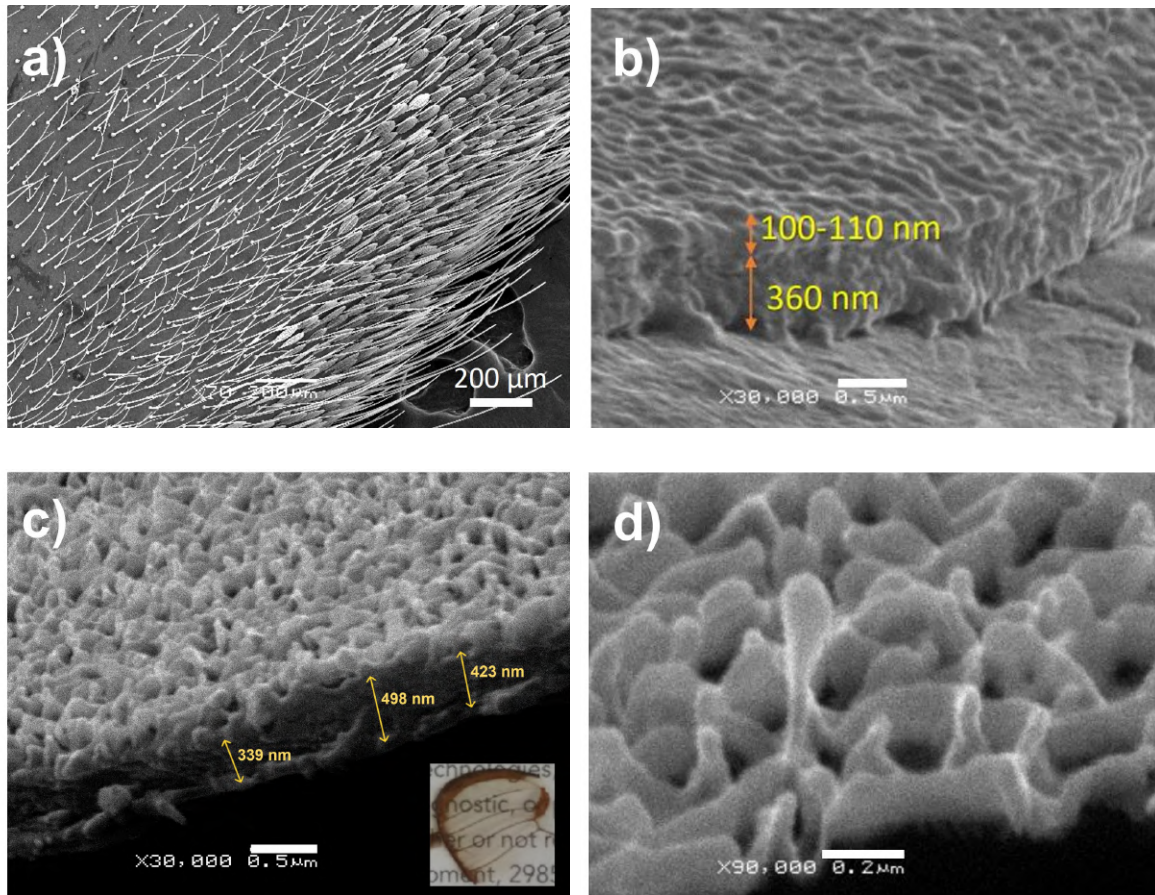


Figure 5.1: SEM micrographs of the wing of the *Episcada hymenaea* translucent butterfly. a) General structure of the wing (scale bar 200 μ m), we see the edge composed of scales and the inner region, both have long bristles. b) Image along the edge of the wing, where there appears to be two layers on the wing membrane, a bottom bulk and a top corrugated region (scale 500nm). c) Image at the edge of the wing, and example of 3 sections sampled for the thickness, the scale bar represents 500 nm, the bottom inset is an optical image of the studied wing, sample 1. d) Highest magnification (scale 200nm) close to the sample surface, we see the general shape of the wing surface, which displays an irregular structure formed by lobes.

The transparent region of the wings of the *Saturniidae Heliconisa pagenstecheri* common moth is shown in figures 5.2a and 5.2b. It is clear that the surface characteristics are different: while it is not smooth, it does not have the rough structure seen in the case of the translucent butterfly as can be seen in the inset of figure 5.2a compared to figure 5.1c. While the scales are different, it can be qualitatively seen that the moth wing surface appears smoother. We also see that the surface has scales, which are absent from the transparent region of the other species, and that the scale shows a reticular structure. Further, there are several “bases” that hold the scales and bristle in place.

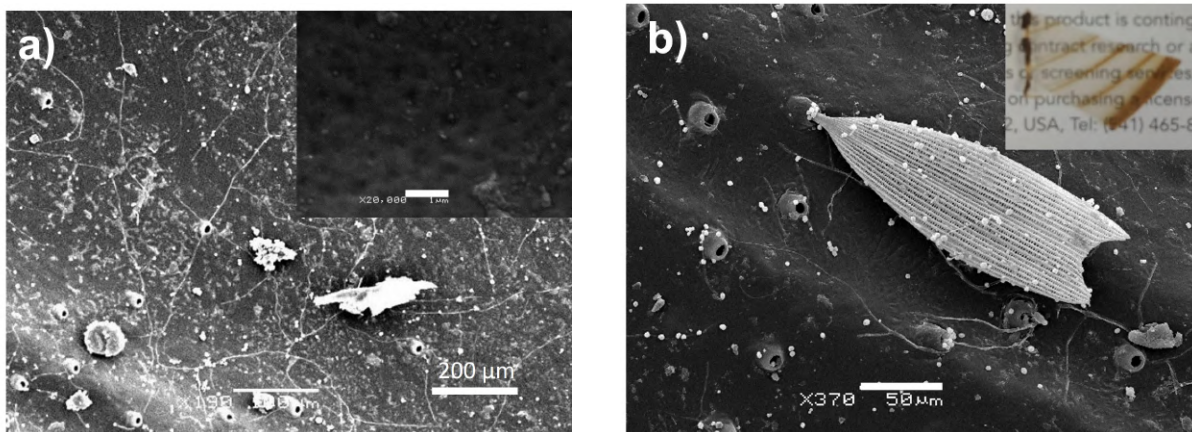


Figure 5.2: SEM micrographs of the wing of a Saturniidae *Heliconisa pagenstecheri* common moth specimen. a) Transparent region away from scale and inset a close up of that region, where we see there is no nanostructure, the scale bars represent 100 μm and 1 μm, respectively. b) Image of a single scale on the wing (scale bar 50 μm, in the inset an optical image of the studied wing).

5.2. UV-vis absorbance

The absorbance spectrum of both samples in the transparent region appear in figure 5.3. They present a clear peak near $\lambda = 280$ nm, the previously reported absorption edge of chitin [125, 126]. This is consistent with the reported composition of the membrane of the wings [127–129], and therefore confirms the presence of chitin. Further, the feature is sharper in the moth, as can be estimated from the wavelength where the intensity decays to $1/e$ of the maximum value. This however, can be a consequence of reflectance or scattering, as previously discussed (section 3.2.5).

The fact that the moth has higher absorbance when compared to the butterfly can be attributed in principle to higher concentrations of chitin and other proteins. However, as shown in the next sections, the *Saturniidae Heliconisa pagenstecheri* has both higher reflectance and scattering compared to the *Episcada hymenaea* which possibly explains the differences with a similar argument to that of the previous paragraph.

Notably, we see that in the visible region of the spectrum there are no absorption bands. This indicates that probing in that region will lead to high signals and is the first confirmation of what is observed by simple inspection: the regions are transparent under natural illumination. However, the absorbance in this region is not negligible. We can compare the spectra with expected values by computing the absorption from previously reported extinction coefficients of chitin. This is done by employing equation 5.1 [1], where d is the thickness of the sample. In the inset of figure 5.3 we can see the calculated absorption for chitin using the values for κ reported by Azofeifa et.al. [125] and assuming a

thickness of $1\mu\text{m}$, which as seen in the previous section, overestimates the thickness of the *Episcada hymenaea* wing and is of the order of magnitude of moth wings [130–132]. The general shape of the calculated and measured spectra are similar, but the experimental values are one order of magnitude higher. While it is possible that the samples have different absorption compared to pure chitin, specially because it depends on the degree of deacetylation of the polymer [133–135], the discrepancy is expected to arise from the considerations mentioned when measuring absorbance instead of absorptance. As we will see, both samples display non negligible scattering and reflectance, which reduces the light incident on the detector and increases absorbance (i.e. S and R in equation 3.4 are not ≈ 0).

$$A = \alpha d = \frac{4\pi\kappa}{\lambda}d \quad (5.1)$$

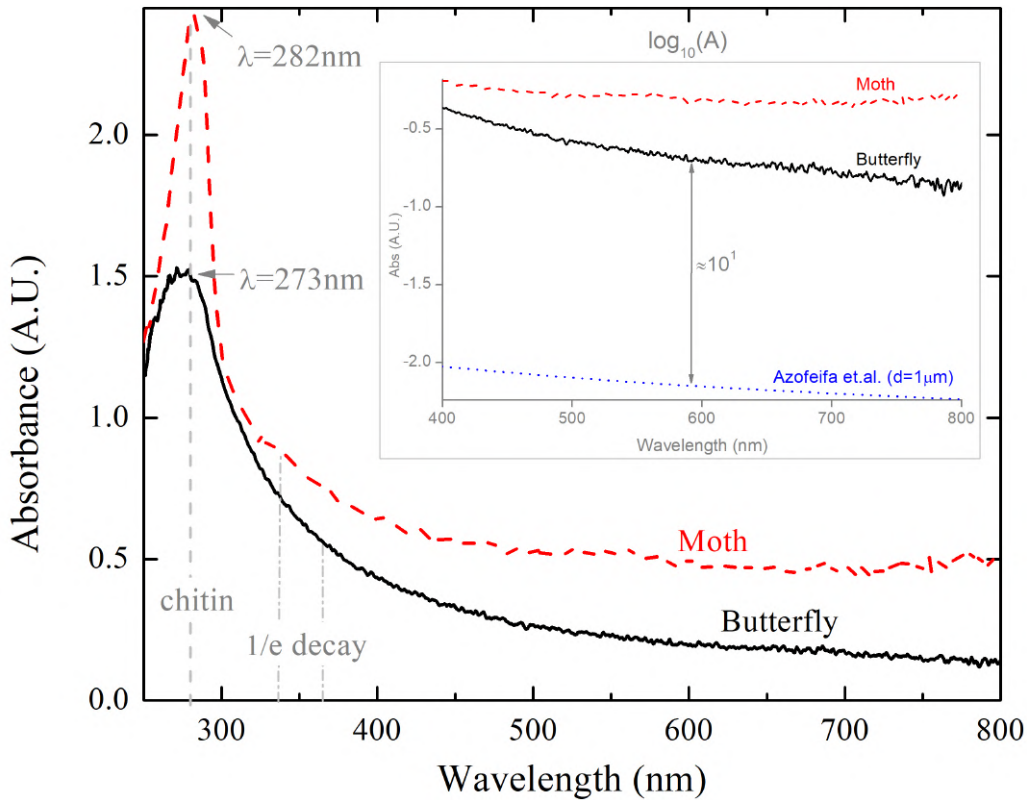


Figure 5.3: UV-vis absorbance spectrum of the butterfly (*Episcada hymenaea*) and the moth (*Saturniidae Heliconisa pagenstecheri*). Arrows indicate the position of the maximum. In the insert the logarithm of the absorbances in the range 400 nm to 800 nm are displayed, alongside the absorbance of pure chitin calculated from the κ values reported by Azoifeifa et.al and assuming a sample thickness of $1\mu\text{m}$. The reported absorption band of chitin at $\lambda = 280\text{ nm}$ is indicated, alongside the position of the $1/e$ decay of the peaks, to aid in width visualization.

5.3. Integrating Sphere measurements

5.3.1. Total transmittance

The total transmittance spectra for different angles of incidence for the butterfly and moth are displayed in figures 5.4a and 5.4b respectively. Clearly the butterfly wing is more transparent. At normal incidence ($\phi_i = 0$) the first species has a transmittance between 80% and 96%, while for the moth it is between 59% and 92%. There is an apparent higher absorption in the near UV-vis range, which likely contributes to the moth's 30% variation in transmittance within the visible spectrum. This is consistent with the observations regarding the UV-vis spectra (section 5.2), where the moth wing showed larger absorbance.

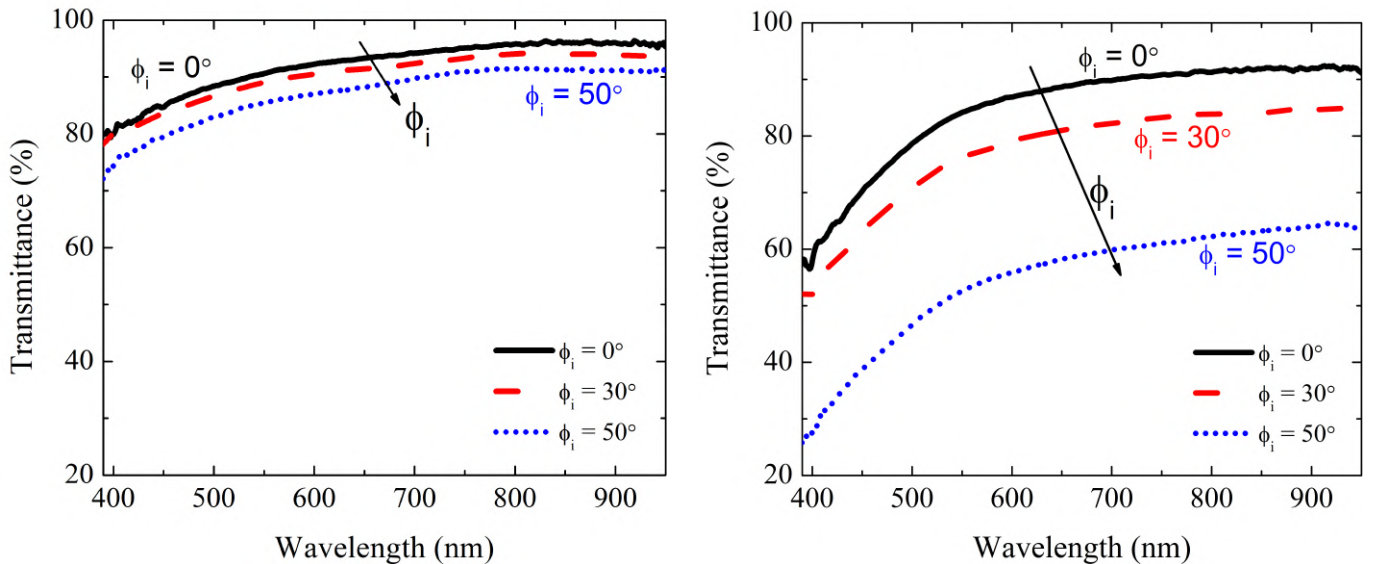


Figure 5.4: Total transmittance spectra at different angles of incidence for the a) *Episcada hymenaea* translucent butterfly and the b) *Saturniidae Heliconisa pagenstecheri* common moth.

One of the most notable differences becomes apparent when the angle of incidence is increased. The translucent butterfly's wing maintains a high level of transparency across all studied angles, with a decrease of less than 10% at any given angle. According to the principle of energy conservation, we have the relation $T_T + R_T + A = 1$, where T_T , R_T , and A represent total transmittance, total reflectance, and absorptance, respectively [22]. Note that the scattered light is either diffuse reflectance or diffuse transmittance and thus the S that appeared in equation 3.4 is included inside T_T and R_T . In this case, the absorptance A is expected to be small because there are no absorption bands in the visible range, implying that $T_T \approx 1 - R_T$. Therefore, a small reflectance corresponds to a high transmittance and the results are consistent with previous reports of low omnidirectional

reflectance in similar butterfly species [98, 136].

The moth species exhibits a significant decrease in transmittance as the angle of incidence increases, which can be attributed to two factors. First, when the angle of incidence increases, the light traverses a longer path through the sample, which increases the absorptance [1]. However, as the transmittance at normal incidence is high, specially for wavelength above 500 nm, indicating a small absorption coefficient, and the path length increases with the angle of incidence as the inverse of $\cos(\phi_i)$, this is not expected to be the primary cause of the decrease in transmittance. Instead, the decrease is primarily a consequence of increasing specular reflectance with higher angles of incidence, as predicted by the Fresnel coefficients [27]. Further, a larger angle of incidence can result in increased backscattered light for two reasons. First, as the path through the sample increases, the light beam interacts with more scattering centers. Secondly, the scattering cross sections may increase, but this depends on the exact geometry and orientation of the scatterers.

5.3.2. Total reflectance

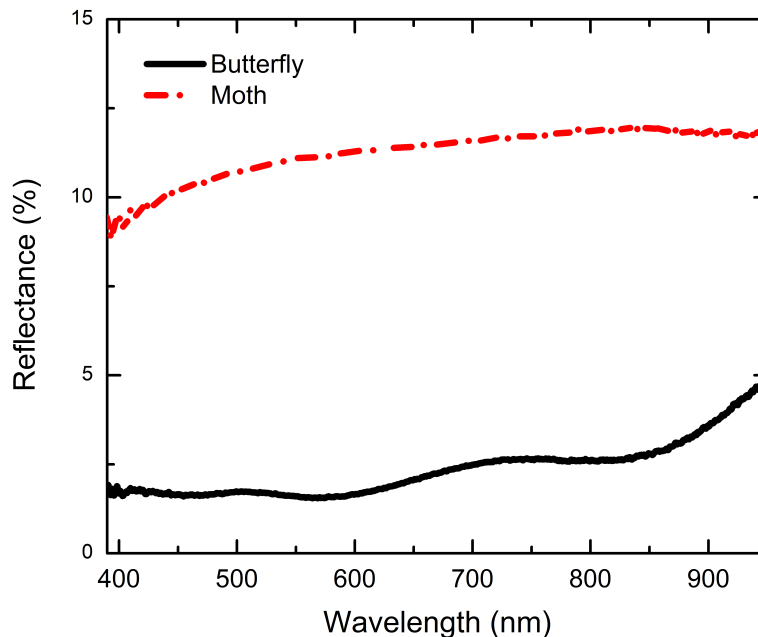


Figure 5.5: Total reflectance spectra of specimen 1 of *Episcada hymenaea* translucent butterfly and of Saturniidae *Heliconisa pagenstecheri* moth. The angle of incidence is $\phi_i = 8^\circ$

To investigate whether the decreased transmittance of the moth’s wing compared to *Episcada hymenaea* is indeed a result of increased reflectance, total reflectance measurements were conducted on both samples. The results are shown in figure 5.5. The total

reflectance of *Saturniidae Heliconisa pagenstecheri* is approximately 3 to 4 times higher than that of *Episcada hymenaea*. This disparity in reflectance accounts for the reduced transmittance observed and implies that the wing structures of the moth do not achieve as low an optical impedance as those of the translucent butterfly. Importantly, the reflectance is approximately constant over all the studied wavelengths in both species. As a consequence, the reflected light is mostly white, with a spectral distribution similar to the background illumination. Adaptive strategies based on tuning the reflection spectra to match the background illumination have previously been reported in other species [137–139].

5.3.3. Effective refractive index of the *Episcada hymenaea* translucent butterfly

To determine the effective refractive index for the wing of the *Episcada hymenaea* three specimens were tested, numbered 1 through 3. Sample 2 was big enough that allowed measurements in two regions of the transparent part. The other results reported in this chapter, unless otherwise stated, are all from sample 1. Total transmittance measurements at normal incidence were used, taken from the variable angle of incidence data, and reflectance at normal incidence was recorded. The procedure developed by Nichelatti [37] and described in section 2.5.1.2 was employed to obtain the real (n) and imaginary part (k) of the complex refractive index $\hat{n}_e = n - ik$.

The total transmittance and reflectance results at normal incidence for specimen 1 of the *Episcada hymenaea* are presented in figure 5.6a. As expected, the specimen shows remarkably high transmittance and low reflectance. It is clear that the transmittance exhibits a smooth profile, while the reflectance displays oscillatory behaviour, indicating the presence of interference effects and the departure from completely incoherent propagation, as assumed by equations 2.56 and 2.56. Although the oscillations are relatively small considering that the overall magnitude of reflectance is low, directly employing these spectra in the calculations would introduce non-physical oscillatory behavior in the index of refraction n . To address this, a smoothing technique was applied by fitting a line through the oscillations in the reflectance spectra, effectively accounting for the incoherent part of the propagation.

SEM images were available only for sample 1. Consequently, the exact thickness of the other specimens were not available, which adds to the difficulty of determining one value of thickness given the irregularities observed in the wing structure. Therefore, a thickness of 450 nm was assumed for all samples, a value in close agreement with those found in section 5.1. With said thickness and the reflectance and transmittance spectra, the effective refractive index was calculated. The obtained value was used as the input for

the transfer matrix method to model the spectra considering totally coherent propagation.

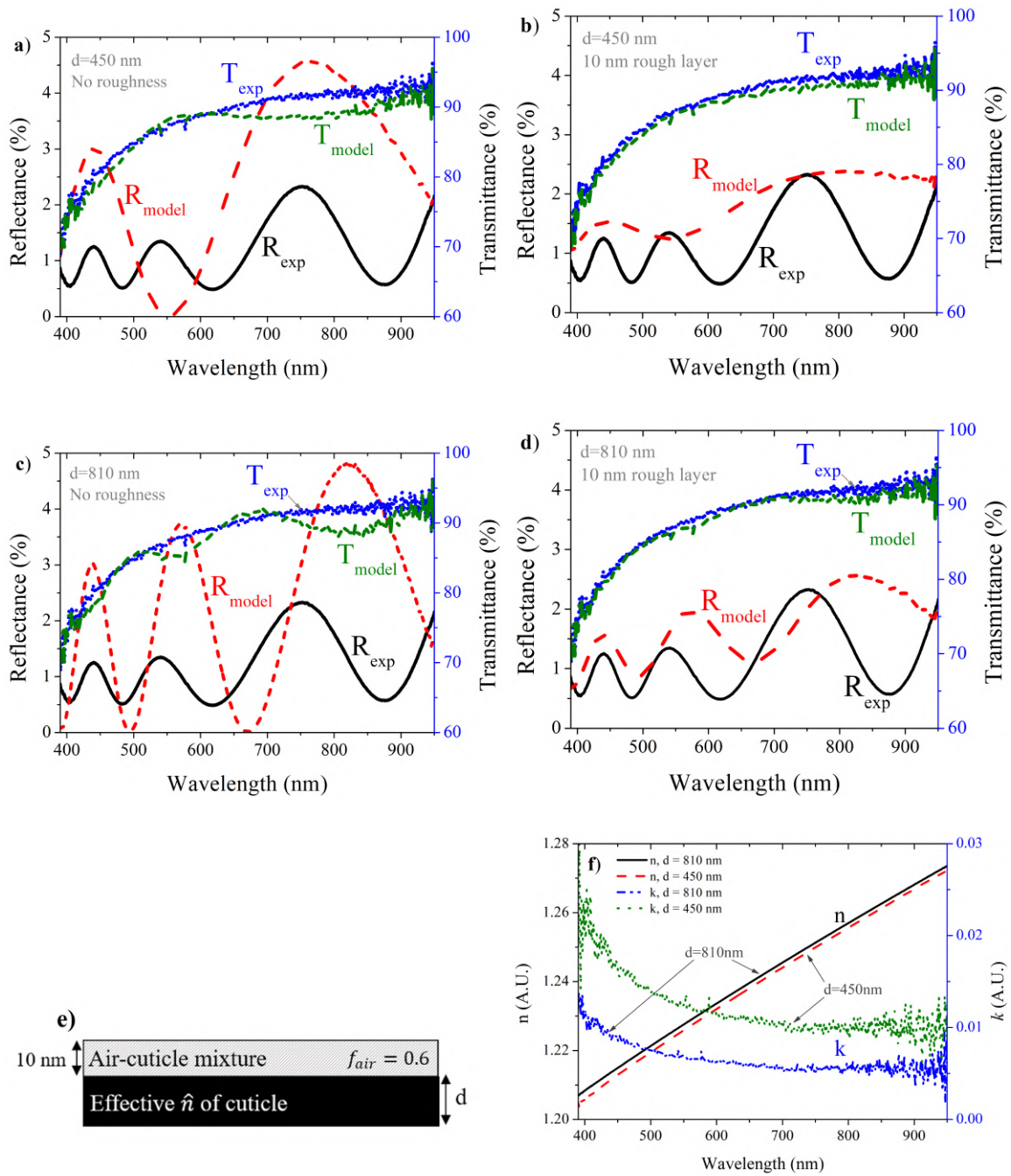


Figure 5.6: a-d) Experimental reflectance (black solid line) and transmittance (blue spheres) with the calculated spectra (dashed red and blue lines, respectively) using the obtained effective refractive index (\hat{n}) of the wing membrane for a smooth layer of thickness a) 450 nm and d) 810 nm. Models including a top roughness layer of 10 nm thickness composed of a membrane air mixture with air fraction equal 0.6 on top of a layer of membrane of thickness b) 450 nm and e) 810 nm). A schematic of the model described is shown in c). f) The obtained effective refractive indices obtained through Nichelatti's procedure for both thicknesses, where it is clear that the difference in the real part (n) is negligible.

The results for sample 1 are presented in figure 5.6a. It is clear that, except for the amplitude of the oscillations (which is addressed below), there is in general a good agreement between experimental and theoretical spectra. However, there are differences between the periods of oscillation in the reflectance spectra. For a given refractive index, the periods of oscillation depend on the thickness. To match the peaks, an iterative approach can be employed, where the thickness is modified until the periods match. A new, estimated thickness is used to recalculate the refractive index, which is then used to model the spectra. The process is repeated until good agreement between model and experiment is found. The process converges rapidly because the the index of refraction is only affected by the thickness through k , which is itself small.

For the case of sample 1 the procedure leads to a thickness of 810 nm, which generates the spectra presented in figure 5.6c. As seen from SEM images, this is not the real thickness of the wing. Therefore, it appears that the model is not enough to account for the exact propagation inside the samples. As will be seen in a later section (5.5), there appears to be polarization conversion effects induced by the structures in the wing of *Episcada hymenaea*. These effects are derived from scattering [140–144] or anisotropies [145–147], which are not accounted for in the model. As the departure is expected to be small considering the magnitude of the observed effects, the model still accounts adequately for most of the characteristics of the propagation, except the period of the interference oscillations displayed in the reflectance spectra. The deviations in amplitude are going to be addressed in the next paragraph. Notably, the departures are prevalent in reflectance which, as seen in section 5.5 is dominated by scattering. In any case, as can be seen in figure 5.6f, the thickness affects mainly the extinction coefficient, and the index of refraction is almost unaltered. For our purposes, we are interested in this last quantity, particularly because the absorption is extremely small in the visible region, and therefore the problem posed by the period of oscillations is of theoretical and not immediate practical interest.

While the experimental and simulated spectra exhibit similarities, it is noticeable that the interference oscillations obtained with the model appear more pronounced. The observed attenuation of interference oscillations in real samples is a well-known phenomenon attributed to coherence-reducing effects, such as interface roughness, inhomogeneities, and non-parallel surfaces [148–150]. Considering the surface characteristics observed in the samples (figure 5.1d), these effects are expected. To account for them, a common approach is to include a thin layer consisting of a mixture of the sample and air in the model, where light propagates incoherently [149]. The refractive index of this layer is determined using an effective medium approximation (EMA) [151]. The propagation in the stack of multilayers is calculated using the transfer matrix approach, adapted for incoherent propagation following previous works [39, 41] (see section 5.1d). In this study, the

addition of a top layer with a thickness of 10 nm and a refractive index calculated using the Bruggeman effective medium, with a fraction of air (f_{air}) equal to 0.6 (see figure 5.6e), yielded the results shown in figures 5.6b and 5.6d for 450nm and 810nm thickness (d), respectively. The inclusion of this roughness layer significantly improves the agreement with the experimental spectra, indicating that the propagation of light in the wings is only partially coherent.

The described procedure was repeated on three different specimens, along with two different regions within specimen 2. The results for the calculated index of refraction (n) and extinction coefficient (k) are displayed in figures 5.7a and 5.7b, respectively. In all cases the thickness that better matched the spectra was used (for example 810 nm for sample 1). As previously explained, the most reliable and interesting value in the context of this work is the index of refraction (n), which is almost unmodified with a change of thickness. Notably, the real part of the refractive index consistently exhibits values lower than those of chitin and chitosan [125], which are the primary constituents of the wing structure [122]. The obtained values range from 71% to 81% of the average refractive index (1.56) previously reported for butterfly chitin [128]. Further, there is good agreement with the average refractive index of 1.16 obtained by Saranathan et.al. [152] for other species from the *Papilionidae* and *Lycaenidae* families, particularly when compared with our results for sample 3 and sample 2 in zone 1.

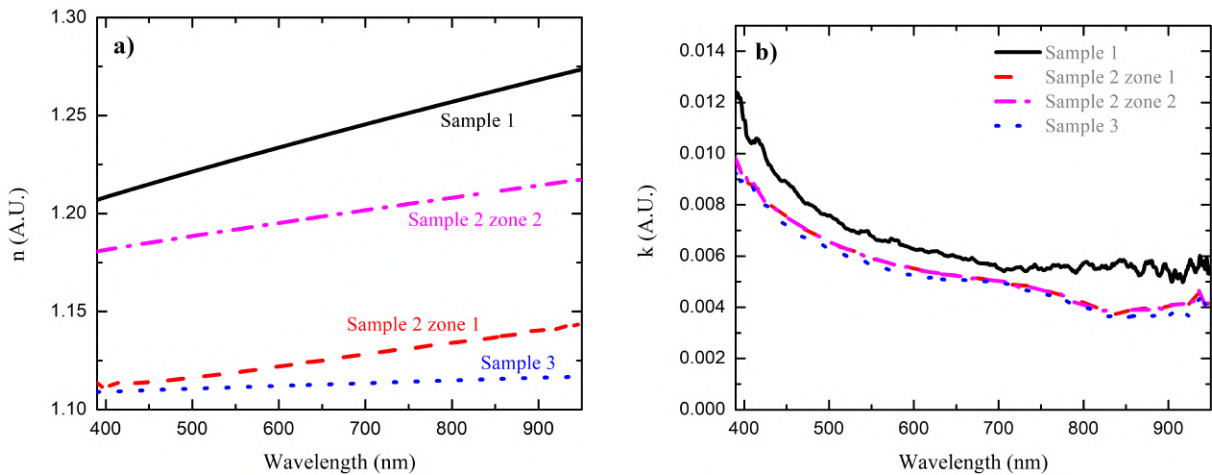


Figure 5.7: a) Real and b) imaginary parts of the calculated effective refractive index for the wing material following Nichelatti's procedure, for three different samples and two regions in sample 2. In all cases the thickness that better matched the spectra (better coincidence with the period of the reflectance spectra) was used.

The reduction in the effective refractive index of the wing structure compared to its constituent materials can account for the remarkable transparency observed in the *Episcada hymenaea* translucent butterfly, as it minimizes the refractive index mismatch

between the wing and the surrounding air. This effective refractive index value cannot be achieved through a simple mixture of chitin and chitosan, as it is bounded by the refractive indices of the individual constituents (section 2.6.1). This suggests that the low effective refractive index is a consequence of the nanostructures present on the wing. In other species it has been demonstrated that nanostructures can induce a gradual increase in refractive index instead of a sharp discontinuity, leading to a significant enhancement in transparency [153, 154].

Sample	A x10 ⁻⁵ (1/nm)	B	A ₀	q (nm)	y ₀
1	11.8	1.16	0.341	98.0	0.00546
2 zone 1	5.89	1.09	0.0280	257	0.00372
2 zone 2	6.49	1.16	0.0253	255	0.00316
3	1.44	1.10	0.0149	355	0.00274

Table 5.1: Best fit parameters for the complex refractive index, where $n = A\lambda + B$ and $k = A_0e^{-\frac{\lambda}{q}} + y_0$ with λ the wavelength of light in nm

To enhance flexibility and facilitate the utilization of the obtained refractive index in various calculations, the results were fitted using ad hoc functions. It is evident that the index of refraction exhibits an approximate linear relationship, while the extinction coefficient follows the shape of a decaying exponential. The first was fitted by the function $n = A\lambda + B$ and the extinction coefficient was fitted using $k = A_0e^{-\frac{\lambda}{q}} + y_0$. The parameters that best fit the data are shown in table 5.1. These functions allow other collaborations to use the data simply without relying on the exact calculated data set and, by smoothing the results, allows to more efficient computer calculations.

The spectra obtained with the calculated refractive indices exhibit excellent agreement with the experimental data at normal incidence, as can be seen in figure 5.6d. This agreement, however, is partially expected, as the refractive indices (\hat{n}) were determined from that same spectra. In order to further verify the results, we compared simulated and measured spectra of the dependence of total transmittance with incident angle. The results for sample 1, first discussed in section 5.3.1, are presented in figure 5.8. The model employed in the calculations consisted of a 10 nm layer of an air-sample mixture on top of an 810 nm thick layer with the calculated refractive index. The results exhibit good agreement with the simulations, particularly at near-normal incident angles. The primary deviation arises from interference oscillations, which become more pronounced as the angle of incidence increases due to the longer path traversed through the sample [36]. Introducing additional coherence-reducing effects into the model could further mitigate this effect.

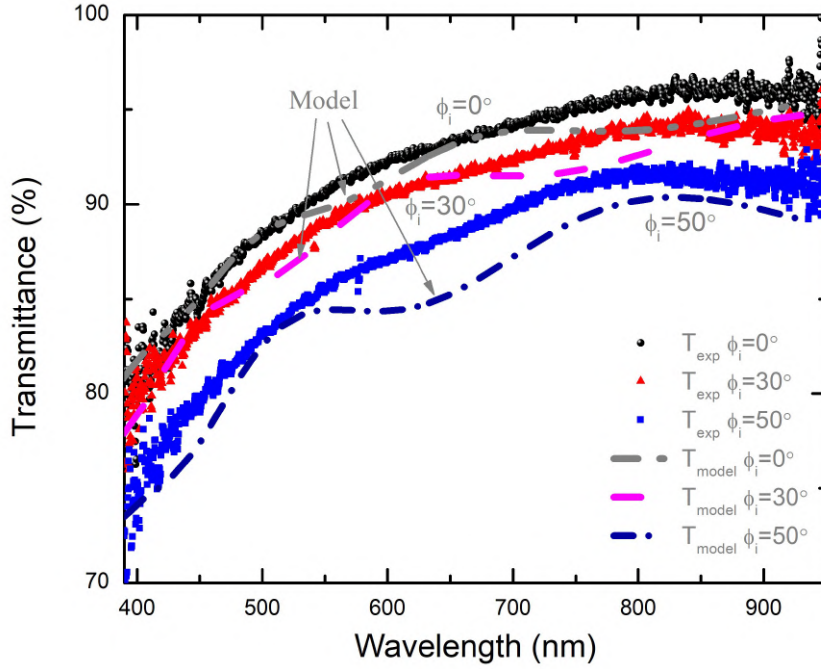


Figure 5.8: Measured angle dependant total transmittance spectra for sample 1 with the simulated results using the calculated refractive index assuming a layer of thickness 810 nm and an incoherent 10nm layer to account for roughness.

5.3.3.1. Gradient index model

A gradual spatial change in the refractive index as opposed to a discontinuity is known as a gradient index. It finds application in, for example, anti reflection coatings[155, 156]. This scheme has also been reported in several insect species[98, 157, 158]. We have mentioned that the higher than expected transmittance in the wings of the *Episcada hymenaea* could derive from the nanostructure observed on the wing surface. In this section we attempt a qualitative description of the effect using the transfer matrix method. Using the previously reported refractive indices of both chitin and chitosan [125] we will try different refractive index profiles and show that the gradient index approach can suitably describe the results.

The membrane of the wing is composed of both chitin and chitosan produced from the deacetylation of chitin [108, 109]. The ratio of chitosan to chitin is sometimes called the deacetylation factor [110]. To approach an index of refraction as low as that obtained from the experiments, it is expected that the deacetylation factor is large (the proportion of chitosan is large), because chitosan has a lower refractive index. An attempt to fit the proportion as a parameter results in a proportion of 1 (all chitosan). Previous reports have shown that the concentration of chitosan is between 0.6 and 0.8 in several organisms [159], so a deacetylation factor of 0.7 was employed in all calculations. This proportion could be later refined by chemical composition analysis, but it is not fundamental for the

qualitative understanding of the mechanism. In all cases a layer of total thickness 450 nm was considered.

As discussed in section 5.2 the absorbance of our sample is a lot higher than the one expected from chitin results presented in the literature, which exhibits negligible k . This, along with the small variations of n in the spectral range, means that the response is mostly flat, with no drop in transmittance towards the blue region. However, our experimental results do show this decrease with lower wavelengths, and thus the reported refractive indices are not entirely suitable. To address this issue we fitted the absorption coefficient obtained from the absorption spectra considering a 450nm thick wing with a Lorentzian curve, which partially models the index of refraction with the Lorentz Oscillator model [1, 22]. The model is only partial, or ad-hoc, because the real part of the refractive index was not derived from the model: the n reported by Azofeifa and others [125] was employed. The fitting was very good ($R^2 \approx 0.99$, see appendix D for details). While only k is obtained from the application of the oscillator model to our results, it is possible that the index of refraction follows the Kramers-Kronig relations [22] if other absorptions are present outside of the measurement region. It is more likely that the “absorption” we are assigning to chitin is either due to another compound in the wing or actually modeling the effects of scattering. The second option is less likely because the drop is observed in total transmittance, which accounts for the scattered light and that, coupled with the almost constant reflectance (figure 5.5, suggests that there is absorption in the blue region). A more detailed chemical characterization of the wing could determine if the absorption we are ascribing to the chitin is actually of another compound. There are reports of other butterfly species having lipids or a wax coating on the surface of their wings [115, 160, 161] which could cause the higher absorption. For our purposes we consider the indices of refraction of chitin and chitosan reported by Azofeifa et.al [125] and use the calculated extinction coefficient for chitin.

As a baseline for comparison we first model a bulk layer of chitin-chitosan mixture. The transmittances at angles of incidence of 0 and 40 degrees are shown in figure 5.9a. While the general shape and the difference between the two angles of incidence are similar to the experimental results, the transmittance for the single layer is around 9% lower. This appears to confirm the fact that the constituents themselves are not sufficient to account for the high transparency of the wing and that there are morphological effects at play.

How do we account for the effects of the nanostructure? From the SEM images (figure 5.1c) there appears to be a region of the wing, approximately 110 nm thick, where the membrane and air coexist, placed over a region of solid membrane. Further, due to the shape of the lobes in the intermixing region, it seems that as we move further into that region towards the bulk of the membrane, the fraction of air decreases. This general

observation is consistent with the idea that a gradual decrease in refractive index is responsible for the remarkably high transparency. Now the question is how do we model the mixture at different points in the top layer. We start with the simplest possible approach: linear mixing. A reasonable supposition is that the top of the layer is composed entirely of air, at least in the first nanometers, and the bottom entirely of chitin-chitosan mixture. We consider that the decrease in air is linear, and discretize the values by considering 100 layers. This means that each layer is 1.1 nm thick, which is way beyond our resolution, making the suppositions valid and resulting in a smooth enough profile while not being computationally intensive.

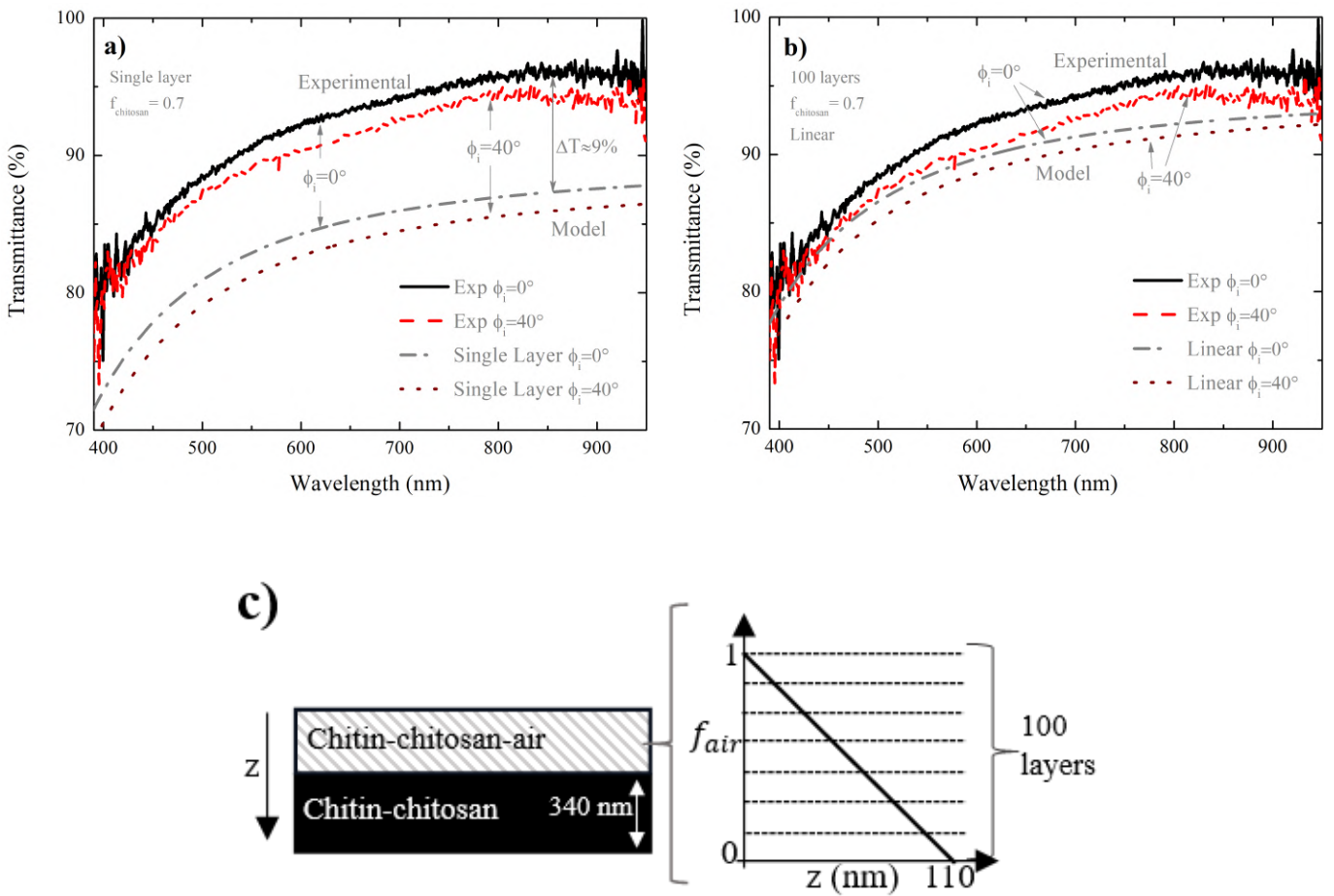


Figure 5.9: a) Transmittance spectra of a single layer of chitin-chitosan with $f_{\text{chitosan}} = 0.7$ and experimental results, both for 0 and 40 degrees incident angle. b) Calculated spectra with the linear mixing model compared to experimental data, a schematic of the model is shown in c)

A schematic of the model and the results are shown in figures 5.9c and 5.9b, respectively. It is clear that this configuration better represents the experimental results. The transmittance is considerably higher and the difference between the two angles is of inci-

dence is smaller, approaching the experimental values. From this simple model it is clear that the air-membrane layer plays an important role in the transparency characteristics of the wing of the *Episcada hymenaea*.

Now we want to implement a more refined model that accounts for the observed morphology of the wing. We see that the mixing region is formed by lobes of different shapes and sizes and that the thinner lobes are taller. Following the work of Siddique et al. [98] we introduce randomness by generating different profiles with a parameter sampled from a probabilistic distribution, calculating the spectra for each and then averaging over the results. However, unlike that work, no clear shape of the structures can be distinguished from the images. As an approximation we consider the profile of the lobes to follow a Gaussian shape. It is a well defined and studied profile, which allows simple inversion, and depends only on a single parameter—the standard deviation (σ). Crucially, it has “built-in” that a wider shape (larger σ) is less tall, just as is observed in the lobes, assuming constant total area. A representation of the model and workflow are shown in figure 5.10a. We consider the maximum of the cell (probability density 1 in a standard normal distribution) to be 110 nm, and know that the width (w) of a Gaussian at any height (h) is given by equation 5.2 (Appendix D). To convert from width to fraction of chitin-chitosan we consider that the total width of the cell is four standard deviations (4σ), which includes around 95% of the total area of the membrane. We choose this instead of 6σ to try and account for the fact that close to the solid membrane layer it appear that the lobes overlap. Then for that height the fraction of chitin-chitosan mixture to air is given by equation 5.3. For heights greater than the maximum height of the curve (h_c), where the width is not defined, we have air ($f_{ch} = 0$). We again discretize the values by considering 100 layers dividing the Gaussian profile.

$$w(h) = 2\sqrt{-2\sigma^2 \ln(h\sigma\sqrt{2\pi})} \quad (5.2)$$

$$f_{ch} = \frac{w(h)}{4\sigma} \quad (5.3)$$

As mentioned, to account for the random shapes we sample the parameter σ from a statistical distribution. To obtain this we measured the width of the lobes at approximately the middle of its height (L_{FWHM}) and obtained its sigma (sigma measured, σ_m) from equation 5.4, where we used the fact that the FWHM of a normal distribution is given by $FWHM = 2\sqrt{2\ln 2}\sigma \approx 2.355\sigma$ and we normalized by the height of the cell (110 nm). The histogram with the results for the distinguishable lobes appears in figure 5.10b. The most frequent values are around 0.2 and 0.7 and so, to simplify the calculations, given the low number of sampled lobes, we sample the value of σ in the model from a uniform

distribution between those bounds.

$$\sigma_m = \frac{L_{FWHM}}{2.355} \frac{1}{110} \quad (5.4)$$

In the first step the parameter is sampled, and then the transmittance is calculated for that profile. This is repeated 1000 times and the final transmittance is calculated as the average over the transmittance profiles. The results for this approach appear in figure 5.10c. We see that the results are slightly better than the linear model, specially at lower wavelengths. This suggests that to achieve a better reproduction of the experimental results, it is a suitable approach to model the mixing region considering the specific morphology.

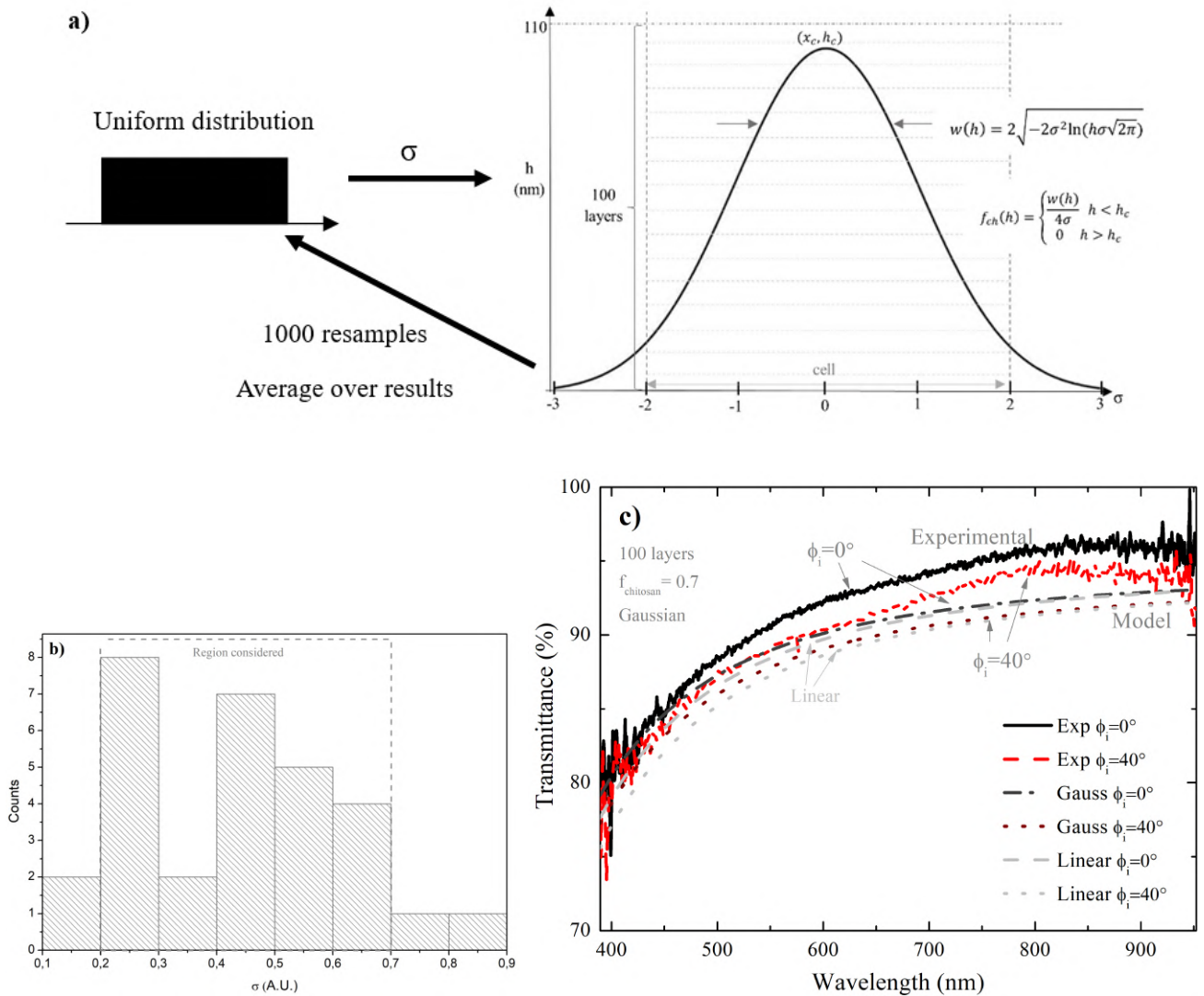


Figure 5.10: a) Schematic of the Gaussian profile approach for chitin-chitosan-air mixing. b) Statistic of the measured standard deviation (σ_m) of the lobes in the wing surface and c) Results of the model after averaging over 1000 profiles. For comparison with the linear model see the light gray dashed and dotted lines.

The results could be improved with a better understanding of the specific profiles. This could be done by taking images over other regions of the sample, which would improve the statistical analysis and allow for a more precise sampling of the σ parameter in the model. Further, this could also allow to better determine the specific shape of the lobes, specially if images of the cross section were available. Another approach is to determine experimentally the profile of the lobes, instead of modelling them with a mathematical curve. The volume fraction at varying depth can be obtained from SEM images by threshold segmentation computations [162, 163]. It is also possible to determine the profile by AFM [164, 165]. However, as the membrane is brittle, cantilever can damage it. To protect it, a very thin layer of a protective metal can be sputtered, and then the profile can be corrected for the excess thickness introduced.

5.4. Scattering Properties

In previous sections we have discussed the total transmittance and reflectance properties of both the *Saturniidae Heliconisa pagenstecheri* moth and the *Episcada hymenaea* translucent butterfly. While those refer to the total magnitude, it is important to consider the angular distribution of light. If the reflectance is very diffuse, meaning that most of the light is scattered, the reflected intensity can be distributed in a very wide angle. As a result, within the solid angle covered by a detector (the eye of a predator for example), which may only encompass a fraction of the angular distribution of reflected light, the actual intensity can be significantly lower than what would be predicted based on total reflectance. A schematic of the situation is shown in figures 5.11a and 5.11b. Conversely, when looking at the transmitted light through a highly scattering specimen, the resulting blurred spot can suggest the presence of an object.

To evaluate these aspects, we studied the haze, defined as the ratio of diffuse to total light, in both reflectance and transmittance, at $\phi_i = 8^\circ$ and $\phi_i = 0^\circ$, respectively, using the capabilities of the integrating spheres described in section 3.1.

The haze in reflection is displayed in figure 5.12c. Both species display the same general trend and remarkable scattering properties. In effect, most of the light is scattered instead of specularly reflected. The preponderance of diffuse light has previously been reported on other butterfly species [166, 167]. The wing of the *Episcada hymenaea* is around 10% more diffusive than the moth's. The spectral composition of the scattered light can be better understood by looking at the diffuse reflectance spectra (figure 5.12a). In the whole spectral range both samples display an almost flat response, meaning that the scattered light is mostly white. While the moth only shows a variation of 1.5%, the butterfly wings have a 3% variation. However, notice that in the visible range (up until around 750 nm)

is only $\approx 1\%$. The increase in diffuse (and total) reflectance in the infrared region could be related to thermal regulation as previously reported for other species [107, 111, 168].

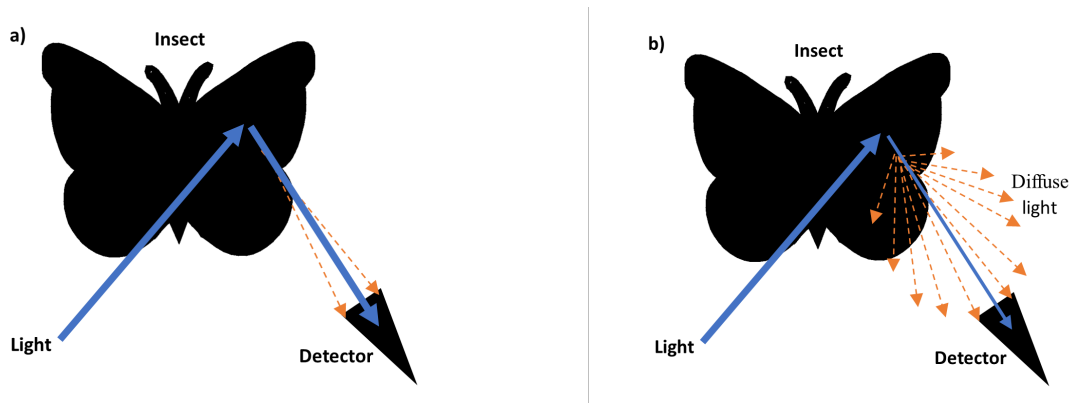


Figure 5.11: Schematic of the reflection process for the cases of a surface with a) low scattering and b) high scattering. The thickness of the arrows represents the amount of light. The width of the arrows represent the intensity of light. Solid and dashed arrows correspond to specular and diffuse components, respectively. In the high scattering case, b), a large fraction of the reflected light is deviated from the main beam and is not incident upon the detector

The behaviour changes dramatically when we consider the haze in transmittance, displayed in figure 5.12d. The translucent butterfly has very low haze, between 5% and 8%. Further, the response is quite flat, meaning that approximately the same fraction of light is scatter for all wavelengths. Coupled with the flat response in transmittance presented in section 5.3.1 this implies that both the diffuse and specular components are mostly white, improving the insect's ability to blend with the background illumination. For a cleared picture consider figure 5.12b, where we observe a total variation of 4% in the measured range, with a $\approx 2\%$ difference in the visible.

The scattering properties in transmittance of the wing of the moth are very different. The scattering varies between 40% near the blue region of the spectrum, to 25% in the near infra-red. The scattering is considerably higher than those of the translucent butterfly, decreasing the perceived transparency. The response is not flat, it varies around 15% in the considered wavelength range. However, the increased scattering near the blue region compensates the reduction in transmittance due to absorption, resulting in mostly white diffused light. This can be verified in the diffuse transmittance, displayed in figure 5.12b, where the total difference in the range is only 6% and around 5% in the visible.

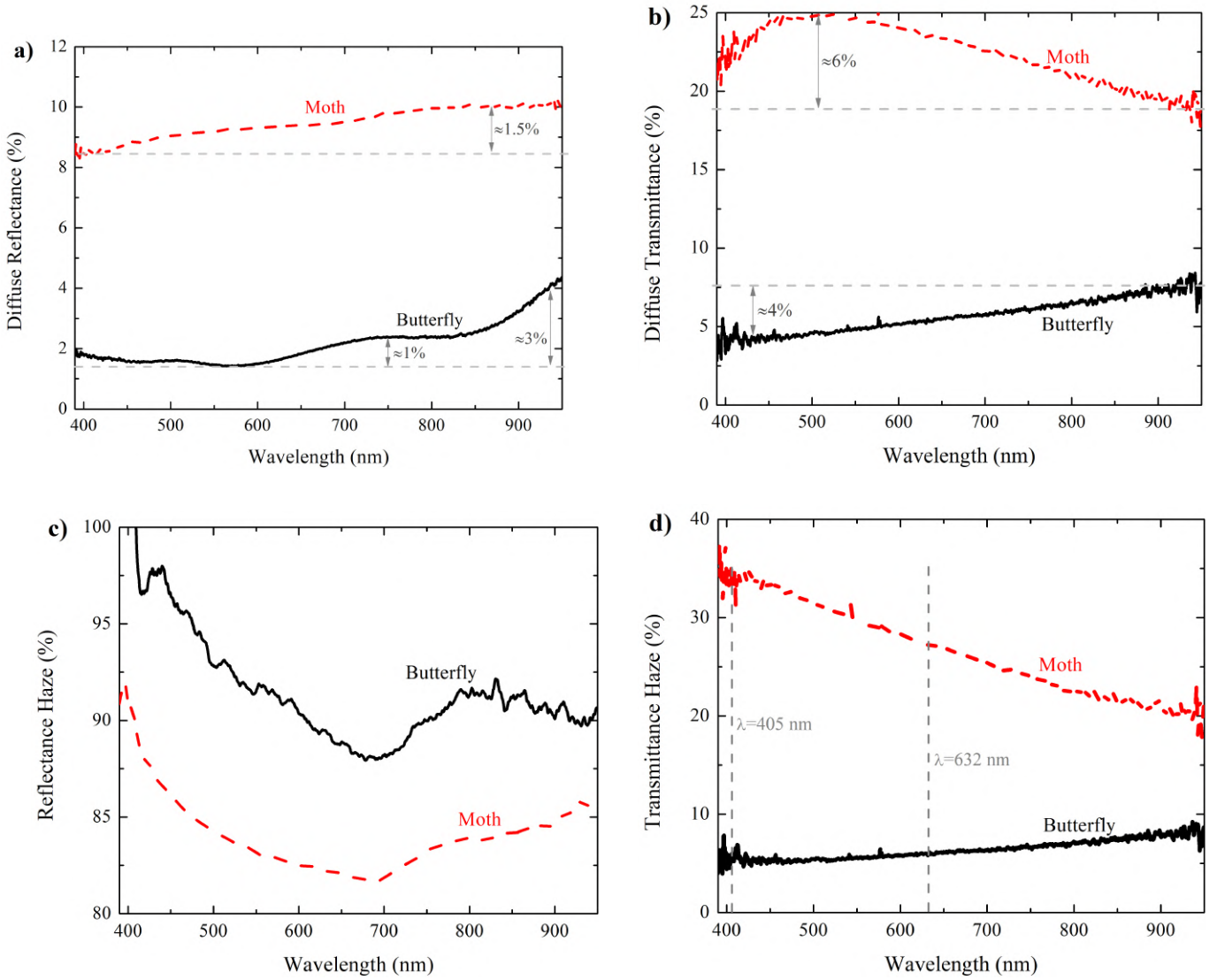


Figure 5.12: a) Diffuse reflectance at $\phi_i = 8^\circ$, b) diffuse transmittance at $\phi_i = 0^\circ$ c) Reflectance haze, obtained from measurements performed at an angle of incidence of $\phi_i = 8^\circ$ and d) Transmittance haze at normal incidence ($\phi_i = 0^\circ$). Notice the vertical grey dashed lines, which indicate the wavelengths that will be used in the angle resolved transmittance measurements.

In order to gain a better understanding of the scattering behaviour of the samples, angle resolved transmittance measurements were performed with two different wavelength of light: 405 and 632 nm. Notice that the wavelengths are indicated in figure 5.12d for comparison. For a description of the setup see section 3.2.3. The wing of the *Episcada hymenaea* translucent butterfly yielded a prominent point centered at 0° , which immediately dropped off to negligible values within experimental uncertainty (around 1°). This is reasonable considering the low haze in transmittance previously discussed. Of substantially more interest are the results for the wing of the moth, presented in figures 5.13a and 5.13b. Notice that the inset in the latter shows a schematic with the definition of

the incident (ϕ_i) and measurement (θ_a) angles. For both wavelengths it is noticeable that not all light is concentrated in one position, but rather is distributed around the main beam. The data points were fitted with either Gaussian or Lorentzian functions in order to estimate the spread through the function's width (FWHM). The widths are indicated in the figures with grey double sided arrows. It is clear that the peaks are wider for lower wavelength and that it tends to increase with increasing angle of incidence.

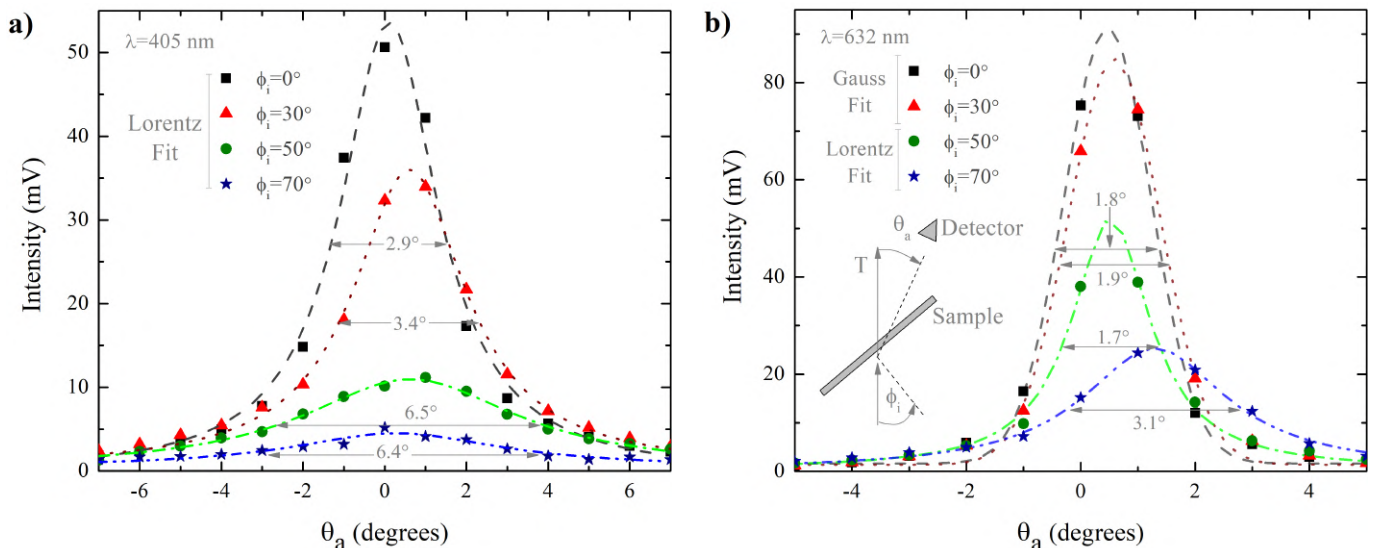


Figure 5.13: Measured intensity for monochromatic transmittance through the moth sample around the main beam position for different angles of incidence. In a) the incident wavelength is $\lambda = 405$ nm and all the data sets were fitted with Lorentzian curves in order to estimate the FWHM. In b) the incident wavelength is $\lambda = 632$ nm and some data were fitted with a Gaussian curve, the fitting curve used are indicated next to the legend. The insert shows a schematic of the experimental setup.

Total diffuse transmittance and angular spread of the scattered light are not exactly the same, because in theory diffuse light could still be extremely concentrated in a particular direction, just not along the direction of directly transmitted light [24]. However, it is reasonable to expect that a highly diffusive sample also spreads light in a wide angle. With this in mind we see that the results shown in figure 5.13 are in good agreement with the the haze measurements. From figure 5.12d we see that the sample is more diffusive for blue light, which can be correlated with the increased width of the curves for 405 nm compared to 632 nm, for all angles of incidence. This is expected given that the lower the wavelength, the larger the relative size of the scattering centers in the wing, which increases the scattering cross section [169, 170]. The decrease in intensity with increasing angle of incidence can be correlated to reduced transmittance, as shown in figure 5.4b. However, nothing can be concluded from the difference in intensities for different wavelengths, because this is also related to laser power.

Further, it is clear that for both wavelengths the width of the fitted curves increases when the angle of incidence increases. This can be related to the larger path length through the sample, which means interaction with more scattering centers. Nevertheless, it is also possible that this is a consequence of the scattering properties of the scatterers themselves, such as dimensions, size distributions and orientation relative to the wing’s surface, as these determine the angular dependence of the scattering cross sections [169, 171]. There also appears to be a small shift in the position of the maximum of the curves, away from 0° which is not expected from theory [172]. The shift is not significant in this experiment, because it is well within experimental resolution.

5.5. Behaviour of the butterfly wings under polarized light

In this section we discuss the properties of the *Episcada hymenaea* wings under polarized light. We begin with the spectral direct transmittance measurements, where we observe a peculiar behaviour—they do not follow what is expected for homogeneous isotropic media. Then we characterize the polarizations at specific wavelengths for different angles of incidence, and again find a departure from the predictions of Fresnel coefficients. We present a possible pathway to model this behaviour, and discuss differences between probing with collimated, monochromatic light from a laser and white light from a lamp. Finally we exploit the observed phenomena to unveil interference oscillations in the crossed transmittance spectra and use them to obtain the thickness of the sample in excellent agreement with the one determined from SEM images.

5.5.1. Spectral direct transmittance

The transmittance spectra for both direct configurations (aligned polarizer-analyzer pair) T_{11} and T_{22} at different angles of incidence appears in figure 5.14. The shape of the spectra is similar to the total transmittance spectra presented in figure 5.4a, but the magnitude is lower, specially for higher angles of incidence. This deviation can be explained by the fact that this configuration does not capture the total light transmitted: some is not incident on the detector due to scattering effects.

What is surprising from these results is that both polarization configurations almost “mimic” each other. Not only that, the transmittance decreases monotonically as the angle of incidence increases. This is not the expected behaviour from the Fresnel coefficients calculated from the constituents, where one polarization tends to increase and the other decrease as Brewster’s angle is approached [27] from normal incidence. This extends to

the calculations from the TMM for isotropic homogeneous media, as can be seen in figure 5.15a for the gradient index model presented in section 5.3.3.1 and in figure 5.15b for a layer of the effective refractive index for sample 1 calculated in section 5.3.3. As shown, those models capture most of the behaviour under white light, where the total transmittance is relevant. However, it is evident that they do not represent at all the effects when considering polarized light. While the effective refractive index better approximated the values, it still has an initial increase in one of the polarizations when increasing the angle of incidence from 0° (see inset). This inconsistency suggests that there are other polarization mechanisms that this model can not account for.

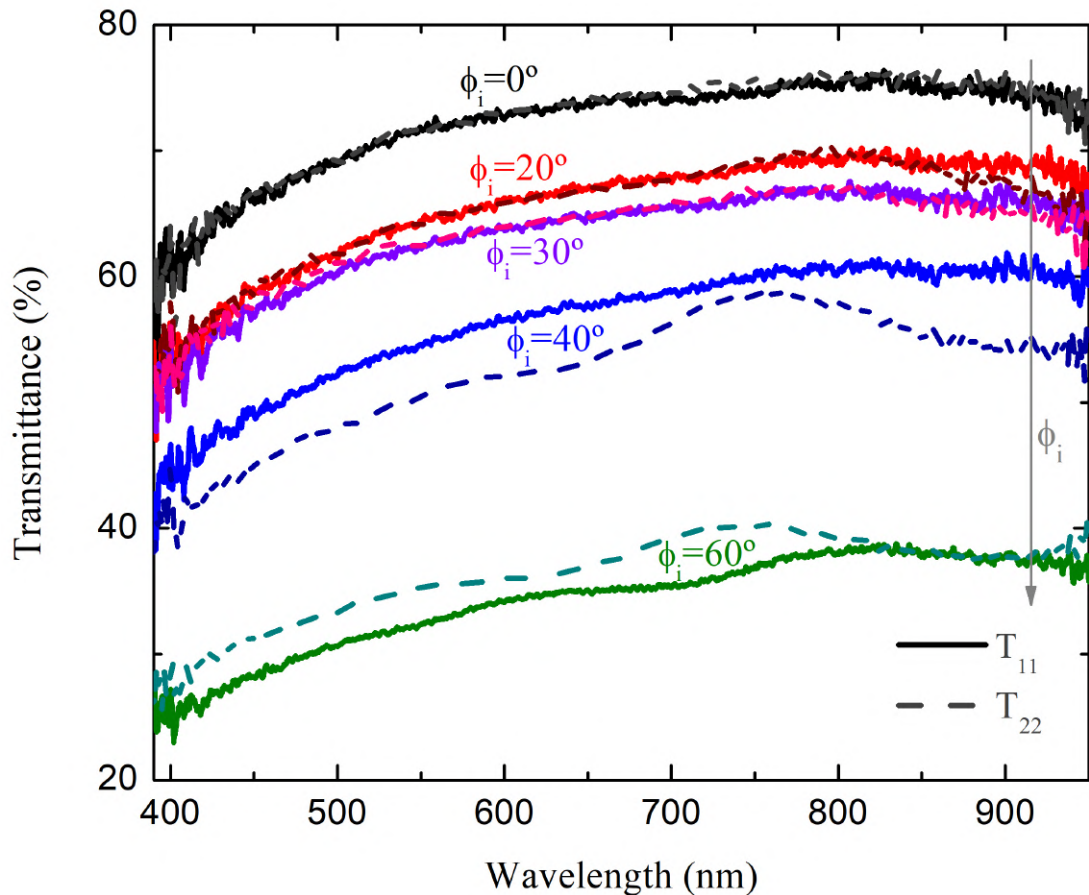


Figure 5.14: Direct transmittance spectra for both configurations and different angles of incidence. The full lines correspond to the configuration 11 (T_{11}) and the dashed lines to T_{22} . Note that both polarizations mimic each other, a behaviour that is not expected from the Fresnel coefficients, that assume isotropic homogeneous surfaces.

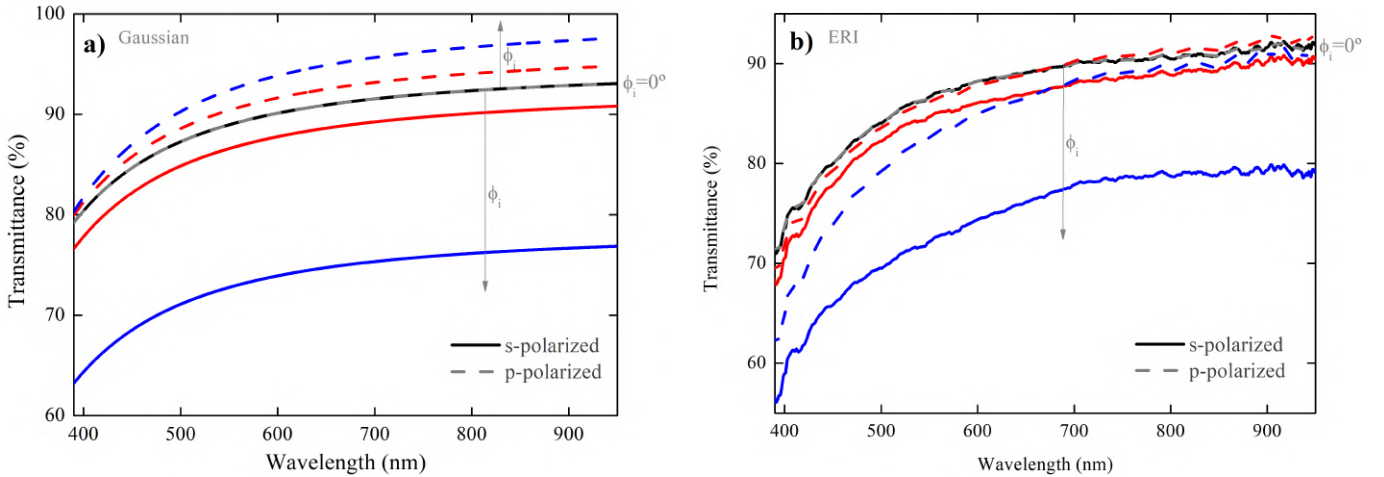


Figure 5.15: Modeled transmittance of each polarization using the TMM for a) Gaussian gradient index and b) the effective refractive index (ERI) previously calculated from reflection and transmission spectra. Solid lines correspond to s-polarized light and dashed lines to p-polarized. Black and grey lines are for $\phi_i = 0^\circ$, while red and blue are for $\phi_i = 30^\circ$ and $\phi_i = 60^\circ$, respectively.

5.5.2. Variable angle transmittance under laser illumination

Given the curious nature of the polarized transmittance spectra presented in the previous section, we wanted to test the wings of the *Episcada hymenaea* using a laser. The high coherence and collimation of the laser makes it less sensitive to alignment issues and allows for a smaller spot size, which means less influence from macroscopic inhomogeneities. Further, the alignment of the beam is not as critical in this setup because it uses a photodetector, which is less sensitive to alignment than the collimator, which needs to correctly couple the light to the fiber.

The results are displayed on figures 5.16a and 5.16b. Clearly for both wavelength the direct polarizations follow each other, as was observed in the previous direct spectra. Further, we see non negligible crossed polarization signals which suggests that the sample is somehow rotating the polarization direction of the incoming beam.

These polarization behaviour suggests that there are polarization conversion effects present, as was reported for other butterfly species [94–97, 102, 161]. It is possible that there are slight anisotropies that introduce a phase difference between the polarization components that results in increased cross polarization transmittance.

The TMM developed in the majority of this work is for isotropic samples and thus can not account for polarization conversion effects. As a first attempt of an explanation, we want to know if indeed an anisotropic structure can produce similar results. To do this, we implemented in Matlab a transfer matrix method for anisotropic media (TMMA) developed by Berreman and others [173–176]. This model employs the same logic as the

TMM for isotropic media but makes use of 4x4 matrices because of the need to track the electric and magnetic fields separately. In this case only isotropic propagation was implemented. Seven parameters are needed to define each layer: the refractive indices along the principal axes (3), the Euler angles [177] that indicate the orientation of the principal axes relative to the lab axes (3) and the thickness of the layer.

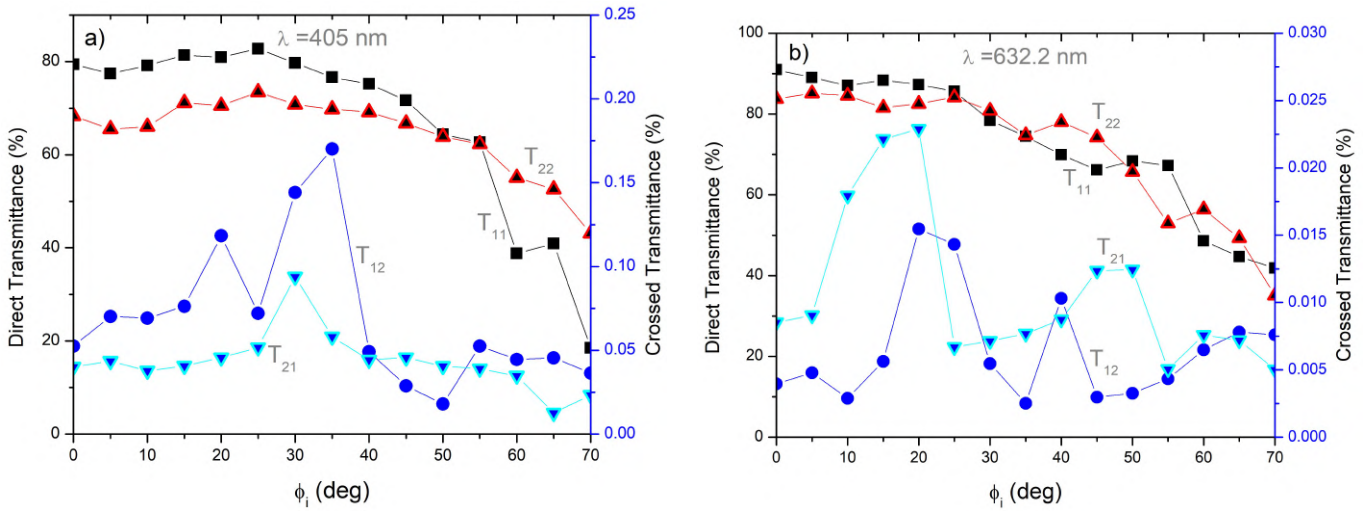


Figure 5.16: Direct and crossed transmittance spectra as a function of the angle of incidence (ϕ_i) probed with a laser of wavelength a) 405 nm and b) 632.2 nm

As a first estimation we consider a stack of two layers, the first of 110 nm thickness and the other of 350 nm. Both have the refractive index of chitin along the \hat{x} and \hat{y} directions and that of chitosan along \hat{z} . The previous values from the literature were used. The Euler angles (α, β, γ) are $(45, 45, 0)$ and $(-45, -45, 0)$ for the top and bottom layer, respectively. A schematic is shown in figure 5.17c. The results for both wavelengths are displayed in figures 5.17a and 5.17b. Note that the total transmittance is shown for each polarization for clarity. The total transmittance at the output is simply the sum of the direct and crossed polarized transmittances that match the first index (i.e. $T_1 = T_{11} + T_{12}$). We see that with this model it is indeed possible to have both polarization directions mimic each other, which is not possible from the isotropic model—see the result expected from the isotropic model for a single layer of chitin-chitosan also shown in figures 5.17a and 5.17b. The modelled and measured transmittances are relatively close, particularly at 405 nm. The model has interference oscillations that are not present in the spectra because it considers coherent propagation only.

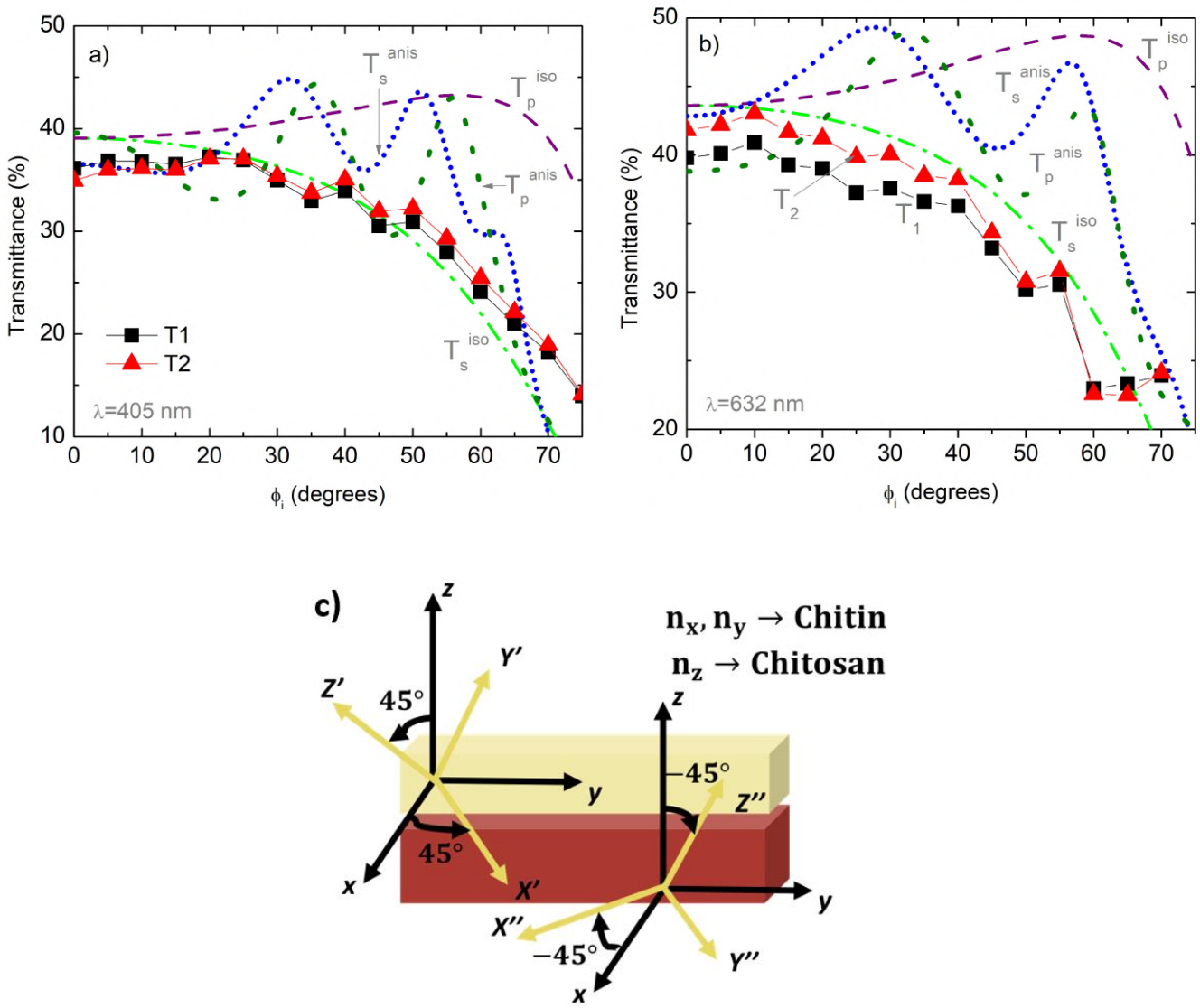


Figure 5.17: a) Polarized transmittance as a function of the angle of incidence at a) 405 nm and b) 632.2 nm. Shown are the experimental data for the total polarized transmittance ($T_i = T_{ii} + T_{ij}$), with T_1 in black squares and T_2 is red triangles. The results from the isotropic model (iso) are shown with dashed and dot dashed lines, while the spectra calculated with the anisotropic (anis) model are shown with dotted curves.. In c) a schematic of the model used for anisotropic calculations.

We can not say that the model is a good representation of the real structure. However, what it does show is that anisotropy can cause the observed transmittances, by allowing orthogonal polarizations to mimic each other, something which is not possible if the layers are isotropic. This variable rotation of the principal axes of the material at different depths is reminiscent of twisted media, something that has been reported in other insect species [152, 161, 178, 179]. While this structure could exist in the wings of the *Episcada hymenaea*, a lot more work is required to assert it.

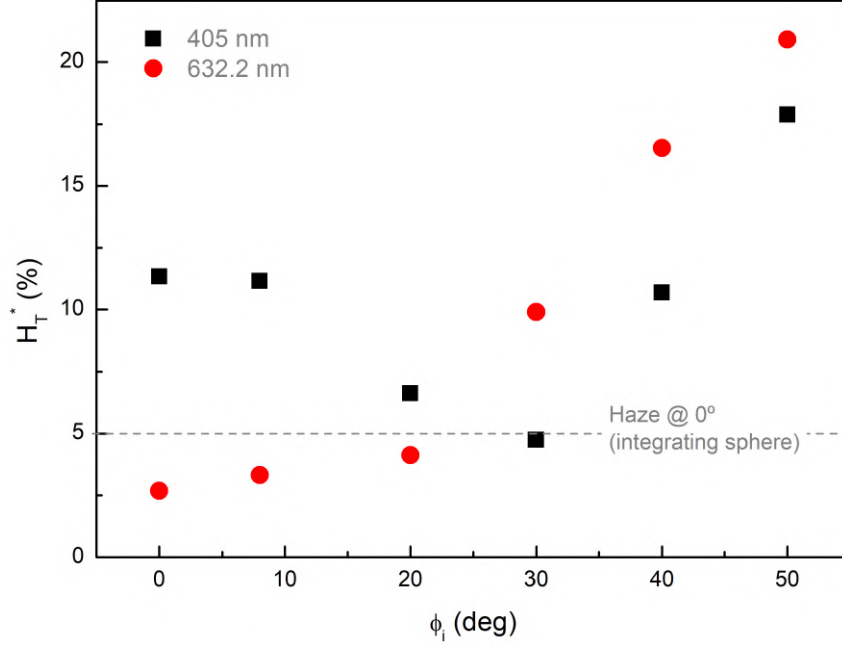


Figure 5.18: Estimation of the haze as a function of the angle of incidence. For reference, the value obtained with the integrating sphere ($\phi_i = 0^\circ$) for low wavelengths is shown (horizontal dashed line)

As the laser detection system is less sensitive to alignment issues, we can use the results to approximate the haze in transmittance at angles of incidence different than 0° , which was the only one available with the integrating sphere. As the silicon detectors are relatively far from the sample, we can consider the measured light to be the specular component (T_E , specular transmittance). The haze is defined as $\frac{T_D}{T_T}$. The diffuse transmittance is equal to the total transmittance minus the specular transmittance, so we have $HT = 1 - \frac{T_E}{T_T}$ (see section 2.2.2). If we take T_T as the measurement with the integrating sphere, we obtain the results shown in figure 5.18.

These are not necessarily the values of the actual haze, because this is defined in terms of a specific solid angle encompassed by the detector, and there are differences between experimental setups. This is why we name this estimate H_T^* . Now, as the setup and solid angle encompassed by the detector is the same for all angles, the basic tendencies are expected to be accurate. Note that the estimated haze is similar to that obtained with the integrating sphere, specially for $\lambda = 632$ nm. For this wavelength the haze increases slowly until roughly 20 degrees and then increases rapidly, whereas blue light is less scattered when the angle of incidence increases, until around the same angle, and then increases with a slope similar to the one for red light. The fact that the slope changes at around the same angle for both wavelengths suggests that it could be associated with the dimensions or orientations of the scatterers. This would be a very interesting aspect to study in another work.

5.5.3. Crossed Polarized transmittance

After observing polarization conversion effects in the results presented in the previous section, we opted to study the crossed polarized transmittance spectra of the wings. The results are shown in figure 5.19a and 5.19b for the configurations T_{12} and T_{21} , respectively. An intriguing observation, in line with the results presented in figure 5.17, is the rise in transmittance when the sample is positioned between the polarizers, a effect that becomes more pronounced with an increasing angle of incidence. This phenomenon implies that the sample induces a rotation in the polarization direction of the incident light, leading to an enhanced projection of light in the orthogonal direction. A material causing a rotation in the plane of polarization of linearly polarized light is termed optically active [180]. Earlier studies have documented optical activity in the wings of various butterfly species, coupled with angle-dependent polarization conversion effects [94–97].

Recent research has documented optical activity in both chitin [181] and chitosan [182]. Additionally, several studies have unveiled polarization conversion effects originating from nanostructures present in the wings of various butterfly species [94–97]. The tiny bristles or micro-hairs found on the transparent portion of the wing (figure D.1) closely resemble the organized structures seen in those species. It is conceivable that these bristles contribute to the rotation of polarization, as the incident light spot, with a diameter of about 2 mm, interacts with several of them. Another study presented fascinating polarization-dependent transmittance in the transparent part of the wings of the *Chorinea sylphina* species [85], which lacks reticular structures in the bulk of its wing but is covered with scales resembling the bristles observed in our species. The precise nature of the optical activity in the *Episcada hymenaea* is presently under investigation. It remains an open question whether it stems from metastructures, the arrangement of the constituent molecules, or a combination of both.

Interference oscillations appear as the angle of incidence increases. These were not present in the direct spectra, and do not appear in the lamp signal (purple dashed curve), measured with the same setup. This oscillations, akin to the ones described in section 2.5.1.1 suggest that it is possible to apply equation 2.54 to obtain the thickness of the wing membrane. Indeed, the wings of the *Episcada hymenaea* demonstrate a significant level of uniformity at visible wavelengths, especially within the layer’s bulk (figure 5.1). Notably, both chitin and chitosan show minimal frequency dependence (low dispersion) of the refractive index within the examined spectral range, along with negligible absorption [125, 128]. Additionally, the expected polarization conversion effects, crucial for the emergence of the oscillations, are anticipated to be small. Taken together, these factors make the use of equation 2.54 a reasonable approximation.

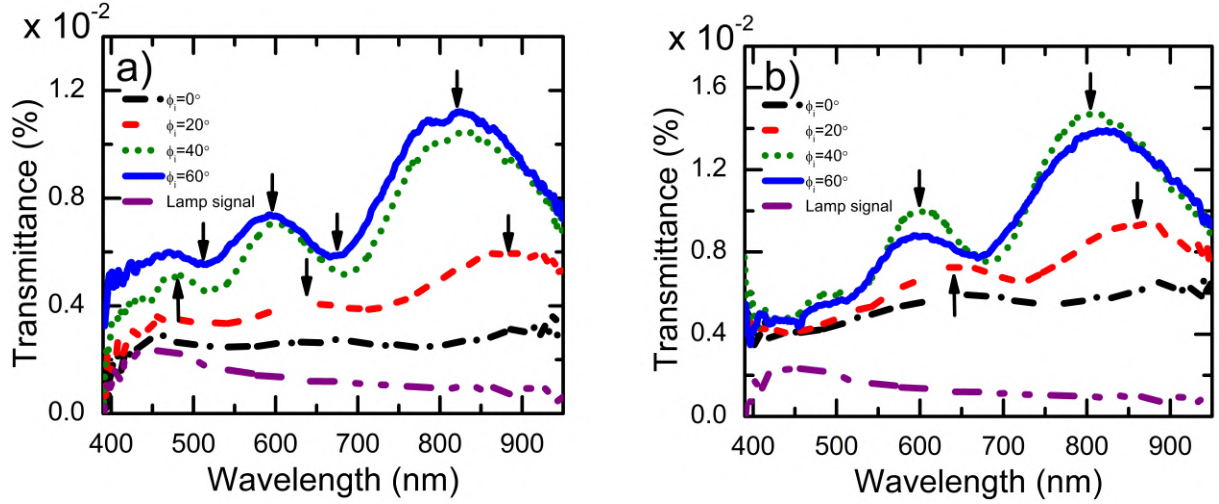


Figure 5.19: *Transmittance spectra for the a) T_{12} and b) T_{21} configurations with varying angles of incidence. As a visual aid, the arrows indicate the position of the extrema used in the thickness calculation.*

In figuring out the thickness, it is crucial to consider the refractive index of the sample. As discussed in previous sections, this value is not easy to determine because a) we do not know the exact chemical composition and b) formally if there is anisotropy the refractive index is a tensor, not a number [29]. This second point was addressed in the previous paragraph noting that the expected polarization conversion effects (and thus the anisotropy) is small. While the exact value is unknown in this study, we initially used a common refractive index of 1.56 for insect chitin [125, 128]. To check the reliability of the technique and to get a range of thicknesses, we also looked at two other values. For the lower end, we used 1.62, which is close to the highest reported refractive index of chitin within the spectral range [125]. We calculated an upper limit using $n_s = 1.51$, a value that comes close to the lowest refractive index reported for chitosan. Chitosan has a lower refractive index than chitin within the experimental wavelength range [125]. The results of these calculations are detailed in table 5.2.

There is a close match between all calculated thickness values and the measurement extracted from the SEM image. Noteworthy is the average thickness, considering the values from both configurations, demonstrating a maximum relative difference of 13% and a minimum of 5%. This observation is particularly notable given the non-uniform thickness of the wing and the fact that transmittance measurements were conducted near the center, while the edge is observed in the SEM image.

Evidently, the thickness values derived from the T_{21} configuration exhibit a closer proximity to the reference thickness and manifest smaller deviations. This result can be ascribed to the higher transmittance linked with this polarization configuration, which

enhances the signal-to-noise ratio and refines the definition of observed maxima and minima. Nevertheless, it's crucial to acknowledge that due to the reduced number of extrema apparent in the spectra (figure 5.19b), the averaging process involves fewer data points, potentially explaining the observed decrease in standard deviation.

Bound	Upper	Middle	Lower
n_s	1.51	1.56	1.62
Thickness $T_{12} \times 10^{-1}$ (nm)	42 ± 4	40 ± 4	38 ± 3
Thickness $T_{21} \times 10^{-1}$ (nm)	43.9 ± 0.4	42.2 ± 0.2	40.3 ± 0.1
Average thickness (nm) $\times 10^{-1}$	42 ± 4	41 ± 3	30 ± 3

Table 5.2: *Calculated thickness values obtained for the *Episcada hymenaea* butterfly wing using various refractive indices. The presented values include measurements for each individual configuration, as well as an average that incorporates all extrema observed in both configurations. The reported values represent the average of results from different extrema, the standard deviation was used as the uncertainty.*

In understanding the properties and optimizing applications, accurate knowledge of wing thickness is crucial, as it directly influences optical and mechanical performance, and often serves as a prerequisite for determining other parameters, such as the refractive index. Optical techniques are an attractive proposition because of they are contact-less, usually non destructive and precise. Currently available techniques for measuring thickness, such as ellipsometry [42] and interferometry [183], are very reliable but possess certain limitations, including their specialized nature and high cost. One of the simplest ways to obtain the thickness is from the interference oscillations in the transmittance spectra, as discussed in section 2.5.1.1. However, due to the high transparency of the wings, these are not discernible in the direct spectra (figures 5.4a and 5.14) which in principles makes it impossible to apply this technique. The implementation of a novel crossed-polarization measurement approach that effectively exploits the polarization conversion effects within the nanoscale structure enhances contrast and unveils the oscillations necessary for precise thickness determination, employing only linear polarizers [184]. These results form a solid basis for the study of other materials displaying polarization conversion effects.

5.6. Conclusion and future perspectives

We successfully showed the high omnidirectional transparency in the central region of the wings of the *Episcada hymenaea*. By measuring the total spectral transmittance and reflectance at normal incidence we were able to obtain a range of effective refractive indices for the wings of different specimens, finding values well below what is expected from the constituents. This suggests that the structure of the wings help achieve the remarkably

high transparency. It was shown that this could be a consequence of the intermixing region on top of the wing's surface that introduces a gradual increase of the refractive index, greatly reducing reflectance. Both the calculated effective refractive index and the results from the gradient index approach reproduce well the angle dependence of transmittance, showing the accuracy of the results. Remarkably, the transparency of the *Saturniidae Heliconisa pagenstecheri* moth—which lacks this intermixing structure—is lower, particularly at larger angles of incidence. For future work, a better characterization of the intermixing profile and the determination of the deacetylation factor from chemical analysis (like FTIR or Raman spectroscopy) could improve the accuracy and reliability of the model. Considering that this work was done in conjunction with the groups of Entomology and Analytical B biochemistry of the faculty of sciences, we believe we succeeded in the two main objectives of the study: a) we proved that the morphology of the wings play an important role in the transparency mechanism by allowing high transparency and b) obtained an effective refractive index that can be used to model the transmission and reflection, allowing for the study of the structure's behaviour on its natural habitat under white light.

A brief study of the scattering properties was performed and found that the reflection off the wings of both species is almost completely diffuse. This could be a camouflage mechanism, effectively decreasing the energy density of reflected light. The transmission in the wings of the translucent butterfly is mostly specular, which could aid in remaining unnoticed by not introducing disturbances to light. The moth is instead more diffusive, which could be attributed to the large hairs present in the surface of the wing. The study of the microbristles is of great interest and would allow for a more complete characterization of the transparent region. To measure the effects of the structures, the bristles could be removed by carefully removing the hairs by using scotch tape, similar to what was done in the case of the *Greta oto* [98]. The effect of the isolated bristles could be studied by placing individual hairs in controlled, low scattering structures like a glass plate or suspended in solution. Using tools previously developed by the group of solid state physics (GFES), Mie theory could be utilized to model the scattering effect of the hairs considering a distribution of sizes, similar to previous used to model the scattering of light of nanorod arrays [185]. This would allow us to separate the scattering effects coming from the bulk of the wing with those generated by the microbristles.

A CCD camera is another tool that could be used to obtain more precise insights on the scattering phenomenon. This tool is well established in dynamic light and other scattering techniques[186–188] which can be used to obtain the size, refractive index or roughness of small particles[189–191] . It would allow for a full 2D mapping of the scattered light, with greater spatial resolution than the setup used in this work. Similar techniques have

been employed to map the scattered light from the scales of some iridescent butterfly wings[192–194], but, to our knowledge, they have not been applied to transparent or scale-less surfaces. It is possible to probe single, suspended scales or bristles as well as the whole structure in order to differentiate between the optical properties of single structures and the collective effect on the macrostructure of the wing.

The wings of the *Episcada hymenaea* displayed an interesting behaviour under polarized light which suggests polarization conversion characteristics. These could be further studied by employing techniques like polarized light microscopy [195–197], allowing for a polarization map of different regions. Further, depolarization effects have previously been related to the internal structure of the scatterers [189]. Fittings with Mie theory, stratified media or neural networks could be used to extract information—like size and distribution—on the scattering centers from the resulting images [198].

Clearly all the proposed work relies on improving the optical imaging and analysis tools available. In this context, collaborations with the group of Applied Optics of the Faculty of Engineering would be immensely fruitful, given their expertise and recent works in optical imaging and polarized microscopy [199–203]. Further, a common effort could be made to integrate Mueller matrix ellipsometry capabilities to the ellipsometric setup currently being developed in our lab. This technique has shown great success in the study of polarization converting metamaterials [204–206].

Further insights are required to understand the polarization properties of the studied structure and their relationship with the morphology and chemical composition of the wing. Employing the TMMA model developed requires information from other characterization techniques to better understand the material structure and chemical composition. Other computational tools like rigorous coupled wave analysis (RCWA) [207] or finite different time domain (FDTD) [208–210] could be employed to better understand the mechanisms of light propagation in the wings.

A simpler, readily available approach, is to focus on the optical performance of the system as was done for the effective refractive index calculations. It is possible to obtain the elements of the Jones matrix of the sample by performing transmittance measurements while the sample is rotated between two linear polarizers [211]. This would allow us to characterize the polarization effect of the samples on the polarization state of light, and the Jones matrix can be employed to model the propagation when other optical elements are at play. Just as the effective refractive index, this information could be a valuable asset for understanding the behaviour and mechanism behind the wing structure. Further, it has been proven that the structure of the Jones matrix can be correlated with one of five classes of metamaterials [212], which means this measurement has the potential to elucidate aspects of the internal structure.

In order to expand the findings of this work, further discussions and collaborations with the Entomology and Analytical Biochemistry of the Faculty of Sciences are being explored. Their expertise can shed light on the chemical and structural composition. Crucially, they can contextualize the observed properties by relating them to the specific needs of the species in its environment—like camouflage, thermal regulation, mating and signaling [97, 168, 213].

The study of the optical properties of the wings of the *Episcada hymenaea* and the *Saturniidae Heliconisa pagenstecheri* moth brought more questions than answers. This is probably what must be expected from scientific endeavours and, in particular, when starting a new line of research in the country. Several results from this work are interesting and improve the knowledge on these species, which have been mostly ignored in the literature in favour of others more “exotic” or those inhabiting countries in the global north. However, maybe the most exciting aspect of this work is the demonstration that the optical characterization of biological samples is a fantastic playground to apply knowledge in fundamental physics and opening the door to collaborations with partners from diverse backgrounds. The possibilities of collaborative and multidisciplinary research are endless, promoting a deep understanding of the underlying phenomena and fostering disruptive ideas.

Chapter 6

ZnO nanorods sensitized with SnS

Zinc oxide (ZnO) has emerged as a remarkably versatile semiconductor material, attracting significant attention due to its intriguing optical and electronic properties. Its wide direct bandgap (~ 3.37 eV) and large exciton binding energy (~ 60 meV) [214] make it an ideal candidate for optoelectronic applications such as ultraviolet (UV) light emitters, transparent conductors, and photodetectors. Not only is it inexpensive [215], it is also bio-compatible, biodegradable and bio-safe [216]. In particular, 1-dimensional nanostructures, such as nanorods (NR) and nanowires (NW)—which can be easily grown in many substrates by low cost techniques [217]—have received widespread attention for their potential applications as building blocks for other structures [216]: in solar cells [4, 217], sensors [218], and for photocatalytic devices [215], among others. These nanostructures enhance their functionality by providing high surface-to-volume ratios, tunable optical properties, and the possibility of quantum confinement effects [219, 220].

Some of the disadvantages of ZnO for photoelectrochemical applications is that it only absorbs light in the UV range, it suffers from severe charge recombination rates, and reduced photostability [215]. Sensitization with suitable materials offers a promising strategy to address these limitations [220]. By integrating materials with complementary bandgaps and electronic properties, the light absorption range of ZnO based devices can be extended into the visible region, significantly enhancing its photoconversion efficiency [221, 222]. Additionally, the formation of heterojunctions at the sensitizer-ZnO interface can promote charge separation, suppressing recombination losses and boosting overall performance [223, 224]. Furthermore, certain sensitizers can act as protective layers, shielding ZnO from photocorrosion and improving its stability [225, 226].

The success of this approach has been demonstrated in various applications. For instance, sensitization of ZnO nanorods with CdS quantum dots has led to significant improvements in solar cell efficiency, with power conversion efficiencies exceeding those of bare ZnO devices [227]. Similarly, coating ZnO with narrow bandgap semiconductors like

Cu_2O and Bi_2S_3 has resulted in enhanced photocatalytic activity for water splitting and degradation of organic pollutants [228–230].

Among potential sensitizers, SnS has garnered significant interest due to its unique combination of properties. It possesses a layered structure with strong in-plane covalent bonding and weak van der Waals interactions between the layers, similar to materials from the transition metal dichalcogenides (TMDs) family [231] like MoS_2 , SnS_2 and WS_2 , which have shown great promise for photovoltaic applications [232–234]. The layered structure in these materials, leads to exceptional light absorption characteristics and bandgaps that can be strategically tailored depending on the specific composition and thickness, making them versatile candidates for sensitizing various wide-bandgap semiconductors [235]. Most research to date has centered on TMDs. Some works, for example, have found that the addition of TMD QDs can optimize the energy level arrangement of the device, expand the range of absorption, reduce surface defects and improve electron-hole transport [236–238].

SnS is comparatively less explored. It is a particularly promising candidate because it is abundant and environmentally friendly [236], it has been shown to improve the photoelectric conversion efficiency in solar cells [239] and has high electron mobility [240]. Previous research has demonstrated the possibility to tune band alignment with application in solar cells [241]. Furthermore, has demonstrated the potential of SnS-ZnO composites for enhancing photoelectrochemical performance. For instance, a significant increase in photocurrent generation for SnS-sensitized ZnO photoelectrodes compared to pristine ZnO was reported [242]. This improvement was attributed to the efficient light absorption by SnS and the formation of a heterojunction that facilitated charge separation and transfer to the underlying ZnO core. In this configuration, the intimate contact between sensitizer and ZnO creates a well-defined interface that optimizes charge transfer across the heterojunction [243]. This minimizes recombination losses and promotes efficient electron injection from the excited SnS to the ZnO core, ultimately leading to improved photoconversion efficiency [244]. Additionally, the SnS shell can act as a protective layer, shielding the ZnO core from photocorrosion and environmental degradation, thereby enhancing the overall stability of the photoelectrode [245]. Some works have reported enhanced photoconversion efficiency in ZnO-SnS nanostructures [246]. Moreover, Core-shell structures based on a ZnO platform but using other sensitizing materials have shown promise in various applications, including photovoltaics [247], photocatalysis [248], and photodetectors. For example, core-shell ZnO-CdSe nanostructures have been demonstrated as efficient photocatalysts for hydrogen production from water splitting, as reported by Miao and others [249].

One effective method for fabricating such core-shell nanostructures is Successive Ionic

Layer Adsorption and Reaction (SILAR). This solution-based technique stands out from other deposition methods due to its advantages of precision, simplicity, and scalability [250]. SILAR involves a sequential process of immersing a substrate in solutions containing precursor ions, followed by rinsing steps—this cyclical approach allows for precise control over the thickness of the deposited layer, down to the sub-nanometer level. This fine-tuning of the shell thickness is crucial for optimizing light absorption and charge transfer dynamics in core-shell nanostructures. Moreover, SILAR is renowned for its simplicity, requiring minimal equipment and operating under ambient conditions, making it a highly scalable method. The ability to scale up production is particularly relevant for applications like photoelectrodes that require large surface areas. Additionally, SILAR’s versatility allows deposition of a vast range of materials, including oxides, sulfides, and selenides, expanding its applicability for exploring different core-shell heterojunctions. Previous studies demonstrate the successful application of SILAR in depositing controlled CdS and CdO shells onto ZnO nanorods, resulting in enhanced photocatalytic and photovoltaic performance [251, 252].

In this chapter we study the optical and morphological properties of ZnO NRs sensitized with SnS by SILAR method. The samples were prepared by the group of Prof. Humberto Gómez Meier in the Pontificia Universidad Católica de Valparaíso. We begin with a brief description of the fabrication procedure, followed by morphological characterization by means of SEM images. Interestingly, the SEM analysis reveals the formation of nanotubes during SnS deposition. This unexpected observation is attributed to the etching caused by the basic solution used in SILAR along the longitudinal direction of the ZnO NRs.

Next, we explore the spectral properties of the samples, including transmittance, reflectance, and haze. Significant differences are observed, particularly a red-shift (shift towards longer wavelengths) in the reflectance and transmittance spectra upon SnS deposition. Utilizing Tauc’s plot method on the absorption spectra, we determine the bandgap energy of the deposited SnS. These edges exhibit deviations from reported values, which could be attributed to quantum confinement effects within the nanostructures. Additionally, the fitting procedure reveals the presence of Urbach tails, with the differences between the samples potentially arising from variations in strain within the SnS shell, as supported by numerical simulations.

Our investigation continues with an attempt to fit the spectra using the Transfer Matrix Method (TMM). However, this approach yielded limited success, highlighting its limitations in accurately modeling complex, highly dispersive nanomaterials like these core-shell structures. Finally, we explore the relationship between the nanostructures and the degree of polarization in the transmitted and reflected light. We find a correlation

between increased multiple scattering events within the samples and a decrease in the degree of polarization.

6.1. Sample fabrication

6.1.1. Deposition of ZnO nanorods

Fluorine doped tin oxide (FTO) substrates were prepared for electrolysis by successive cleaning with diluted aqueous soap solution, 1:1 solution of Acetone/ethanol and deionized water in an ultrasonic bath. Nitrogen gas flow was used to dry the samples. In order to improve the quality and alignment of the nanorods (NRs) [52, 253, 254] a ZnO seed layer was deposited by spin-coating using zinc acetate and sodium acetate in 1.0/0.1 M solution at a speed of 1500 rpm. The nanorods were grown in an electrochemical bath at a electrostatic potential of -0.86 V for 45 minutes. A platinum counter electrode and a Ag/AgCl reference electrode were used. To study the effects of parameter variation, 4mM and 12mM concentrations of precursor $ZnO(NO_3)_2$ solution adjust at pH=6.76, prepared with deionized water at 80°C, were used.

6.1.2. SnS nanoparticle deposition

SnS quantum dots (QDs) were synthesized using the Successive Ionic Layer Adsorption and Reaction (SILAR) method [250]. This method involves the sequential immersion of ZnO-FTO-Glass substrates in four different solutions. The first solution contains precursor cations of Sn^{2+} , derived from $SnCl_2$, while the third solution holds precursor anions of S^{2-} obtained from a $(NH_4)_2S$ solution, both with a concentration of 25 mM. Deionized water (DI) is used in intermediate steps to remove excess reactants from the preceding stages. Each submersion step lasts for 30 seconds. The completion of all four steps constitutes one cycle, with the number of cycles being a variable parameter in this study. Specifically, 10 and 15 cycles were investigated.

6.2. Morphological characterization by SEM microscopy

FE-SEM images of the samples were acquired with a Helios Nanolab 650 Dual Beam from FEI company equipment by our collaborators at the University of Malaga. They appear in figure 6.1 and reveal significant differences between samples. Figures 6.1a and 6.1b confirm the successful electrodeposition of ZnO nanorods (NRs) on the FTO

substrate. These unsensitized NRs exhibit disorder, a broad size distribution, and a tendency for larger diameters at higher ZnO precursor concentrations.

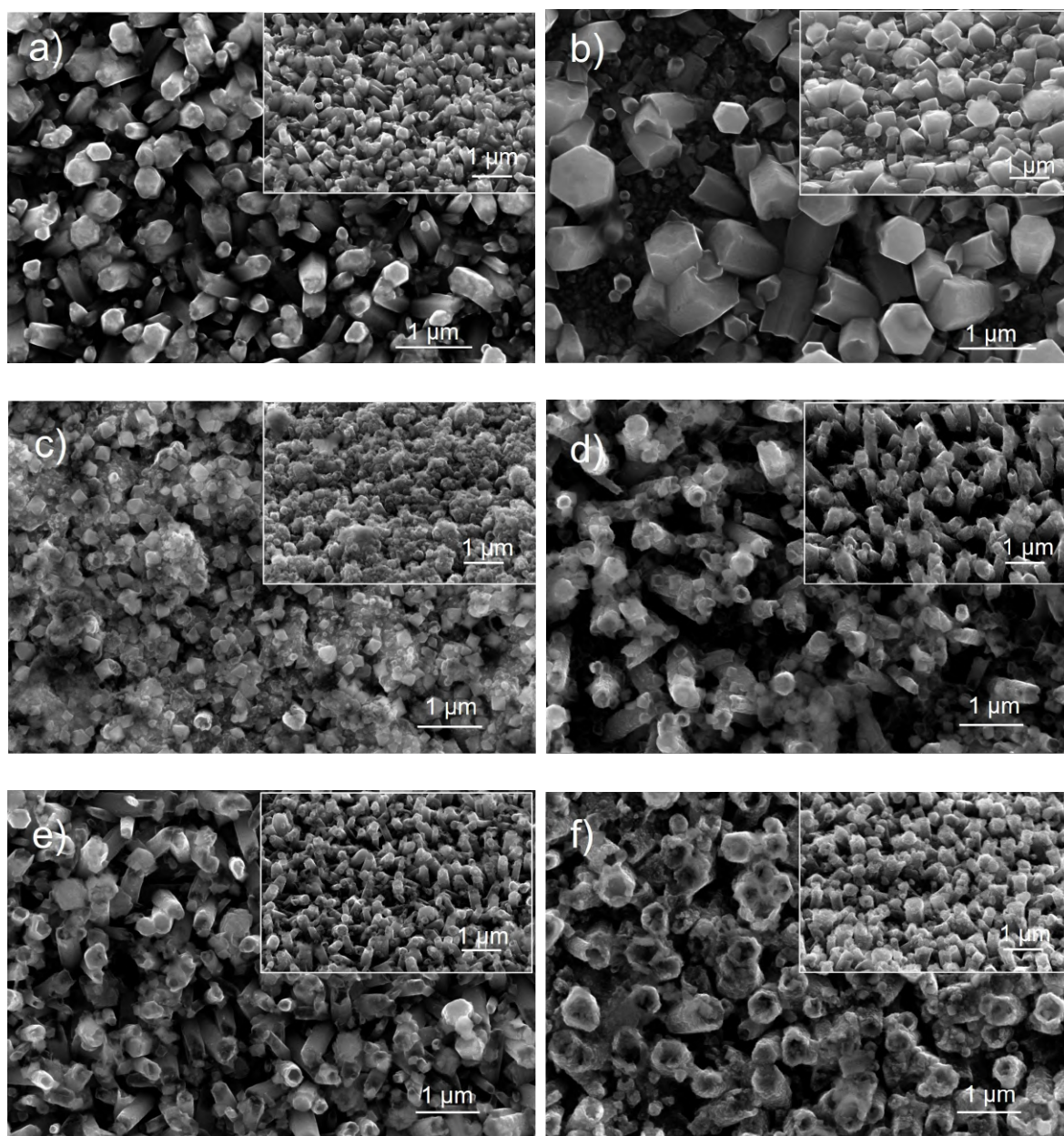


Figure 6.1: SEM images of samples prepared with a ZnO precursor concentration of a),c) and e) 4 mM and b),d),f) 12 mM, with 0 (a and b), 10 (c, d) and 15 (e, f) SILAR cycles. The insets show images of the samples at 45°

After 10 SILAR cycles, both 4mM and 12mM samples (6.1c and 6.1d) display small crystal formations attributed to SnS deposition. However, the 4mM sample becomes completely covered, obscuring the NRs, while NRs remain distinguishable in the 12mM sample. Additionally, nanotubes (NTs) are observed in Figure 6.1d. Increasing SnS

deposition (6.1f) leads to more NRs transforming into NTs, as seen in figure 6.1f. A similar trend occurs in the 4mM samples (6.1e), though with fewer NTs, indicating 12mM concentration is more conducive to NT formation.

The measured NR/NT average diameters vary visibly. A stark diameter difference exists between bare NRs (6.1a and 6.1b), as shown in table 6.1. This diameter increase with higher precursor concentration aligns with previous findings [6, 255]. In 4mM NRs, SnS addition slightly increases diameter, likely due to the SnS layer. Interestingly, 12mM NRs show a substantial diameter decrease after 10 SILAR cycles, but better diameter preservation with more cycles. Notably, both concentrations exhibit a significant reduction in diameter spread after sensitization (approximately 20% standard deviation compared to 40% for unsensitized NRs).

A similar pattern appears in apparent length (L_{app}), measured at a 45° angle. 12mM NRs are longer, consistent with prior reports [255]. Sensitization significantly reduces length, especially in the 12mM NRs. Conversely, sensitization has minimal impact on the L_{app} of NRs prepared with a lower ZnO concentration. It is important to note that, unlike diameter, L_{app} is influenced by NR orientation due to the angled measurement.

ZnO nanotubes are typically formed through the selective dissolution of the central region of pre-existing nanorods [256, 257]. This preferential dissolution can occur in either acidic or basic environments due to the amphoteric nature of ZnO [258]. The formation of NTs may be attributed to corrosion of the ZnO NR along the longitudinal preferential direction by immersion in the $(NH_4)_2S$ bath utilized in the SILAR method, which has a basic pH [259]. Two primary hypotheses explain the increased susceptibility of the nanorod center. Firstly, the metastable and chemically active (0001) crystal planes, the hexagonal cross sections (also called basal planes), exhibit a faster dissolution rate compared to the stable {1000} planes along the sides [260, 261]. Secondly, defects tend to concentrate along the (0001) direction, promoting dissolution through enhanced absorption of cations or anions, depending on the solution's pH. Experiments where nanorods were annealed to redistribute defects support this hypothesis, as etching became impossible [258]. Furthermore, previous work have shown that nanorods with diameters below 100 nm showed greater stability due to the reduced size of the (0001) plane and could not be etched, while at around 300 nm they were completely transformed into nanotubes [262]. This is consistent with our results, where larger diameter nanorods resulted in a larger proportion of nanotubes, as can be seen by comparing figures 6.1e and 6.1f.

The reduction in average diameter may be a result of corrosion along the exterior of the NRs. This is supported by the observation that the 12 mM 10-cycle sample exhibits the smallest diameter compared to other 12 mM samples but shows few NTs. In contrast, the 15-cycle sample preserves diameter while forming many nanotubes. This suggests that

corrosion primarily occurred along the center of the NRs in the 15-cycle case, whereas the 10-cycle sample experienced more widespread external corrosion. The reduction in standard deviation could also be attributed to this effect, potentially due to the complete corrosion of smaller NRs. There are previous reports showing that NRs can be over-etched, resulting in large external corrosion[259]. Furthermore, the reduction in length shown by our samples is consistent with previous reports on length reduction with increased etching time [257, 262]. A more thorough analysis, using images before and after deposition, is needed to definitively distinguish between corrosion, the potential obscuring of small NRs by SnS deposits skewing the results and variations in the electrochemical growth step. Regardless, these results demonstrate that the deposition method offers interesting potential for both targeted deposition and the generation of complex nanotube structures.

Con (mM)	cycles	$D \times 10^2$ (nm)	$L_{app} \times 10^2$ (nm)	Cover (%)	$D_{cluster} \times 10^1$ (nm)	D_{nc} (nm)
4	0	2.3 ± 0.6	4.6 ± 0.9	53	-	-
4	10	-	-	84	17 ± 4	39 ± 5
4	15	2.5 ± 0.5	4.5 ± 0.9	69	-	27 ± 7
12	0	4 ± 2	10 ± 4	82	-	-
12	10	2.5 ± 0.5	7 ± 2	65	13 ± 2	21 ± 7
12	15	3.8 ± 0.7	5.7 ± 0.9	67	13 ± 2	28 ± 8

Table 6.1: Values of morphological features for each sample taken from the SEM images. The average and the standard deviation of different measurements within each sample were employed as the nominal value and uncertainty, respectively. The apparent length (L_{app}) is taken from the images at 45° (see inset of figure 6.1). The coverage factor is calculated using the color threshold with boundaries of 35 and 255. Con stands for concentration.

To quantify the approximate area covered by nanorods (NRs), we used the contrast threshold method in ImageJ with selection boundaries from 35 to 255 intensity, which by visual inspection resulted in the most accurate selection of the NR/NTs (see Appendix E for details). Table 6.1 summarizes the coverage results. In samples prepared with 4mM concentration, coverage increases with SnS deposition, likely due to increasing NR diameter. As anticipated from image 6.1c, the sample with 10 SILAR cycles exhibits the highest coverage, forming a compact layer without distinguishable NRs.

Conversely, at 12mM concentration, the unsensitized sample shows the largest coverage. This is again attributable to diameter, which decreases with SnS deposition in this case. Notably, the diameter increase observed at 15 SILAR cycles corresponds to a larger coverage compared to the sample with 10 cycles. It's important to remember that this measurement reflects apparent area based on intensity contrast; smaller NRs might be obscured within the shadows of larger surrounding structures. However, the length is relatively constant for the 4mM samples, while the 12mM unsensitized sample has the longest NRs, ensuring the validity of the trends in coverage percentages. SEM images

at higher magnification are shown in Appendix E, which could aid in the observations presented.

Energy Dispersive X-ray Spectroscopy (EDX) [263] was performed on the sensitized samples (see Appendix E. S and Zn are uniquely associated with SnS and ZnO respectively, whereas the other elements detected by EDX, like oxygen or tin, are also present in the glass plate or the FTO substrate, making their signature not unique to the formation of sensitized NRs. In the 12 mM set, an increase in deposition cycles led to a rise in the weight percentage of sulfur (S) from 1.73% to 2.34%. Unexpectedly, in the case of the 4 mM samples, additional SILAR cycles resulted in a reduction of the S weight percentage from 2.26% to 1.70%. This discrepancy may elucidate the observed morphology on the 10 cycle sample, providing evidence that the altered deposition of nanoparticles affects the visibility of the nanorods in figure 6.1c.

In the 12 mM 10 cycles sample, it was possible to map both the orifice and the side of the same NT. S and Zn weight percentages on the NT sidewall were 1.56% and 41.3% respectively, while the orifice showed 1.9% of S and 29.41% of Zn. This higher sulfur concentration and reduced Zn content within the orifice may support the hypothesis that SnS precursor solution corrodes the ZnO NRs due to a higher number of reactive sites along the preferential direction, which leads to a higher concentration of S anions.

Some samples display large agglomerates of what appears to be SnS, with an average cluster diameter ($D_{cluster}$) of around 130 nm. The origin of this clusters is undetermined, but could be generated by excess deposition relative to the underlying NRs. Furthermore, the very small crystals that appear in the surface of the NR/NTs were measured, and their average diameters are indicated as D_{nc} . These structures could be small nanoparticles or small agglomerated of several particles and give an idea of the amount of material deposited on the underlying NR/NT structures.

6.3. Transmittance and Reflectance spectra

This section investigates the impact of SnS deposition on the optical properties of ZnO nanorods (NRs), focusing on spectral reflectance and transmittance. It highlights how SnS enhances absorption below 600 nm, evidenced by changes in Total Reflectance (TR) and Diffuse Reflectance (DR) spectra, suggesting increased absorption due to SnS's absorption onset. Additionally, the study observes a decrease in total transmittance (TT) at shorter wavelengths with more SnS deposition, indicating significant alterations in the optical behavior of sensitized ZnO NRs. These findings contribute to understanding the role of SnS sensitization in modifying the photonic characteristics of ZnO NRs, with varying effects across different sensitization levels and deposition cycles.

6.3.1. Reflectance spectra

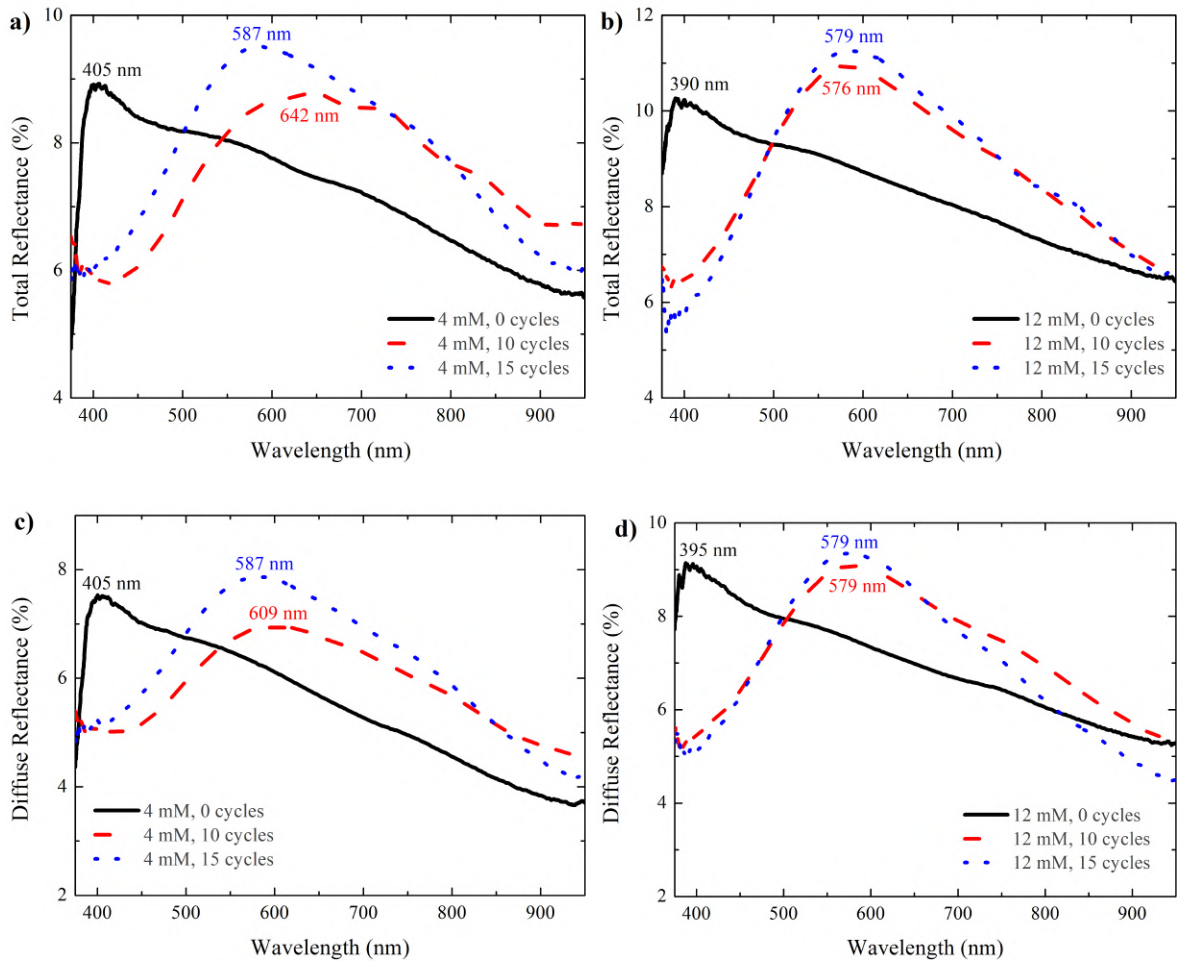


Figure 6.2: Total and diffuse reflectance (TR and DR) of the 4mM (a and c, respectively) and 12mM (b and d) sets. Notice that the maximum of each spectra is indicated next to the corresponding curve.

Figure 6.2 reveals significant changes in the reflectance spectra due to SnS deposition. In the Total Reflectance (TR) graphs (6.2a and 6.2b), SnS reduces reflectance below 600 nm, hinting at increased absorption in that range. This shift is caused by the onset of absorption of SnS (see section 6.3.4 for the calculation of the absorption edges). Above 600 nm, reflectance generally increases with deposition, though it depends on the wavelength range. In the 4 mM set, the reflectance of the 15 cycle sample is larger than the 10 cycle one in the visible range (up until $\approx 750\text{nm}$). In the 12 mM set there is a slight increase in the maximum reflectance with 15 cycles, but a small decrease near the UV when compared to the 10 cycles sample. This appears to contradict reports linking longer nanowires to increased total reflectance [264]. The departure could be caused by the formation of NTs. Notice that the 4 mM set is difficult to compare because the 10 cycle sample

does not display NRs. Previous works have found a redshift in the total reflectance with larger diameter NW [265], which is not seen in our samples. Remarkably, both sensitized samples in the 12 mM set display similar behaviours, suggesting that either a) morphology differences in this range do not affect reflectance, which is unlikely or b) that the effect of the nanotubes is counteracting effects due to diameter and length. Notice that the maximums are indicated in the figures, and occur at almost the same wavelengths in the 12 mM set, something that is not replicated in the other group.

Diffuse Reflectance (DR) spectra (figures 6.2c and 6.2d) closely follow their corresponding TR graphs. This suggests diffuse reflectance dominates, implying near-unity haze. At higher wavelengths, both TR and DR converge with the spectra of unsensitized NRs. This occurs because light at those wavelengths scatters mainly from the overall NR shape, with minimal impact from the smaller nanoparticles, which are approximately an order of magnitude smaller, as seen in table 6.1. Notably, the sensitized samples retain a DR shape similar to bare NRs, except for the shifted absorption edge. This suggests that the main factor affecting diffuse reflectance is the underlying nanorod.

6.3.2. Transmittance spectra

Figures 6.3a and 6.3b present total transmittance (TT) spectra for the 4 mM and 12 mM ZnO NR samples, respectively. The unsensitized ZnO NRs (black lines) exhibit a feature around 375 nm due to the ZnO absorption edge (~ 3.35 eV) [52, 266–268]. This aligns with the expected composition, as confirmed by UV-Vis characterization of the absorption edge (see section 6.3.4).

SnS sensitization dramatically alters the TT spectra, especially at shorter wavelengths where transmittance significantly decreases. Previous works on ZnO-sensitized samples have shown a decrease in transmittance with more sensitized cycles [265, 267–269]. In our samples this is not observed clearly. For the 4 mM set transmittance increases with 15 cycles relative to the 10 cycles sample, which may be due to the formation of NR/NTs instead of the film-like structure seen in the 10 cycle sample. The spectra of the sensitized 12 mM set is almost unaltered, except at high wavelengths where the 15 cycle sample has higher transmittance, matching that of the bare NRs. Notice that the decrease in transmittance and the onset of absorbance at around 550nm in the sensitized samples indicate the presence of SnS.

Unexpectedly, figure 6.3a shows the 10-cycle sample as the most absorbing, contradicting the usual trend. This anomaly might be explained by the substantial SnS deposition obscuring the NRs (6.1c), resulting in a compact layer with fewer low-absorption regions (supported by coverage data in 6.1).

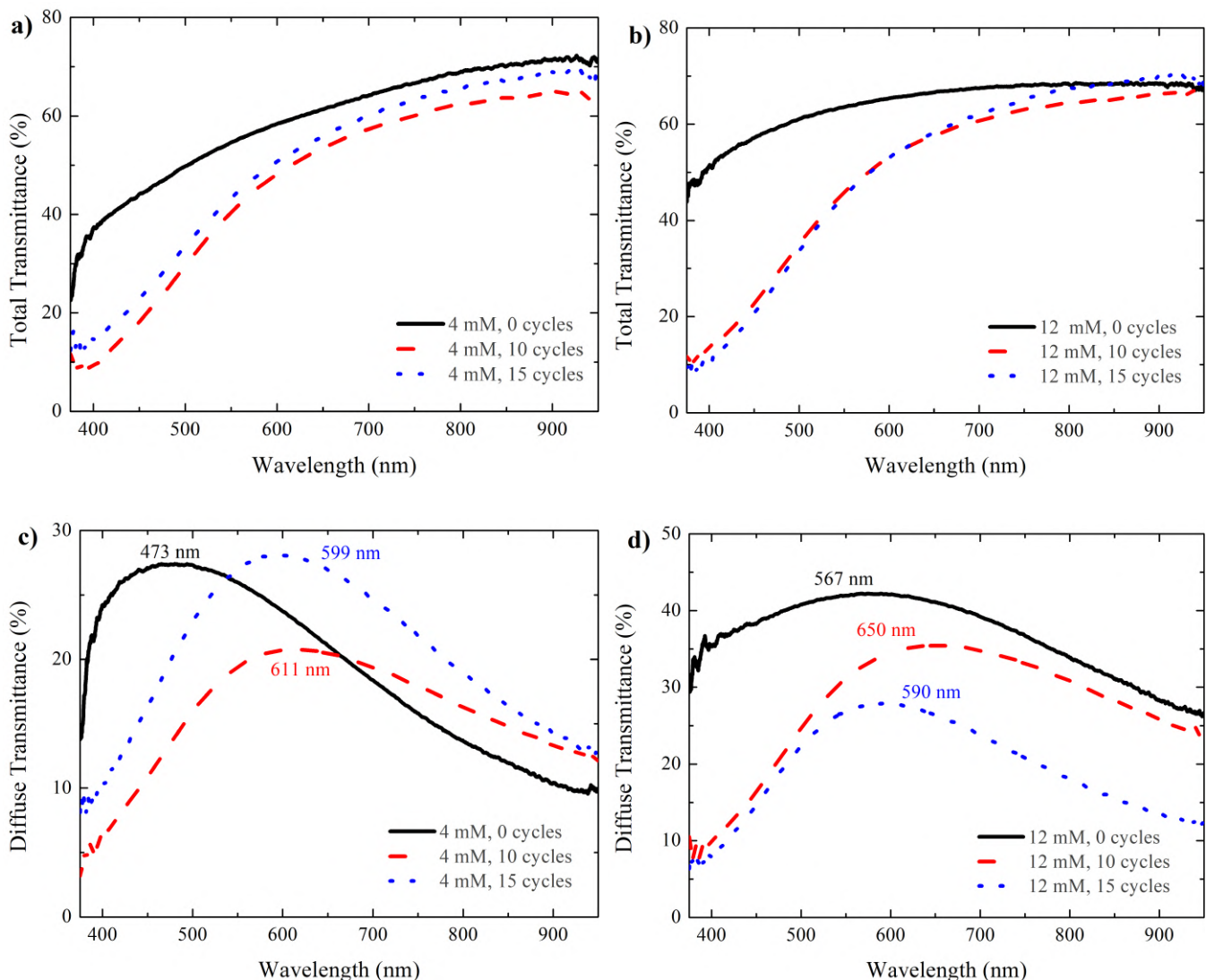


Figure 6.3: Total and diffuse transmittance (TT and DT , respectively) of the $4mM$ (a and c, respectively) and $12mM$ (b and d) sets. Notice that in the diffuse transmittance spectra, the positions of the maxima of each curve are indicated.

Diffuse Transmittance (DT) spectra (Figs. 6.3c and 6.3d) offer further insights into morphology changes. As observed previously [265], the DT peak shifts towards the near-infrared (NIR) with sensitization. However, this shift is non-uniform; the 10-cycle samples exhibit a more pronounced shift than the 15-cycle ones. Despite this, sensitization largely preserves the spectral shape reminiscent of bare ZnO NRs, suggesting their morphology remains dominant. This is specially noticeable at higher wavelengths, where scattering is determined by overall size rather than small crystal dimensions and we see the sensitized spectra tend towards the unsensitized sample.

6.3.3. Haze

Figure 6.4 reveals contrasting haze trends in the 4mM and 12mM sample sets. While haze increases with SnS deposition in the 4mM set, it decreases in the 12mM set. Previous studies have shown that elongated NRs enhance multiple scattering, while a larger diameter contributes to augmented scattering in the long wavelength range due to the increase in size of the scattering center [264]. Taking into account these findings, along with the morphology (see figure 6.1) and dimensions (table 6.1) of the samples, we propose a qualitative explanation for the varying haze behavior under different SILAR cycles, involving the interplay of these parameters.

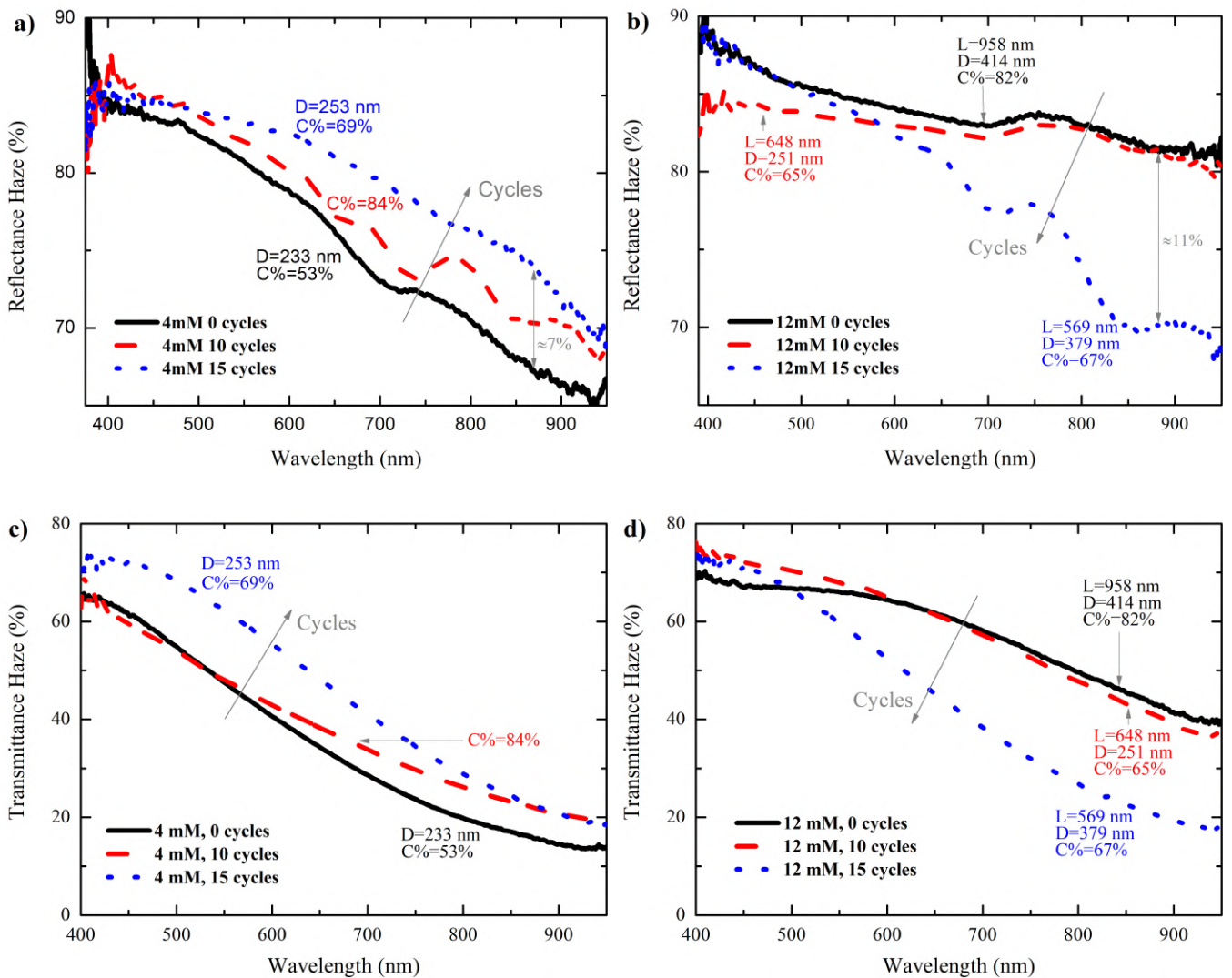


Figure 6.4: Reflectance and transmittance transmittance (RH and TH) of the 4mM (a and c, respectively) and 12mM (b and d) sets. The arrow remarks the tendencies with the number of SILAR cycles. The length (L), diameter (D) and coverage factor (C%) presented in table 6.1 are displayed next to the curves to aid in the discussion.

In the 4mM set, NR length remains largely unchanged during deposition, suggesting minimal impact on haze. However, a $\sim 10\%$ diameter increase likely contributes to heightened haze at higher wavelengths, as larger scattering centers generally enhance scattering in this range. Crucially, increased coverage due to deposition results in denser scatterer distribution, promoting multiple scattering events and thus elevating overall haze. The 10-cycle sample, which lacks visible NRs, suggests a film-like structure. This could counteract the increased effect of scatterer density (larger coverage) by mitigating multiple scattering associated with the NRs, leading to a haze level similar to bare NRs.

The 12mM set exhibits a significant decrease in NR length with SnS deposition, aligning with the observed haze reduction. Additionally, the SILAR process reduces the coverage factor, creating wider spacing between nanostructures and diminishing multiple scattering events. Interestingly, the 10-cycle sample has a smaller diameter than the 15-cycle sample, yet the latter shows lower haze. This may be due to the prevalence of nanotubes in the 15-cycle sample. Nanotubes, with their significant internal air volume, have smaller effective scatterer dimensions. This reduction in the actual dimensions of the scatterer could account for the significant decrease in haze at high wavelengths for the 15 cycle sample, even though the external diameter is larger than in the case of 10 cycles.

To improve the analysis, factors such as the degree of verticality and uniformity of the NRs should be taken into account. Furthermore, gaining a deeper understanding of the distinctions in scattering between nanorods and nanowires is essential for a comprehensive evaluation. A more comprehensive understanding of these elements may be the subject of future work.

6.3.4. Absorption Edges

The absorbance spectra (figure 6.5) reveal shifts in the absorption edge with variations in synthesis parameters. This was evident in the TT spectra, where NRs without SILAR cycles display the distinct ZnO absorption edge around 3.37 eV (369 nm) [270, 271]. Upon SnS deposition, the SnS bandgap becomes apparent. We quantified these differences using the Tauc plot method [4]. While absorbance ($-\ln T$) serves as a proxy for absorptance (α) in this context, its features correlate with absorptance due to a lack of resonant features in the spectra.

The Tauc method involves successively fitting the low-energy absorbance using the fact that $(\alpha h\nu)^{1/r} \propto h\nu$ where $r = 1/2$ for direct allowed and $r = 2$ for indirect allowed transitions [272] (see section 2.1.2). Once one absorption edge is identified, its contribution is subtracted, and the process continues until the entire spectrum is modeled. Note that the “zero” absorption line may be shifted, modeled as an indirect background absorbance

(α_{back}) [4].

Reported SnS bandgap energies vary. An indirect bandgap commonly falls within 1.05 – 1.71 eV [239, 273], supported by theoretical calculations (1.07 eV indirect, 1.47 eV optical absorption onset) [274]. However, some studies find direct bandgaps in SnS thin films and nanoparticles ranging from 1.2 – 2.0 eV [275–279], with even higher values (2.13 – 2.28 eV) reported [280, 281].

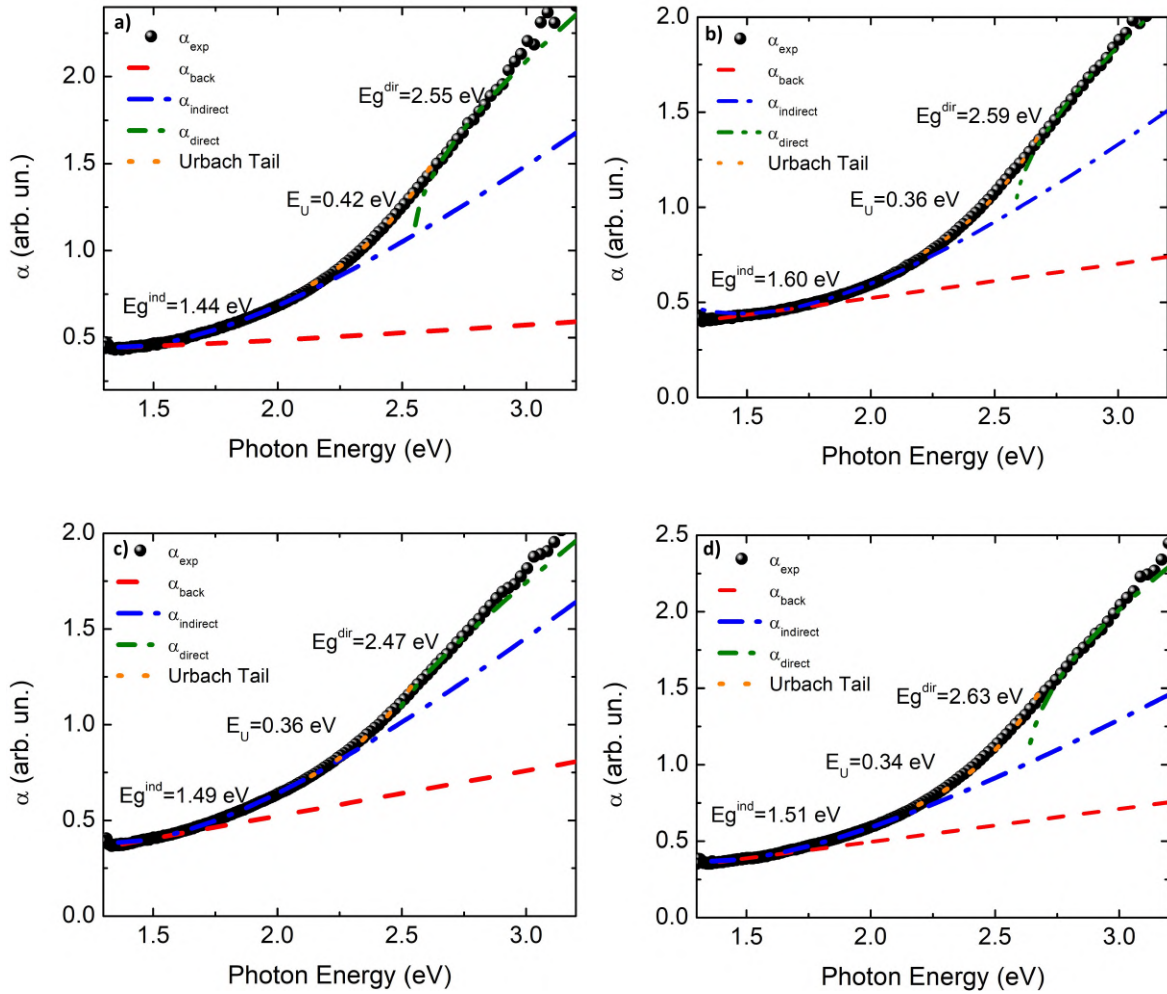


Figure 6.5: Absorbance spectra and fitted absorbance contributions for a) 4mM 10 cycles, b) 12mM 10 cycles, c) 4mM 15 cycles and d) 12mM 15 cycles.

Figure 6.5 presents absorbance plots and fitted results. All samples exhibited both a direct (α_{direct}) and an indirect ($\alpha_{indirect}$) band gap, aligning with previous findings [282]. Table 6.2 summarizes the energies. Our indirect bandgap values (E_g^{ind}) exceed typical reports but are consistent with the observed ~ 1.45 eV absorption onset. The unusually large direct transition values suggest a blue shift in absorption edges, potentially due to quantum confinement effects from the small size of the deposited nanoparticles.

The quantum-size effects on the band gap energy can be calculated from Brus's formula[19–21], equation 2.10. The equation is reiterated below for clarity, where μ is the reduced effective mass of the electron-hole pair, e is the elemental charge of the electron and ϵ is the dielectric constant of the material. Given the bandgap energy for the confined quantum dot (E_{QD}) it is possible to obtain the radius knowing the bulk bandgap (E_{Bulk}) and dielectric constant of the material.

$$E_{QD} = E_{Bulk} + \frac{\hbar^2}{2\mu} \left(\frac{\pi}{R}\right)^2 - 1.786 \frac{e^2}{\epsilon R}$$

The application of this equation is not straightforward in the samples presented in this work. Firstly, the dielectric constant of SnS is not well established, and it was shown to depend on the temperature, the deposition conditions, the crystalline phase and the number of layers [283–285], varying between 15 and 25 in the energy range of the results presented. As the third term in equation 2.10, which models the effects of the Coulomb interaction in an electron-hole pair, is small, with a $1/R$ dependence, differences in ϵ are not critical and therefore in the calculations we employ an average value of 20. The masses of the electron and hole ($m_e = 0.5m_0$ and $m_h = 1.5m_0$, respectively) reported by Vidal et al [274] for the a crystalline direction were used in the calculation of the reduced effective mass.

The results of this section show that the fabricated samples display both a direct and an indirect bandgap. Therefore, is it necessary to consider the quantization energy of both. This introduces a further complication given the vast range of reported bulk bandgap energies reported in the literature, particularly for the indirect edge. To address this, we consider the upper and lower bounds of the bandgaps reported in the literature: 1.05 to 1.47 eV and 2.13 to 2.28 eV for indirect and direct transitions, respectively. The first range aligns with the intersection between experimental and theoretical evidence, and is a gap smaller than most of the measured samples, meaning that confinement is possible. The second range corresponds to reports specific for nanoparticles.

The results of the range of optical radii calculated for the indirect gap (R_{op}^{ind}) and direct gap (R_{op}^{dir}) appear in table 6.2. Notice that the 4mM 10 cycle sample only displays one value for R_{op}^{ind} because the measured gap energy is smaller than the upper bound used. As expected, there are larger variation in the size range calculated with the indirect gap. Clearly, the size of the nanoparticles must be the same in both calculations, and therefore the actual radius should be in the overlap between the two ranges. Thus, the expected radii of the deposited SnS nanoparticles is between 3 and 5 nm, consistent with previous reported dimensions of SILAR deposited nanoparticles [286].

These calculated dimensions are significantly smaller than the measured nanocrystal sizes (D_{nc}) from SEM images and presented in table 6.1, suggesting that the latter may

Con (mM)	Cycles	E_g^{ind} (eV)	E_g^{dir} (eV)	E_g^{ZnO} (eV)	E_U (eV)	$R_{\text{op}}^{\text{ind}}$ (Å)	$R_{\text{op}}^{\text{dir}}$ (Å)
4	0	-	-	3.31	-	-	-
4	10	1.44	2.55	3.28	0.42	33	32-40
4	15	1.49	2.47	3.36	0.36	31-145	35-47
12	0	-	-	3.35	-	-	-
12	10	1.60	2.59	3.33	0.36	28-57	30-37
12	15	1.51	2.63	3.34	0.34	30-103	29-35

Table 6.2: *Parameters obtained from the Tauc plot method*

represent agglomerations rather than individual (monocrystalline) quantum dots. In any case, the QD sizes obtained through the bandgap are beyond the resolution of the SEM images. Further analysis could be employed to determine crystalline sizes, for example from XDR measurements by means of Scherrer formula [287]. The application of XRD at the GFES did not allow to resolve the SnS peaks, prohibiting this analysis.

Zinc oxide (ZnO) is typically acknowledged as a direct semiconductor with a bulk bandgap energy close to 3.37 eV [266]. However, in ZnO nanorod arrays, slight deviations in bandgap energies ranging from 3.28 to 3.36 eV have been reported [254, 267–269]. To obtain the gap energies of ZnO the Tauc plot method was employed on UV-vis transmittance spectra. The experiments and calculations are prior to the work of this thesis, and are only presented for completeness. The obtained energies of the studied samples (E_g^{ZnO}) appear in table 6.2. They display small variations, possibly indicating good reproducibility in the ZnO NRs array synthesis.

6.3.4.1. The Urbach tail parameter E_U

The Urbach tail [288, 289]—an exponential absorption onset at energies below the band-gap—results from transitions involving mid-gap states. The Urbach tail arises from three primary sources: structural disorder (grain boundaries, defects and mechanical stress), impurity scattering of the carrier from donors or acceptors, and phonons [10–13].

The samples under study displayed varying Urbach tail energy (E_U) with the deposition conditions as can be seen in table 6.2. Notably, SnS deposition with 15 SILAR cycles, producing nanotubes, lowered E_U , indicating reduced absorption from SnS mid-gap states [290]. Given the similarity of the deposition conditions, it is expected that the carrier concentrations (which are very low in the undoped semiconductor [291]), the geometry of the grains, degree of crystallinity and number of defects remain constant. Therefore, the differences should arise from changes in strain and phonon scattering.

As an approximation, the core-shell structure can be modeled as a pair of concentric cylinders of infinite length, which admits simple analytical solutions to the heat trans-

fer equation, as explained in appendix F. Calculating the shell temperature with the parameters presented in section F.3 of the appendix, results in no noticeable increase in temperature. This result was corroborated by solving the hexagonal structure numerically with the finite difference method. Furthermore, the simulations demonstrated no change in the average temperature with length or diameter. The incident radiant power used in this study is not enough to increase the temperature of the nanostructures given the rapid cooling due to the large surface area and the high thermal conductivity of ZnO. As a consequence, it is expected that there are no substantial differences in phonon scattering phenomena between the nanostructures.

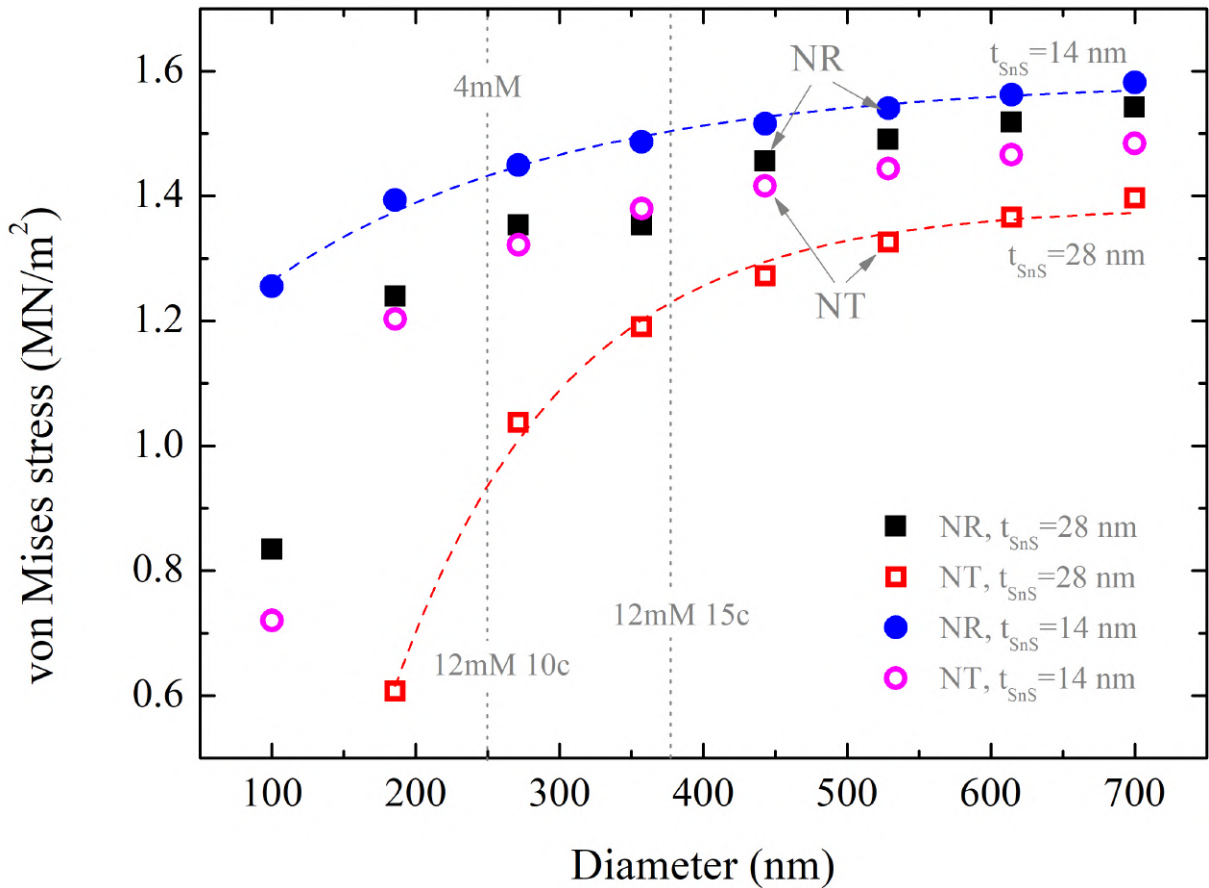


Figure 6.6: Simulated von Mises stress as a function of diameter for NRs (closed symbols) and NTs (open symbols), for two different thicknesses of the shell (t_{SnS}), 14 nm (circles) and 28 nm (squares). The length and the ratio of inner hole to total diameter are kept at 700 nm and 0.6, respectively. The two outermost datasets show an exponential decay fit intended to aid the viewer in identifying the general tendency. In dotted vertical lines the average diameter for the sensitized 12mM samples is displayed.

On the other hand, important differences were revealed when simulating the stress in the nanostructures. The results of the average von Mises stress (explained in Appendix G) in the SnS shell as a function of diameter are shown in figure 6.6. The simulations are

carried out with the same parameters and with the continuum mechanics modules coupled to the heat transfer module of COMSOL[®]. It is immediately clear that the NT structure reduces shell stress when compared with the NR of the same diameter. Furthermore, an increase in SnS shell thickness (t_{SnS}) results in a large decrease in mechanical stress, specially in the case of the nanotube nanoarchitecture.

Therefore, we propose that the decrease in Urbach energy parameter (E_U) when increasing the number of SILAR cycles from 10 to 15 is due to the simultaneous occurrence of the two factors. First, when increasing the total time spent in the basic solution, more nanotubes are formed. Second, the increase in the deposition due to increased number of cycles results in a thicker SnS shell. The interplay between these two factors reduces the stress in the shell, decreasing the absorption from mid-gap states. The results of the simulations using the measured dimensions (table 6.1) for the 12mM set, with the nanocrystal diameter (D_{nc}) as the thickness of the shell, appear in figure 6.7. The NR with the 10 cycle parameters displays an average stress of 1.39 MN/m^2 , whereas in the case of the nanotube with the 15 cycles dimensions it is $1,22 \text{ MN/m}^2$. The relative difference is 12%, close to the almost 6% variation in E_U observed in our samples.

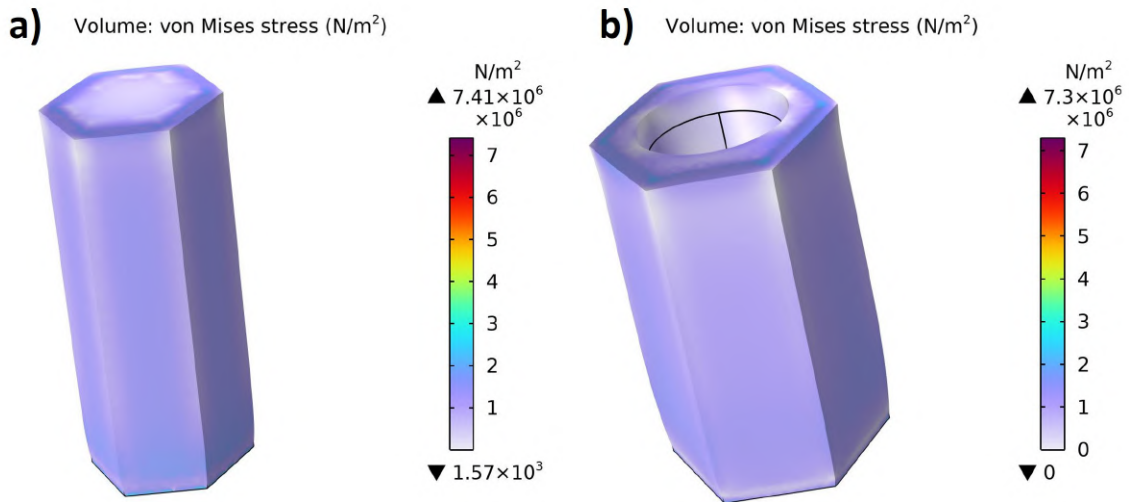


Figure 6.7: Simulated von Mises stress for a) 12mM 10 cycle nanorod and b) 12mM 15 cycle nanotube. The parameters are taken from the SEM measurements of the samples, which appear in table 6.1.

Mechanical stress has been shown to increase the Urbach tail in SnS by spreading band edges into the gap [292]. Amato and others found a positive correlation between the Urbach tail energy and mechanical losses, demonstrated by a reduction in the Urbach tail after annealing [293], a result replicated by another group [294]. Previous works have found Urbach energies of around 400 meV in binary compounds, which was related with

structural stress [295]. In SnS in particular, Urbach energies of around 250 meV have been reported [296], consistent with the fitted E_U in our samples.

The results show the potential of the nanotube architecture for modifying the absorption spectra, making it a potential design parameter for nanodevices. Future research will explore in greater detail the relationship between structural stress and the Urbach tail. In particular, it would be interesting to test whether the Urbach energy follows a similar exponential trend as observed for the stress as a function of diameter. Furthermore, while the temperature remains constant for the utilized incident irradiance, simulations for higher energy result in differences in the temperature profile of the nanoarchitectures. This could also yield changes in the absorption spectra and should be tested with higher intensity illumination.

6.4. Application of the TMM

In order to obtain insights into the behaviour of the samples, the TMM method is used to fit the air and SnS volume fractions in the total transmittance spectra (see the description of the EMA, section 2.6, for the physical meaning of the volume fraction in the context of the TMM). They are modeled as a SnS-ZnO-air layer over a 50nm layer of FTO deposited over a 1.25 mm thick glass plate. The thickness of the top layer is the projection of the corresponding apparent length (L_{app}) into the vertical direction, $L = \frac{L_{app}}{\cos(45)}$. The refractive indices are taken from the existing literature [297, 298]. The fractions of SnS and air in the top layer that best fit the spectra appear in table 6.3, while figures 6.8a and 6.8b show the fitted spectra alongside the experimental values.

It is immediately noticeable that while the calculated spectra follow the general shape of the experimental curves, there are large deviations, in particular in the case of the unsensitized (0 cycle) samples. Furthermore, for all samples the position of the absorption edge is roughly matched, showcasing how the deposition of SnS shifts the spectra when compared to bare ZnO NRs, as expected.

There are appreciable differences in the quantitative values of the transmittance, specially in the case of the bare NRs and at low wavelength in the sensitized samples, which are dominated by the properties of ZnO. This suggests that the deviations can be partially attributed to the use of a dielectric function of the ZnO inappropriate to our case. Indeed, the data available that better matches our structures is for very thin films, not for nanorods, which is not reported in the literature. It is well established that the optical properties, in particular at the nanoscale, are strongly dependant on the morphology, dimensions, defects and crystalline orientations. For instance, previous works have demonstrated massive absorption in nanorods and nanowires, attributed to enhanced coupling

in the longitudinal direction of the nanostructure [299, 300]. The enhanced absorption of the nanostructures, which do not substantially modify the absorption edge, could improve the fitting, as it would reduce the transmittance in the visible range.

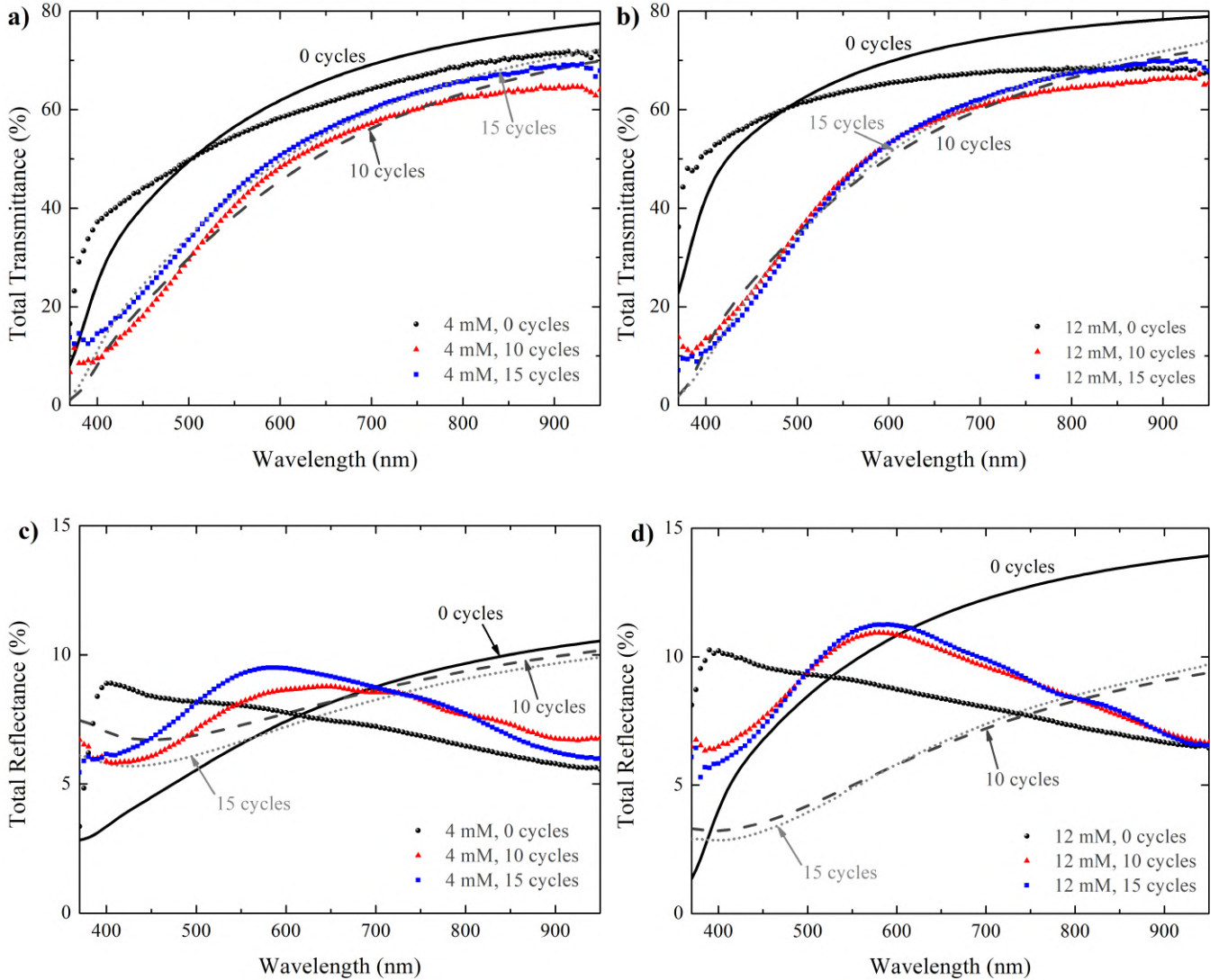


Figure 6.8: *Experimental and fitted total transmittance spectra for the a) 4 mM and b) 12 mM sets. The fitted curves are represented with grey lines, solid, dash-and short dot corresponding to 0, 10 and 15 cycles, respectively. The corresponding reflectance spectra and the obtained from the model with the fitted parameters appear in c) and d) for the 4 mM and 12 mM sets, respectively.*

Furthermore, SnS is a relatively new material, with few studies reporting on its dielectric function [285]. Notably, it is heavily dependant on the direction in the crystalline structure [283, 285]. In this work the values in the b crystalline direction reported by Banai et al. [297] were employed, as this is the direction that better matches the position of the absorption edge observed in our samples. However, we do not have information on the crystalline structure or the orientation of the deposited SnS QDs, and the deposited

nanoparticles are expected to be polycrystalline. Therefore, it is possible that the resulting spectra is a superposition of contributions from different crystalline directions. Considering the massive scattering in the nanostructure, accounted for by the haze, it is expected that light is incident on the nanoparticle on all directions, resulting in interactions of the EM fields with all the crystal directions.

On the other hand, the calculated reflectance spectra (figures 6.8c and 6.8d) display no resemblance to the experimental spectra presented in figures 6.2a and 6.2b except for the general range of values, between 2% and 12%. The range is generally determined by the constituent materials, while the spectra shape depends on both the dielectric functions and the morphology. Indeed, our results suggest that the TMM is not an appropriate tool to model the samples. Their enormous diffusivity, coupled with features, like diameter and length, of the order of the probing wavelength, renders the hypothesis of the model inadequate. Furthermore, notice that the biggest departure is in reflectance, which displays higher haze compared to the transmittance, as can be seen in figure 6.4. The results indicate that these samples should be studied in diffusive regimes using tools like the two-flux and four-flux models. Previous works have applied the two-flux model, also called Kubelka-Munk model [301, 302], to study the spectral properties of NRs, with excellent results. For example, recent work by our group on bare ZnO NRs, which display a reflectance spectra similar to the one of our samples, applied the model with scattering coefficients obtained from Mie theory to explain the behaviour of the samples [185].

Con (mM)	cycles	f_{air}	f_{SnS}
4	0	0.57	0
4	10	0.19	$9.9e^{-13}$
4	15	0.29	$4.1e^{-13}$
12	0	0.83	0
12	10	0.52	$0.22e^{-13}$
12	15	0.57	0.011

Table 6.3: Volume fractions of air (f_{air}) and SnS (f_{SnS}) obtained from fitting of the experimental transmittance spectra.

In table 6.3 we present the volume fractions that better fit the spectra. Notice that the reciprocal of the fraction of air ($1-f_{\text{air}}$), corresponds very well with the coverage factor presented in table 6.1, except for the 12 mM 0 cycle sample. The obtained fraction of SnS (f_{SnS}) is expected to be small, with previous reports indicating a thickness of the shell in core-shell nanostructures fabricated by SILAR of around 5 nm [286]. However, the values obtained through the fitting procedure are exceedingly small for most samples. Interestingly, the 4 mM sample with 10 cycles, which in the SEM images is shown to be covered by SnS has a higher f_{SnS} compared to the 15 cycle sample of the same set. The 12

mM 15 cycle sample also shows a larger fraction of SnS compared to the 10 cycle sample, as expected. However, the quantitative values are of no significance, given the issues of the TMM in adequately modelling these samples.

In conclusion, while the TMM could approximate well the transmittance spectra, it is not suitable to model the spectral behavior of these samples due to their high scattering and their features being close to the wavelength of probing light. This, unlike what was seen in other chapters of this thesis, highlights the limitations of the TMM. The results could be improved using a dielectric function specific for ZnO NRs. However, an adequate treatment should involve the use of diffusive models.

6.5. Polarized light analysis

Recent studies have unveiled that ZnO nanorods exhibit pronounced optical anisotropy and polarization-sensitive photoluminescence (PL) due to their unique crystal structure and morphology [303]. This anisotropy is pivotal for the development of polarization-dependent devices, such as polarized light emitters and detectors, where the manipulation of light polarization is crucial [304]. Furthermore, the capability of ZnO nanorods to exhibit strong polarized emission has been exploited in enhancing the performance of ultraviolet (UV) photodetectors, offering a pathway to high-sensitivity and polarization-selective UV sensing [305]. The inherent polarization properties of ZnO nanorods are attributed to their wurtzite crystal structure, which facilitates the separation of electric field components parallel and perpendicular to the rod axis, leading to differential absorption and emission properties [306, 307]. In this context, we studied the polarization behaviour of our samples through the Stokes parameters at a wavelength of 785 nm, a wavelength far from the absorption edges of the constituents, resulting in negligible absorption.

The anisotropy results in birefringence, a material property where there is a direction dependent refractive index. In general, the birefringence of the bulk ZnO crystal is very small, and nanorods and nanowire arrays have been proposed as “external” macroscopic birefringent materials, in which the effect arises from the ordered 1D morphology. A smooth anisotropic crystal, like those used in waveplates (like HWP and QWP), alters the polarization state of light but maintains the degree of polarization (P), as it does not introduce randomness (see section 2.7.1 for an introduction on polarization in the context of statistical optics). The study of the degree of polarization serves to a) evaluate the suitability of the as synthesized NR/NT arrays for polarization sensitive applications and b) it may give insights into the uniformity of the nanorod distribution. An ordered, uniform ensemble should preserve the degree of polarization by eliminating randomness

associated with a distribution of different scatterers, resulting in an external macroscopic waveplate-like sample.

In principle, the deposited nanoparticles themselves are not expected to affect the degree of polarization, as they are small in comparison to the wavelength of light and thus scatter in the Rayleigh regime [308], resulting in well defined polarizations. However, the complex architecture of our samples promotes multiple scattering events, leading to randomization of light paths and a consequent mix of polarization states, identified as a primary mechanism for polarization loss as discussed in section 2.7. This multiple scattering events should be mainly a consequence of a) a distribution of nanorods of different dimensions and orientations and b) a non uniform distribution of SnS, specially of the larger clusters, the diameters of which are comparable to the dimensions of the nanorods (see $D_{cluster}$ in table 6.1). The surface roughness of SnS particles on NR/NT surfaces might also influence depolarization, although its impact is presumed minimal due to the relative scale of surface roughness compared to the larger scale inhomogeneities presented by the disordered nanorod arrays. It's also worth noting that the structural stability of the samples and negligible heating effects at the incident power used suggest no significant temporal variations in properties, with measurements conducted at equilibrium.

We now focus our attention towards figures 6.9a and 6.9c which show the degree of polarization (P) as a function of angle of incidence for the 4 mM set, in transmittance and reflectance, respectively. Notice that the corresponding degree of polarization for a glass plate appears as a grey dashed line, which gives a reference of the behaviour of a relatively smooth, uniform sample. In transmittance (6.9a) we see that all samples show almost the same polarization around the normal direction, within 2%. A similar trend is observed in reflectance (6.9c), where the general behaviour of all samples is similar. These samples all have similar average dimensions, as can be seen in table 6.1, which could explain the similarities in P. This in turn suggest that the deposition of SnS by itself does not modify substantially the degree of polarization, as expected.

The transmittance is flat, which suggest that there is no preferential orientation of the nanorod arrays around the normal incidence. In reflectance the samples have a similar behaviour between each other, but there tends to be an increase in the degree of polarization as the angle of incidence increases, which may be a consequence of two factors. Firstly, at large angles of incidence the reflectance of the glass plate is very large, while that of the disordered NRs is expected to be similar at every angle, which means that the response may be dominated by the polarization-conserving glass substrate. Secondly, Brewster's angle of bulk ZnO is around 60 degrees. At this angle, reflected light is perfectly polarized and it is possible that the ZnO seed layer contributes to the high degree of polarization. Clearly this does not apply to the ZnO NR/NTs, as their orientation means that light is

not necessarily reflected from their walls at the critical angle condition. The reflectance curves do not show very sharp features, suggesting that there is no preferential growth direction in the nanorod array. An exception may be the 4 mM 15 cycle sample, which shows what appears to be a feature close to 38 degrees, and may indicate the presence of a preferential direction, but with a very large standard deviation in the distribution, as the feature is not sharp. Finally, notice that the degree of polarization in transmittance is similar to that of the glass plate, while there is a large loss in P in reflectance. This may be related to the fact that at $\lambda = 785$ nm, the haze in reflectance is around 75% whereas that in transmittance is only around 25%.

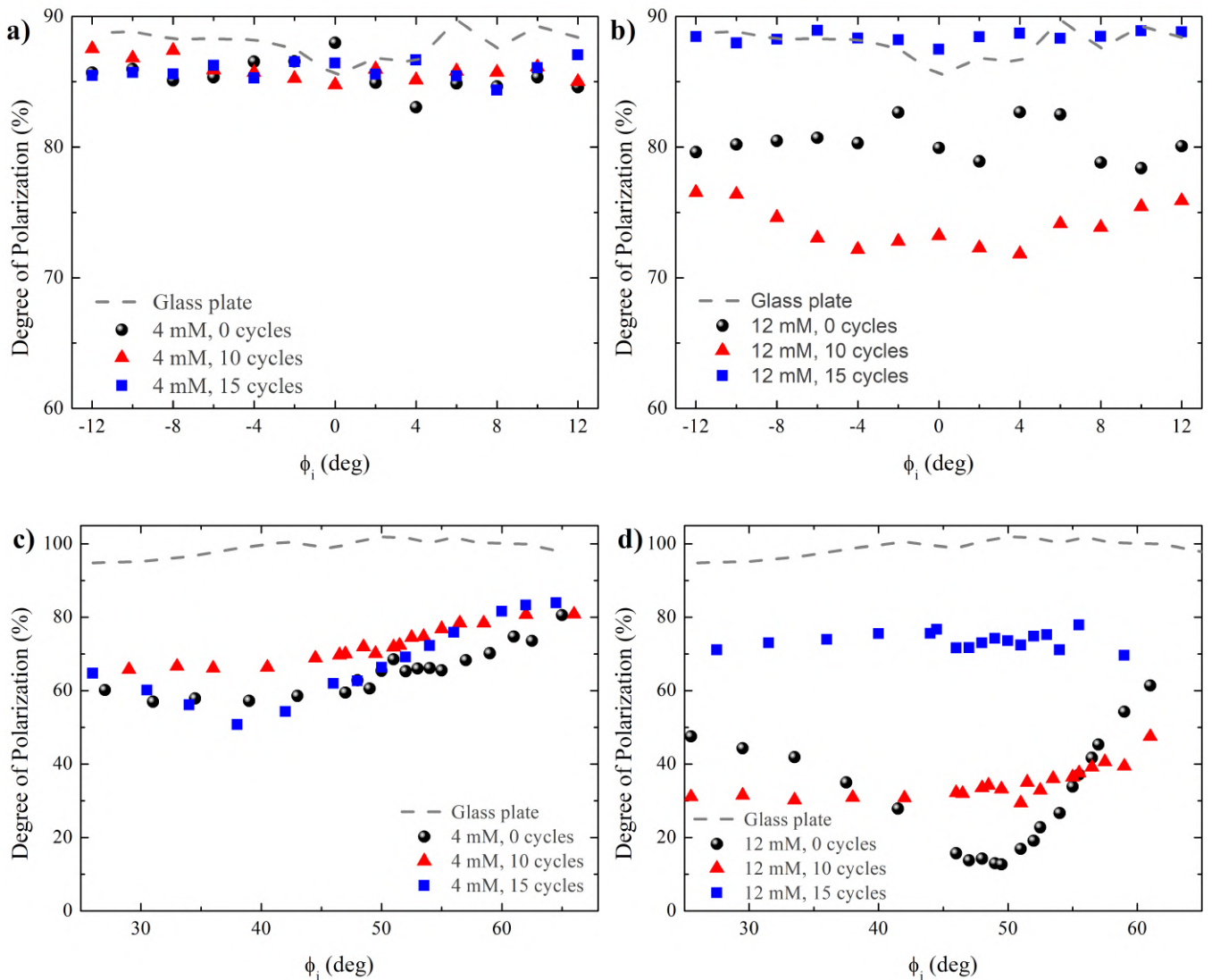


Figure 6.9: Degree of polarization as a function of the angle of incidence in transmittance for the a) 4 mM and b) 12 mM sets and in reflectance for the c) 4 mM and d) 12 mM sets. All plots have a dashed line that indicates the measured degree of polarization for a glass slide 1.25 mm thick.

The 12 mM set shows a different behaviour. From figure 6.9b we see that the degree of polarization for all samples is mostly flat, indicating that there is no preferential direction close to the substrate normal. However, we see a decrease in P in the 0 cycles and specially the 10 cycles sample. These set shows large discrepancies in dimensions, which could explain why there are differences in the degree of polarization between the samples, unlike what was observed in the case of the 4 mM set. The 15 cycle sample preserves polarization as much as the glass plate, which may be related to the fact that the haze is around 25% compared to the 50% of the other samples (see figure 6.4d). This effect could be attributed to the relatively uniform dimensions of the NR/NTs, captured in the small standard deviations of the diameter and apparent length in table 6.1. This deviations are of the order of those found in the 4 mM set, which displayed a very similar degree of polarization around normal incidence. On the contrary, the 0 and 10 cycle samples have a wider distribution of sizes and higher transmittance haze, which may explain the decrease in the degree of polarization observed in figure 6.9b.

In reflectance, figure 6.9d, we see that the sensitized samples show a response that is mostly flat, indicative of a lack of preferential direction. This contrasts with the 0 cycle sample, which displays a very clear feature near 50° . This may suggest the existence of a preferential growth direction compared to the other samples. Unlike the 4 mM, 15 cycle sample, this feature is pronounced, which may indicate that there is a relatively narrower distribution of orientations. All samples show an increase in the degree of polarization when the angle of incidence increases, as was the case for the 4 mM set, suggesting that it is indeed an effect of the substrate, which is common to all samples. This set reduces the degree of polarization when compared to the glass plate, which can be associated with the large haze, as shown in figure 6.4b. Notice that the 12mM 15 cycle sample has a reflectance haze at 785 nm similar to that of the 4 mM set, around 75%, while they also share a similar degree of polarization, close to 70%. On the contrary, the 12 mM samples with 0 and 10 cycles have more haze and a lower degree of polarization.

The correlation between features in the degree of polarization and the existence of a preferential direction of growth in the nanorod arrays can be qualitatively understood as follows. If the incident light is aligned to the preferential growth direction of the nanorods (c-axis) then some rays will find gaps between the nanorods and will not be scattered. Others will be scattered, but the interaction with the nanorods will be minimized. This situation is depicted in figure 6.10a. Compare this situation to that shown in figure 6.10b, where light is incident at an oblique angle relative to the preferential direction. In this case the light will be incident upon the side of the nanorods, which results in more occurrences of scattering events while it traverses the sample. As more scattering events result in a greater degree of polarization loss, it is expected that in the second case the light will be

more depolarized. If the distribution of nanorods is totally random, meaning that there is no preferential direction, these situations can not be distinguished and there should not be a dependence with the angle of incidence.

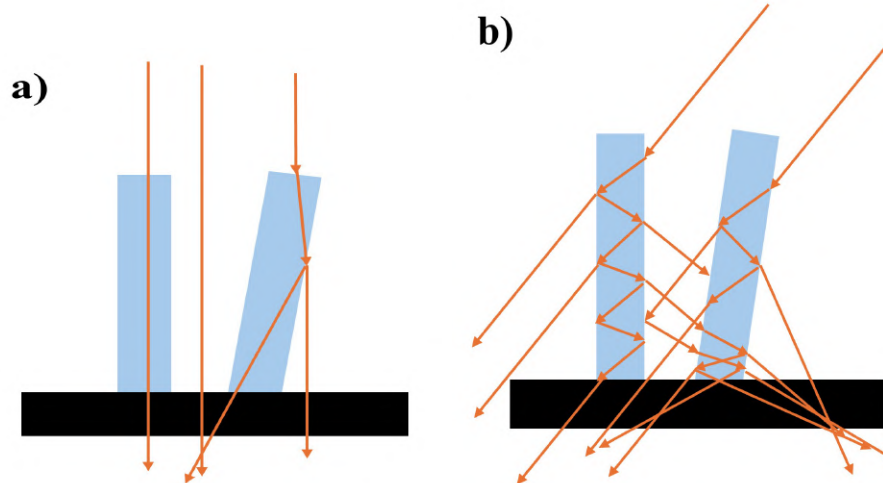


Figure 6.10: Schematics used to discuss the angular dependence of the degree of polarization. in a) the angle of incidence is close to the preferential growth direction, and the light rays can go straight through caps, while at b) oblique incidence there are more interactions with the nanorods, enhancing multiple scattering.

The degree of polarization in the 4 mM is similar for most samples, while in the 12 mM set the behaviours are different. As can be seen in table 6.1 the first set has similar dimensions, while the second displays large differences. This suggests that the changes in degree of polarization are due to changes in morphology between the samples, which may affect multiple scattering. In order to quantify the effects of morphology, we calculate the aspect ratio, L_{app}/D , for the samples using the values obtained from the SEM images. Figures 6.11a and 6.11b show the average degree of polarization and the haze at $\lambda = 785nm$ as a function of the aspect ratio, for transmittance and reflectance, respectively.

We can clearly see in both cases that, as the aspect ratio increases, P decreases. This dependency with the aspect ratio has already been reported in the literature by our group [309]. This suggests that the main factor affecting the degree of polarization is not the presence of SnS nanoparticles themselves, but rather the difference in the dimensions of the nanostructures. This is consistent with the idea that the main mechanisms leading to a decrease in the degree of polarization is multiple scattering.

Figure 6.11 also highlights the relationship between degree of polarization and haze. In general, the less dispersive samples better preserve the degree of polarization, consistent with the link of multiple scattering and polarization loss previously reported by our

group[310]. The 4 mM 10 cycles sample is not shown because it does not have a defined aspect ratio due to lack of visible NRs. These relationship between haze and aspect ratio also helps to explain the tendencies observed in the spectral dependence of the haze, shown in figure 6.4.

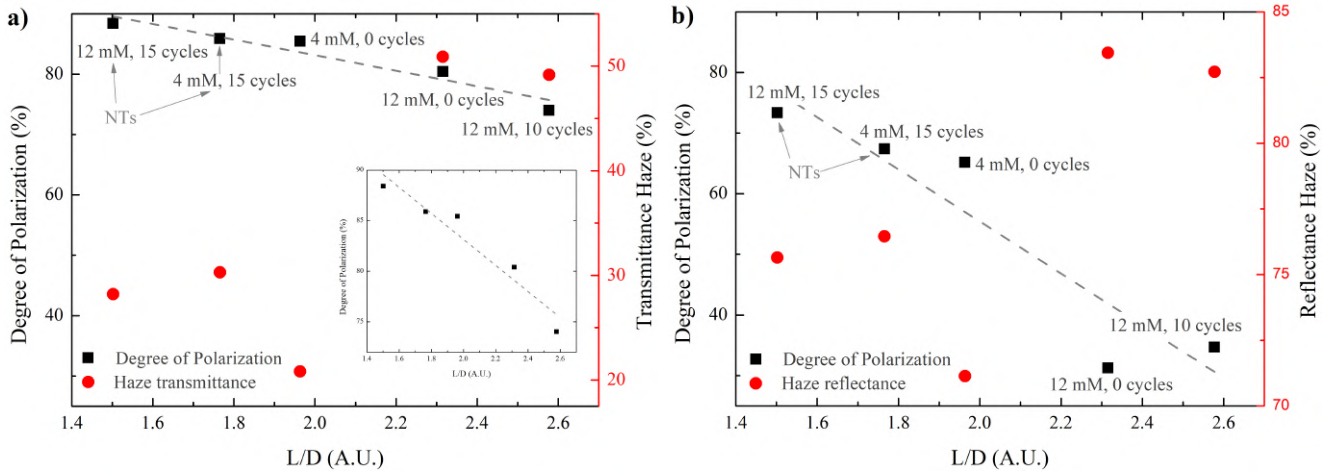


Figure 6.11: Average degree of Polarization (P) and Haze as at $\lambda = 785\text{nm}$ in the cases of a) transmittance, where the inset shows a close up of the degree of polarization, and b) reflectance. Dashed gray line indicates the linear fit for the polarization of the samples. The samples that show nanotubes (NTs) are indicated.

The results presented in this section highlight the variety of behaviours achievable with NRs/NTs arrays by controlling the morphology in the nanostructures. An important insight is that, at this wavelength in the transparent region of the materials, it depends mainly on the underlying nanostructures and not on the deposited material. Although multiple scattering, mainly affected by NR dimensions, appears to be the main contributor to the effects of the degree of polarization, it is possible that other factors such as crystallinity, surface roughness, the random distribution of sensitizer, or the presence of NTs also play a role. In order to study the influence of these factors, the effects should be isolated by working with samples with controlled parameters. In particular, it would be of great interest fabricating pairs of samples of the same dimensions, one with nanorods and the other with nanotubes, to elucidate the difference in the interaction of the structures with polarized light. As can be seen in the figures, the highly sensitized samples displaying nanotubes tend to result in the highest degrees of polarization. However, this effect can not be separated from those resulting from size differences in this set of samples.

6.6. Conclusions and future perspectives

In this chapter, we investigated the morphological and optical properties of ZnO nanorods sensitized with SnS via SILAR. Scanning electron microscopy (SEM) revealed the formation of ZnO nanorods, with some samples exhibiting nanotube structures after sensitization. Spectral reflectance and transmittance measurements were conducted, with the shift in the spectra upon sensitization highlighting the potential of the technique to tailor the absorption. The absorption edges were fitted through the Tauc plot method, successfully reconstructing the absorbance spectra. Both a direct and indirect bandgap were observed with gap energies consistent with quantum confinement effects.

The Urbach energy, a parameter defining the width of the Urbach tail, also displayed variations potentially linked to the specific nanostructures. Our simulations demonstrate that while there is no temperature increase in our experimental conditions, nanotubes with thicker SnS walls have less stress in the SnS shell, consistent with a thinner Urbach tail.

We further attempted to model the light propagation within the samples using the transfer matrix method; however, the results indicated limitations in its applicability to these complex nanomaterials. Even though the transmittance spectra could be reproduced by fitting the volume fractions in the air-ZnO-SnS layer, the corresponding reflectance spectra showed almost no similarities compared to experiments, except for the overall range of values. These results, and considering that the samples are highly diffusive as demonstrated by the haze measurements, suggest that diffusive models are more appropriate to study the propagation in these samples.

Finally, the degree of polarization was studied, revealing a negative correlation with the aspect ratio, consistent with previous reports for nanorod arrays. Furthermore, it was shown that the more diffusive samples, tended to be the ones which lowered the degree of polarization of light the most, suggesting that the main mechanism of polarization loss is multiple scattering. This could be expected because the surface roughness and the spatial variations in the refractive index introduced by the SnS are small, at least in the transparent region, compared to the large scale inhomogeneities of the underlying NR/NTs structure.

To further elucidate the observed phenomena, future research should involve the investigation of larger sample sets with well-isolated and controlled properties. This systematic approach, where only one parameter is varied at a time, would enable a more precise understanding of the individual effects of the fabrication parameters on the structural and optical characteristics.

Moreover, the development of more sophisticated diffusive models specifically tailored to these types of nanomaterials is needed. Such models could provide deeper insights

into light propagation within the ZnO-SnS nanostructures, leading to the design and optimization of materials with desired optical properties for various applications. A good starting point are the two-flux models previously employed by our group in the study of NR arrays.

Finally, first-principles or DFT calculations [311, 312] are crucial for investigating the dependence of the Urbach tail energy on the structural differences between nanorods and nanotubes. This is important for two key reasons. Firstly, the simulations employed solve for the continuum and assume bulk-like properties. However, there may be large deviations at the nanoscale, especially as dimensions approach the phonon mean free path. Previous studies indicate relevant contributions to thermal conductivity from phonons with mean free paths up to 15 nm [313], which is larger than both the nanocrystal sizes calculated from the absorption edge shifts (using the Brus formula) and the typical SILAR-deposited thicknesses of 5 nm. Secondly, DFT calculations can provide the phonon dispersion relationships in nanorods and nanotubes. Though temperature may not be a significant factor in our samples, variations in phonon modes between the two structures could provide valuable insights.

Chapter 7

Conclusion and future perspectives

Throughout this work we studied the optical properties of very different nanostructured materials, beginning with dielectric thin films of SiO_2 , then working with the wings of the translucent butterfly and the common moth and lastly with ZnO NR/NTs sensitized with SnS. In all chapters the application and suitability of the developed and implemented TMM was evaluated. We found that for the films the application of the model is straightforward and accurate. On the other hand, the limitations of the model were highlighted by the other samples, particularly the ZnO NRs. In the case of the insect wings, we found that the polarization conversion effects made the TMM incapable of modelling the polarization behaviour of the samples, even though when evaluating unpolarized light the results were satisfactory. In the later samples, we observed that the TMM is not suitable for their analysis, and diffusive models should be applied.

The first outcome of this thesis is the TMM and related codes, including the possibility to work with incoherent layers and mixed media through the EMA. This adds another tool to the library of the group, with the possibility to aid in the explanation of other materials and devices in the future. In order to gain a better understanding of the model, and to take maximum advantage, more suitable samples than the ones used in the later part of this work are required. It would be interesting to apply it to stack of thin films, in particular using the semiconductor materials currently under study in the group. After the characterization of their optical properties, for example, the TMM could be used to optimize the thicknesses in a stack of multilayers to maximize solar absorption, with potential application in photovoltaic solar cells. It could be promising to build on the silicon dioxide platform, as these films are simple to fabricate, low cost, and have smooth surfaces with high levels of homogeneity.

The other outcomes refer to the specific interesting properties of each of the complex samples. In the case of the wings of the translucent butterfly and the common moth, the polarization conversion effects were particularly remarkable. As detailed in that section,

a more comprehensive study of this phenomena is needed, and promises very interesting challenges. Understanding this phenomenon would not only contribute to scientific knowledge, but also develop the group's tools to work and understand the effects of complex structures on polarized light. Maybe the biggest achievement of this section of the work was the setup of a collaboration with the groups of Analytical Biochemistry and Entomology at the Faculty of Sciences, which promises to be an avenue for fruitful discussions in the future.

In the NR/NTs samples the most novel aspect was the formation of NTs, as detailed throughout chapter 6. This is very interesting because, even though the GFES has vast experience working with ZnO NRs, it had never encountered NTs. Future work should focus on obtaining samples with well defined characteristics, trying to have NRs and NTs with the same dimensions (length, external diameter and coverage), in order to elucidate the differences between the nanostructures.

Overall, from this work a new tool for result analysis was developed, and its application in different materials successfully evaluated. Due to the very different nature of the samples, a wide variety of potential research directions can be taken from this work.

7.1. List of publications

7.1.1. In peer reviewed Journals

Martinez Juan P. et al. "Crossed polarization optical transmittance spectra as a way of determining wing thickness of the *Episcada Hymenaea* translucent butterfly". In: *MRS Advances* (July 24, 2023). ISSN: 2059-8521. DOI: [10.1557/s43580-023-00614-1](https://doi.org/10.1557/s43580-023-00614-1)

7.1.2. Congress presentations

1. Poster: Martinez Juan Pedro et al. "Propiedades ópticas de nanorods de ZnO sensibilizados con SnS". in: *Reunión de la Sociedad Uruguaya de Física, XVII SUF 2022 "José A. Ferrari"*. XVII SUF 2022 "José A. Ferrari". Nueva Helvecia, Uruguay, Nov. 4, 2022
2. Poster: Pereyra Mariana et al. "Transparency in Insects: A Study of the Physicochemical, Optical, and Morphological Factors". In: *Proceedings of the 7th International Meeting for Researchers in Materials and Plasma Technology*. 7th International Meeting for Researchers in Materials and Plasma Technology. Cartagena de Indias, Colombia, June 2023

3. Poster: Martinez Juan Pedro et al. “Elementos ópticos de origen natural: Caracterización y modelado”. In: *II Encuentro de Investigadores en Ciencia de Materiales*. II Encuentro de Investigadores en Ciencia de Materiales. Montevideo, Uruguay, Apr. 20, 2023

References

- [1] Fox Anthony Mark. “Introduction”. In: *Optical Properties of Solids*. Oxford University Press, 2001, p. 6. ISBN: 978-0-19-850612-6.
- [2] Makuła Patrycja, Pacia Michał, and Macyk Wojciech. “How To Correctly Determine the Band Gap Energy of Modified Semiconductor Photocatalysts Based on UV–Vis Spectra”. In: *The Journal of Physical Chemistry Letters* 9.23 (Dec. 6, 2018), pp. 6814–6817. ISSN: 1948-7185, 1948-7185. DOI: [10.1021/acs.jpcllett.8b02892](https://doi.org/10.1021/acs.jpcllett.8b02892).
- [3] Yu Peter Y. and Cardona Manuel. *Fundamentals of Semiconductors: Physics and Materials Properties*. Graduate Texts in Physics. Berlin, Heidelberg: Springer Berlin Heidelberg, 2010. ISBN: 978-3-642-00709-5 978-3-642-00710-1. DOI: [10.1007/978-3-642-00710-1](https://doi.org/10.1007/978-3-642-00710-1).
- [4] Pereyra C. J. et al. “Optical Properties of Sensitized Zinc Oxide Nanorods Electrochemically Prepared”. In: *Energy and Environment Focus* 2.4 (Feb. 2014). Publisher: American Scientific Publishers, pp. 257–269. ISSN: 2326-3040. DOI: [10.1166/eef.2013.1061](https://doi.org/10.1166/eef.2013.1061).
- [5] Aragonès Albert C. et al. “Study and improvement of aluminium doped ZnO thin films: Limits and advantages”. In: *Electrochimica Acta* 109 (Oct. 2013), pp. 117–124. ISSN: 00134686. DOI: [10.1016/j.electacta.2013.07.053](https://doi.org/10.1016/j.electacta.2013.07.053).
- [6] Pereyra C. J. et al. “Optical Properties of Sensitized Zinc Oxide Nanorods Electrochemically Prepared”. In: *Energy and Environment Focus* 2.4 (Dec. 1, 2013), pp. 257–269. ISSN: 2326-3040. DOI: [10.1166/eef.2013.1061](https://doi.org/10.1166/eef.2013.1061).
- [7] Chavez M et al. “Optical band gap energy and urbach tail of CdS:Pb²⁺ thin films”. In: *THIN FILMS* (2016).
- [8] Dow John D. and Redfield David. “Toward a Unified Theory of Urbach’s Rule and Exponential Absorption Edges”. In: *Physical Review B* 5.2 (Jan. 15, 1972), pp. 594–610. ISSN: 0556-2805. DOI: [10.1103/PhysRevB.5.594](https://doi.org/10.1103/PhysRevB.5.594).

- [9] Thouless D.J. “Electrons in disordered systems and the theory of localization”. In: *Physics Reports* 13.3 (Oct. 1974), pp. 93–142. ISSN: 03701573. DOI: [10.1016/0370-1573\(74\)90029-5](https://doi.org/10.1016/0370-1573(74)90029-5).
- [10] Piccardo Marco et al. “Localization landscape theory of disorder in semiconductors. II. Urbach tails of disordered quantum well layers”. In: *Physical Review B* 95.14 (Apr. 18, 2017), p. 144205. ISSN: 2469-9950, 2469-9969. DOI: [10.1103/PhysRevB.95.144205](https://doi.org/10.1103/PhysRevB.95.144205).
- [11] Iribarren A. et al. “Modeling of the disorder contribution to the band-tail parameter in semiconductor materials”. In: *Physical Review B* 60.7 (Aug. 15, 1999), pp. 4758–4762. ISSN: 0163-1829, 1095-3795. DOI: [10.1103/PhysRevB.60.4758](https://doi.org/10.1103/PhysRevB.60.4758).
- [12] Iribarren A. et al. “Band-tail parameter modeling in semiconductor materials”. In: *Physical Review B* 58.4 (July 15, 1998), pp. 1907–1911. ISSN: 0163-1829, 1095-3795. DOI: [10.1103/PhysRevB.58.1907](https://doi.org/10.1103/PhysRevB.58.1907).
- [13] Caballero-Briones F. et al. “Disruption of the Chemical Environment and Electronic Structure in p-Type Cu_2O Films by Alkaline Doping”. In: *The Journal of Physical Chemistry C* 116.25 (June 28, 2012), pp. 13524–13535. ISSN: 1932-7447, 1932-7455. DOI: [10.1021/jp3023937](https://doi.org/10.1021/jp3023937).
- [14] Cody G. D. et al. “Disorder and the Optical-Absorption Edge of Hydrogenated Amorphous Silicon”. In: *Physical Review Letters* 47.20 (Nov. 16, 1981), pp. 1480–1483. ISSN: 0031-9007. DOI: [10.1103/PhysRevLett.47.1480](https://doi.org/10.1103/PhysRevLett.47.1480).
- [15] Abay B. et al. “Temperature dependence of the optical energy gap and Urbach–Martienssen’s tail in the absorption spectra of the layered semiconductor $\text{Tl}_2\text{GaInSe}_4$ ”. In: *Journal of Physics and Chemistry of Solids* 62.4 (Apr. 2001), pp. 747–752. ISSN: 00223697. DOI: [10.1016/S0022-3697\(00\)00236-5](https://doi.org/10.1016/S0022-3697(00)00236-5).
- [16] He Huan et al. “Temperature dependence of the bandgap and Urbach’s tail in the transmittance spectra of wurtzite AlN film”. In: *Vacuum* 100 (Feb. 2014), pp. 33–35. ISSN: 0042207X. DOI: [10.1016/j.vacuum.2013.07.027](https://doi.org/10.1016/j.vacuum.2013.07.027).
- [17] Ledinsky Martin et al. “Temperature Dependence of the Urbach Energy in Lead Iodide Perovskites”. In: *The Journal of Physical Chemistry Letters* 10.6 (Mar. 21, 2019), pp. 1368–1373. ISSN: 1948-7185, 1948-7185. DOI: [10.1021/acs.jpcclett.9b00138](https://doi.org/10.1021/acs.jpcclett.9b00138).
- [18] Kittel Charles. *Introduction to solid state physics*. 8. ed., [repr.] Hoboken, NJ: Wiley. 680 pp. ISBN: 978-0-471-41526-8.

- [19] Brus Louis. “Electronic wave functions in semiconductor clusters: experiment and theory”. In: *The Journal of Physical Chemistry* 90.12 (June 1986), pp. 2555–2560. ISSN: 0022-3654, 1541-5740. DOI: [10.1021/j100403a003](https://doi.org/10.1021/j100403a003).
- [20] Kayanuma Yosuke. “Quantum-size effects of interacting electrons and holes in semiconductor microcrystals with spherical shape”. In: *Physical Review B* 38.14 (Nov. 15, 1988), pp. 9797–9805. ISSN: 0163-1829. DOI: [10.1103/PhysRevB.38.9797](https://doi.org/10.1103/PhysRevB.38.9797).
- [21] Chukwuocha Ephrem O., Onyeaju Michael C., and Harry Taylor S. T. “Theoretical Studies on the Effect of Confinement on Quantum Dots Using the Brus Equation”. In: *World Journal of Condensed Matter Physics* 02.2 (2012), pp. 96–100. ISSN: 2160-6919, 2160-6927. DOI: [10.4236/wjcmp.2012.22017](https://doi.org/10.4236/wjcmp.2012.22017).
- [22] Stenzel Olaf. *The Physics of Thin Film Optical Spectra: An Introduction*. 1st ed. Vol. 1. Springer Berlin Heidelberg, 2009. 49-52.
- [23] Zhao Lin et al. “Theoretical and experimental investigation of haze in transparent aerogels”. In: *Optics Express* 27.4 (Feb. 18, 2019), A39. ISSN: 1094-4087. DOI: [10.1364/OE.27.000A39](https://doi.org/10.1364/OE.27.000A39).
- [24] ASTM. *Standard Test Method for Haze and Luminous Transmittance of Transparent Plastics*. Version 21. 2021. DOI: [10.1520/D1003-21](https://doi.org/10.1520/D1003-21).
- [25] Ramírez Daniel et al. “Electrochemical synthesis of CuSCN nanostructures, tuning the morphological and structural characteristics: From nanorods to nanostructured layers”. In: *Materials Science in Semiconductor Processing* 68 (Sept. 2017), pp. 226–237. ISSN: 13698001. DOI: [10.1016/j.mssp.2017.06.030](https://doi.org/10.1016/j.mssp.2017.06.030).
- [26] Bassan Paul et al. “Resonant Mie scattering in infrared spectroscopy of biological materials – understanding the ‘dispersion artefact’”. In: *The Analyst* 134.8 (2009), p. 1586. ISSN: 0003-2654, 1364-5528. DOI: [10.1039/b904808a](https://doi.org/10.1039/b904808a).
- [27] Hecht E. *Optics*. 4th ed. Pearson education. Addison-Wesley, 2002. ISBN: 978-0-321-18878-6.
- [28] Pedrotti Frank L., Pedrotti Leno M., and Pedrotti Leno S. *Introduction to Optics*. Cambridge University Press, Dec. 2017. ISBN: 978-1-108-42826-2. DOI: [10.1017/9781108552493](https://doi.org/10.1017/9781108552493).
- [29] Born Max et al. *Principles of Optics*. Cambridge University Press, Oct. 1999. ISBN: 978-0-521-64222-4. DOI: [10.1017/CBO9781139644181](https://doi.org/10.1017/CBO9781139644181).
- [30] Ohman G. P. “The pseudo-Brewster angle”. In: *IEEE Transactions on Antennas and Propagation* 25 (Nov. 1977), p. 903. DOI: [10.1109/TAP.1977.1141718](https://doi.org/10.1109/TAP.1977.1141718).

- [31] Elshazly-Zaghloul M. and Azzam R. M. A. “Brewster and pseudo-Brewster angles of uniaxial crystal surfaces and their use for determination of optical properties”. In: *Journal of the Optical Society of America* 72.5 (May 1982). Publisher: Optica Publishing Group, p. 657. ISSN: 0030-3941. DOI: [10.1364/JOSA.72.000657](https://doi.org/10.1364/JOSA.72.000657).
- [32] Hecht Eugene. “Interference”. In: *Optics*. 5th ed. Pearson Education, Incorporated, 2017, pp. 385–438. ISBN: 978-0-13-397722-6.
- [33] Saito Akira. “Material design and structural color inspired by biomimetic approach”. In: *Science and Technology of Advanced Materials* 12.6 (Dec. 2011), p. 064709. ISSN: 1468-6996, 1878-5514. DOI: [10.1088/1468-6996/12/6/064709](https://doi.org/10.1088/1468-6996/12/6/064709).
- [34] Dushkina Natalia and Lakhtakia Akhlesh. “Structural Colors”. In: *Engineered Biomimicry*. Elsevier, 2013, pp. 267–303. ISBN: 978-0-12-415995-2. DOI: [10.1016/B978-0-12-415995-2.00011-8](https://doi.org/10.1016/B978-0-12-415995-2.00011-8).
- [35] Saleh Bahaa E. A. and Teich Malvin Carl. *Fundamentals of Photonics*. 1st ed. Wiley, Aug. 14, 1991. ISBN: 978-0-471-83965-1 978-0-471-21374-1. DOI: [10.1002/0471213748](https://doi.org/10.1002/0471213748).
- [36] Stenzel Olaf. “Thick Slabs and Thin Films”. In: *The Physics of Thin Film Optical Spectra: An Introduction*. Ed. by Stenzel Olaf. 2nd ed. Springer Series in Surface Sciences. Cham: Springer International Publishing, 2016, pp. 131–161. ISBN: 978-3-319-21602-7. DOI: [10.1007/978-3-319-21602-7_7](https://doi.org/10.1007/978-3-319-21602-7_7).
- [37] Nichelatti Enrico. “Complex refractive index of a slab from reflectance and transmittance: analytical solution”. In: *Journal of Optics A: Pure and Applied Optics* 4.4 (July 2002), pp. 400–403. ISSN: 14644258. DOI: [10.1088/1464-4258/4/4/306](https://doi.org/10.1088/1464-4258/4/4/306).
- [38] Azzam R. M. and Bashara N. M. *Ellipsometry and Polarized Light*. 1st ed. Vol. 1. North-Holland, 1977. 332-340.
- [39] Centurioni Emanuele. “Generalized matrix method for calculation of internal light energy flux in mixed coherent and incoherent multilayers”. In: *Applied Optics* 44.35 (Dec. 2005), p. 7532. ISSN: 0003-6935, 1539-4522. DOI: [10.1364/AO.44.007532](https://doi.org/10.1364/AO.44.007532).
- [40] Troparevsky M. Claudia et al. *Transfer-matrix formalism for the calculation of optical response in multilayer systems: from coherent to incoherent interference*. 2010.
- [41] Katsidis Charalambos C. and Siapakas Dimitrios I. “General transfer-matrix method for optical multilayer systems with coherent, partially coherent, and incoherent interference”. In: *Applied Optics* 41.19 (July 2002), p. 3978. ISSN: 0003-6935, 1539-4522. DOI: [10.1364/AO.41.003978](https://doi.org/10.1364/AO.41.003978).

- [42] Tompkins Harland G. and Hilfiker James N. “Optical Data Analysis”. In: *Spectroscopic Ellipsometry: Practical Application to Thin Film Characterization*. 1st ed. NY: Momentum Press, Dec. 2015, pp. 89–92. ISBN: 978-1-60650-728-5.
- [43] Nazarov Ravshanjon, Zhang Tianmiao, and Khodzitsky Mikhail. “Effective medium theory for multi-component materials based on iterative method”. In: *Photonics* 7.4 (Dec. 2020). Publisher: MDPI AG, pp. 1–8. ISSN: 23046732. DOI: [10.3390/photonics7040113](https://doi.org/10.3390/photonics7040113).
- [44] Roussel Ph J., Vanhellemont J., and Maes H. E. *Numerical aspects of the implementation of effective-medium approximation models in spectroscopic ellipsometry regression software*. Publication Title: Thin Solid Films Volume: 234. 1993, pp. 423–427.
- [45] Voshchinnikov N. V., Il'in V. B., and Henning Th. “Modelling the optical properties of composite and porous interstellar grains”. In: *Astronomy & Astrophysics* 429.2 (Jan. 2005), pp. 371–381. ISSN: 0004-6361, 1432-0746. DOI: [10.1051/0004-6361:200400081](https://doi.org/10.1051/0004-6361:200400081).
- [46] Tuononen Heikki et al. “Wiener Bounds for Complex Permittivity in Terahertz Spectroscopy: Case Study of Two-Phase Pharmaceutical Tablets”. In: *Applied Spectroscopy* 64.1 (Jan. 2010), pp. 127–131. ISSN: 0003-7028, 1943-3530. DOI: [10.1366/000370210792966170](https://doi.org/10.1366/000370210792966170).
- [47] Milton G. W. “Bounds on the complex permittivity of a two-component composite material”. In: *Journal of Applied Physics* 52.8 (Aug. 1, 1981), pp. 5286–5293. ISSN: 0021-8979, 1089-7550. DOI: [10.1063/1.329385](https://doi.org/10.1063/1.329385).
- [48] Flossmann Florian et al. “Stokes parameters in the unfolding of an optical vortex through a birefringent crystal”. In: *Optics Express* 14.23 (2006), p. 11402. ISSN: 1094-4087. DOI: [10.1364/OE.14.011402](https://doi.org/10.1364/OE.14.011402).
- [49] Shurcliff William A. *Polarized Light: Production and Use*. Cambridge, MA and London, England: Harvard University Press, 1962. ISBN: 978-0-674-42413-5. DOI: [doi:10.4159/harvard.9780674424135](https://doi.org/10.4159/harvard.9780674424135).
- [50] Tompkins Harland and Irene Eugene A. *Handbook of Ellipsometry*. 1st ed. Vol. 1. William Andrew, 2005. 289-290.
- [51] Chu Wei-Ping et al. “Using high haze ($> 90\%$) light-trapping film to enhance the efficiency of a-Si:H solar cells”. In: *Optics Communications* 285.15 (July 2012), pp. 3325–3328. ISSN: 00304018. DOI: [10.1016/j.optcom.2012.02.088](https://doi.org/10.1016/j.optcom.2012.02.088).

- [52] Campo Lucia et al. “The Effect of a Sputtered Al-Doped ZnO Seed Layer on the Morphological, Structural and Optical Properties of Electrochemically Grown ZnO Nanorod Arrays”. In: *Journal of The Electrochemical Society* 163.8 (2016). Publisher: The Electrochemical Society, pp. D392–D400. ISSN: 0013-4651. DOI: [10.1149/2.0611608jes](https://doi.org/10.1149/2.0611608jes).
- [53] ThorLabs. *RP20 - Reflection Probe*. 2014.
- [54] Kawanishi Tetsuya et al. “Brewster’s scattering angle and quasi-anomalous scattering in random scattering from dielectric interfaces”. In: *Journal of the Optical Society of America A* 16.2 (Feb. 1, 1999), p. 339. ISSN: 1084-7529, 1520-8532. DOI: [10.1364/JOSAA.16.000339](https://doi.org/10.1364/JOSAA.16.000339).
- [55] Cocolezzi G. H. and Wang S. “Resonant scattering of light by excitonic rough surfaces”. In: *Physical Review B* 48.23 (Dec. 15, 1993), pp. 17413–17417. ISSN: 0163-1829, 1095-3795. DOI: [10.1103/PhysRevB.48.17413](https://doi.org/10.1103/PhysRevB.48.17413).
- [56] Lagendijk Ad and Van Tiggelen Bart A. “Resonant multiple scattering of light”. In: *Physics Reports* 270.3 (May 1996), pp. 143–215. ISSN: 03701573. DOI: [10.1016/0370-1573\(95\)00065-8](https://doi.org/10.1016/0370-1573(95)00065-8).
- [57] Basalaeva L.S. et al. “Resonance reflection of light by ordered silicon nanopillar arrays with the vertical p-n junction”. In: *Thin Solid Films* 672 (Feb. 2019), pp. 109–113. ISSN: 00406090. DOI: [10.1016/j.tsf.2019.01.007](https://doi.org/10.1016/j.tsf.2019.01.007).
- [58] Vennberg Felix, Ravishankar Ajith Padyana, and Anand Srinivasan. “Manipulating light scattering and optical confinement in vertically stacked Mie resonators”. In: *Nanophotonics* 11.21 (Nov. 30, 2022), pp. 4755–4764. ISSN: 2192-8614. DOI: [10.1515/nanoph-2022-0605](https://doi.org/10.1515/nanoph-2022-0605).
- [59] Massoud Hisham Z. “The onset of the thermal oxidation of silicon from room temperature to 1000°C”. In: *Microelectronic Engineering. Insulating Films on Semiconductors* 28.1 (June 1, 1995), pp. 109–116. ISSN: 0167-9317. DOI: [10.1016/0167-9317\(95\)00026-5](https://doi.org/10.1016/0167-9317(95)00026-5).
- [60] Hashim U. et al. “Comparison of deal grove model growth rate with dry thermal oxidation process for ultra-thin silicon dioxide film”. In: *2015 2nd International Conference on Biomedical Engineering (ICoBE)*. 2015 2nd International Conference on Biomedical Engineering (ICoBE). Penang, Malaysia: IEEE, Mar. 2015, pp. 1–4. ISBN: 978-1-4799-1749-5. DOI: [10.1109/ICoBE.2015.7235905](https://doi.org/10.1109/ICoBE.2015.7235905).
- [61] Dutta Tirthankar and Ravindra N. M. “Simulation and Modeling of Kinetics of Silicon Oxidation in the thin Oxide Regime”. In: *MRS Proceedings* 237 (1991), p. 649. ISSN: 0272-9172, 1946-4274. DOI: [10.1557/PROC-237-649](https://doi.org/10.1557/PROC-237-649).

- [62] Sarti G. C., Santarelli F., and Camera Roda G. “Kinetics of thermal growth of thin silicon oxide films”. In: *Chemical Engineering Science* 41.10 (Jan. 1, 1986), pp. 2699–2705. ISSN: 0009-2509. DOI: [10.1016/0009-2509\(86\)80059-8](https://doi.org/10.1016/0009-2509(86)80059-8).
- [63] Chabal Yves J., ed. *Fundamental Aspects of Silicon Oxidation*. Red. by Zunger Alex et al. Vol. 46. Springer Series in Materials Science. Berlin, Heidelberg: Springer Berlin Heidelberg, 2001. ISBN: 978-3-642-62583-1 978-3-642-56711-7. DOI: [10.1007/978-3-642-56711-7](https://doi.org/10.1007/978-3-642-56711-7).
- [64] Athanassouli A et al. “Morphology and oxidation kinetics of SiO₂ layers on silicon”. In: *Semiconductor Science and Technology* 17.1 (Jan. 1, 2002), pp. 65–76. ISSN: 0268-1242. DOI: [10.1088/0268-1242/17/1/311](https://doi.org/10.1088/0268-1242/17/1/311).
- [65] Reed Michael L. and Fedder Gary K. “Photolithographic Microfabrication”. In: *Handbook of Sensors and Actuators*. Vol. 6. Elsevier, 1998, pp. 13–61. ISBN: 978-0-444-82363-2. DOI: [10.1016/S1386-2766\(98\)80003-0](https://doi.org/10.1016/S1386-2766(98)80003-0).
- [66] Massoud Hisham Z., Plummer James D., and Irene Eugene A. “Thermal Oxidation of Silicon in Dry Oxygen Growth-Rate Enhancement in the Thin Regime: I . Experimental Results”. In: *Journal of The Electrochemical Society* 132.11 (Nov. 1, 1985), pp. 2685–2693. ISSN: 0013-4651, 1945-7111. DOI: [10.1149/1.2113648](https://doi.org/10.1149/1.2113648).
- [67] Gerlach Gerald and Maser Karl. “A Self-Consistent Model for Thermal Oxidation of Silicon at Low Oxide Thickness”. In: *Advances in Condensed Matter Physics* 2016 (Apr. 19, 2016). Publisher: Hindawi, e7545632. ISSN: 1687-8108. DOI: [10.1155/2016/7545632](https://doi.org/10.1155/2016/7545632).
- [68] Mutilin S. V. and Khasanov T. “The refractive index of homogeneous SiO₂ thin films”. In: *Optics and Spectroscopy* 105.3 (Sept. 2008), pp. 461–465. ISSN: 0030-400X, 1562-6911. DOI: [10.1134/S0030400X0809018X](https://doi.org/10.1134/S0030400X0809018X).
- [69] Lukosz W. and Pliska P. “Determination of thickness and refractive index of SiO₂ films on silicon wafers using an Abbe refractometer”. In: *Optics Communications* 85.5 (Oct. 1991), pp. 381–384. ISSN: 00304018. DOI: [10.1016/0030-4018\(91\)90567-W](https://doi.org/10.1016/0030-4018(91)90567-W).
- [70] Pliskin W. A. and Esch R. P. “Refractive Index of SiO₂ Films Grown on Silicon”. In: *Journal of Applied Physics* 36.6 (June 1, 1965), pp. 2011–2013. ISSN: 0021-8979, 1089-7550. DOI: [10.1063/1.1714393](https://doi.org/10.1063/1.1714393).
- [71] Hryciw Aaron. *nanoFAB - sithox — toolbox.nanofab.ualberta.ca*.
- [72] Muduli Manisha and Yamamoto Hiromichi. “Thin Dry Silicon Oxide Films Grown by Thermal Oxidation”. In: (2020).

- [73] Schaeffer H.A. “Silica”. In: *Concise Encyclopedia of Advanced Ceramic Materials*. Elsevier, 1991, pp. 416–419. ISBN: 978-0-08-034720-2. DOI: [10.1016/B978-0-08-034720-2.50114-3](https://doi.org/10.1016/B978-0-08-034720-2.50114-3).
- [74] Deal B. E. and Grove A. S. “General Relationship for the Thermal Oxidation of Silicon”. In: *Journal of Applied Physics* 36.12 (Dec. 1, 1965), pp. 3770–3778. ISSN: 0021-8979, 1089-7550. DOI: [10.1063/1.1713945](https://doi.org/10.1063/1.1713945).
- [75] Illinois Urbana-Champaign University of. *ECE Illinois - ece444: GT7 - Oxide Thickness Color Chart*. URL: <https://fabweb.ece.illinois.edu/gt/gt/gt7.aspx> (visited on 01/20/2024).
- [76] Gao L., Lemarchand F., and Lequime M. “Refractive index determination of SiO₂ layer in the UV/Vis/NIR range: spectrophotometric reverse engineering on single and bi-layer designs”. In: *Journal of the European Optical Society: Rapid Publications* 8 (Jan. 31, 2013), p. 13010. ISSN: 1990-2573. DOI: [10.2971/jeos.2013.13010](https://doi.org/10.2971/jeos.2013.13010).
- [77] Schinke Carsten et al. “Uncertainty analysis for the coefficient of band-to-band absorption of crystalline silicon”. In: *AIP Advances* 5.6 (June 1, 2015), p. 067168. ISSN: 2158-3226. DOI: [10.1063/1.4923379](https://doi.org/10.1063/1.4923379).
- [78] Hidayat Romel et al. “Selective etching mechanism of silicon oxide against silicon by hydrogen fluoride: a density functional theory study”. In: *Physical Chemistry Chemical Physics* 25.5 (2023), pp. 3890–3899. ISSN: 1463-9076, 1463-9084. DOI: [10.1039/D2CP05456F](https://doi.org/10.1039/D2CP05456F).
- [79] Wang R. Z. et al. “Deformation mechanisms in nacre”. In: *Journal of Materials Research* 16.9 (Sept. 2001), pp. 2485–2493. ISSN: 0884-2914, 2044-5326. DOI: [10.1557/JMR.2001.0340](https://doi.org/10.1557/JMR.2001.0340).
- [80] Bhushan Bharat, Jung Yong Chae, and Koch Kerstin. “Micro-, nano- and hierarchical structures for superhydrophobicity, self-cleaning and low adhesion”. In: *Philosophical Transactions of the Royal Society A: Mathematical, Physical and Engineering Sciences* 367.1894 (May 2009), pp. 1631–1672. ISSN: 1364-503X, 1471-2962. DOI: [10.1098/rsta.2009.0014](https://doi.org/10.1098/rsta.2009.0014).
- [81] Koch Kerstin et al. “Fabrication of artificial Lotus leaves and significance of hierarchical structure for superhydrophobicity and low adhesion”. In: *Soft Matter* 5.7 (2009), p. 1386. ISSN: 1744-683X, 1744-6848. DOI: [10.1039/b818940d](https://doi.org/10.1039/b818940d).
- [82] Dean Brian and Bhushan Bharat. “Shark-skin surfaces for fluid-drag reduction in turbulent flow: a review”. In: *Philosophical Transactions of the Royal Society A: Mathematical, Physical and Engineering Sciences* 368.1929 (Oct. 2010), pp. 4775–4806. ISSN: 1364-503X, 1471-2962. DOI: [10.1098/rsta.2010.0201](https://doi.org/10.1098/rsta.2010.0201).

- [83] Wang Yayun, Naleway Steven E., and Wang Bin. “Biological and bioinspired materials: Structure leading to functional and mechanical performance”. In: *Bioactive Materials* 5.4 (Dec. 2020), pp. 745–757. ISSN: 2452-199X. DOI: [10.1016/j.bioactmat.2020.06.003](https://doi.org/10.1016/j.bioactmat.2020.06.003).
- [84] Zi Jian et al. “Coloration strategies in peacock feathers”. In: *Proceedings of the National Academy of Sciences* 100.22 (Oct. 28, 2003), pp. 12576–12578. ISSN: 0027-8424, 1091-6490. DOI: [10.1073/pnas.2133313100](https://doi.org/10.1073/pnas.2133313100).
- [85] Dushkina Natalia, Erten Sema, and Lakhtakia Akhlesh. “Coloration and Structure of the Wings of *Chorinea sylphina* Bates”. In: *Journal of the Lepidopterists’ Society* 71.1 (Mar. 2017), pp. 1–11. ISSN: 0024-0966. DOI: [10.18473/lepi.v71i1.a2](https://doi.org/10.18473/lepi.v71i1.a2).
- [86] Li Run, Zhang Shiliang, and Zhang Rufan. “Recent progress in artificial structural colors and their applications in fibers and textiles”. In: *Chemistry–Methods* n/a (n/a Feb. 2023), e202200081. ISSN: 2628-9725. DOI: [10.1002/cmt.202200081](https://doi.org/10.1002/cmt.202200081).
- [87] Feng Li et al. “Review of recent advancements in the biomimicry of structural colors”. In: *Dyes and Pigments* 210 (Feb. 1, 2023), p. 111019. ISSN: 0143-7208. DOI: [10.1016/j.dyepig.2022.111019](https://doi.org/10.1016/j.dyepig.2022.111019).
- [88] Dumanli Ahu Gümrah and Savin Thierry. “Recent advances in the biomimicry of structural colours”. In: *Chemical Society Reviews* 45.24 (2016), pp. 6698–6724. ISSN: 0306-0012, 1460-4744. DOI: [10.1039/C6CS00129G](https://doi.org/10.1039/C6CS00129G).
- [89] Blandin P. *The Systematics of Genus Morpho, Fabricius, 1807: (Lepidoptera, Nymphalidae, Morphinae)*. Hillside Books, 2007.
- [90] Le Moulton E. & Réal P. *Les Morpho d’Amérique du Sud et Centrale : historique, morphologie, systématique / / E. Le Moulton & P. Réal*. Vol. 2. 2 vols. Novitates entomologicae. Supplément ; – A. Paris: Éditions du Cabinet Entomologique E. Le Moulton, 1962.
- [91] Llaurens Violaine et al. “Convergence in sympatry: Evolution of blue-banded wing pattern in *Morpho* butterflies”. In: *Journal of Evolutionary Biology* 34.2 (Feb. 2021), pp. 284–295. ISSN: 1010-061X, 1420-9101. DOI: [10.1111/jeb.13726](https://doi.org/10.1111/jeb.13726).
- [92] Zhang Sichao and Chen Yifang. “Nanofabrication and coloration study of artificial *Morpho* butterfly wings with aligned lamellae layers”. In: *Scientific Reports* 5.1 (Nov. 2015), p. 16637. ISSN: 2045-2322. DOI: [10.1038/srep16637](https://doi.org/10.1038/srep16637).
- [93] Zobl Sigrid et al. “*Morpho peleides* butterfly wing imprints as structural colour stamp”. In: *Bioinspiration & Biomimetics* 11.1 (Feb. 2016), p. 016006. ISSN: 1748-3190. DOI: [10.1088/1748-3190/11/1/016006](https://doi.org/10.1088/1748-3190/11/1/016006).

- [94] Zhang Ke et al. “Polarization-sensitive color in butterfly scales: polarization conversion from ridges with reflecting elements”. In: *Optics Express* 22.22 (Nov. 2014), p. 27437. ISSN: 1094-4087. DOI: [10.1364/OE.22.027437](https://doi.org/10.1364/OE.22.027437).
- [95] Liu Feng et al. “Structural colouration and optical effects in the wings of *Papilio peranthus*”. In: *Journal of Optics* 12.6 (June 2010), p. 065301. ISSN: 2040-8978, 2040-8986. DOI: [10.1088/2040-8978/12/6/065301](https://doi.org/10.1088/2040-8978/12/6/065301).
- [96] Stavenga Doekele G., Giraldo Marco A., and Leertouwer Hein L. “Butterfly wing colors: glass scales of *Graphium sarpedon* cause polarized iridescence and enhance blue/green pigment coloration of the wing membrane”. In: *Journal of Experimental Biology* 213.10 (May 2010), pp. 1731–1739. ISSN: 1477-9145, 0022-0949. DOI: [10.1242/jeb.041434](https://doi.org/10.1242/jeb.041434).
- [97] Stavenga Doekele G. “The wing scales of the mother-of-pearl butterfly, *Protopionomorpha parhassus*, are thin film reflectors causing strong iridescence and polarization”. In: *Journal of Experimental Biology* 224.15 (Aug. 2021), jeb242983. ISSN: 0022-0949, 1477-9145. DOI: [10.1242/jeb.242983](https://doi.org/10.1242/jeb.242983).
- [98] Siddique Radwanul Hasan, Gomard Guillaume, and Hölscher Hendrik. “The role of random nanostructures for the omnidirectional anti-reflection properties of the glasswing butterfly”. In: *Nature Communications* 6.1 (Apr. 2015), p. 6909. ISSN: 2041-1723. DOI: [10.1038/ncomms7909](https://doi.org/10.1038/ncomms7909).
- [99] Han Zhiwu et al. “Bioinspired Omnidirectional Self-Stable Reflectors with Multiscale Hierarchical Structures”. In: *ACS Applied Materials & Interfaces* 9.34 (Aug. 30, 2017), pp. 29285–29294. ISSN: 1944-8244, 1944-8252. DOI: [10.1021/acsami.7b08768](https://doi.org/10.1021/acsami.7b08768).
- [100] Barrera-Patiño C. P. et al. “Photonic effects in natural nanostructures on *Morpho cypris* and *Greta oto* butterfly wings”. In: *Scientific Reports* 10.1 (Apr. 1, 2020). Number: 1 Publisher: Nature Publishing Group, p. 5786. ISSN: 2045-2322. DOI: [10.1038/s41598-020-62770-w](https://doi.org/10.1038/s41598-020-62770-w).
- [101] Proietti Zaccaria Remo. “Butterfly wing color: A photonic crystal demonstration”. In: *Optics and Lasers in Engineering* 76 (Jan. 2016), pp. 70–73. ISSN: 01438166. DOI: [10.1016/j.optlaseng.2015.04.008](https://doi.org/10.1016/j.optlaseng.2015.04.008).
- [102] Corkery Robert W. and Tyrode Eric C. “On the colour of wing scales in butterflies: iridescence and preferred orientation of single gyroid photonic crystals”. In: *Interface Focus* 7.4 (Aug. 6, 2017), p. 20160154. ISSN: 2042-8898, 2042-8901. DOI: [10.1098/rsfs.2016.0154](https://doi.org/10.1098/rsfs.2016.0154).

- [103] Lee Jinwoo et al. “Biomimetic reconstruction of butterfly wing scale nanostructures for radiative cooling and structural coloration”. In: *Nanoscale Horizons* 7.9 (2022), pp. 1054–1064. ISSN: 2055-6756, 2055-6764. DOI: [10.1039/D2NH00166G](https://doi.org/10.1039/D2NH00166G).
- [104] Potyrailo Radislav A. et al. “Morpho butterfly wing scales demonstrate highly selective vapour response”. In: *Nature Photonics* 1.2 (Feb. 2007), pp. 123–128. ISSN: 1749-4885, 1749-4893. DOI: [10.1038/nphoton.2007.2](https://doi.org/10.1038/nphoton.2007.2).
- [105] Osotsi Maurice I et al. “Butterfly wing architectures inspire sensor and energy applications”. In: *National Science Review* 8.3 (Mar. 2021), nwa107. ISSN: 2095-5138, 2053-714X. DOI: [10.1093/nsr/nwaa107](https://doi.org/10.1093/nsr/nwaa107).
- [106] Garrett Natalie L. et al. “Bio-sensing with butterfly wings: naturally occurring nano-structures for SERS-based malaria parasite detection”. In: *Physical Chemistry Chemical Physics* 17.33 (Aug. 2015), pp. 21164–21168. ISSN: 1463-9084. DOI: [10.1039/C4CP04930F](https://doi.org/10.1039/C4CP04930F).
- [107] Tsai Cheng-Chia et al. “Physical and behavioral adaptations to prevent overheating of the living wings of butterflies”. In: *Nature Communications* 11.1 (Jan. 28, 2020). Publisher: Nature Publishing Group, p. 551. ISSN: 2041-1723. DOI: [10.1038/s41467-020-14408-8](https://doi.org/10.1038/s41467-020-14408-8).
- [108] Goularte Nicolette F., Kalle Till, and Cegelski Lynette. “Chemical and Molecular Composition of the Chrysalis Reveals Common Chitin-Rich Structural Framework for Monarchs and Swallowtails”. In: *Journal of Molecular Biology* 434.5 (Mar. 2022), p. 167456. ISSN: 00222836. DOI: [10.1016/j.jmb.2022.167456](https://doi.org/10.1016/j.jmb.2022.167456).
- [109] Lin Tze-Chung et al. “Gyroid-structured nanoporous chitosan from block copolymer template for UVC reflection”. In: *NPG Asia Materials* 15.1 (Mar. 31, 2023). Number: 1 Publisher: Nature Publishing Group, pp. 1–9. ISSN: 1884-4057. DOI: [10.1038/s41427-022-00440-1](https://doi.org/10.1038/s41427-022-00440-1).
- [110] Yu R.-R. et al. “LmCDA1 organizes the cuticle by chitin deacetylation in *Locusta migratoria*”. In: *Insect Molecular Biology* 28.3 (June 2019), pp. 301–312. ISSN: 0962-1075, 1365-2583. DOI: [10.1111/imb.12554](https://doi.org/10.1111/imb.12554).
- [111] Munro Joshua T. et al. “Climate is a strong predictor of near-infrared reflectance but a poor predictor of colour in butterflies”. In: *Proceedings of the Royal Society B: Biological Sciences* 286.1898 (Mar. 13, 2019), p. 20190234. ISSN: 0962-8452, 1471-2954. DOI: [10.1098/rspb.2019.0234](https://doi.org/10.1098/rspb.2019.0234).

- [112] Krishna Anirudh et al. “Air temperature drives the evolution of mid-infrared optical properties of butterfly wings”. In: *Scientific Reports* 11.1 (Dec. 17, 2021). Publisher: Nature Publishing Group, p. 24143. ISSN: 2045-2322. DOI: [10.1038/s41598-021-02810-1](https://doi.org/10.1038/s41598-021-02810-1).
- [113] Slegers Nathan et al. “Beneficial aerodynamic effect of wing scales on the climbing flight of butterflies”. In: *Bioinspiration & Biomimetics* 12.1 (Jan. 2017). Publisher: IOP Publishing, p. 016013. ISSN: 1748-3190. DOI: [10.1088/1748-3190/aa551d](https://doi.org/10.1088/1748-3190/aa551d).
- [114] Vukusic Peter and Sambles J. Roy. “Shedding light on butterfly wings”. In: International Symposium on Optical Science and Technology. Ed. by Lalanne Philippe. San Diego, CA, USA, Dec. 26, 2001, p. 85. DOI: [10.1117/12.451481](https://doi.org/10.1117/12.451481).
- [115] Ghiradella Helen. “Structure of butterfly scales: Patterning in an insect cuticle”. In: *Microscopy Research and Technique* 27.5 (Apr. 1994), pp. 429–438. ISSN: 1059-910X, 1097-0029. DOI: [10.1002/jemt.1070270509](https://doi.org/10.1002/jemt.1070270509).
- [116] Neville Anthony C. *Biology of the Arthropod Cuticle*. Berlin, Heidelberg: Springer Berlin Heidelberg, 1975. ISBN: 978-3-642-80912-5 978-3-642-80910-1. DOI: [10.1007/978-3-642-80910-1](https://doi.org/10.1007/978-3-642-80910-1).
- [117] Niu Shichao et al. “Excellent Structure-Based Multifunction of Morpho Butterfly Wings: A Review”. In: *Journal of Bionic Engineering* 12.2 (June 2015), pp. 170–189. ISSN: 1672-6529, 2543-2141. DOI: [10.1016/S1672-6529\(14\)60111-6](https://doi.org/10.1016/S1672-6529(14)60111-6).
- [118] Finet Cédric et al. “Multi-scale dissection of wing transparency in the clear-wing butterfly *Phanus vitreus*”. In: *Journal of The Royal Society Interface* 20.202 (May 31, 2023). Publisher: Royal Society, p. 20230135. DOI: [10.1098/rsif.2023.0135](https://doi.org/10.1098/rsif.2023.0135).
- [119] Kim Seungho et al. “How a raindrop gets shattered on biological surfaces”. In: *Proceedings of the National Academy of Sciences* 117.25 (June 23, 2020), pp. 13901–13907. ISSN: 0027-8424, 1091-6490. DOI: [10.1073/pnas.2002924117](https://doi.org/10.1073/pnas.2002924117).
- [120] Greve Roberto R. et al. “Butterflies (Lepidoptera: Papilionoidea) of Iguazu National Park and surrounding areas in southern Brazil: a long-term survey, with six new records for the Brazilian fauna”. In: *Biota Neotropica* 23 (Sept. 15, 2023). Publisher: Instituto Virtual da Biodiversidade — BIOTA - FAPESP, e20231487. ISSN: 1676-0611. DOI: [10.1590/1676-0611-BN-2023-1487](https://doi.org/10.1590/1676-0611-BN-2023-1487).
- [121] Willmott Keith R. and Freitas André V. L. “Higher-level phylogeny of the Ithomiinae (Lepidoptera: Nymphalidae): classification, patterns of larval hostplant colonization and diversification”. In: *Cladistics* 22.4 (2006). -

- eprint: <https://onlinelibrary.wiley.com/doi/pdf/10.1111/j.1096-0031.2006.00108.x>, pp. 297–368. ISSN: 1096-0031. DOI: [10.1111/j.1096-0031.2006.00108.x](https://doi.org/10.1111/j.1096-0031.2006.00108.x).
- [122] Binetti Valerie R. et al. “The natural transparency and piezoelectric response of the Greta oto butterfly wing”. In: *Integrative Biology* 1.4 (2009), p. 324. ISSN: 1757-9694, 1757-9708. DOI: [10.1039/b820205b](https://doi.org/10.1039/b820205b).
- [123] Arias Mónica et al. “Partial wing transparency works better when disrupting wing edges: Evidence from a field experiment”. In: *Journal of Evolutionary Biology* 34.11 (2021). eprint: <https://onlinelibrary.wiley.com/doi/pdf/10.1111/jeb.13943>, pp. 1840–1846. ISSN: 1420-9101. DOI: [10.1111/jeb.13943](https://doi.org/10.1111/jeb.13943).
- [124] Gomez Doris et al. “Wing transparency in butterflies and moths: structural diversity, optical properties, and ecological relevance”. In: *Ecological Monographs* 91.4 (2021). eprint: <https://onlinelibrary.wiley.com/doi/pdf/10.1002/ecm.1475>, e01475. ISSN: 1557-7015. DOI: [10.1002/ecm.1475](https://doi.org/10.1002/ecm.1475).
- [125] Azoifeifa Daniel E., Arguedas Humberto J., and Vargas William E. “Optical properties of chitin and chitosan biopolymers with application to structural color analysis”. In: *Optical Materials* 35.2 (Dec. 2012), pp. 175–183. ISSN: 09253467. DOI: [10.1016/j.optmat.2012.07.024](https://doi.org/10.1016/j.optmat.2012.07.024).
- [126] Abd El-Kader F.H., Gaafer S.A., and Abd El-Kader M.F.H. “Characterization and optical studies of 90/10 (wt/wt%) PVA/-chitin blend irradiated with -rays”. In: *Spectrochimica Acta Part A: Molecular and Biomolecular Spectroscopy* 131 (Oct. 2014), pp. 564–570. ISSN: 13861425. DOI: [10.1016/j.saa.2014.04.088](https://doi.org/10.1016/j.saa.2014.04.088).
- [127] Ravi Kumar Majeti N. V. “A review of chitin and chitosan applications”. In: *Reactive and Functional Polymers* 46.1 (Nov. 1, 2000), pp. 1–27. ISSN: 1381-5148. DOI: [10.1016/S1381-5148\(00\)00038-9](https://doi.org/10.1016/S1381-5148(00)00038-9).
- [128] Leertouwer Hein L., Wilts Bodo D., and Stavenga Doekele G. “Refractive index and dispersion of butterfly chitin and bird keratin measured by polarizing interference microscopy”. In: *Optics Express* 19.24 (Nov. 2011), pp. 24061–24066. ISSN: 1094-4087. DOI: [10.1364/OE.19.024061](https://doi.org/10.1364/OE.19.024061).
- [129] Ragaie Mohamed, Sabry Al-Kazafy Hassan, and Abdel-Rahman Atef. “Insect’s photonic crystals and their applications”. In: ()
- [130] Deparis Olivier et al. “Assessment of the antireflection property of moth wings by three-dimensional transfer-matrix optical simulations”. In: *Physical Review E* 79.4 (Apr. 8, 2009), p. 041910. ISSN: 1539-3755, 1550-2376. DOI: [10.1103/PhysRevE.79.041910](https://doi.org/10.1103/PhysRevE.79.041910).

- [131] Yoshioka S et al. “Coloration using higher order optical interference in the wing pattern of the Madagascan sunset moth”. In: *Journal of The Royal Society Interface* 5.21 (Nov. 13, 2007). Publisher: Royal Society, pp. 457–464. DOI: [10.1098/rsif.2007.1268](https://doi.org/10.1098/rsif.2007.1268).
- [132] Stavenga Doekele G. et al. “Classical lepidopteran wing scale colouration in the giant butterfly-moth *Paysandisia archon*”. In: *PeerJ* 6 (Apr. 11, 2018). Publisher: PeerJ Inc., e4590. ISSN: 2167-8359. DOI: [10.7717/peerj.4590](https://doi.org/10.7717/peerj.4590).
- [133] Negrea P et al. “THE STUDY OF INFRARED SPECTRUM OF CHITIN AND CHITOSAN EXTRACT AS POTENTIAL SOURCES OF BIOMASS”. In: ().
- [134] Baxter A. et al. “Improved method for i.r. determination of the degree of N-acetylation of chitosan”. In: *International Journal of Biological Macromolecules* 14.3 (June 1992), pp. 166–169. ISSN: 0141-8130. DOI: [10.1016/s0141-8130\(05\)80007-8](https://doi.org/10.1016/s0141-8130(05)80007-8).
- [135] Shigemasa Yoshihiro et al. “Evaluation of different absorbance ratios from infrared spectroscopy for analyzing the degree of deacetylation in chitin”. In: *International Journal of Biological Macromolecules* 18.3 (Apr. 1996), pp. 237–242. ISSN: 01418130. DOI: [10.1016/0141-8130\(95\)01079-3](https://doi.org/10.1016/0141-8130(95)01079-3).
- [136] Vu Tuan Duc et al. “A universal robust bottom-up approach to engineer Greta-oto-inspired anti-reflective structure”. In: *Cell Reports Physical Science* 2.7 (July 21, 2021), p. 100479. ISSN: 2666-3864. DOI: [10.1016/j.xcrp.2021.100479](https://doi.org/10.1016/j.xcrp.2021.100479).
- [137] Hanlon Roger T et al. “White reflection from cuttlefish skin leucophores”. In: *Bioinspiration & Biomimetics* 13.3 (Mar. 20, 2018), p. 035002. ISSN: 1748-3190. DOI: [10.1088/1748-3190/aaa3a9](https://doi.org/10.1088/1748-3190/aaa3a9).
- [138] Mähger Lydia M. et al. “Bright White Scattering from Protein Spheres in Color Changing, Flexible Cuttlefish Skin”. In: *Advanced Functional Materials* 23.32 (Aug. 26, 2013), pp. 3980–3989. ISSN: 1616-301X, 1616-3028. DOI: [10.1002/adfm.201203705](https://doi.org/10.1002/adfm.201203705).
- [139] Vukusic Pete, Hallam Benny, and Noyes Joe. “Brilliant Whiteness in Ultrathin Beetle Scales”. In: *Science* 315.5810 (Jan. 19, 2007), pp. 348–348. ISSN: 0036-8075, 1095-9203. DOI: [10.1126/science.1134666](https://doi.org/10.1126/science.1134666).
- [140] Ni Y. X. et al. “Controlling light scattering and polarization by spherical particles with radial anisotropy”. In: *Optics Express* 21.7 (Apr. 8, 2013), p. 8091. ISSN: 1094-4087. DOI: [10.1364/OE.21.008091](https://doi.org/10.1364/OE.21.008091).

- [141] Sromovsky L.A. “Effects of Rayleigh-scattering polarization on reflected intensity: a fast and accurate approximation method for atmospheres with aerosols”. In: *Icarus* 173.1 (Jan. 2005), pp. 284–294. ISSN: 00191035. DOI: [10.1016/j.icarus.2004.07.016](https://doi.org/10.1016/j.icarus.2004.07.016).
- [142] Kim Arnold D. et al. “Polarized light propagation and scattering in random media”. In: *BiOS 2001 The International Symposium on Biomedical Optics*. Ed. by Duncan Donald D., Jacques Steven L., and Johnson Peter C. San Jose, CA, July 9, 2001, p. 90. DOI: [10.1117/12.434691](https://doi.org/10.1117/12.434691).
- [143] Cheng Qian, Wang Ying-min, and Zhang Ying-luo. “Analysis of the polarization characteristics of scattered light of underwater suspended particles based on Mie theory”. In: *Optoelectronics Letters* 17.4 (Apr. 2021), pp. 252–256. ISSN: 1673-1905, 1993-5013. DOI: [10.1007/s11801-021-0039-0](https://doi.org/10.1007/s11801-021-0039-0).
- [144] Chen Weijin et al. “Global Mie Scattering: Polarization Morphologies and the Underlying Topological Invariant”. In: *ACS Omega* 5.23 (June 16, 2020), pp. 14157–14163. ISSN: 2470-1343, 2470-1343. DOI: [10.1021/acsomega.0c01843](https://doi.org/10.1021/acsomega.0c01843).
- [145] Fesenko Volodymyr I. and Sukhoivanov Igor A. “Polarization Conversion in Inhomogeneous Anisotropic Multilayer Structures”. In: *Lasers, Sources, and Related Photonic Devices*. Advances in Optical Materials. San Diego, California: OSA, 2012, JTh2A.7. ISBN: 978-1-55752-933-6. DOI: [10.1364/AIOM.2012.JTh2A.7](https://doi.org/10.1364/AIOM.2012.JTh2A.7).
- [146] Saba Matthias et al. “Group theory of circular-polarization effects in chiral photonic crystals with four-fold rotation axes applied to the eight-fold intergrowth of gyroid nets”. In: *Physical Review B* 88.24 (Dec. 11, 2013), p. 245116. ISSN: 1098-0121, 1550-235X. DOI: [10.1103/PhysRevB.88.245116](https://doi.org/10.1103/PhysRevB.88.245116).
- [147] Whitney Barbara A. and Wolff Michael J. “Scattering and Absorption by Aligned Grains in Circumstellar Environments”. In: *The Astrophysical Journal* 574.1 (July 20, 2002), pp. 205–231. ISSN: 0004-637X, 1538-4357. DOI: [10.1086/340901](https://doi.org/10.1086/340901).
- [148] Nichelatti E., Montecchi M., and Montereali R.M. “Optical reflectance and transmittance of a multilayer coating affected by refractive-index inhomogeneity, interface roughness, and thickness wedge”. In: *Journal of Non-Crystalline Solids* 355.18 (July 2009), pp. 1115–1118. ISSN: 00223093. DOI: [10.1016/j.jnoncrysol.2008.11.040](https://doi.org/10.1016/j.jnoncrysol.2008.11.040).
- [149] Montecchi Marco, Montereali Rosa Maria, and Nichelatti Enrico. “Reflectance and transmittance of a slightly inhomogeneous thin film bounded by rough, unparallel interfaces”. In: *Thin Solid Films* 396.1 (Sept. 2001), pp. 264–275. ISSN: 00406090. DOI: [10.1016/S0040-6090\(01\)01253-6](https://doi.org/10.1016/S0040-6090(01)01253-6).

- [150] Tikhonravov A. V. et al. “Influence of small inhomogeneities on the spectral characteristics of single thin films”. In: *Applied Optics* 36.28 (Oct. 1997), p. 7188. ISSN: 0003-6935, 1539-4522. DOI: [10.1364/AO.36.007188](https://doi.org/10.1364/AO.36.007188).
- [151] Stroud D. “The effective medium approximations: Some recent developments”. In: *Superlattices and Microstructures* 23.3 (Mar. 1998), pp. 567–573. ISSN: 07496036. DOI: [10.1006/spmi.1997.0524](https://doi.org/10.1006/spmi.1997.0524).
- [152] Saranathan Vinodkumar et al. “Structure, function, and self-assembly of single network gyroid ($I432$) photonic crystals in butterfly wing scales”. In: *Proceedings of the National Academy of Sciences* 107.26 (June 2010), pp. 11676–11681. ISSN: 0027-8424, 1091-6490. DOI: [10.1073/pnas.0909616107](https://doi.org/10.1073/pnas.0909616107).
- [153] Stoddart P R et al. “Optical properties of chitin: surface-enhanced Raman scattering substrates based on antireflection structures on cicada wings”. In: *Nanotechnology* 17.3 (Feb. 2006), pp. 680–686. ISSN: 0957-4484, 1361-6528. DOI: [10.1088/0957-4484/17/3/011](https://doi.org/10.1088/0957-4484/17/3/011).
- [154] Jacucci Gianni et al. “Light Management with Natural Materials: From Whiteness to Transparency”. In: *Advanced Materials* 33.28 (July 2021), p. 2001215. ISSN: 0935-9648, 1521-4095. DOI: [10.1002/adma.202001215](https://doi.org/10.1002/adma.202001215).
- [155] Kotsidas Panagiotis, Modi Vijay, and Gordon Jeffrey M. “Gradient-index lenses for near-ideal imaging and concentration with realistic materials”. In: *Optics Express* 19.16 (Aug. 1, 2011), p. 15584. ISSN: 1094-4087. DOI: [10.1364/OE.19.015584](https://doi.org/10.1364/OE.19.015584).
- [156] Moore Duncan T. “Gradient-index optics: a review”. In: *Applied Optics* 19.7 (Apr. 1, 1980), p. 1035. ISSN: 0003-6935, 1539-4522. DOI: [10.1364/AO.19.001035](https://doi.org/10.1364/AO.19.001035).
- [157] Han Z.W. et al. “Antireflective surface inspired from biology: A review”. In: *Bio-surface and Biotribology* 2.4 (Dec. 2016), pp. 137–150. ISSN: 24054518. DOI: [10.1016/j.bsbt.2016.11.002](https://doi.org/10.1016/j.bsbt.2016.11.002).
- [158] Yang Shikuan et al. “Ultra-antireflective synthetic brochosomes”. In: *Nature Communications* 8.1 (Nov. 3, 2017). Number: 1 Publisher: Nature Publishing Group, p. 1285. ISSN: 2041-1723. DOI: [10.1038/s41467-017-01404-8](https://doi.org/10.1038/s41467-017-01404-8).
- [159] Muthukrishnan Subbaratnam et al. “Insect Cuticular Chitin Contributes to Form and Function”. In: *Current pharmaceutical design* 26.29 (2020), pp. 3530–3545. ISSN: 1381-6128. DOI: [10.2174/1381612826666200523175409](https://doi.org/10.2174/1381612826666200523175409).
- [160] Smentkowski V et al. “Exploration of a Butterfly Wing Using a Diverse Suite of Characterization Techniques”. In: *Microscopy and Microanalysis* 12 (S02 Aug. 2006), pp. 1228–1229. ISSN: 1431-9276, 1435-8115. DOI: [10.1017/S1431927606067845](https://doi.org/10.1017/S1431927606067845).

- [161] Michielsen K and Stavenga D.G. “Gyroid cuticular structures in butterfly wing scales: biological photonic crystals”. In: *Journal of the Royal Society Interface* 5.18 (Jan. 6, 2008), pp. 85–94. ISSN: 1742-5689. DOI: [10.1098/rsif.2007.1065](https://doi.org/10.1098/rsif.2007.1065).
- [162] Santos Antonio et al. “Simultaneous Optical and Electrical Characterization of GaN Nanowire Arrays by Means of Vis-IR Spectroscopic Ellipsometry”. In: *The Journal of Physical Chemistry C* XXXX (Jan. 2019). DOI: [10.1021/acs.jpcc.9b10556](https://doi.org/10.1021/acs.jpcc.9b10556).
- [163] Garum Mohamed et al. “Ultrahigh-Resolution 3D Imaging for Quantifying the Pore Nanostructure of Shale and Predicting Gas Transport”. In: *Energy & Fuels* 35.1 (Jan. 7, 2021), pp. 702–717. ISSN: 0887-0624, 1520-5029. DOI: [10.1021/acs.energyfuels.0c03225](https://doi.org/10.1021/acs.energyfuels.0c03225).
- [164] Dallaeva Dinara Sultanovna and Tomanek Pavel. “AFM Study of Structure Influence on Butterfly Wings Coloration”. In: *Advances in Electrical and Electronic Engineering* 10.2 (June 30, 2012), pp. 120–124. ISSN: 1804-3119, 1336-1376. DOI: [10.15598/aeee.v10i2.616](https://doi.org/10.15598/aeee.v10i2.616).
- [165] Dallaeva Dinara et al. “AFM Imaging of Natural Optical Structures”. In: *APPLIED PHYSICS* 12.6 (2014).
- [166] Priyanka et al. “Smart strategy of butterfly wing scales to control the light diffusion and absorption”. In: *Journal of the Optical Society of America B* 38.8 (Aug. 1, 2021), p. 2297. ISSN: 0740-3224, 1520-8540. DOI: [10.1364/JOSAB.426003](https://doi.org/10.1364/JOSAB.426003).
- [167] Stavenga D. G., Giraldo M. A., and Hoenders B. J. “Reflectance and transmittance of light scattering scales stacked on the wings of pierid butterflies”. In: *Optics Express* 14.11 (May 29, 2006). Publisher: Optica Publishing Group, pp. 4880–4890. ISSN: 1094-4087. DOI: [10.1364/OE.14.004880](https://doi.org/10.1364/OE.14.004880).
- [168] Krishna Anirudh et al. “Infrared optical and thermal properties of microstructures in butterfly wings”. In: *Proceedings of the National Academy of Sciences* 117.3 (Jan. 21, 2020), pp. 1566–1572. ISSN: 0027-8424, 1091-6490. DOI: [10.1073/pnas.1906356117](https://doi.org/10.1073/pnas.1906356117).
- [169] Frezza Fabrizio, Mangini Fabio, and Tedeschi Nicola. “Introduction to electromagnetic scattering: tutorial”. In: *Journal of the Optical Society of America A* 35.1 (Jan. 1, 2018), p. 163. ISSN: 1084-7529, 1520-8532. DOI: [10.1364/JOSAA.35.000163](https://doi.org/10.1364/JOSAA.35.000163).
- [170] Sun Wenbo, Loeb Norman G., and Lin Bing. “Light Scattering by an Infinite Circular Cylinder Immersed in an Absorbing Medium”. In: *Applied Optics* 44.12 (Apr. 20, 2005), p. 2338. ISSN: 0003-6935, 1539-4522. DOI: [10.1364/AO.44.002338](https://doi.org/10.1364/AO.44.002338).

- [171] Bohren Craig F. and Huffman Donald R. *Absorption and Scattering of Light by Small Particles*. 1st ed. Wiley, Apr. 23, 1998. ISBN: 978-0-471-29340-8 978-3-527-61815-6. DOI: [10.1002/9783527618156](https://doi.org/10.1002/9783527618156).
- [172] Zhou Jianyang and Zhao Daomu. “Scattering of a random electromagnetic beam from a random medium with spectral dependence”. In: *Optics Express* 25.15 (July 24, 2017), p. 17114. ISSN: 1094-4087. DOI: [10.1364/OE.25.017114](https://doi.org/10.1364/OE.25.017114).
- [173] Berreman Dwight W. “Optics in Stratified and Anisotropic Media: 4×4 -Matrix Formulation”. In: *Journal of the Optical Society of America* 62.4 (Apr. 1, 1972), p. 502. ISSN: 0030-3941. DOI: [10.1364/JOSA.62.000502](https://doi.org/10.1364/JOSA.62.000502).
- [174] Yeh Pochi. “Electromagnetic propagation in birefringent layered media”. In: *Journal of the Optical Society of America* 69.5 (May 1, 1979), p. 742. ISSN: 0030-3941. DOI: [10.1364/JOSA.69.000742](https://doi.org/10.1364/JOSA.69.000742).
- [175] Yeh Pochi. “Optics of anisotropic layered media: A new 4×4 matrix algebra”. In: *Surface Science* 96.1 (June 1980), pp. 41–53. ISSN: 00396028. DOI: [10.1016/0039-6028\(80\)90293-9](https://doi.org/10.1016/0039-6028(80)90293-9).
- [176] Schubert Mathias. “Polarization-dependent optical parameters of arbitrarily anisotropic homogeneous layered systems”. In: *Physical Review B* 53.8 (Feb. 15, 1996), pp. 4265–4274. ISSN: 0163-1829, 1095-3795. DOI: [10.1103/PhysRevB.53.4265](https://doi.org/10.1103/PhysRevB.53.4265).
- [177] Goldstein Herbert, Poole Charles P., and Safko John L. *Classical Mechanics*. Google-Books-ID: tJCuQgAACAAJ. Addison Wesley, 2002. 638 pp. ISBN: 978-0-201-65702-9.
- [178] Arwin Hans et al. “Chirality-induced polarization effects in the cuticle of scarab beetles: 100 years after Michelson”. In: *Philosophical Magazine* 92.12 (Apr. 21, 2012), pp. 1583–1599. ISSN: 1478-6435, 1478-6443. DOI: [10.1080/14786435.2011.648228](https://doi.org/10.1080/14786435.2011.648228).
- [179] Scarangella Adriana, Soldan Vanessa, and Mitov Michel. “Biomimetic design of iridescent insect cuticles with tailored, self-organized cholesteric patterns”. In: *Nature Communications* 11.1 (Aug. 14, 2020). Number: 1 Publisher: Nature Publishing Group, p. 4108. ISSN: 2041-1723. DOI: [10.1038/s41467-020-17884-0](https://doi.org/10.1038/s41467-020-17884-0).
- [180] Wang Xiaoming and Yan Yanfa. “Optical activity of solids from first principles”. In: *Physical Review B* 107.4 (Jan. 2023), p. 045201. ISSN: 2469-9950, 2469-9969. DOI: [10.1103/PhysRevB.107.045201](https://doi.org/10.1103/PhysRevB.107.045201).

- [181] Belamie E., Davidson P., and Giraud-Guille M. M. “Structure and Chirality of the Nematic Phase in -Chitin Suspensions”. In: *The Journal of Physical Chemistry B* 108.39 (Sept. 2004), pp. 14991–15000. ISSN: 1520-6106, 1520-5207. DOI: [10.1021/jp048152u](https://doi.org/10.1021/jp048152u).
- [182] Shipovskaya Anna B., Shmakov Sergei L., and Gegel Natalia O. “Optical activity anisotropy of chitosan-based films”. In: *Carbohydrate Polymers* 206 (Feb. 2019), pp. 476–486. ISSN: 01448617. DOI: [10.1016/j.carbpol.2018.11.026](https://doi.org/10.1016/j.carbpol.2018.11.026).
- [183] Kim Jaeho, Kim Kwangrak, and Pahk Heui Jae. “Thickness Measurement of a Transparent Thin Film Using Phase Change in White-Light Phase-Shift Interferometry”. In: *Current Optics and Photonics* 1.5 (Oct. 2017), pp. 505–513. DOI: [10.3807/COPP.2017.1.5.505](https://doi.org/10.3807/COPP.2017.1.5.505).
- [184] Martinez Juan P. et al. “Crossed polarization optical transmittance spectra as a way of determining wing thickness of the *Episcada Hymenaea* translucent butterfly”. In: *MRS Advances* (July 24, 2023). ISSN: 2059-8521. DOI: [10.1557/s43580-023-00614-1](https://doi.org/10.1557/s43580-023-00614-1).
- [185] Pereyra C. J. et al. “Scattering of light by ZnO nanorod arrays”. In: *Optics Letters* 46.10 (May 15, 2021). Publisher: Optica Publishing Group, pp. 2360–2363. ISSN: 1539-4794. DOI: [10.1364/OL.422706](https://doi.org/10.1364/OL.422706).
- [186] Zakharov Pavel et al. “Multiple-scattering suppression in dynamic light scattering based on a digital camera detection scheme”. In: *Applied Optics* 45.8 (Mar. 10, 2006), p. 1756. ISSN: 0003-6935, 1539-4522. DOI: [10.1364/AO.45.001756](https://doi.org/10.1364/AO.45.001756).
- [187] Wong Apollo P. Y. and Wiltzius P. “Dynamic light scattering with a CCD camera”. In: *Review of Scientific Instruments* 64.9 (Sept. 1, 1993), pp. 2547–2549. ISSN: 0034-6748, 1089-7623. DOI: [10.1063/1.1143864](https://doi.org/10.1063/1.1143864).
- [188] Rector D et al. “Spatio-temporal mapping of rat whisker barrels with fast scattered light signals”. In: *NeuroImage* 26.2 (June 2005), pp. 619–627. ISSN: 10538119. DOI: [10.1016/j.neuroimage.2005.02.030](https://doi.org/10.1016/j.neuroimage.2005.02.030).
- [189] Neukammer Jörg et al. “Angular distribution of light scattered by single biological cells and oriented particle agglomerates”. In: *Applied Optics* 42.31 (Nov. 1, 2003), p. 6388. ISSN: 0003-6935, 1539-4522. DOI: [10.1364/AO.42.006388](https://doi.org/10.1364/AO.42.006388).
- [190] Lequime Michel et al. “A goniometric light scattering instrument with high-resolution imaging”. In: *Optics Communications* 282.7 (Apr. 2009), pp. 1265–1273. ISSN: 00304018. DOI: [10.1016/j.optcom.2008.12.053](https://doi.org/10.1016/j.optcom.2008.12.053).

- [191] Barnes M. D. et al. “A CCD based approach to high-precision size and refractive index determination of levitated microdroplets using Fraunhofer diffraction”. In: *Review of Scientific Instruments* 68.6 (June 1, 1997), pp. 2287–2291. ISSN: 0034-6748, 1089-7623. DOI: [10.1063/1.1148134](https://doi.org/10.1063/1.1148134).
- [192] Medina José M. et al. “Detailed experimental characterization of reflectance spectra of *Sasakia charonda* butterfly using multispectral optical imaging”. In: *Optical Engineering* 53.3 (Mar. 31, 2014), p. 033111. ISSN: 0091-3286. DOI: [10.1117/1.OE.53.3.033111](https://doi.org/10.1117/1.OE.53.3.033111).
- [193] Mann Seth E. “Spectral imaging, reflectivity measurements, and modeling of iridescent butterfly scale structures”. In: *Optical Engineering* 40.10 (Oct. 1, 2001), p. 2061. ISSN: 0091-3286. DOI: [10.1117/1.1404431](https://doi.org/10.1117/1.1404431).
- [194] Fu Jinxin et al. “Imaging optical scattering of butterfly wing scales with a microscope”. In: *Interface Focus* 7.4 (Aug. 6, 2017), p. 20170016. ISSN: 2042-8898, 2042-8901. DOI: [10.1098/rsfs.2017.0016](https://doi.org/10.1098/rsfs.2017.0016).
- [195] Koike-Tani Maki et al. “Polarized light microscopy in reproductive and developmental biology”. In: *Molecular Reproduction and Development* 82.7 (July 2015), pp. 548–562. ISSN: 1040-452X, 1098-2795. DOI: [10.1002/mrd.22221](https://doi.org/10.1002/mrd.22221).
- [196] Oldenbourg Rudolf. “Polarized Light Microscopy: Principles and Practice”. In: *Cold Spring Harbor Protocols* 2013.11 (Nov. 2013), p. top078600. ISSN: 1940-3402, 1559-6095. DOI: [10.1101/pdb.top078600](https://doi.org/10.1101/pdb.top078600).
- [197] Vidal Benedicto de Campos. “Butterfly scale form birefringence related to photonics”. In: *Micron* 42.8 (Dec. 1, 2011), pp. 801–807. ISSN: 0968-4328. DOI: [10.1016/j.micron.2011.04.006](https://doi.org/10.1016/j.micron.2011.04.006).
- [198] Bayraktar Bulent et al. “Feature extraction from light-scatter patterns of *Listeria* colonies for identification and classification”. In: *Journal of Biomedical Optics* 11.3 (2006), p. 034006. ISSN: 10833668. DOI: [10.1117/1.2203987](https://doi.org/10.1117/1.2203987).
- [199] Demczyklo Roman and Fernández Ariel. “Single-shot 3×3 Mueller matrix microscopy with color polarization encoding”. In: ().
- [200] Fernández Ariel, Demczyklo Roman, and Silva Diego. “Mueller matrix polarimetric imaging of whole-slide tissue samples”. In: *Advances in Microscopic Imaging IV*. Advances in Microscopic Imaging. Ed. by Beaurepaire Emmanuel, Ben-Yakar Adela, and Park YongKeun. Munich, Germany: SPIE, Aug. 9, 2023, p. 42. ISBN: 978-1-5106-6469-2 978-1-5106-6470-8. DOI: [10.1117/12.2669789](https://doi.org/10.1117/12.2669789).

- [201] Fernández Ariel and Demczyklo Roman. “Real-time polarimetric microscopy of biological tissue”. In: *Biophotonics Congress: Optics in the Life Sciences 2023 (OMA, NTM, BODA, OMP, BRAIN)*. Novel Techniques in Microscopy. Vancouver, British Columbia: Optica Publishing Group, 2023, NW1C.2. ISBN: 978-1-957171-21-0. DOI: [10.1364/NTM.2023.NW1C.2](https://doi.org/10.1364/NTM.2023.NW1C.2).
- [202] Fernández Ariel and Demczyklo Roman. “Space-division multiplexing for snapshot polarimetric imaging of tissue samples”. In: *Computational Imaging VII*. Computational Imaging VII. Ed. by Petruccioli Jonathan C. and Preza Chrysanthe. Orlando, United States: SPIE, June 14, 2023, p. 3. ISBN: 978-1-5106-6160-8 978-1-5106-6161-5. DOI: [10.1117/12.2663891](https://doi.org/10.1117/12.2663891).
- [203] Llaguno Juan M., Lecumberry Federico, and Fernández Ariel. “Snapshot polarimetric imaging in multi-view microscopy”. In: *Applied Optics* 61.9 (Mar. 20, 2022), F62. ISSN: 1559-128X, 2155-3165. DOI: [10.1364/AO.445096](https://doi.org/10.1364/AO.445096).
- [204] Arwin Hans et al. “Cuticle structure of the scarab beetle *Cetonia aurata* analyzed by regression analysis of Mueller-matrix ellipsometric data”. In: *Optics Express* 21.19 (Sept. 23, 2013), p. 22645. ISSN: 1094-4087. DOI: [10.1364/OE.21.022645](https://doi.org/10.1364/OE.21.022645).
- [205] Arteaga Oriol et al. “Mueller matrix microscopy on a Morpho butterfly”. In: *Journal of Physics: Conference Series* 605.1 (Apr. 2015). Publisher: IOP Publishing, p. 012008. ISSN: 1742-6596. DOI: [10.1088/1742-6596/605/1/012008](https://doi.org/10.1088/1742-6596/605/1/012008).
- [206] Mendoza-Galván A. et al. “Birefringence of nanocrystalline chitin films studied by Mueller-matrix spectroscopic ellipsometry”. In: *Optical Materials Express* 6.2 (Feb. 1, 2016), p. 671. ISSN: 2159-3930. DOI: [10.1364/OME.6.000671](https://doi.org/10.1364/OME.6.000671).
- [207] Onishi Michihisa, Crabtree Karlton, and Chipman Russell A. “Formulation of rigorous coupled-wave theory for gratings in bianisotropic media”. In: *JOSA A* 28.8 (Aug. 1, 2011). Publisher: Optica Publishing Group, pp. 1747–1758. ISSN: 1520-8532. DOI: [10.1364/JOSAA.28.001747](https://doi.org/10.1364/JOSAA.28.001747).
- [208] Barkstrom Bruce R. “A finite difference method of solving anisotropic scattering problems”. In: *Journal of Quantitative Spectroscopy and Radiative Transfer* 16.9 (Sept. 1, 1976), pp. 725–739. ISSN: 0022-4073. DOI: [10.1016/0022-4073\(76\)90001-7](https://doi.org/10.1016/0022-4073(76)90001-7).
- [209] Soler J. A. et al. “A new conservative finite-difference scheme for anisotropic elliptic problems in bounded domain”. In: *Journal of Computational Physics* 405 (Mar. 15, 2020), p. 109093. ISSN: 0021-9991. DOI: [10.1016/j.jcp.2019.109093](https://doi.org/10.1016/j.jcp.2019.109093).

- [210] Yang D. H. et al. “Finite-difference modelling in two-dimensional anisotropic media using a flux-corrected transport technique”. In: *Geophysical Journal International* 148.2 (Feb. 1, 2002), pp. 320–328. ISSN: 0956-540X. DOI: [10.1046/j.0956-540x.2001.01575.x](https://doi.org/10.1046/j.0956-540x.2001.01575.x).
- [211] Kilchoer Cédric et al. “Determining the complex Jones matrix elements of a chiral 3D optical metamaterial”. In: *APL Photonics* 4.12 (Dec. 1, 2019), p. 126107. ISSN: 2378-0967. DOI: [10.1063/1.5127169](https://doi.org/10.1063/1.5127169).
- [212] Menzel Christoph, Rockstuhl Carsten, and Lederer Falk. “Advanced Jones calculus for the classification of periodic metamaterials”. In: *Physical Review A* 82.5 (Nov. 15, 2010), p. 053811. ISSN: 1050-2947, 1094-1622. DOI: [10.1103/PhysRevA.82.053811](https://doi.org/10.1103/PhysRevA.82.053811).
- [213] Stavenga Doekele G., Leertouwer Heinrich L., and Arikawa Kentaro. “Butterfly Wing Translucence Enables Enhanced Visual Signaling”. In: *Insects* 14.3 (Feb. 26, 2023), p. 234. ISSN: 2075-4450. DOI: [10.3390/insects14030234](https://doi.org/10.3390/insects14030234).
- [214] Yoo Kangeun et al. “Low-temperature large-area fabrication of ZnO nanowires on flexible plastic substrates by solution-processible metal-seeded hydrothermal growth”. In: *Nano Convergence* 7.1 (Dec. 2020). Publisher: Korea Nano Technology Research Society. ISSN: 21965404. DOI: [10.1186/s40580-020-00235-6](https://doi.org/10.1186/s40580-020-00235-6).
- [215] Xu Tingting et al. “Ternary system of ZnO nanorods/reduced graphene oxide/CuInS₂ quantum dots for enhanced photocatalytic performance”. In: *Journal of Alloys and Compounds* 734 (Feb. 2018). Publisher: Elsevier Ltd, pp. 196–203. ISSN: 09258388. DOI: [10.1016/j.jallcom.2017.10.275](https://doi.org/10.1016/j.jallcom.2017.10.275).
- [216] Zhang Yangyang et al. “Synthesis, characterization, and applications of ZnO nanowires”. In: *Journal of Nanomaterials* 2012 (2012). ISSN: 16874110. DOI: [10.1155/2012/624520](https://doi.org/10.1155/2012/624520).
- [217] Wibowo Arie et al. “ZnO nanostructured materials for emerging solar cell applications”. In: *RSC Advances* 10.70 (Nov. 2020). Publisher: Royal Society of Chemistry, pp. 42838–42859. ISSN: 20462069. DOI: [10.1039/d0ra07689a](https://doi.org/10.1039/d0ra07689a).
- [218] Li Ludong, Lou Zheng, and Shen Guozhen. “Flexible Broadband Image Sensors with SnS Quantum Dots/Zn₂SnO₄ Nanowires Hybrid Nanostructures”. In: *Advanced Functional Materials* 28.6 (Feb. 2018). Publisher: Wiley-VCH Verlag. ISSN: 16163028. DOI: [10.1002/adfm.201705389](https://doi.org/10.1002/adfm.201705389).
- [219] Zhao Xinyuan et al. “Quantum Confinement and Electronic Properties of Silicon Nanowires”. In: *Physical Review Letters* 92.23 (June 11, 2004), p. 236805. ISSN: 0031-9007, 1079-7114. DOI: [10.1103/PhysRevLett.92.236805](https://doi.org/10.1103/PhysRevLett.92.236805).

- [220] Deng Jiao et al. “Nanowire Photoelectrochemistry”. In: *Chemical Reviews* 119.15 (Aug. 14, 2019), pp. 9221–9259. ISSN: 0009-2665, 1520-6890. DOI: [10.1021/acs.chemrev.9b00232](https://doi.org/10.1021/acs.chemrev.9b00232).
- [221] Karmakar Keshab et al. “Stable and Enhanced Visible-Light Water Electrolysis Using C, N, and S Surface Functionalized ZnO Nanorod Photoanodes: Engineering the Absorption and Electronic Structure”. In: *ACS Sustainable Chemistry & Engineering* 4.10 (Oct. 3, 2016), pp. 5693–5702. ISSN: 2168-0485, 2168-0485. DOI: [10.1021/acssuschemeng.6b01604](https://doi.org/10.1021/acssuschemeng.6b01604).
- [222] Kim Jae-Hun et al. “Pd functionalization on ZnO nanowires for enhanced sensitivity and selectivity to hydrogen gas”. In: *Sensors and Actuators B: Chemical* 297 (Oct. 2019), p. 126693. ISSN: 09254005. DOI: [10.1016/j.snb.2019.126693](https://doi.org/10.1016/j.snb.2019.126693).
- [223] Xie Jiale, Guo Chunxian, and Li Chang Ming. “Interface functionalization with polymer self-assembly to boost photovoltage of Cu₂O/ZnO nanowires solar cells”. In: *International Journal of Hydrogen Energy* 39.28 (Sept. 2014), pp. 16227–16233. ISSN: 03603199. DOI: [10.1016/j.ijhydene.2014.04.108](https://doi.org/10.1016/j.ijhydene.2014.04.108).
- [224] Cammi Davide et al. “Enhancement of the Sub-Band-Gap Photoconductivity in ZnO Nanowires through Surface Functionalization with Carbon Nanodots”. In: *The Journal of Physical Chemistry C* 122.3 (Jan. 25, 2018), pp. 1852–1859. ISSN: 1932-7447, 1932-7455. DOI: [10.1021/acs.jpcc.7b10288](https://doi.org/10.1021/acs.jpcc.7b10288).
- [225] Han Chuang et al. “Improving the photocatalytic activity and anti-photocorrosion of semiconductor ZnO by coupling with versatile carbon”. In: *Physical Chemistry Chemical Physics* 16.32 (July 11, 2014), p. 16891. ISSN: 1463-9076, 1463-9084. DOI: [10.1039/C4CP02189D](https://doi.org/10.1039/C4CP02189D).
- [226] Sun Guotai et al. “Ascorbic acid functionalized CdS–ZnO core–shell nanorods with hydrogen spillover for greatly enhanced photocatalytic H₂ evolution and outstanding photostability”. In: *Journal of Materials Chemistry A* 9.15 (2021), pp. 9735–9744. ISSN: 2050-7488, 2050-7496. DOI: [10.1039/D1TA01089A](https://doi.org/10.1039/D1TA01089A).
- [227] Zhou Chunyan et al. “Controllable synthesis of CdS quantum dots and their photovoltaic application on quantum-dot-sensitized ZnO nanorods”. In: *Journal of Solid State Electrochemistry* 20.2 (Feb. 2016), pp. 533–540. ISSN: 1432-8488, 1433-0768. DOI: [10.1007/s10008-015-3075-5](https://doi.org/10.1007/s10008-015-3075-5).
- [228] Zou Xinwei et al. “Synthesis of Cu₂O/ZnO hetero-nanorod arrays with enhanced visible light-driven photocatalytic activity”. In: *CrystEngComm* 16.6 (2014), pp. 1149–1156. ISSN: 1466-8033. DOI: [10.1039/C3CE42144A](https://doi.org/10.1039/C3CE42144A).

- [229] Xitao Wang, Rong Lv, and Kang Wang. “Synthesis of ZnO@ZnS–Bi₂S₃ core–shell nanorod grown on reduced graphene oxide sheets and its enhanced photocatalytic performance”. In: *J. Mater. Chem. A* 2.22 (2014), pp. 8304–8313. ISSN: 2050-7488, 2050-7496. DOI: [10.1039/C4TA00696H](https://doi.org/10.1039/C4TA00696H).
- [230] Mohammed Reem. and Ali Mohamed E.M. “Decorated ZnO nanorods with Bi₂S₃ nanosheets for enhanced photocatalytic removal of antibiotics and analgesics: Degradation mechanism and pathway”. In: *Environmental Nanotechnology, Monitoring & Management* 20 (Dec. 2023), p. 100885. ISSN: 22151532. DOI: [10.1016/j.enmm.2023.100885](https://doi.org/10.1016/j.enmm.2023.100885).
- [231] Chia Xinyi et al. “Layered SnS versus SnS₂ : Valence and Structural Implications on Electrochemistry and Clean Energy Electrocatalysis”. In: *The Journal of Physical Chemistry C* 120.42 (Oct. 27, 2016), pp. 24098–24111. ISSN: 1932-7447, 1932-7455. DOI: [10.1021/acs.jpcc.6b06977](https://doi.org/10.1021/acs.jpcc.6b06977).
- [232] Zhao Guodong et al. “Fabrication of CdS quantum dots sensitized ZnO nanorods/TiO₂ nanosheets hierarchical heterostructure films for enhanced photoelectrochemical performance”. In: *Electrochimica Acta* 304 (May 2019). Publisher: Elsevier Ltd, pp. 334–341. ISSN: 00134686. DOI: [10.1016/j.electacta.2019.03.022](https://doi.org/10.1016/j.electacta.2019.03.022).
- [233] Manzeli Sajedeh et al. “2D transition metal dichalcogenides”. In: *Nature Reviews Materials* 2.8 (June 13, 2017), p. 17033. ISSN: 2058-8437. DOI: [10.1038/natrevmats.2017.33](https://doi.org/10.1038/natrevmats.2017.33).
- [234] Zhang Shijie et al. “Current advances of transition metal dichalcogenides in electromagnetic wave absorption: A brief review”. In: *International Journal of Minerals, Metallurgy and Materials* 30.3 (Mar. 2023), pp. 428–445. ISSN: 1674-4799, 1869-103X. DOI: [10.1007/s12613-022-2546-9](https://doi.org/10.1007/s12613-022-2546-9).
- [235] Kang Mingu et al. “Universal Mechanism of Band-Gap Engineering in Transition-Metal Dichalcogenides”. In: *Nano Letters* 17.3 (Mar. 8, 2017), pp. 1610–1615. ISSN: 1530-6984, 1530-6992. DOI: [10.1021/acs.nanolett.6b04775](https://doi.org/10.1021/acs.nanolett.6b04775).
- [236] Zhou Yankai et al. “Selection, Preparation and Application of Quantum Dots in Perovskite Solar Cells”. In: *International Journal of Molecular Sciences* 23.16 (Aug. 2022). Publisher: MDPI. ISSN: 14220067. DOI: [10.3390/ijms23169482](https://doi.org/10.3390/ijms23169482).
- [237] Rasal Akash S. et al. “Stability of quantum dot-sensitized solar cells: A review and prospects”. In: *Nano Energy* 94 (Apr. 2022). Publisher: Elsevier Ltd. ISSN: 22112855. DOI: [10.1016/j.nanoen.2021.106854](https://doi.org/10.1016/j.nanoen.2021.106854).

- [238] Malankowska Anna et al. “The Effect of AgInS₂, SnS, CuS₂, Bi₂S₃ Quantum Dots on the Surface Properties and Photocatalytic Activity of QDs-Sensitized TiO₂ Composite”. In: *Catalysts* 10.4 (Apr. 2020). Publisher: MDPI. ISSN: 20734344. DOI: [10.3390/catal10040403](https://doi.org/10.3390/catal10040403).
- [239] Luo Xuanhui et al. “SnS quantum dots with different sizes in active layer for enhancing the performance of perovskite solar cells”. In: *Applied Physics A: Materials Science and Processing* 127.5 (May 2021). Publisher: Springer Science and Business Media Deutschland GmbH. ISSN: 14320630. DOI: [10.1007/s00339-021-04474-0](https://doi.org/10.1007/s00339-021-04474-0).
- [240] Modi Krishna H. et al. “Self-powered photodetector functionalized by SnS quantum dots”. In: *Optical Materials* 129 (July 2022). Publisher: Elsevier B.V. ISSN: 09253467. DOI: [10.1016/j.optmat.2022.112504](https://doi.org/10.1016/j.optmat.2022.112504).
- [241] Sun Leizhi et al. “Band alignment of SnS/Zn(O,S) heterojunctions in SnS thin film solar cells”. In: *Applied Physics Letters* 103.18 (Oct. 28, 2013), p. 181904. ISSN: 0003-6951, 1077-3118. DOI: [10.1063/1.4821433](https://doi.org/10.1063/1.4821433).
- [242] Bu Ian Y.Y. “Investigation of novel heterojunction: P-type SnS coated n-type ZnO nanowire”. In: *Superlattices and Microstructures* 88 (Dec. 2015), pp. 704–710. ISSN: 07496036. DOI: [10.1016/j.spmi.2015.10.037](https://doi.org/10.1016/j.spmi.2015.10.037).
- [243] Strothkämper Christian et al. “Multiple-Trapping Governed Electron Transport and Charge Separation in ZnO/In₂S₃ Core/Shell Nanorod Heterojunctions”. In: *The Journal of Physical Chemistry C* 116.1 (Jan. 12, 2012), pp. 1165–1173. ISSN: 1932-7447, 1932-7455. DOI: [10.1021/jp2071748](https://doi.org/10.1021/jp2071748).
- [244] Braiek Z. et al. “Impact of In₂S₃ shells thickness on the electrochemical and optical properties of oriented ZnO/In₂S₃ core/shell nanowires”. In: *International Journal of Hydrogen Energy* 42.9 (Mar. 2017), pp. 5694–5707. ISSN: 03603199. DOI: [10.1016/j.ijhydene.2017.01.015](https://doi.org/10.1016/j.ijhydene.2017.01.015).
- [245] Wang Lijing et al. “3D porous ZnO–SnS p–n heterojunction for visible light driven photocatalysis”. In: *Physical Chemistry Chemical Physics* 19.25 (2017). Publisher: Royal Society of Chemistry, pp. 16576–16585. DOI: [10.1039/C7CP01687E](https://doi.org/10.1039/C7CP01687E).
- [246] Zhu Laipan et al. “Piezo-Phototronic Effect Enhanced Flexible Solar Cells Based on n-ZnO/p-SnS Core–Shell Nanowire Array”. In: *Advanced Science* 4.1 (2017). eprint: <https://onlinelibrary.wiley.com/doi/pdf/10.1002/advs.201600185>, p. 1600185. ISSN: 2198-3844. DOI: [10.1002/advs.201600185](https://doi.org/10.1002/advs.201600185).

- [247] Liang Yuan-Chang, Lung Tsai-Wen, and Xu Nian-Cih. “Photoexcited Properties of Tin Sulfide Nanosheet-Decorated ZnO Nanorod Heterostructures”. In: *Nanoscale Research Letters* 12.1 (Apr. 7, 2017), p. 258. ISSN: 1556-276X. DOI: [10.1186/s11671-017-2022-z](https://doi.org/10.1186/s11671-017-2022-z).
- [248] Jayswal Shefali and Moirangthem Rakesh S. “Construction of a solar spectrum active SnS/ZnO p–n heterojunction as a highly efficient photocatalyst: the effect of the sensitization process on its performance”. In: *New Journal of Chemistry* 42.16 (2018), pp. 13689–13701. ISSN: 1144-0546, 1369-9261. DOI: [10.1039/C8NJ02098A](https://doi.org/10.1039/C8NJ02098A).
- [249] Miao Jianwei et al. “Electrochemical fabrication of ZnO–CdSe core–shell nanorod arrays for efficient photoelectrochemical water splitting”. In: *Nanoscale* 5.22 (2013), p. 11118. ISSN: 2040-3364, 2040-3372. DOI: [10.1039/c3nr03425a](https://doi.org/10.1039/c3nr03425a).
- [250] Kumar Pawan et al. “Fabrication of n-ZnS/p-SnS, n-ZnO/p-SnS, and n-SnO₂/p-SnS heterojunctions by 2-step SILAR process for photodetector applications”. In: *Optics & Laser Technology* 168 (Jan. 2024), p. 109980. ISSN: 00303992. DOI: [10.1016/j.optlastec.2023.109980](https://doi.org/10.1016/j.optlastec.2023.109980).
- [251] Yashaswini M. and Gopalakrishna Naik K. “Fabrication of ZnO nanorods and ZnO/CdS core–shell nanorods for the ultraviolet photosensing application”. In: *Inorganic Chemistry Communications* 154 (Aug. 2023), p. 110975. ISSN: 13877003. DOI: [10.1016/j.inoche.2023.110975](https://doi.org/10.1016/j.inoche.2023.110975).
- [252] Kim Wooseok, Baek Minki, and Yong Kijung. “Fabrication of ZnO/CdS, ZnO/CdO core/shell nanorod arrays and investigation of their ethanol gas sensing properties”. In: *Sensors and Actuators B: Chemical* 223 (Feb. 2016), pp. 599–605. ISSN: 09254005. DOI: [10.1016/j.snb.2015.09.158](https://doi.org/10.1016/j.snb.2015.09.158).
- [253] Song Jaejin and Lim Sangwoo. “Effect of Seed Layer on the Growth of ZnO Nanorods”. In: *The Journal of Physical Chemistry C* 111.2 (Jan. 1, 2007), pp. 596–600. ISSN: 1932-7447, 1932-7455. DOI: [10.1021/jp0655017](https://doi.org/10.1021/jp0655017).
- [254] Castillo-Rodriguez Judith et al. “Seed layer effect on morphological, structural, and optical properties of electrochemically grown ZnO nanowires over different SnO₂:F/glass substrates”. In: *Journal of Solid State Electrochemistry* 24.4 (Apr. 2020), pp. 797–808. ISSN: 1432-8488, 1433-0768. DOI: [10.1007/s10008-020-04527-z](https://doi.org/10.1007/s10008-020-04527-z).
- [255] Skompska Magdalena and Zarebska Kamila. “Electrodeposition of ZnO Nanorod Arrays on Transparent Conducting Substrates—a Review”. In: *Electrochimica Acta* 127 (May 2014), pp. 467–488. ISSN: 00134686. DOI: [10.1016/j.electacta.2014.02.049](https://doi.org/10.1016/j.electacta.2014.02.049).

- [256] Zhou Yi et al. “Effect of KOH treatment on structural and photovoltaic properties of ZnO nanorod arrays”. In: *Transactions of Nonferrous Metals Society of China* 22.11 (Nov. 2012), pp. 2736–2741. ISSN: 10036326. DOI: [10.1016/S1003-6326\(11\)61526-4](https://doi.org/10.1016/S1003-6326(11)61526-4).
- [257] Schlur Laurent, Calado Jeremy Ramos, and Spitzer Denis. “Synthesis of zinc oxide nanorods or nanotubes on one side of a microcantilever”. In: *Royal Society Open Science* 5.8 (Aug. 2018), p. 180510. ISSN: 2054-5703. DOI: [10.1098/rsos.180510](https://doi.org/10.1098/rsos.180510).
- [258] She Guang-Wei et al. “Controlled synthesis of oriented single-crystal ZnO nanotube arrays on transparent conductive substrates”. In: *Applied Physics Letters* 92.5 (Feb. 4, 2008), p. 053111. ISSN: 0003-6951, 1077-3118. DOI: [10.1063/1.2842386](https://doi.org/10.1063/1.2842386).
- [259] Liu Zhifeng et al. “Controlled synthesis of ZnO and TiO₂ nanotubes by chemical method and their application in dye-sensitized solar cells”. In: *Renewable Energy* 36.4 (Apr. 2011), pp. 1177–1181. ISSN: 09601481. DOI: [10.1016/j.renene.2010.09.019](https://doi.org/10.1016/j.renene.2010.09.019).
- [260] Yao C. Y., Chen G. J., and Tseng T. Y. “Preparation and Characterizations of ZnO Nanotubes by Acidic Etching Nanowires”. In: *Journal of Nanoscience and Nanotechnology* 8.9 (Sept. 1, 2008), pp. 4432–4435. ISSN: 1533-4880. DOI: [10.1166/jnn.2008.473](https://doi.org/10.1166/jnn.2008.473).
- [261] Wang Hongqiang et al. “Surfactant-Assisted in situ Chemical Etching for the General Synthesis of ZnO Nanotubes Array”. In: *Nanoscale Research Letters* 5.7 (July 2010), pp. 1102–1106. ISSN: 1931-7573, 1556-276X. DOI: [10.1007/s11671-010-9608-z](https://doi.org/10.1007/s11671-010-9608-z).
- [262] Gan Xiaoyan et al. “Investigation on chemical etching process of ZnO nanorods toward nanotubes”. In: *Journal of Alloys and Compounds* 481.1 (July 2009), pp. 397–401. ISSN: 09258388. DOI: [10.1016/j.jallcom.2009.03.013](https://doi.org/10.1016/j.jallcom.2009.03.013).
- [263] Mishra Raghvendra Kumar, Zachariah Ajesh K., and Thomas Sabu. “Energy-Dispersive X-ray Spectroscopy Techniques for Nanomaterial”. In: *Microscopy Methods in Nanomaterials Characterization*. Elsevier, 2017, pp. 383–405. ISBN: 978-0-323-46141-2. DOI: [10.1016/B978-0-323-46141-2.00012-2](https://doi.org/10.1016/B978-0-323-46141-2.00012-2).
- [264] Tena-Zaera Ramón, Elias Jamil, and Lévy-Clément Claude. “ZnO nanowire arrays: Optical scattering and sensitization to solar light”. In: *Applied Physics Letters* 93.23 (Dec. 8, 2008), p. 233119. ISSN: 0003-6951, 1077-3118. DOI: [10.1063/1.3040054](https://doi.org/10.1063/1.3040054).

- [265] Solís-Cortés Daniel et al. “Optimization of Ag₂S Quantum Dots Decorated ZnO Nanorod Array Photoanodes for Enhanced Photoelectrochemical Performances”. In: *Journal of The Electrochemical Society* 168.5 (May 1, 2021), p. 056516. ISSN: 0013-4651, 1945-7111. DOI: [10.1149/1945-7111/ac001a](https://doi.org/10.1149/1945-7111/ac001a).
- [266] Özgür Ü. et al. “A comprehensive review of ZnO materials and devices”. In: *Journal of Applied Physics* 98.4 (Aug. 15, 2005), p. 041301. ISSN: 0021-8979, 1089-7550. DOI: [10.1063/1.1992666](https://doi.org/10.1063/1.1992666).
- [267] Guerguerian Gariné et al. “ZnO nanorod/CdS nanocrystal core/shell-type heterostructures for solar cell applications”. In: *Nanotechnology* 22.50 (Dec. 16, 2011), p. 505401. ISSN: 0957-4484, 1361-6528. DOI: [10.1088/0957-4484/22/50/505401](https://doi.org/10.1088/0957-4484/22/50/505401).
- [268] Guerguerian Gariné et al. “ZnO/Cu₂O heterostructure nanopillar arrays: synthesis, structural and optical properties”. In: *Journal of Physics D: Applied Physics* 45.24 (June 20, 2012), p. 245301. ISSN: 0022-3727, 1361-6463. DOI: [10.1088/0022-3727/45/24/245301](https://doi.org/10.1088/0022-3727/45/24/245301).
- [269] Campo Lucia et al. “Electrochemically Grown ZnO Nanorod Arrays Decorated with CdS Quantum Dots by Using a Spin-Coating Assisted Successive-Ionic-Layer-Adsorption and Reaction Method for Solar Cell Applications”. In: *ECS Journal of Solid State Science and Technology* 2.9 (2013), Q151–Q158. ISSN: 2162-8769, 2162-8777. DOI: [10.1149/2.016309jss](https://doi.org/10.1149/2.016309jss).
- [270] Kamarulzaman Norlida, Kasim Muhd Firdaus, and Rusdi Roshidah. “Band Gap Narrowing and Widening of ZnO Nanostructures and Doped Materials”. In: *Nanoscale Research Letters* 10.1 (Dec. 2015). Publisher: Springer New York LLC. ISSN: 1556276X. DOI: [10.1186/s11671-015-1034-9](https://doi.org/10.1186/s11671-015-1034-9).
- [271] Davis Klinton et al. “Band gap engineered zinc oxide nanostructures: Via a sol-gel synthesis of solvent driven shape-controlled crystal growth”. In: *RSC Advances* 9.26 (2019). Publisher: Royal Society of Chemistry, pp. 14638–14648. ISSN: 20462069. DOI: [10.1039/c9ra02091h](https://doi.org/10.1039/c9ra02091h).
- [272] Zanatta A. R. “Revisiting the optical bandgap of semiconductors and the proposal of a unified methodology to its determination”. In: *Scientific Reports* 9.1 (Aug. 2, 2019). Publisher: Nature Publishing Group, p. 11225. ISSN: 2045-2322. DOI: [10.1038/s41598-019-47670-y](https://doi.org/10.1038/s41598-019-47670-y).
- [273] Oda Yoshiaki et al. “Energetic alignment in nontoxic SnS quantum dot-sensitized solar cell employing spiro-OMeTAD as the solid-state electrolyte”. In: *Science and Technology of Advanced Materials* 15.3 (June 2014). Publisher: IOP Publishing, p. 035006. ISSN: 1468-6996. DOI: [10.1088/1468-6996/15/3/035006](https://doi.org/10.1088/1468-6996/15/3/035006).

- [274] Vidal Julien et al. “Band-structure, optical properties, and defect physics of the photovoltaic semiconductor SnS”. In: *Applied Physics Letters* 100.3 (Jan. 2012). ISSN: 00036951. DOI: [10.1063/1.3675880](https://doi.org/10.1063/1.3675880).
- [275] Devika M. et al. “The physical properties of SnS films grown on lattice-matched and amorphous substrates”. In: *physica status solidi (a)* 207.8 (Aug. 2010), pp. 1864–1869. ISSN: 1862-6300, 1862-6319. DOI: [10.1002/pssa.200925379](https://doi.org/10.1002/pssa.200925379).
- [276] Devika M., Reddy N. Koteeswara, and Gunasekhar K.R. “Structural, electrical, and optical properties of as-grown and heat treated ultra-thin SnS films”. In: *Thin Solid Films* 520.1 (Oct. 2011), pp. 628–632. ISSN: 00406090. DOI: [10.1016/j.tsf.2011.07.074](https://doi.org/10.1016/j.tsf.2011.07.074).
- [277] Devika M. et al. “Thickness Effect on the Physical Properties of Evaporated SnS Films”. In: *Journal of The Electrochemical Society* 154.2 (2007), H67. ISSN: 00134651. DOI: [10.1149/1.2398816](https://doi.org/10.1149/1.2398816).
- [278] Vikraman Dhanasekaran et al. “Shape- and size-tunable synthesis of tin sulfide thin films for energy applications by electrodeposition”. In: *Applied Surface Science* 479 (June 2019), pp. 167–176. ISSN: 01694332. DOI: [10.1016/j.apsusc.2019.02.056](https://doi.org/10.1016/j.apsusc.2019.02.056).
- [279] Riveros G. et al. “Electrodeposition of Single Phase SnS Thin Films: Effect of Electrolytic Bath Temperature on the Final Film Properties”. In: *Journal of The Electrochemical Society* 166.2 (2019), pp. D44–D51. ISSN: 0013-4651, 1945-7111. DOI: [10.1149/2.0661902jes](https://doi.org/10.1149/2.0661902jes).
- [280] Cheng Shuying and Conibeer Gavin. “Physical properties of very thin SnS films deposited by thermal evaporation”. In: *Thin Solid Films* 520.2 (Nov. 2011), pp. 837–841. ISSN: 00406090. DOI: [10.1016/j.tsf.2011.01.355](https://doi.org/10.1016/j.tsf.2011.01.355).
- [281] Rana Chandan and Saha Satyajit. “Fabrication and characterization of natural dye-sensitized solar cells based on tin sulfide nanoparticles”. In: *Emergent Materials* 5.3 (June 2022), pp. 945–955. ISSN: 2522-5731, 2522-574X. DOI: [10.1007/s42247-021-00245-y](https://doi.org/10.1007/s42247-021-00245-y).
- [282] Kawamura Fumio et al. “Tunability of the bandgap of SnS by variation of the cell volume by alloying with A.E. elements”. In: *Scientific Reports* 12.1 (May 6, 2022). Publisher: Nature Publishing Group, p. 7434. ISSN: 2045-2322. DOI: [10.1038/s41598-022-11074-2](https://doi.org/10.1038/s41598-022-11074-2).
- [283] Shaaban E R et al. “Spectroscopic ellipsometry investigations of the optical constants of nanocrystalline SnS thin films”. In: *Physica Scripta* 86.1 (July 1, 2012), p. 015702. ISSN: 0031-8949, 1402-4896. DOI: [10.1088/0031-8949/86/01/015702](https://doi.org/10.1088/0031-8949/86/01/015702).

- [284] Banai R. E. et al. “Optical Properties of Sputtered SnS Thin Films for Photovoltaic Absorbers”. In: *IEEE Journal of Photovoltaics* 3.3 (July 2013), pp. 1084–1089. ISSN: 2156-3381, 2156-3403. DOI: [10.1109/JPHOTOV.2013.2251758](https://doi.org/10.1109/JPHOTOV.2013.2251758).
- [285] Nguyen Hoang Tung et al. “Temperature dependence of the dielectric function and critical points of -SnS from 27 to 350 K”. In: *Scientific Reports* 10.1 (Oct. 27, 2020), p. 18396. ISSN: 2045-2322. DOI: [10.1038/s41598-020-75383-0](https://doi.org/10.1038/s41598-020-75383-0).
- [286] Tsukigase Hiroki et al. “Synthesis of SnS Nanoparticles by SILAR Method for Quantum Dot-Sensitized Solar Cells”. In: *Journal of Nanoscience and Nanotechnology* 11.3 (Mar. 1, 2011), pp. 1914–1922. ISSN: 15334880. DOI: [10.1166/jnn.2011.3582](https://doi.org/10.1166/jnn.2011.3582).
- [287] Rabiei Marzieh et al. “Comparing Methods for Calculating Nano Crystal Size of Natural Hydroxyapatite Using X-Ray Diffraction”. In: *Nanomaterials* 10.9 (Aug. 19, 2020), p. 1627. ISSN: 2079-4991. DOI: [10.3390/nano10091627](https://doi.org/10.3390/nano10091627).
- [288] Cody G.D. “Chapter 2 The Optical Absorption Edge of a-Si: H”. In: *Semiconductors and Semimetals*. Vol. 21. Elsevier, 1984, pp. 11–82. ISBN: 978-0-12-752148-0. DOI: [10.1016/S0080-8784\(08\)62910-5](https://doi.org/10.1016/S0080-8784(08)62910-5).
- [289] Migliorini Francesca et al. “To optical properties of carbon nanoparticles: A need in comprehending Urbach energy”. In: *Carbon Trends* 8 (July 2022), p. 100184. ISSN: 26670569. DOI: [10.1016/j.cartre.2022.100184](https://doi.org/10.1016/j.cartre.2022.100184).
- [290] Yaghoubi Houman et al. “Toward a Visible Light-Driven Photocatalyst: The Effect of Midgap-States-Induced Energy Gap of Undoped TiO₂ Nanoparticles”. In: *ACS Catalysis* 5.1 (Jan. 2, 2015), pp. 327–335. ISSN: 2155-5435, 2155-5435. DOI: [10.1021/cs501539q](https://doi.org/10.1021/cs501539q).
- [291] Bipasha Ferdaushi Alam et al. “Intrinsic properties and dopability effects on the thermoelectric performance of binary Sn chalcogenides from first principles”. In: *Frontiers in Electronic Materials* 2 (Nov. 24, 2022), p. 1059684. ISSN: 2673-9895. DOI: [10.3389/femat.2022.1059684](https://doi.org/10.3389/femat.2022.1059684).
- [292] Zandalazini C.I. et al. “Contribution of lattice parameter and vacancies on anisotropic optical properties of tin sulphide”. In: *Journal of Alloys and Compounds* 746 (May 2018), pp. 9–18. ISSN: 09258388. DOI: [10.1016/j.jallcom.2018.02.262](https://doi.org/10.1016/j.jallcom.2018.02.262).
- [293] Amato Alex et al. “Observation of a Correlation Between Internal friction and Urbach Energy in Amorphous Oxides Thin Films”. In: *Scientific Reports* 10.1 (Feb. 3, 2020), p. 1670. ISSN: 2045-2322. DOI: [10.1038/s41598-020-58380-1](https://doi.org/10.1038/s41598-020-58380-1). arXiv: [1903.06094\[cond-mat,physics:physics\]](https://arxiv.org/abs/1903.06094).

- [294] Mohammad Tauheed et al. “Tin Sulfide (SnS) Films Deposited by an Electric Field-Assisted Continuous Spray Pyrolysis Technique with Application as Counter Electrodes in Dye-Sensitized Solar Cells”. In: *ACS Omega* 7.44 (Nov. 8, 2022), pp. 39690–39696. ISSN: 2470-1343, 2470-1343. DOI: [10.1021/acsomega.2c03454](https://doi.org/10.1021/acsomega.2c03454).
- [295] Caballero-Briones F. et al. “Evidence and analysis of parallel growth mechanisms in Cu₂O films prepared by Cu anodization”. In: *Electrochimica Acta* 55.14 (May 2010), pp. 4353–4358. ISSN: 00134686. DOI: [10.1016/j.electacta.2009.10.031](https://doi.org/10.1016/j.electacta.2009.10.031).
- [296] Gupta Yashika and Arun P. “Influence of Urbach tail on the refractive index of p-SnS thin films”. In: *physica status solidi c* 14.1 (Jan. 2017), p. 1600207. ISSN: 1862-6351, 1610-1642. DOI: [10.1002/pssc.201600207](https://doi.org/10.1002/pssc.201600207).
- [297] Banai R. E. et al. “Ellipsometric characterization and density-functional theory analysis of anisotropic optical properties of single-crystal -SnS”. In: *Journal of Applied Physics* 116.1 (July 7, 2014), p. 013511. ISSN: 0021-8979. DOI: [10.1063/1.4886915](https://doi.org/10.1063/1.4886915).
- [298] Aguilar Omar et al. “Optoelectronic characterization of Zn_{1-x}Cd_xO thin films as an alternative to photonic crystals in organic solar cells”. In: *Optical Materials Express* 9.9 (Sept. 1, 2019). Publisher: Optica Publishing Group, pp. 3638–3648. ISSN: 2159-3930. DOI: [10.1364/OME.9.003638](https://doi.org/10.1364/OME.9.003638).
- [299] Singh Manpreet, Song Sheng, and Hahm Jong-in. “Unique temporal and spatial biomolecular emission profile on individual zinc oxide nanorods”. In: *Nanoscale* 6.1 (2014), pp. 308–315. ISSN: 2040-3364, 2040-3372. DOI: [10.1039/C3NR05031A](https://doi.org/10.1039/C3NR05031A).
- [300] Anttu N. and Xu H. Q. “Coupling of Light into Nanowire Arrays and Subsequent Absorption”. In: *Journal of Nanoscience and Nanotechnology* 10.11 (Nov. 1, 2010), pp. 7183–7187. ISSN: 15334880. DOI: [10.1166/jnn.2010.2907](https://doi.org/10.1166/jnn.2010.2907).
- [301] Yang Li and Kruse Björn. “Revised Kubelka–Munk theory I Theory and application”. In: *Journal of the Optical Society of America A* 21.10 (Oct. 1, 2004), p. 1933. ISSN: 1084-7529, 1520-8532. DOI: [10.1364/JOSAA.21.001933](https://doi.org/10.1364/JOSAA.21.001933).
- [302] Alcaraz De La Osa R. et al. “The extended Kubelka–Munk theory and its application to spectroscopy”. In: *ChemTexts* 6.1 (Mar. 2020), p. 2. ISSN: 2199-3793. DOI: [10.1007/s40828-019-0097-0](https://doi.org/10.1007/s40828-019-0097-0).
- [303] Chen Cheng-Ying et al. “Giant optical anisotropy of oblique-aligned ZnO nanowire arrays”. In: *Optics Express* 20.3 (Jan. 30, 2012). Publisher: Optica Publishing Group, pp. 2015–2024. ISSN: 1094-4087. DOI: [10.1364/OE.20.002015](https://doi.org/10.1364/OE.20.002015).

- [304] Wang J. “Highly Polarized Photoluminescence and Photodetection from Single Indium Phosphide Nanowires”. In: *Science* 293.5534 (Aug. 2001). Publisher: American Association for the Advancement of Science (AAAS), pp. 1455–1457. DOI: [10.1126/science.1062340](https://doi.org/10.1126/science.1062340).
- [305] Soci C. et al. “ZnO Nanowire UV Photodetectors with High Internal Gain”. In: *Nano Letters* 7.4 (Apr. 1, 2007), pp. 1003–1009. ISSN: 1530-6984, 1530-6992. DOI: [10.1021/nl070111x](https://doi.org/10.1021/nl070111x).
- [306] Ruda H. E. and Shik A. “Polarization-sensitive optical phenomena in semiconducting and metallic nanowires”. In: *Physical Review B* 72.11 (Sept. 2005). Publisher: American Physical Society (APS). DOI: [10.1103/physrevb.72.115308](https://doi.org/10.1103/physrevb.72.115308).
- [307] Ruda H. E. and Shik A. “Polarization-sensitive optical phenomena in thick semiconducting nanowires”. In: *Journal of Applied Physics* 100.2 (July 2006). Publisher: AIP Publishing, p. 024314. DOI: [10.1063/1.2216879](https://doi.org/10.1063/1.2216879).
- [308] Stephen Michael J. and Cwilich Gabriel. “Rayleigh scattering and weak localization: Effects of polarization”. In: *Physical Review B* 34.11 (Dec. 1, 1986), pp. 7564–7572. ISSN: 0163-1829. DOI: [10.1103/PhysRevB.34.7564](https://doi.org/10.1103/PhysRevB.34.7564).
- [309] Valente P. et al. “Depolarizing optical effect by ZnO nanowire arrays”. In: *Physica E: Low-dimensional Systems and Nanostructures* 114 (Oct. 2019). Publisher: Elsevier BV, p. 113600. DOI: [10.1016/j.physe.2019.113600](https://doi.org/10.1016/j.physe.2019.113600).
- [310] Valente Paulo et al. “Comparative analysis between nanorods and nanowires by using depolarized and diffuse light”. In: *Optics Communications* 478 (Jan. 2021), p. 126393. ISSN: 00304018. DOI: [10.1016/j.optcom.2020.126393](https://doi.org/10.1016/j.optcom.2020.126393).
- [311] Cuevas J.L. et al. “Theoretical approach to the phonon modes of GaSb nanowires”. In: *Physica E: Low-dimensional Systems and Nanostructures* 143 (Sept. 2022), p. 115372. ISSN: 13869477. DOI: [10.1016/j.physe.2022.115372](https://doi.org/10.1016/j.physe.2022.115372).
- [312] Do T. Anh Thu et al. “Bi₂S₃ Nanowires: First-Principles Phonon Dynamics and Their Photocatalytic Environmental Remediation”. In: *The Journal of Physical Chemistry C* 125.7 (Feb. 25, 2021), pp. 4086–4091. ISSN: 1932-7447, 1932-7455. DOI: [10.1021/acs.jpcc.0c10849](https://doi.org/10.1021/acs.jpcc.0c10849).
- [313] Rundle Jordan and Leoni Stefano. “Layered Tin Chalcogenides SnS and SnSe: Lattice Thermal Conductivity Benchmarks and Thermoelectric Figure of Merit”. In: *The Journal of Physical Chemistry C* 126.33 (Aug. 25, 2022). Publisher: American Chemical Society, pp. 14036–14046. ISSN: 1932-7447. DOI: [10.1021/acs.jpcc.2c02401](https://doi.org/10.1021/acs.jpcc.2c02401).

- [314] Martinez Juan Pedro et al. “Propiedades ópticas de nanorods de ZnO sensibilizados con SnS”. In: *Reunión de la Sociedad Uruguaya de Física, XVII SUF 2022 ”José A. Ferrari”*. XVII SUF 2022 ”José A. Ferrari”. Nueva Helvecia, Uruguay, Nov. 4, 2022.
- [315] Pereyra Mariana et al. “Transparency in Insects: A Study of the Physicochemical, Optical, and Morphological Factors”. In: *Proceedings of the 7th International Meeting for Researchers in Materials and Plasma Technology*. 7th International Meeting for Researchers in Materials and Plasma Technology. Cartagena de Indias, Colombia, June 2023.
- [316] Martinez Juan Pedro et al. “Elementos ópticos de origen natural: Caracterización y modelado”. In: *II Encuentro de Investigadores en Ciencia de Materiales*. II Encuentro de Investigadores en Ciencia de Materiales. Montevideo, Uruguay, Apr. 20, 2023.
- [317] Schaefer Beth et al. “Measuring the Stokes polarization parameters”. In: *Am. J. Phys.* 75.2 (2007).
- [318] *Principles of Lock-in Detection — Zurich Instruments*. Dec. 20, 2019. URL: <https://www.zhinst.com/en/resources/principles-of-lock-in-detection> (visited on 03/11/2024).
- [319] *Wollaston Prisms*. URL: <https://www.thorlabs.com> (visited on 03/11/2024).
- [320] G.Optik. *Basics of Light Measurement*. 2015.
- [321] Paschotta Dr Rüdiger. *beam collimators*. URL: https://www.rp-photonics.com/beam_collimators.html (visited on 03/12/2024).
- [322] *Considerations in Collimation*. URL: <https://www.edmundoptics.es/knowledge-center/application-notes/optics/considerations-in-collimation/> (visited on 03/12/2024).
- [323] Bruker. *What is EDS? — Energy Dispersive Spectroscopy*. URL: <https://www.bruker.com/en/landingpages/bna/technology/what-is-eds.html> (visited on 04/18/2024).
- [324] Oxford Instruments. *What is EDS/EDX? - Nanoanalysis*. Oxford Instruments. URL: <https://nano.oxinst.com/campaigns/what-is-eds/edx> (visited on 04/18/2024).
- [325] Incropera Frank. *Fundamentals of heat and mass transfer*. Sixth edition. Hoboken, NJ: John Wiley, 2007.

- [326] Sulaiman S. et al. “Review on grain size effects on thermal conductivity in ZnO thermoelectric materials”. In: *RSC Advances* 12.9 (Feb. 10, 2022). Publisher: The Royal Society of Chemistry, pp. 5428–5438. ISSN: 2046-2069. DOI: [10.1039/D1RA06133J](https://doi.org/10.1039/D1RA06133J).
- [327] Asfandiyar et al. “High thermoelectric figure of merit $ZT > 1$ in SnS polycrystals”. In: *Journal of Materiomics* 6.1 (Mar. 2020), pp. 77–85. ISSN: 23528478. DOI: [10.1016/j.jmat.2019.12.003](https://doi.org/10.1016/j.jmat.2019.12.003).
- [328] Alam Md Shah et al. “Forced Convective Heat Transfer Coefficient Measurement of Low Concentration Nanorods ZnO–Ethylene Glycol Nanofluids in Laminar Flow”. In: *Nanomaterials* 12.9 (Jan. 2022). Number: 9 Publisher: Multidisciplinary Digital Publishing Institute, p. 1568. ISSN: 2079-4991. DOI: [10.3390/nano12091568](https://doi.org/10.3390/nano12091568).
- [329] Li Man et al. “Parallel measurement of conductive and convective thermal transport of micro/nanowires based on Raman mapping”. In: *Applied Physics Letters* 106.25 (June 22, 2015), p. 253108. ISSN: 0003-6951, 1077-3118. DOI: [10.1063/1.4923189](https://doi.org/10.1063/1.4923189).
- [330] Slaughter William Shewen. *The linearized theory of elasticity*. Boston: Birkhäuser, 2002. ISBN: 978-0-8176-4117-7.
- [331] Feng Kang and Shi Zhongci. *Mathematical theory of elastic structures*. Rev. ed. of the original Chinese ed. Berlin: Springer [u.a.], 1996. 395 pp. ISBN: 978-0-387-51326-3 978-3-540-51326-1.
- [332] Jones Robert M. *Deformation theory of plasticity*. Blacksburg, Va: Bull Ridge Pub, 2009. 622 pp. ISBN: 978-0-9787223-1-9.
- [333] Bathe Klaus-Jürgen. *Finite element procedures*. Boston, Mass.: Bathe, 2006. 1037 pp. ISBN: 978-0-9790049-0-2.

APPENDICES

Appendix A

Proof of the Stokes parameters measurement configuration

There are several intensity measurement schemes used to obtain the Stokes parameters [50, 317]. In this appendix we will demonstrate that the configuration utilized in this work yields the correct Stokes parameters for an arbitrary beam. We will first “guess” the configuration by asking the question: what should the optical elements do to a light beam of known polarization so that the reading at the detectors yield the correct parameter?. Then, using the tools of Jones calculus[27, 28, 49] we will analyze a train of optical elements and formally prove that the configuration that answers the previous question gives the Stokes parameters for any beam.

The Stokes parameters are defined as shown in equation A.1[48].

$$\begin{aligned} S_0 &= I = |E_x|^2 + |E_y|^2 = E_x E_x^* + E_y E_y^* \\ S_1 &= I_{0^\circ} - I_{90^\circ} = E_x E_x^* - E_y E_y^* \\ S_2 &= I_{45^\circ} - I_{135^\circ} = E_x E_y^* + E_y E_x^* \\ S_3 &= I_{RHCP} - I_{LHCP} = i(E_x E_y^* - E_y E_x^*) \end{aligned} \tag{A.1}$$

Any electric field can be decomposed on two orthogonal polarizations[28], and the temporal dependence of the amplitude can be expressed as follows:

$$\begin{aligned} E_x(t) &= E_{0x} e^{i(\omega t + \delta_x)} = E_x e^{i\omega t} \\ E_y(t) &= E_{0y} e^{i(\omega t + \delta_y)} = E_y e^{i\omega t} \end{aligned} \tag{A.2}$$

Now consider the train of optical elements that appears in figure A.1. We have a retarder plate (R) introducing a phase difference of γ with its fast axis making an angle of ϕ with the horizontal (\hat{x}) direction. After this we place a linear polarizer (LP) with transmission axis at an angle θ .

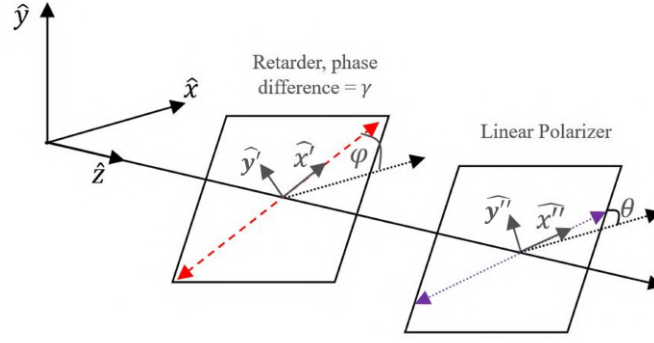


Figure A.1: Train of optical elements used to analyze the state of polarization. First a retarder plate that introduces a phase difference between its fast and slow axes of γ , the fast axis (FA) of which makes an angle of ϕ with the horizontal \hat{x} axis of the lab. After the retarder we have a linear polarizer with a transmission axis making an angle of θ with the \hat{x} axis of the lab

Now we can use the tools of Jones calculus to calculate the effect of both optical components on an incoming beam of arbitrary polarization. We have that in the lab basis (x-y) the electric field at the output can be calculated as follows, where J_{LP} and J_R are the Jones matrices in the x-y basis of the linear polarizer and retarder, respectively:

$$E_{out} = \begin{pmatrix} E_x^{out} \\ E_y^{out} \end{pmatrix} = J_{LP} J_R E_{in} = \begin{pmatrix} \cos^2\theta & \sin\theta\cos\theta \\ \sin\theta\cos\theta & \sin^2\theta \end{pmatrix} \begin{pmatrix} \cos^2\phi e^{i\gamma} + \sin^2\phi & \sin\phi\cos\phi(e^{i\gamma} - 1) \\ \sin\phi\cos\phi(e^{i\gamma} - 1) & \sin^2\phi e^{i\gamma} + \cos^2\phi \end{pmatrix} \begin{pmatrix} E_x \\ E_y \end{pmatrix} \quad (\text{A.3})$$

The experimental setup considered in this work utilizes a Wollaston prism to separate the components of polarization. As the axes of the prism are aligned with the x-y axes of the lab, we can think of it as two simultaneous linear polarizers—one aligned with the horizontal and the other with the vertical direction. This is equivalent to making two simultaneous measurements, the output of one is calculated with $\theta = 0$ (\hat{x} direction) and of the other using $\theta = 90^\circ$ (\hat{y} direction) in equation A.3. These two positions are fixed, and we want the Stokes parameters to be simply calculated as the difference between the horizontal and the vertical polarizer: $S_i = I_{\theta=0^\circ} - I_{\theta=90^\circ} = I_x - I_y$. The S_0 and S_1 are directly obtained from the reading without placing the retarder. The question then becomes, what should the position (ϕ) and phase difference (γ) imposed by the retarder be in order to obtain the remaining Stokes parameters?

A.1. The S_2 Stokes parameter

If the setup gives a correct Stokes parameter for an arbitrary beam, then it obviously must give the correct one to a simple, particular case. We begin with this idea, and then prove that the system used for the particular case gives the correct Stokes parameter for an arbitrary beam.

The S_2 parameter gives the tendency of the beam to be linearly polarized at 45° of the x direction. Imagine that the beam approaching the measurement system is perfectly polarized in this direction. Then, to obtain the correct Stokes parameter we must have that $I_x = I_{total}$. Therefore, the effect of the retarder must be to rotate the incoming beam towards the horizontal direction. It is known that half wave plates (HWP), which introduce a phase difference of $\gamma = \pi$ rotate the plane of polarization of linearly polarized light an angle dependant on the direction of the HWP (ϕ) relative to the polarization direction. We want to find the angle that satisfies our condition, ϕ_2 . Making $\gamma = \pi$ and considering incoming light polarized at 45° , we impose the condition that the output is completely polarized in the horizontal direction in equation A.3, and arrive at the following output *before* the LP:

$$E_{out} = \begin{pmatrix} E_x^{out} \\ E_y^{out} \end{pmatrix} = \begin{pmatrix} -\cos^2\phi + \sin^2\phi & -2\sin\phi\cos\phi \\ -2\sin\phi\cos\phi & -\sin^2\phi + \cos^2\phi \end{pmatrix} \frac{1}{\sqrt{2}} \begin{pmatrix} 1 \\ 1 \end{pmatrix} = \begin{pmatrix} 1 \\ 0 \end{pmatrix} \quad (\text{A.4})$$

Thus we have that the correct position of the HWP relative to the x-y axes, ϕ_2 , is given by the solution of the set of equations A.5. Note that if ϕ_2 is a solution then $\sin^2\phi_2 - \cos^2\phi_2 = -2\sin\phi_2\cos\phi_2$ and, eliminating between the two equations, $-4\sin\phi_2\cos\phi_2 = \sqrt{2}$.

$$\begin{cases} -\cos^2\phi + \sin^2\phi - 2\sin\phi\cos\phi = \sqrt{2} \\ -2\sin\phi\cos\phi - \sin^2\phi + \cos^2\phi = 0 \end{cases} \quad (\text{A.5})$$

Now consider an arbitrary beam. The beam *after* the linear polarizer when its transmission axis is horizontal is given by:

$$E_{out} = \begin{pmatrix} -\cos^2\phi + \sin^2\phi & -2\sin\phi\cos\phi \\ 0 & 0 \end{pmatrix} \begin{pmatrix} E_x \\ E_y \end{pmatrix} \quad (\text{A.6})$$

Then the intensity can be calculated by multiplying the field with its complex conjugate. We do the same for the other polarization direction and arrive at the intensities shown in equation A.7.

$$\begin{aligned}
I_x &= E_x E_x^* (\sin^2 \phi - \cos^2 \phi)^2 + (E_x E_y^* + E_y E_x^*) (-2 \sin \phi \cos \phi) (\sin^2 \phi - \cos^2 \phi) + E_y E_y^* 4 \sin^2 \phi \cos^2 \phi \\
I_y &= E_x E_x^* 4 \sin^2 \phi \cos^2 \phi + (E_x E_y^* + E_y E_x^*) (-2 \sin \phi \cos \phi) (\cos^2 \phi - \sin^2 \phi) + E_y E_y^* (\cos^2 \phi - \sin^2 \phi)^2
\end{aligned} \tag{A.7}$$

If we take the difference between the two intensities we find that:

$$I_x - I_y = E_x E_x^* A + (E_x E_y^* + E_y E_x^*) B + E_y E_y^* C \tag{A.8}$$

Where A,B and C are given by:

$$\begin{aligned}
A &= (\sin^2 \phi - \cos^2 \phi)^2 - 4 \sin^2 \phi \cos^2 \phi \\
B &= -4 \sin \phi \cos \phi (\sin^2 \phi - \cos^2 \phi) \\
C &= 4 \sin^2 \phi \cos^2 \phi - (\cos^2 \phi - \sin^2 \phi)^2
\end{aligned} \tag{A.9}$$

Evaluating A,B and C at the special angle ϕ_2 , which is the solution of the set of equations A.5, we find that $A|_{\phi_2} = C|_{\phi_2} = 0$ and $B|_{\phi_2} = 1$. Therefore, we have proven that by placing the fast axis of the retarder at this angle, the S_2 parameter is the difference between the reading of both detectors for any arbitrary beam:

$$[I_x - I_y]|_{\phi_2} = E_x E_y^* + E_y E_x^* = S_2 \tag{A.10}$$

A.2. The S_3 Stokes parameter

Following the same idea as in the S_2 parameter, note that the S_3 parameter quantifies the tendency of the light beam to be right hand circularly polarized (RHC) versus left hand circularly polarized (LHC). A perfectly RHC beam should then be transformed by the retarder into linearly polarized light aligned with the \hat{x} direction, so that the result of the measurement is $I_x - I_y = 1$.

A circularly polarized beam transforms into linearly polarized when it traverses a quarter wave plate (QWP). RHC polarization occurs when E_y leads E_x by a quarter wave ($\pi/2$) and their magnitudes are equal[28]. If we then place a QWP with the fast axis aligned with E_x we obtain a linearly polarized beam in the first and third quadrant at 45° of the axes of the QWP. Now, if we want this direction to coincide with the \hat{x} axis of the lab, it suffices to place the fast axis of the QWP (\hat{x}') at -45° of the horizontal (\hat{x}) direction.

Now we will prove that this configuration gives the correct reading for an arbitrary beam. Consider equation A.3 with $\gamma = \pi/2$ and $\phi = -\pi/4$ and again extract the intensities for both values of θ . The result for each intensity after the LP is:

$$\begin{aligned}
I_x &= \frac{1}{2}(E_x E_x^* + iE_x E_y^* - iE_y E_x^* + E_y E_y^*) \\
I_y &= \frac{1}{2}(E_x E_x^* + iE_y E_x^* - iE_x E_y^* + E_y E_y^*)
\end{aligned}
\tag{A.11}$$

From here it is immediate that the difference between them is the S_3 parameter, as shown in equation [A.12](#).

$$[I_x - I_y]_{\phi=-\pi/4} = i(E_x E_y^* - E_y E_x^*) = S_3
\tag{A.12}$$

Appendix B

On the specialized equipment used in this work

In this appendix we will give a brief introduction on specific specialized optical and measurement components that were used in this work. The objective is to familiarize the reader with the basic principles of operation and the terminology employed when discussing them in the experimental setups or their possible effects in the measurements

B.1. Lock-in amplifier

Lock in amplifiers are electronic instruments that employ homodyne detection and a low-pass filter to measure a signal amplitude and phase relative to a reference signal [318]. In homodyne detection, a measured (modulated) signal is compared to a reference signal which is the same as the pre-modulated signal. Therefore, both measured and reference signals have the same frequency. By using the knowledge of the time dependence of the signal, these instruments are able to extract signals in a defined frequency band around the reference frequency. This makes them ideal for sensitive detection and filtering noisy signals, improving the signal to noise ratio.

In this work we employ the instrument to measure the photovoltage of silicon detectors used for light intensity measurements. The light source, either lamps or lasers, are continuous. As detection by lock in amplifiers requires modulated signals, a chopper is introduced in the beam path. The instantaneous frequency of the chopper is measured by an encoder and fed into the lock-in amplifier as the reference signal.

The sensing mechanism can be understood as follows. Consider a measured signal (V_s) as shown in equation B.1, where we have expressed the oscillating signal using Euler formula.

$$V_s(t) = A_s \cos(\omega_s t + \delta_s) = \frac{A_s}{2} e^{+i(\omega_s t + \delta_s)} + \frac{A_s}{2} e^{-i(\omega_s t + \delta_s)} \quad (\text{B.1})$$

The reference signal similarly be expressed as:

$$V_r(t) = A_r \cos(\omega_r t) = \frac{A_r}{2} e^{+i(\omega_r t + \delta_r)} + \frac{A_r}{2} e^{-i(\omega_r t + \delta_r)} \quad (\text{B.2})$$

If the signals are passed through a mixer, they are multiplied, with the resulting signal (Z):

$$Z(t) = V_s(t) \dot{V}_r(t) = \frac{A_s}{2} \frac{A_r}{2} \{ e^{i[(\omega_s + \omega_r)t + \delta_s + \delta_r]} + e^{i[(\omega_s - \omega_r)t + \delta_s - \delta_r]} + e^{-i[(\omega_s + \omega_r)t + \delta_s + \delta_r]} + e^{-i[(\omega_s - \omega_r)t + \delta_s - \delta_r]} \} \quad (\text{B.3})$$

If we apply a low pass filter (LPF), we remove the high frequency components ($\omega_s + \omega_r$) and are left with the low frequency portion of the wave ($\omega_s - \omega_r$). Furthermore, if we allow the frequencies of the reference and measured signals to be the same ($\omega_s = \omega_r$) we obtain a signal that is directly proportional to the amplitude of the measured signal and its phase, as shown in equation B.4.

$$Z(t)|_{\omega_s = \omega_r}^{LPF} = \frac{A_s}{2} \frac{A_r}{2} \{ e^{i[\delta_s - \delta_r]} + e^{-i[\delta_s - \delta_r]} \} = A_s \frac{A_r}{2} \cos(\delta_s - \delta_r) \quad (\text{B.4})$$

With only one phase sensitive detector it is possible to measure the signal, but the result depends on the difference between the phases of the reference and measured signals. If there is a second detector then it is possible to use a second reference signal 90° out of phase compared to the first reference signal. This way one obtains an output Z_2 given by:

$$Z_2(t) = A_s \frac{A_r}{2} \sin(\delta_s - \delta_r) \quad (\text{B.5})$$

With these two signals one can obtain the amplitude and phase difference of the measured signal as follows, remembering that the amplitude of the generated reference signal is known:

$$V_s = \frac{\sqrt{2}}{A_r} \sqrt{Z^2 + Z_2^2} \quad (\text{B.6})$$

$$\delta_s - \delta_r = \tan^{-1}\left(\frac{Z_2}{Z}\right)$$

B.2. The Wollaston Prism

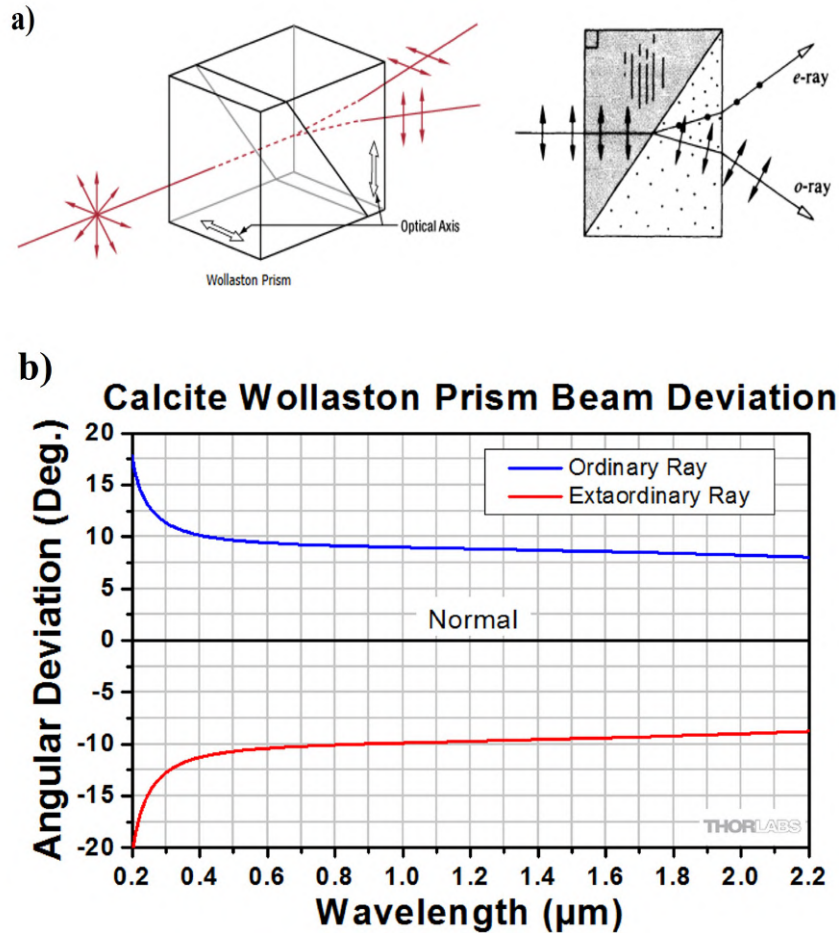


Figure B.1: a) Schematic representation of a Wollaston prism, which separates orthogonal polarization components by employing the birefringence on two calcite crystals. The images are taken from [319] and [27]. b) Spectral dependence of the deviation angle, obtained from [319]

A Wollaston prism is a type of optical device that is used to separate polarized light into two orthogonal polarized beams [28, 32]. It usually consists of two right-angled calcite prisms cemented together, as shown in figure B.1a. Calcite is a birefringent (uniaxial) material, meaning it has two distinct refractive indices depending on the polarization direction of the incoming light, one along the optical axis and another perpendicular to it. The two polarization states separate at the diagonal face. When unpolarized light enters the first prism, it is split into two linearly polarized rays, each with a polarization direction parallel to one of the optical axes of the calcite. These rays are called ordinary (o-ray) and extraordinary (e-ray) rays. When the rays reach the second prism, which has its principal axis at 90° of the first, the o-ray in the first prism becomes the e-ray in the second and vice versa. Therefore, they each experience opposite differences in refractive

index in the interface, and are refracted in opposite directions.

The axis of the device is given by the direction of the principal axis of each prism. Notice that, as any polarization state can be decomposed into two orthogonal polarization states, each of the outgoing beams will be a projection of the polarization state in the prism axis. Therefore, we can think of the prism as equivalent to performing two measurements with linear polarizers aligned with the principal axis of the prism.

The deviation of the rays depends on the refractive indices of along and perpendicular to the principal axis, which are experienced by the o and e rays, respectively. As this depends on the wavelength (dispersion), the angular deviation depends on the wavelength of light, as shown in figure B.1b. Changing the wavelength of light requires a detector realignment.

B.3. The integrating sphere

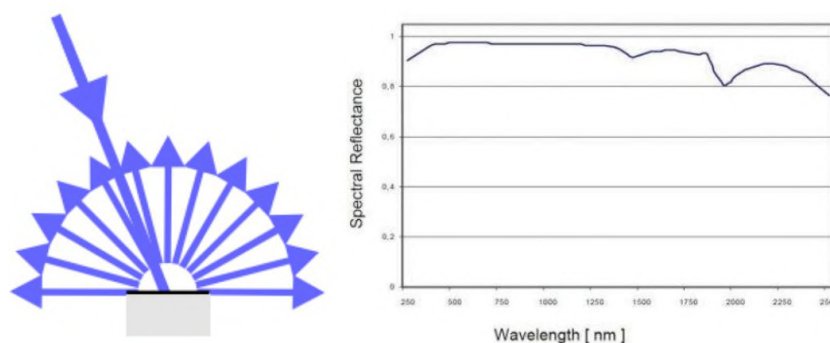


Figure B.2: *On the left we can see a schematic of the radiation reflected by a perfect Lambertian surface. On the right, the reflectance spectra of barium sulfate. The images were obtained from [320]*

Integrating spheres are devices designed to obtain a uniform distribution of optical radiation in its interior. This is achieved by coating the inner walls of the sphere with a material that behaves like a Lambertian surface—one which reflects radiation with constant radiance in all directions of a hemisphere[320]. Most devices, including the ones used in this work, are coated with barium sulfate ($BaSO_4$) based paint, which acts as a good Lambertian surface, while also having high reflectance in a wide spectral range[320]. A schematic of the behaviour of Lambertian surface and the reflectance spectra of barium sulfate are shown in figure B.2.

An ideal integrating sphere has an irradiance in its interior that is only proportional to the incident illumination and inversely proportional to its radius as a result of multiple reflections without a preferential direction. This proves useful because the measurement

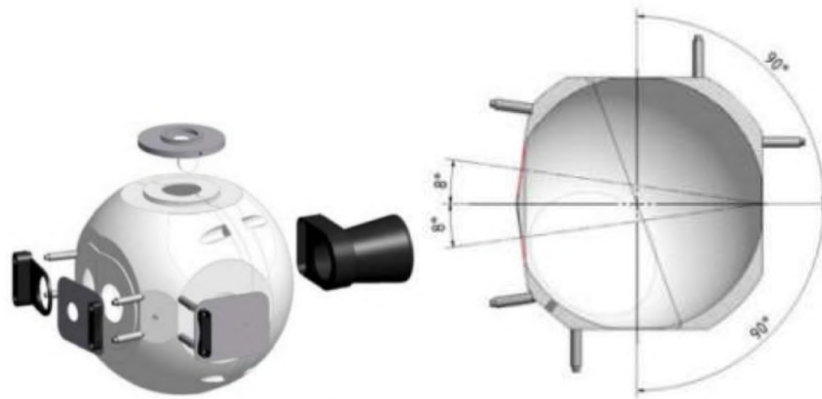


Figure B.3: *On the left we can see a schematic of one model of integrating sphere used. On the right, the distribution of the different ports and baffled located around the equatorial plane. Images obtained from [320]*

is relatively independent on the geometrical path of the light ray, easing alignment requirements, and on any residual polarization present in the source. In practice, the device has a non-flat spectral response, and the presence of ports and baffles affect the signal. A schematic of an integrating sphere is shown in figure B.3. Notice that the presence of baffled, ports and detectors necessary for measurement alter the perfectly spherical shape.

B.4. Waveplates and linear polarizers

Quarter-wave plates (QWP) and half-wave plates (HWP) are optical devices used to manipulate the polarization state of light [27, 28]. They are both types of wave plates, or retarders, made from birefringent materials that have different refractive indices for light polarized along two orthogonal axes. The difference in these indices leads to a phase difference between the two polarization components as they pass through the plate.

Quarter-Wave Plates are designed to introduce a phase shift of 90 degrees ($\lambda/4$) between the fast and slow polarization components of the incident light. When linearly polarized light is incident at a 45-degree angle to the optical axes of the quarter-wave plate, the phase shift converts it into circularly polarized light. Conversely, circularly polarized light incident on a quarter-wave plate is converted into linearly polarized light, with the orientation of the polarization depending on the direction of the circular polarization (left or right-handed) and the axes of the quarter-wave plate.

Half-Wave Plates cause a phase shift of 180 degrees ($\lambda/2$) between the fast and slow polarization components. This phase shift effectively rotates the polarization direction of linearly polarized light. The angle of rotation is twice the angle between the light's initial polarization direction and the optical axis of the half-wave plate. This capability

TABLE 2 SUMMARY OF JONES MATRICES

I. Linear polarizers			
TA horizontal	$\begin{bmatrix} 1 & 0 \\ 0 & 0 \end{bmatrix}$	TA vertical	$\begin{bmatrix} 0 & 0 \\ 0 & 1 \end{bmatrix}$
		TA at 45° to horizontal	$\frac{1}{2}\begin{bmatrix} 1 & 1 \\ 1 & 1 \end{bmatrix}$
II. Phase retarders			
		General	$\begin{bmatrix} e^{i\epsilon_x} & 0 \\ 0 & e^{i\epsilon_y} \end{bmatrix}$
QWP, SA vertical	$e^{-i\pi/4}\begin{bmatrix} 1 & 0 \\ 0 & i \end{bmatrix}$	QWP, SA horizontal	$e^{i\pi/4}\begin{bmatrix} 1 & 0 \\ 0 & -i \end{bmatrix}$
HWP, SA vertical	$e^{-i\pi/2}\begin{bmatrix} 1 & 0 \\ 0 & -1 \end{bmatrix}$	HWP, SA horizontal	$e^{i\pi/2}\begin{bmatrix} 1 & 0 \\ 0 & -1 \end{bmatrix}$
III. Rotator			
Rotator	$(\theta \rightarrow \theta + \beta)$		$\begin{bmatrix} \cos \beta & -\sin \beta \\ \sin \beta & \cos \beta \end{bmatrix}$

Figure B.4: Jones matrices for the different optical elements used in this work. Extracted from [28].

allows half-wave plates to be used for polarization rotation, enabling precise control over the orientation of linearly polarized light.

Linear polarizers (LP) are optical devices designed to transmit light that is polarized in a specific direction (aligned with the transmission axis) while absorbing light polarized in the perpendicular direction to the transmission axis. The core mechanism of a linear polarizer is linear dichroism—selective absorption of light polarized in a particular direction [27, 28].

Optical elements can be conveniently represented by 2x2 matrices in the context of Jones calculus, applicable for completely polarized light. The matrices representing each component appear in figure B.4.

B.5. Collimators

A collimator is an optical device designed to narrow a beam of waves, allowing it to be parallel or to diverge minimally over a certain distance. It transforms a divergent beam into one that propagates essentially in a single direction [27]. When all the rays of a beam propagate parallel to each other the beam is said to be collimated [28]. In the context of photonics and optics, collimators are essential for producing a parallel beam of light from a source that inherently emits light in various directions. This function is pivotal in applications requiring high precision and directionality, such as in laser optics [321, 322].

The principle of operation for a collimator involves the use of lenses or mirrors arranged in such a way that they correct the divergence of the light beam. A simple optical collimator, for example, might consist of a tube containing a convex lens positioned at

one of its focal points relative to the light source. As light rays from the source pass through the lens, they are refracted such that they emerge parallel to the lens axis and to each other.

Appendix C

The Deal-Grove model

The Deal-Grove model [64, 67, 72, 74] is a seminal framework for understanding and predicting the growth kinetics of thermally grown silicon dioxide (SiO_2) layers on silicon (Si) substrates. Developed in the late 1960s by Bruce Deal and Andrew Grove, this model provides a quantitative description of the oxidation process, crucial for the fabrication of semiconductor devices.

It is based on the assumption that the oxidation process comprises three primary steps: (1) the (Fickian) diffusion of oxygen through the already formed SiO_2 layer, (2) the reaction of oxygen with silicon at the Si/SiO_2 interface, and (3) the incorporation of the resulting SiO_2 into the existing oxide layer. The model simplifies the oxidation kinetics into a linear-parabolic rate law, which can be represented as:

$$\frac{dx}{dt} = \frac{B}{A + x} \quad (C.1)$$

Where x is the oxide thickness, t is the time, A is the linear rate constant, and B is the parabolic rate constant. The linear rate constant (A) dominates at the initial stages of oxidation, where the oxide layer is thin and the reaction rate at the $Si - SiO_2$ interface controls the process. As the oxide layer thickens, the diffusion of oxygen through the SiO_2 layer becomes the limiting factor, making the parabolic rate constant (B) more influential.

Equation C.1 can be integrated to yield the following equation:

$$x^2 + Ax = Bt \quad (C.2)$$

This equation describes the oxide thickness (x) as a function of time (t), where the terms involving A and B correspond to the linear and parabolic growth regimes, respectively. By fitting experimental data to this model, one can extract the values of A and B , which are dependent on the oxidation temperature and the ambient atmosphere.

The Deal-Grove model has been remarkably successful in predicting the growth of thermal SiO_2 layers under a wide range of conditions. However, it is important to note that deviations from the model can occur due to factors such as high doping concentrations, very thin oxides, or low-temperature oxidation processes [59, 60].

Appendix D

Further elements of the *Episcada hymenaea* traslucent butterfly wings

This appendix complements the results presented in chapter 5.

D.1. SEM characterization of the bristles

The surface of the wing is covered in high aspect ratio structures akin to hairs, which are usually called piliform scales or bristles [98]. These structures are shown in figures D.1a trough D.1d. The membrane region of the wing, figure D.1b is covered in this bristles which are approximately $5 \mu m$ thick and $\approx 70 \mu m$. They are separated a distance of about $60 \mu m$, and the region between them appears devoid of any nanostructure. In figures D.1c and D.1d we can appreciate the morphology of the bristles, which have a regular arrangement of scales.

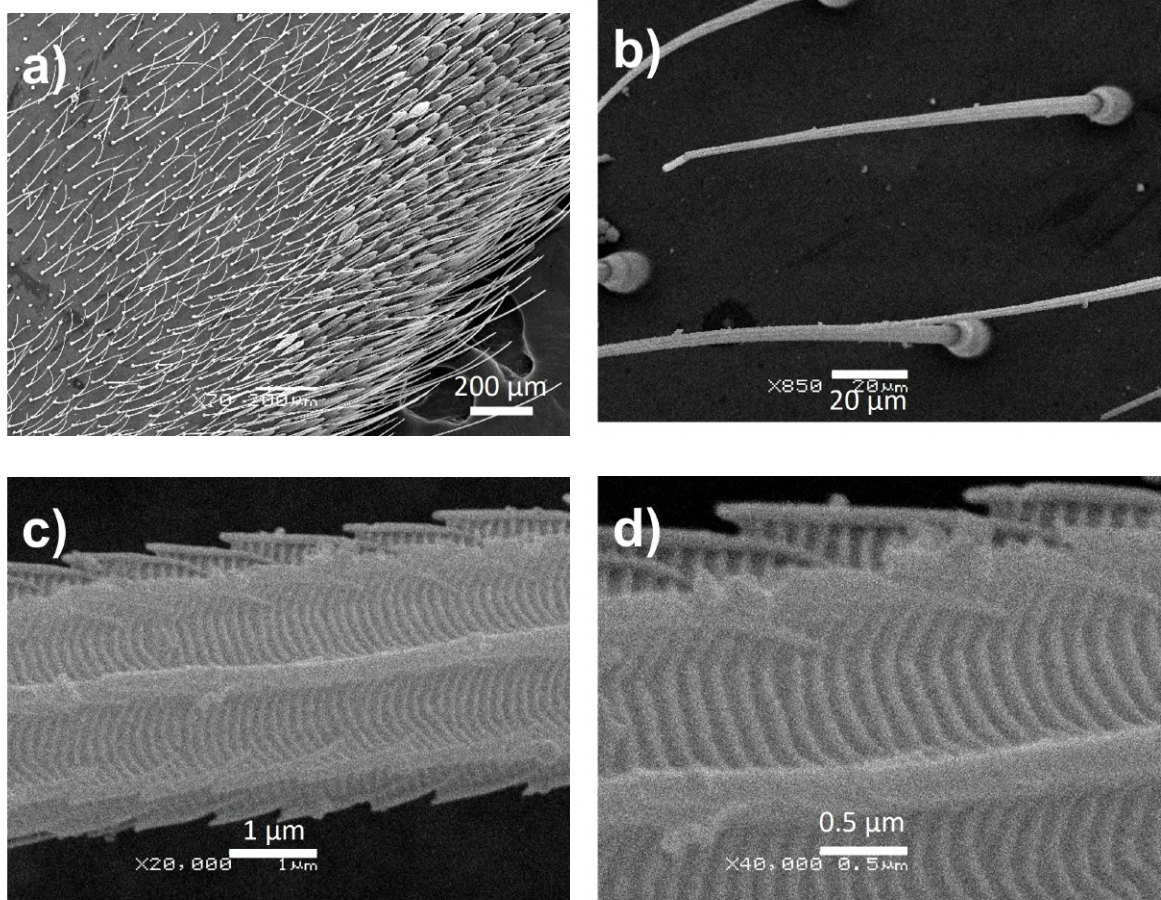


Figure D.1: SEM micrographs of the wing of the *Episcada hymenaea* translucent butterfly. a) General structure of the wing (scale bar $200\mu\text{m}$), we see the edge composed of scales and the inner region, both have long bristles. b) Image of the bristles (scale bar $20\mu\text{m}$), c) close up of a single bristle, where the general structure can be seen (scale bar $1\mu\text{m}$) and d) highest magnification of the structure, where the reticular structure is apparent (scale bar $0.5\mu\text{m}$)

D.2. Gradient index model considerations

In this section some elements of the analysis presented in section 5.3.3.1 are discussed. We begin with the presentation of the fitting of the extinction coefficient, followed by the proof of the width for a given height. Lastly, we show the gradient index profile resulting from the Gaussian lobe model with random widths.

D.2.1. The extinction coefficient of chitin, k

As an approximation, we can take the absorbance (A_b) to be equivalent to the absorbance (A). This is reasonable for the calculation of the total transmittance because a) it includes the scatter and b) the reflectance of the wing is very small. Then, assuming a

wing thickness (d) of 450 nm we can obtain the absorption coefficient (α_b , to distinguish from the real absorption coefficient α) using the following equation:

$$A \equiv A_b = \alpha_b d \quad (\text{D.1})$$

Then, we can use the relationship between extinction coefficient (k) and the absorption coefficient:

$$\alpha = \frac{2k\omega}{c} \quad (\text{D.2})$$

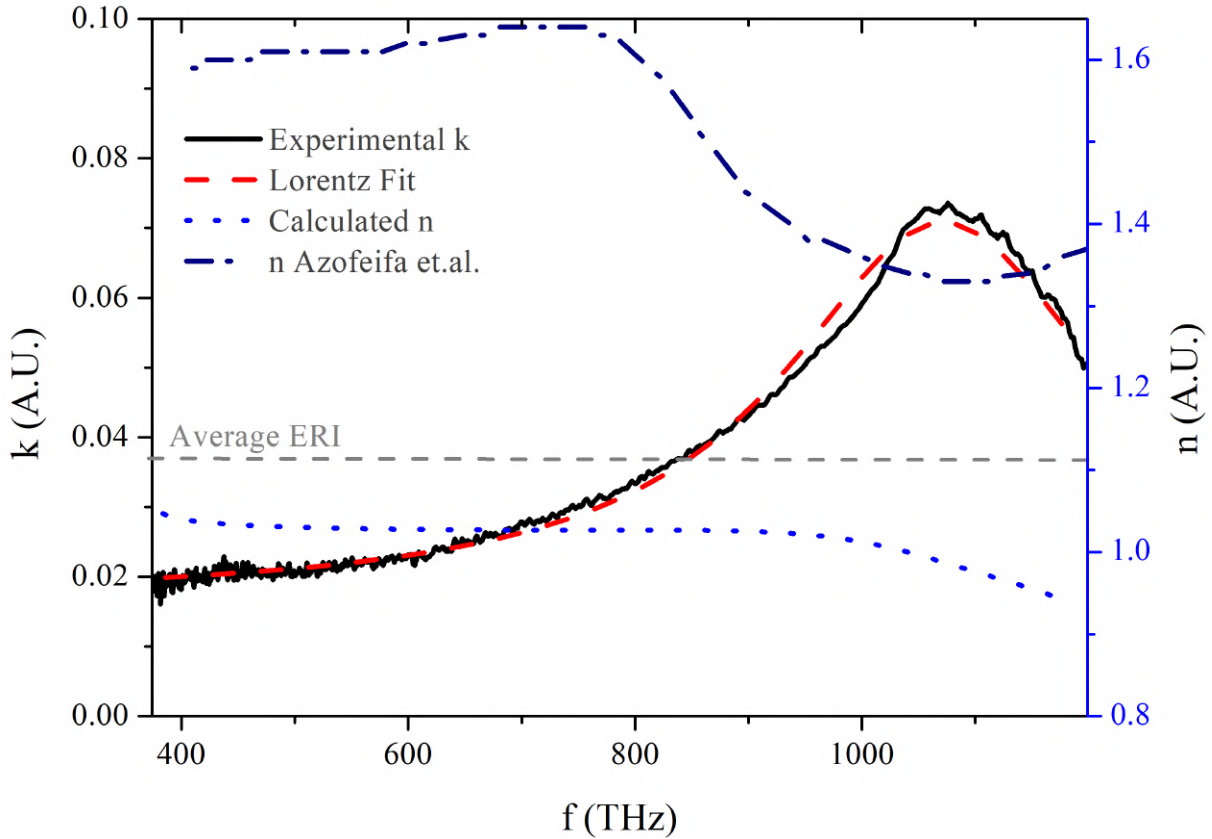


Figure D.2: Extinction coefficient (k) as a function of frequency (f) as a black solid curve. The red dashed line shows the fitting with a Lorentz oscillator, which is in excellent agreement with experiment ($R^2 > 0.99$). The blue dotted line shows the calculated index of refraction (n) using the Kramers-Kronig relations truncated to the shown frequency range. In dark blue dash dotted line the index of refraction reported by Azofeifa and others [125] is shown for comparison.

In order to avoid the noise inherent in the results and propagate them into the calculated spectra, we fit the k using a Lorentz curve, which is one of the classical models for the absorption edges, the Lorentz oscillator [1, 22]. The results of the calculated and fitted extinction coefficient appear in figure D.2. The function describing the Lorentz curve (in terms of angular frequency ω) is shown in equation D.3 and the fitted parameters are displayed in table D.1.

$$k(\omega) = y_0 + \frac{2A}{\pi} \frac{w}{4(\omega - x_c)^2 + w^2} \quad (\text{D.3})$$

The fit is in excellent agreement with experiment, with an R^2 of over 0.99. We know that the real part of the refractive index (the index of refraction, n) is related to k through the Kramers-Kronig relations, where P denotes the Cauchy principal value of the integral:

$$n(\omega) = 1 + \frac{2}{\pi} P \int_0^\infty \frac{\omega' k(\omega')}{\omega'^2 - \omega^2} d\omega' \quad (\text{D.4})$$

As we do not have the absorption spectra from 0 to infinite frequency, we truncate the integral to the available range, which is equivalent to assuming that outside the fitted range the absorption is 0 ($k = 0$). This procedure yields the index of refraction shown in dotted blue line. While it is relatively close to the average effective refractive index (ERI) obtained in section 5.3.3, shown with a horizontal grey line, it is extremely different from the values previously reported for chitin. The index of refraction reported by Azofeifa and others [125] are shown for comparison. If other absorption bands at either higher or lower frequencies were considered, it is possible that both indices of refraction would match. For this work we considered the index of refraction presented in the literature and the fitted extinction coefficient from experiment. While they are not consistent in the spectral range with the Kramers-Kronig relations, it is possible that this is only due to the limited range of frequencies probed.

$\mathbf{A} \times 10^{-15}$ (rad/s)	$\mathbf{x}_c \times 10^{-15}$ (rad/s)	$\mathbf{w} \times 10^{-15}$ (rad/s)	\mathbf{y}_0	\mathbf{R}^2
0.185	6.67	2.18	0.0166	0.993

Table D.1: Best fit parameters for the extinction coefficient (k) using a Lorentzian curve.

D.2.2. The width of the Gaussian curve, $w(h)$

The equation describing a Gaussian function centered at the origin is given by:

$$g(x) = \frac{1}{\sigma\sqrt{2\pi}} \exp\left(-\frac{1}{2} \frac{(x)^2}{\sigma^2}\right) \quad (\text{D.5})$$

We want to obtain the width of the curve at any height h . The values of the abscissa associated with that height h are called x_h so that $g(x_h) = h$. In figure D.3 a diagram of the situation is shown.

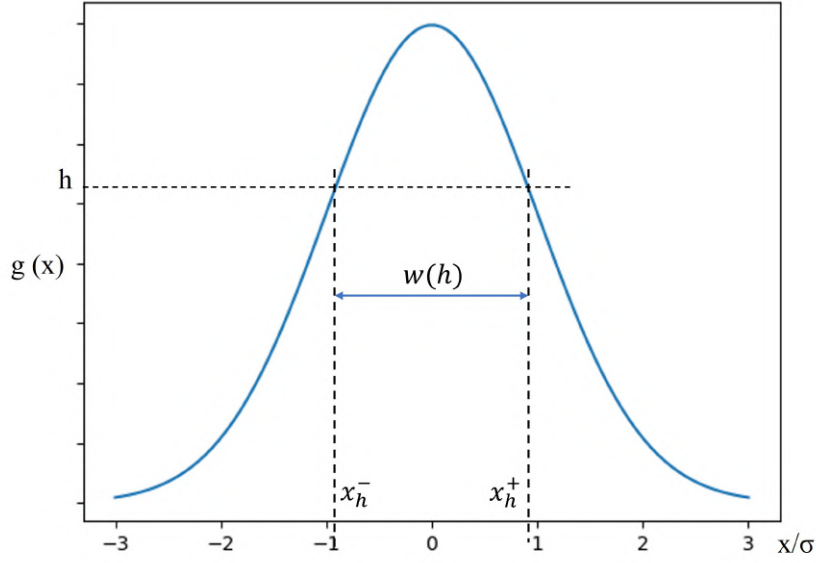


Figure D.3: Schematic of the width at a given height for a Gaussian distribution

It is simple to prove that the values x_h are given by:

$$x_h = \pm \sqrt{-2\sigma^2 \ln(h\sigma\sqrt{2\pi})} \quad (\text{D.6})$$

The width is the differences between those two values and thus we have:

$$w = x_h^+ - x_h^- = 2|x_h| = 2\sqrt{-2\sigma^2 \ln(h\sigma\sqrt{2\pi})} \quad (\text{D.7})$$

D.2.3. Air fraction profile obtain with the Gaussian model

Figure D.4 presents the air fraction profile used in the calculations by assuming a random distribution of Gaussian shaped lobes. For comparison, the linear model is also shown. While the deviations are relatively small, they are still significant, specially at the initial heights, which are the ones that influence reflectance the most. To expand the analysis it would be interesting to use profile that differ more with the linear profile.

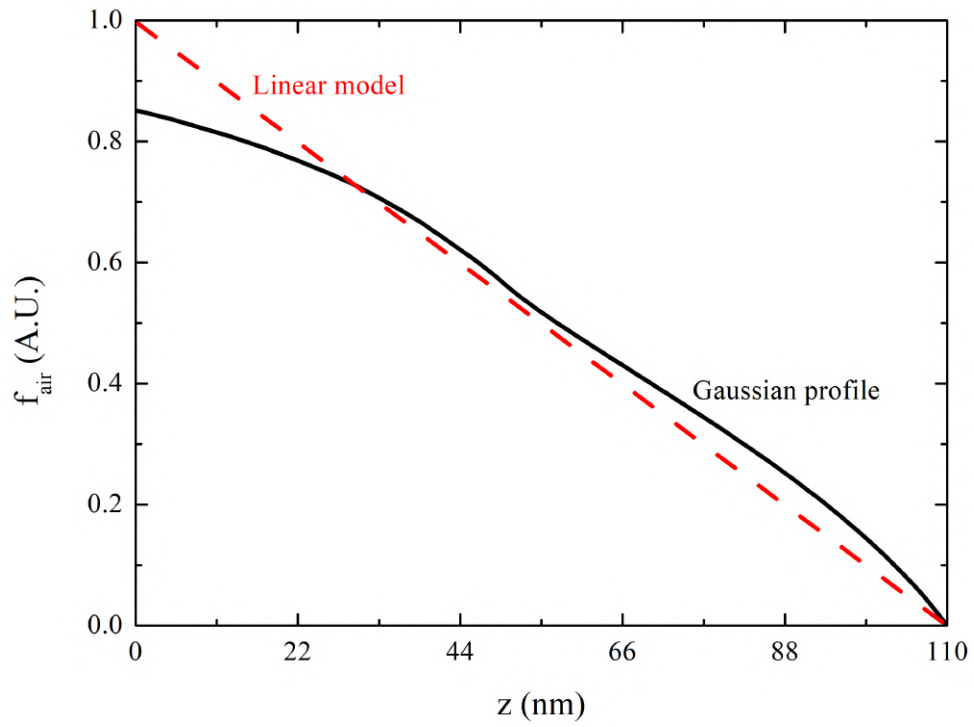


Figure D.4: Resulting Gaussian profile used in gradient index calculations, obtained by averaging the results for 1000 samples of the standard deviation from a uniform distribution. For comparison the linear profile is shown in the red dashed line

Appendix E

Additional elements of the ZnO-SnS NT/NRs analysis

E.1. Additional SEM images

SEM images of the samples at higher magnification are shown in figure [E.1](#). These magnification could aid in the observations of the diameters and coverage factors of each sample.

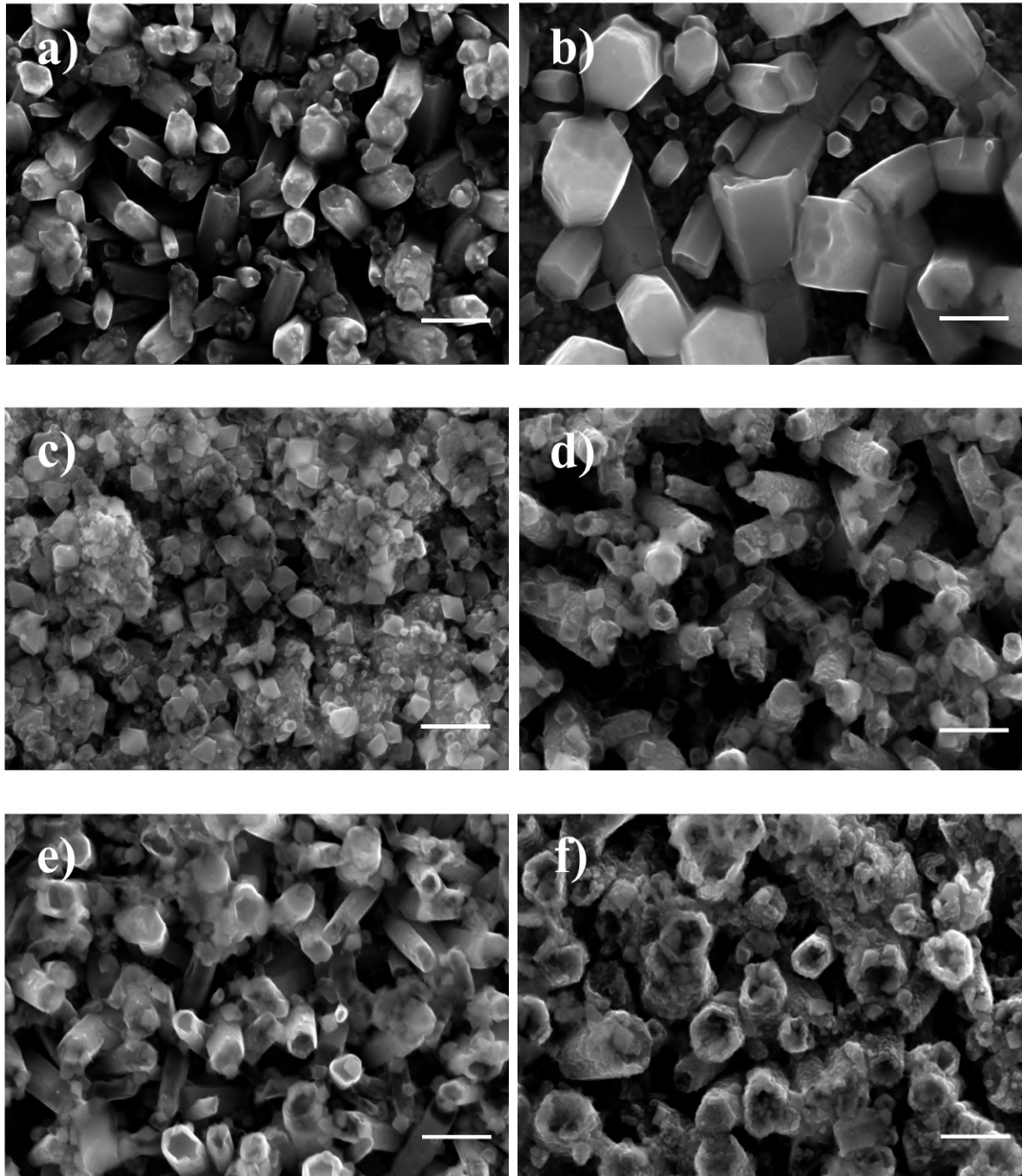


Figure E.1: SEM images of samples prepared with a ZnO precursor concentration of a),c) and e) 4 mM and b),d),f) 12 mM, with 0 (a and b), 10 (c, d) and 15 (e, f) SILAR cycles. The scale bars represent 500 nm.

E.2. Clusters and Nanocrystals

Figure E.2a shows some of the structures called “clusters” in this work. The diameter of these structures was measured and the average diameter reported as $D_{cluster}$. In figure

E.2b a close up of the region of figure E.2a enclosed by a white dashed box is shown, and some of the structures called “nanocrystals” are indicated.

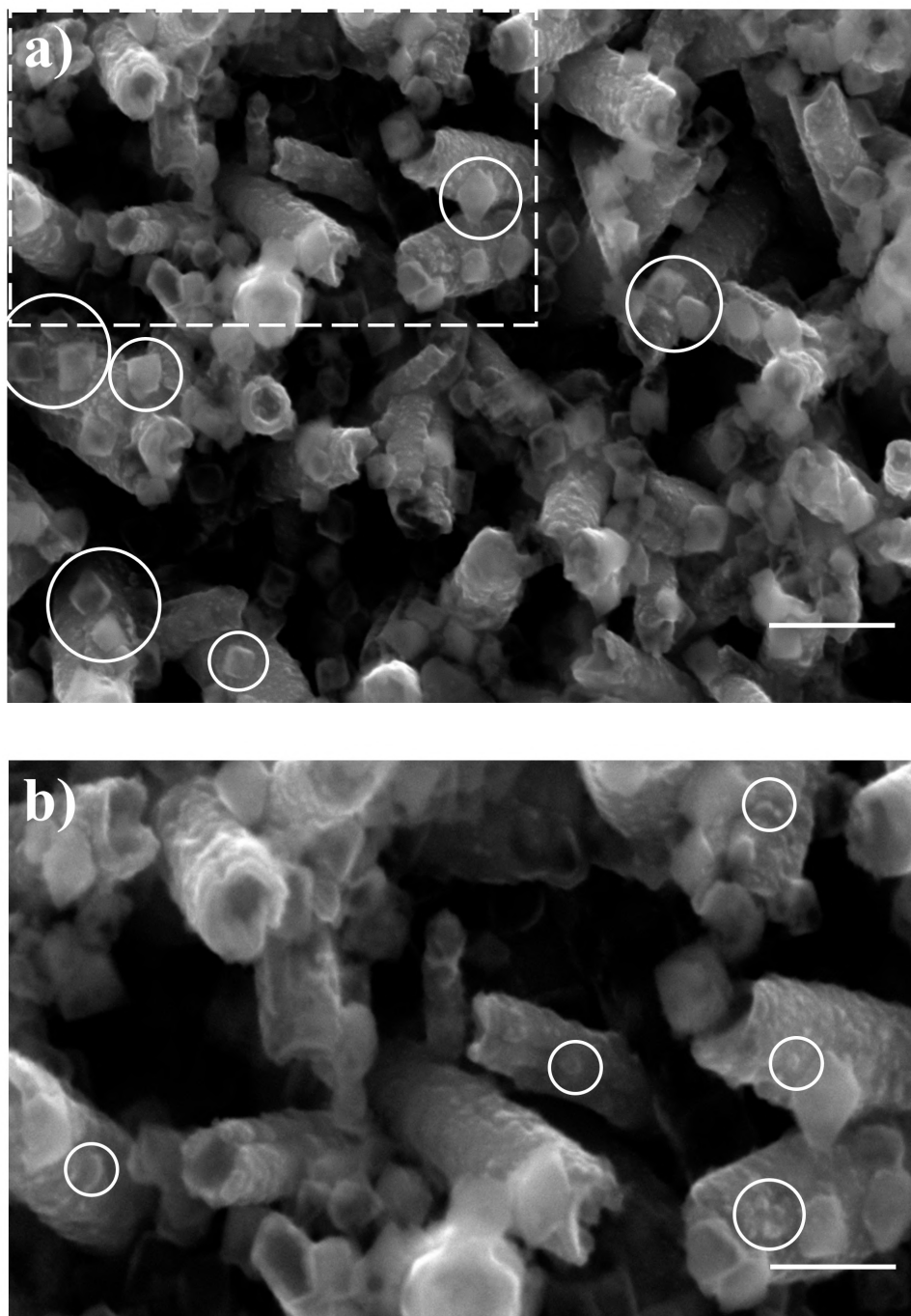


Figure E.2: a) SEM image of the 12 mM 10 cycle sample, where the white circles indicate some of the structures called “clusters” and the white dash box shows the region shown in b). In the closeup b), some of the structures called nanocrystals are shown,. The scale bars represent 500 nm.

E.3. Cover factor and threshold selection

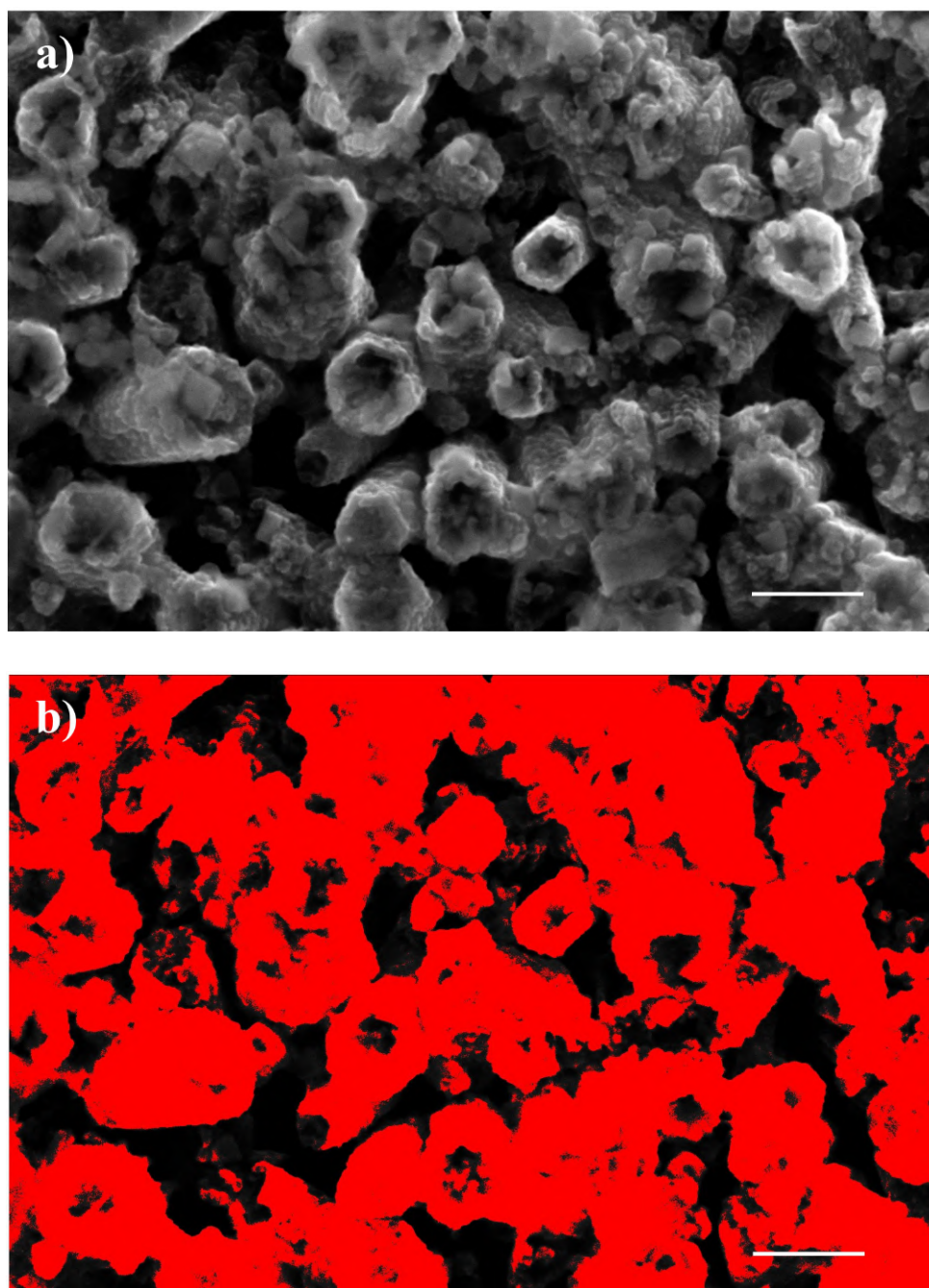


Figure E.3: *Threshold area selection in the program ImageJ with intensity boundaries of 35 to 255 applied to the 12 mM, 15 cycle sample. In a) the original image, and b) the selected nanostructures in red. The scale bars represent 500 nm.*

The program ImageJ was used for area selection. The black and white image has 8 bits of information, resulting in 256 intensity levels. The intensity threshold boundaries were selected based on inspection of an adequate selection of the nanostructures. The

boundaries used were 35 to 255. Figure E.3 shows an example with the 12 mM, 15 cycle sample. The threshold selects the nanostructures and then calculates the total area of the selection. The cover factor is obtained by dividing this area by the total area of the image.

E.4. Energy-dispersive X-ray spectroscopy (EDX)

The EDX module attached to the FE-SEM model Helios Nanolab 650 Dual Beam from FEI company equipment at the University of Malaga was used to analyse the composition of the sensitized samples. Zn and S were used as indicators of the ZnO core and SnS shell, respectively, given that these elements are not present in the substrate. The results for the 4 mM set appears in figure E.4. Notice that the 10 cycle sample (E.4a) has a higher percentage of sulfur (2.26% compared to 1.70%), consistent with the appearance of large clusters of deposited material.

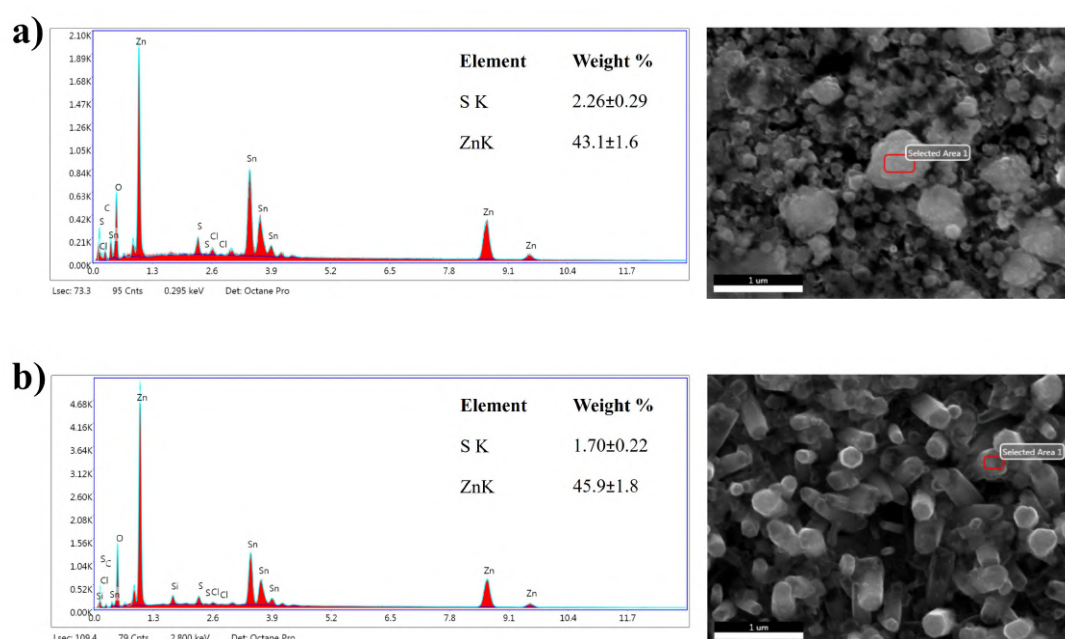


Figure E.4: EDX results for the 4 mM set with a) 10 SILAR cycles and b) 15 SILAR cycles. The images show the analyzed area, and in the top right of the EDX results the weight percentage of each element is shown. The K indicates that the excited electrons related to the K shell, the one closest to the nucleus. Scale bars represent 1 μm .

The results of the analysis for the 12 mM set are shown in figure E.5. In the case of the 10 cycle sample it was possible to map the basal plane (E.5a) and the side wall (E.5b) of the same NR. The basal plane shows an increase in S weight percentage, which could be related to the reduction in ZnO due to selective etching in the basal plane. The

average weight percentage of sulfur in this sample is 1.73%, lower than that of the 15 cycle sample, at 2.34%. This is consistent with an increase in deposited SnS with increasing SILAR cycles.

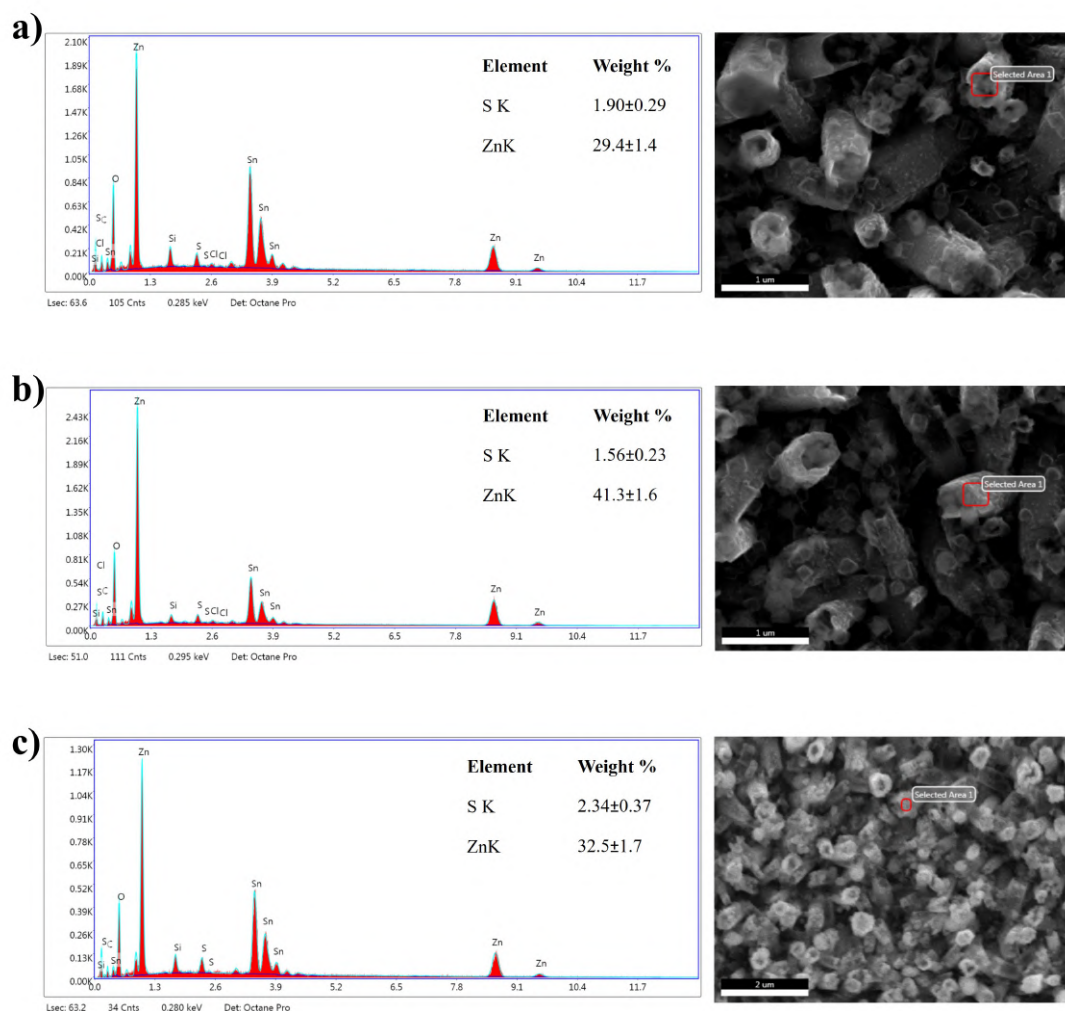


Figure E.5: EDX results for the 12 mM set with a) 10 SILAR cycles on the basal plane and b) on the side wall. In c) the results for the 15 cycles sample. The images show the analyzed area, and in the top right of the EDX results the weight percentage of each element is shown. The K indicates that the excited electrons relaxed to the K shell, the one closest to the nucleus [323, 324]. Scale bars in a) and b) represent 1 μm and that of c) 2 μm .

Appendix F

Heat transfer in the nanorods and nanotubes

In this appendix we will solve the heat transfer equation for two concentric infinite cylinders with the outer cylinder generating uniform heat. This configuration attempts to model high aspect ratio core-shell nanorods (NRs) and nanotubes (NTs) where the outer shell is absorbing light that is dissipated exclusively by non-radiative processes[1], generating heat.

F.1. Nanotube

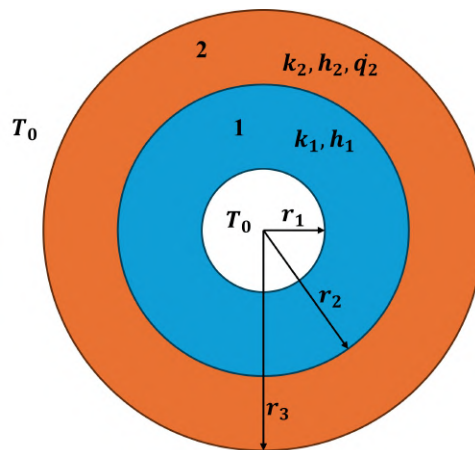


Figure F.1: Schematic of the model of concentric hollow cylinders used to model a nanotube

A schematic of the situation of a nanotube is shown in figure F.1. We have a hollow cylinder of inner radius r_1 and outer radius r_2 forming the core (1) and an outer cylinder (2) of external radius r_3 . The temperature of the ambient air in both the outer and hollow sections is T_0 , considered constant. The thermal conductivities are k_1 and k_2 ,

while the convection coefficient of the surfaces are h_1 and h_2 . They are all assumed to be constant, which is consistent with our final results because, as we will see, there is negligible temperature increase with the heat generated by our samples. The outer cylinder generates constant energy per unit volume (W/m^3) of \dot{q}_2 . By symmetry of the problem, and assuming an infinite cylinder, only the radial dependence is relevant. The heat equation in the steady state (s.s), using cylindrical coordinates becomes [325]:

$$\frac{1}{r} \frac{d}{dr} \left(kr \frac{dT}{dr} \right) + \dot{q}_2 = 0 \quad (s.s) \quad (F.1)$$

This differential equation can be directly integrated by separation of variables. In cylinder 1 we have:

$$\frac{1}{r} \frac{d}{dr} \left(k_1 r \frac{dT_1}{dr} \right) = 0 \rightarrow T_1(r) = \frac{C_1}{k_1} \ln r + C_2, \quad r_1 < r < r_2 \quad (F.2)$$

And for the outer cylinder (2) we have the result shown in equation F.3, where we have made $Q = \frac{\dot{q}_2}{4k_2}$.

$$\frac{1}{r} \frac{d}{dr} \left(k_2 r \frac{dT_2}{dr} \right) + \dot{q}_2 = 0 \rightarrow T_2(r) = -\frac{\dot{q}_2}{4k_2} r^2 + C_3 \ln r + C_4 = -Qr^2 + C_3 \ln r + C_4, \quad r_2 < r < r_3 \quad (F.3)$$

C_i are the integration constants, which will be obtained from applying appropriate boundary conditions. We have that the heat flux density in the outer and inner surfaces must be consistent with the convective heat transfer equation: $q = -k\nabla T = h(T - T_0)$ [325]. Furthermore the temperature and the heat flux density at the boundary between the two cylinders must be continuous. Therefore we have the following equations, where the r dependence of T was dropped for brevity:

$$-k_1 \frac{dT_1}{dr} \Big|_{r=r_1} = h_1 [T_1(r_1) - T_0] \rightarrow -k_1 C_1 \frac{1}{r_1} = h_1 (C_1 \ln r_1 + C_2 - T_0) \quad (F.4)$$

$$T_1(r_2) = T_2(r_2) \rightarrow C_1 \ln r_2 + C_2 = -Qr_2^2 + C_3 \ln r_2 + C_4 \quad (F.5)$$

$$k_1 \frac{dT_1}{dr} \Big|_{r=r_2} = k_2 \frac{dT_2}{dr} \Big|_{r=r_2} \rightarrow \frac{k_1 C_1}{r_2} = k_2 \left[-2Qr_2 + C_3 \frac{1}{r_2} \right] \quad (F.6)$$

$$-k_2 \frac{dT_2}{dr} \Big|_{r=r_3} = h_2 [T_2(r_3) - T_0] \rightarrow -k_2 \left[-2Qr_3 + \frac{C_3}{r_3} \right] = h_2 (-Qr_3^2 + C_3 \ln r_3 + C_4 - T_0) \quad (F.7)$$

Solving for the coefficients C_i we can obtain that C_1 is given by:

$$C_1 \left[\ln \left(\frac{r_2}{r_1} \right) + \frac{k_1}{h_2 r_3} - \frac{k_1}{h_1 r_1} \right] = Q \left[1 + \frac{2k_2}{r_3 h_2} \right] (r_3^2 - r_2^2) \quad (F.8)$$

And with C_1 we can solve for the other coefficients:

$$\begin{aligned}
C_2 &= -C_1 \left(\frac{k_1}{h_1 r_1} + \ln r_1 \right) + T_0 \\
C_3 &= r_2 \left(\frac{k_1 C_1}{k_2 r_2} + 2Qr_2 \right) \\
C_4 &= r_2 \left(\frac{k_1 C_1}{k_2 r_2} + 2Qr_2 \right) \left[\frac{-k_2}{h_2 r_3} - \ln r_3 \right] + Qr_3 \left(2 \frac{k_2}{h_2} + r_3 \right) + T_0
\end{aligned} \tag{F.9}$$

F.2. Nanorod

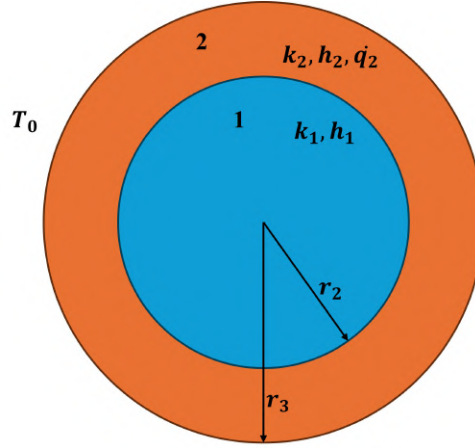


Figure F.2: Schematic of the model of concentric cylinders used to model a nanorod

If we instead have a nanorod, we can model it as two concentric cylinders, as shown in figure F.2. The parameters are defined as shown in the previous section. The heat equations F.2 and F.3 are still valid. The boundary conditions are also the same, except for the condition at r_1 . In this case we require that the heat flux density at the center is 0, as it is a node. Therefore, we replace condition F.4 by:

$$-k_1 \frac{dT_1}{dr} \Big|_{r=0} = 0 \rightarrow -k_1 C_1 \frac{1}{r_1} = 0 \rightarrow C_1 = 0 \tag{F.10}$$

With this we have that:

$$\begin{aligned}
C_3 &= \frac{Qr_2^2}{2} \\
C_4 &= \frac{-k_2}{h_2} \left(\frac{-Qr_3}{2} + \frac{Qr_2^2}{2r_3} \right) + Qr_3^2 - r_2^2 \frac{Q}{2} \ln r_3 + T_0 \\
C_2 &= -Qr_s^2 + C_3 \ln r_3 + C_4
\end{aligned} \tag{F.11}$$

F.3. Application to the measured samples

With the solution to the heat equation in both cases, it is possible to compute the temperature profile at both the core and shell given the parameters of the system. The thermal conductivity values are taken from the literature [313, 326, 327]. The convection coefficient is difficult to calculate at the nanoscale given the massive surface to volume ratio and the changes in thermal transport, and none is reported for ZnO or SnS samples. We utilize reports of the convection coefficient for carbon nanorods [328, 329].

In order to determine the heat energy generation, we will consider an upper limit, where the total energy absorbed by the shell is dissipated by heat. The total irradiance (flux density) of the lamp is P_l . This energy is distributed between N nanostructures. The number of nanostructures can be estimated by the ratio of the incident light spot radius (r_a) and the external radius of the nanostructure (r_3). This ratio is adjusted by the nanostructure cover factor, defined as the fraction of nanostructured area relative to the total area samples: $f = \frac{A_n}{A_t}$ with A_n and A_t the total area covered by the nanorods and the total area, respectively. Then we have that N is given by:

$$N = A_t \frac{f}{\pi r_3^2} = f \frac{r_a}{r_3} \quad (\text{F.12})$$

Each nanostructure absorbs a certain percentage β of the incident energy. This energy is entirely dissipated by non radiative process, generating heat. The energy per unit volume is simply the total energy absorbed divided by the volume of the shell: $V_s = L * \pi(r_3^2 - r_2^2)$.

$$\dot{q}_2 = \frac{P_l}{N} \beta \times \frac{1}{L * \pi(r_3^2 - r_2^2)} \quad (\text{F.13})$$

From the data sheet of our lamp we have that $P_l = 4.7mW/m^2$. We take the external radius $r_3 = 150nm$. The inner radius of the shell, r_2 is taken as 122 nm, so as to have a 28 nm wall thickness, consistent with the measured nanocrystal sizes. We will see that varying this parameter does not affect the temperature distribution. We consider a cover factor of 60% and a spot radius of 1 mm. We consider that each nanostructure absorbs 50% of the incident radiation, based on the total transmittance and reflectance measurements. The length is taken as 1 μm . With this we have that:

$$\dot{q}_2 = \frac{4.7mW/m^2}{4000} 0.5 \times \frac{1}{1\mu m \cdot \pi[(150nm)^2 - (122nm)^2]} = 2.5 \times 10^{13} W/m^3 \quad (\text{F.14})$$

The only parameter left is the inner radius (r_1) in the nanotubes. From the SEM images we can obtain the hole ratio, defined as the ratio of the inner diameter to the total diameter. The results of measuring on the available images are shown in figure F.3. We consider a hole ratio of 0.6 for the calculations, close to the average and median of both sets.

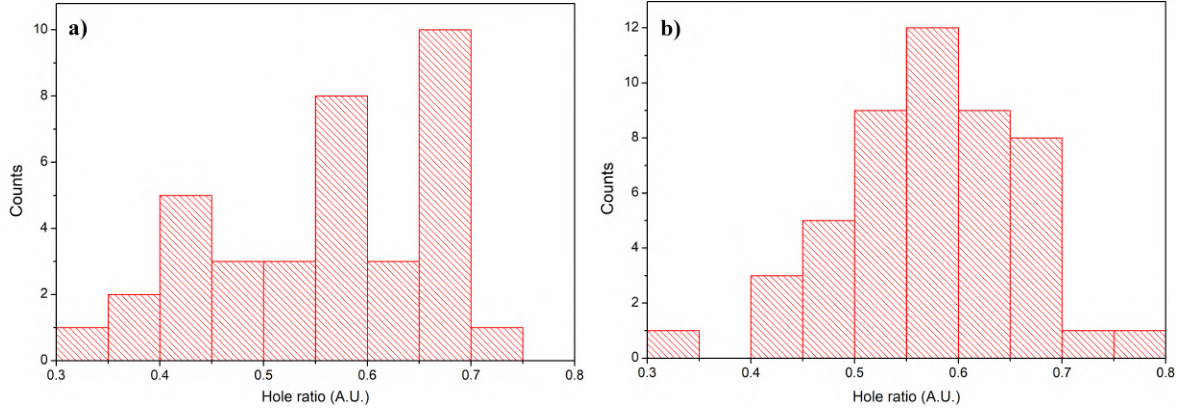


Figure F.3: Histogram of sampled hole ratio (fraction of hole diameter to external diameter) from SEM images for a) 4mM and b) 12 mM nanotubes

With the model we calculate the ratio of the temperature profile in the nanorod compared to that of the nanotube in different positions of the external diameter as a function of shell thickness (figure F.4a) and as a function of external diameter (D) for a wall thickness of 28 nm (figure F.4b). The results appear in figure F.4. Notice that in figure F.4a the distance is normalized as the actual length of the SnS shell varies.

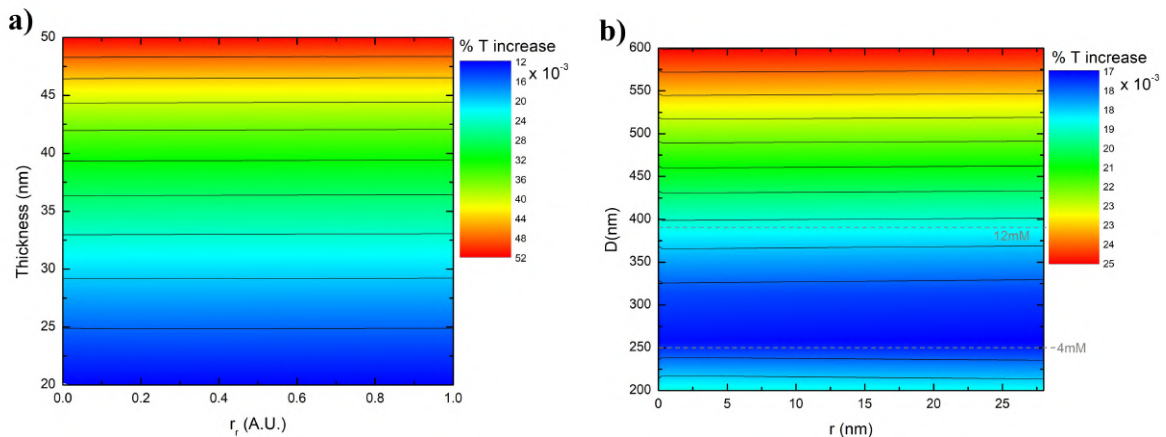


Figure F.4: Percentage temperature increase of a nanorod relative to a nanotube in the profile of the shell with varying a) thickness and b) external diameter. The hole ratio is 0.6. In a) the external diameter is kept fixed at 300 nm and in b) the shell thickness is 28 nm. The power generated is $2.5 \times e^{13} \text{W/m}^3$. Notice that in b) the average diameter of the 15 cycles (which showed NTs) 4 mM and 12 mM samples are indicated with grey dashed lines

We see that the predicted temperature increase with one nanostructure relative to the other is negligible. Further, the temperature profile obtained for each sample is almost the same as the ambient temperature T_0 , taken as 25°C . Thus, at our incident power, there is no expected temperature variation or temperature profile difference in our nanostructures. This is reasonable considering the operation in the steady state of a relatively low power laser and the massive surface-to-volume ratio of the nanostructures.

F.4. Numerical modelling employing COMSOL

To test the results of our model, we computed the temperature profile using the Heat Transfer module in COMSOL multiphysics. Using the same parameters as before, and a height of $1\mu\text{m}$ we obtain the profiles of figure F.5. The basis of the nanostructure is considered fixed to a substrate and held at constant temperature T_0 , which is reasonable given the large thermal conductivity of the FTO and the massive volume of the glass plate relative to the nanostructures.

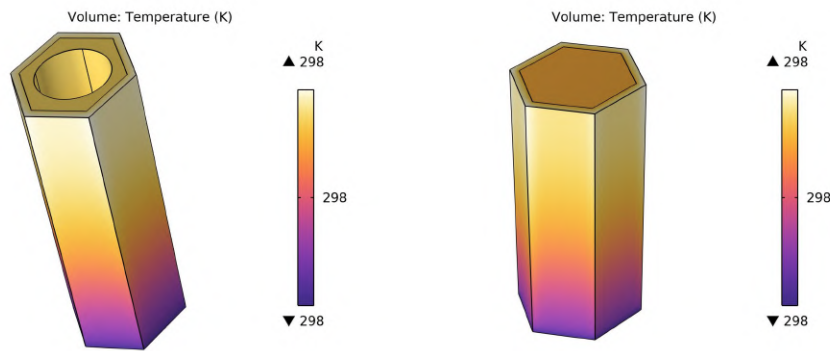


Figure F.5: *Simulated temperature profiles for nanotube and nanorod in COMSOL*

From the simulations it is clear that there is no noticeable temperature increase in either structure, which is in good agreement with the concentric infinite cylinder model.

Appendix G

von Mises stress

The stress is a physical quantity that describes the force per unit area that particles of a continuous material exert on each other. At each point there are 3 normal stresses (perpendicular to the faces of an infinitesimal cube) and 6 shear stresses tangential to the planar faces. This can be seen in figure G.1. These stress directions can be grouped in what is called the stress tensor. The general form of the stress tensor σ is a second-order tensor that represents the state of stress at a point within a material. It encompasses both normal and shear stress components acting on an infinitesimal element of the material [330]. Similarly, the strain (ϵ) is the relative deformation (change of shape) of a material, and can be expressed as a second order tensor in the same 9 directions.

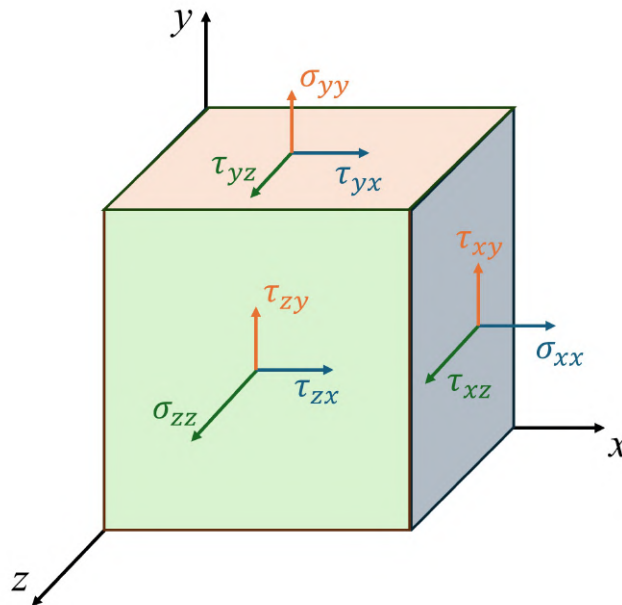


Figure G.1: Schematic of the directions defining the stress tensor

The stress tensor for a three-dimensional state can be represented in matrix form as:

$$\boldsymbol{\sigma} = \begin{bmatrix} \sigma_{xx} & \tau_{xy} & \tau_{xz} \\ \tau_{yx} & \sigma_{yy} & \tau_{yz} \\ \tau_{zx} & \tau_{zy} & \sigma_{zz} \end{bmatrix} \quad (\text{G.1})$$

Where:

- σ_{xx} , σ_{yy} , and σ_{zz} are the normal stresses acting on the x, y, and z faces of the element, respectively.
- τ_{xy} , τ_{yz} , τ_{zx} , etc., are the shear stresses acting on the respective faces of the element.

In an isotropic, linear and homogeneous material, Hooke's law describes the relationship between stress ($\boldsymbol{\sigma}$) and strain ($\boldsymbol{\epsilon}$) [330, 331].

$$\boldsymbol{\sigma} = \lambda \text{tr}(\boldsymbol{\epsilon})\mathbf{I} + 2\mu\boldsymbol{\epsilon} \quad (\text{G.2})$$

Where:

- $\boldsymbol{\sigma}$ is the stress tensor,
- λ and μ are Lamé's first and second parameters, respectively, which are material properties,
- $\text{tr}(\boldsymbol{\epsilon})$ is the trace of the strain tensor $\boldsymbol{\epsilon}$, representing volumetric strain,
- \mathbf{I} is the identity matrix,
- $\boldsymbol{\epsilon}$ is the strain tensor.

The strain tensor $\boldsymbol{\epsilon}$, in turn, is related to the displacement field \mathbf{u} in the material by:

$$\boldsymbol{\epsilon} = \frac{1}{2} (\nabla\mathbf{u} + (\nabla\mathbf{u})^T)$$

This relation defines how the displacements in the material (due to applied loads) translate into strains, which are then related to stresses through the material's constitutive relations.

The von Mises stress is derived from the distortion energy theory. It is also known as the equivalent stress or octahedral shear stress, and is used to simplify the three-dimensional stress state at a point into a single value [332]. This makes it easier to compare against the yield stress of the material or the stress in different objects.

Mathematically, the von Mises stress (σ_{vm}) for a three-dimensional state of stress can be expressed as:

$$\sigma_{vm} = \sqrt{\frac{1}{2} [(\sigma_x - \sigma_y)^2 + (\sigma_y - \sigma_z)^2 + (\sigma_z - \sigma_x)^2] + 3(\tau_{xy}^2 + \tau_{yz}^2 + \tau_{zx}^2)} \quad (\text{G.3})$$

In practice, for complex geometries and loading conditions, the stress tensor components are usually computed numerically using methods such as the finite element method (FEM) [333]. FEM involves discretizing the material into a mesh of elements and applying the equilibrium equations, boundary conditions, and constitutive relations to solve for the unknowns (e.g., displacements), from which stresses and strains are computed. In this work the problem was solved using COMSOL multiphysics.